

Advanced technologies for industrial wastewater reclamation

Edited by

Shihai Deng, Jiangyong Hu, Say Leong Ong, Jie Han and Qilin Li

Published in

Frontiers in Environmental Science



FRONTIERS EBOOK COPYRIGHT STATEMENT

The copyright in the text of individual articles in this ebook is the property of their respective authors or their respective institutions or funders. The copyright in graphics and images within each article may be subject to copyright of other parties. In both cases this is subject to a license granted to Frontiers.

The compilation of articles constituting this ebook is the property of Frontiers.

Each article within this ebook, and the ebook itself, are published under the most recent version of the Creative Commons CC-BY licence. The version current at the date of publication of this ebook is CC-BY 4.0. If the CC-BY licence is updated, the licence granted by Frontiers is automatically updated to the new version.

When exercising any right under the CC-BY licence, Frontiers must be attributed as the original publisher of the article or ebook, as applicable.

Authors have the responsibility of ensuring that any graphics or other materials which are the property of others may be included in the CC-BY licence, but this should be checked before relying on the CC-BY licence to reproduce those materials. Any copyright notices relating to those materials must be complied with.

Copyright and source acknowledgement notices may not be removed and must be displayed in any copy, derivative work or partial copy which includes the elements in question.

All copyright, and all rights therein, are protected by national and international copyright laws. The above represents a summary only. For further information please read Frontiers' Conditions for Website Use and Copyright Statement, and the applicable CC-BY licence.

ISSN 1664-8714
ISBN 978-2-8897-6709-0
DOI 10.3389/978-2-8897-6709-0

About Frontiers

Frontiers is more than just an open access publisher of scholarly articles: it is a pioneering approach to the world of academia, radically improving the way scholarly research is managed. The grand vision of Frontiers is a world where all people have an equal opportunity to seek, share and generate knowledge. Frontiers provides immediate and permanent online open access to all its publications, but this alone is not enough to realize our grand goals.

Frontiers journal series

The Frontiers journal series is a multi-tier and interdisciplinary set of open-access, online journals, promising a paradigm shift from the current review, selection and dissemination processes in academic publishing. All Frontiers journals are driven by researchers for researchers; therefore, they constitute a service to the scholarly community. At the same time, the *Frontiers journal series* operates on a revolutionary invention, the tiered publishing system, initially addressing specific communities of scholars, and gradually climbing up to broader public understanding, thus serving the interests of the lay society, too.

Dedication to quality

Each Frontiers article is a landmark of the highest quality, thanks to genuinely collaborative interactions between authors and review editors, who include some of the world's best academicians. Research must be certified by peers before entering a stream of knowledge that may eventually reach the public - and shape society; therefore, Frontiers only applies the most rigorous and unbiased reviews. Frontiers revolutionizes research publishing by freely delivering the most outstanding research, evaluated with no bias from both the academic and social point of view. By applying the most advanced information technologies, Frontiers is catapulting scholarly publishing into a new generation.

What are Frontiers Research Topics?

Frontiers Research Topics are very popular trademarks of the *Frontiers journals series*: they are collections of at least ten articles, all centered on a particular subject. With their unique mix of varied contributions from Original Research to Review Articles, Frontiers Research Topics unify the most influential researchers, the latest key findings and historical advances in a hot research area.

Find out more on how to host your own Frontiers Research Topic or contribute to one as an author by contacting the Frontiers editorial office: frontiersin.org/about/contact

Advanced technologies for industrial wastewater reclamation

Topic editors

Shihai Deng — Xi'an Jiaotong University, China

Jiangyong Hu — National University of Singapore, Singapore

Say Leong Ong — National University of Singapore, Singapore

Jie Han — Xi'an Jiaotong University, China

Qilin Li — Rice University, United States

Citation

Deng, S., Hu, J., Ong, S. L., Han, J., Li, Q., eds. (2023). *Advanced technologies for industrial wastewater reclamation*. Lausanne: Frontiers Media SA.
doi: 10.3389/978-2-8897-6709-0

Table of contents

- 04 **Editorial: Advanced technologies for industrial wastewater reclamation**
Shihai Deng, Jiangyong Hu, Say-Leong Ong, Qilin Li and Jie Han
- 07 **Cultivation of *Chlorella vulgaris* in Membrane-Treated Industrial Distillery Wastewater: Growth and Wastewater Treatment**
Feng Li, David Kwame Amenorfenyo, Yulei Zhang, Ning Zhang, Changling Li and Xianghu Huang
- 16 **Catalytic Oxidation of Methylene Blue by Attapulgite/TiO₂**
Jianping Shang, Yu Jiang, Xiaoping Qin, Bin Zhao and Xuefei Li
- 25 **Decomplexation Performance of Cu–EDTA and Parameter Optimization by Three-Dimensional Electro-Fenton**
Yameng Ma, Xiao Huang, Qi Han, Jianghua Yu, Fengjiao Yu and Jia Zhu
- 35 **Calcium-Mediated Regulation Promotes the Biofilm Formation of Two Novel Pyridine-Degrading Bacteria**
Fuzhong Xiong, Donghui Wen and Qilin Li
- 49 **Oil Load Reduction of Oilfield-Produced Water by Applying Swirl–Cyclonic Flotation: A Pilot-Scale Investigation**
Jianfei Liu, Huihui Wang, Yongfeng Zhao, Yi Zhang, Hongbing Zhao, Weilong Zhao, Yongsheng Zhang, Xiaowei Wang, Xue Li and Ming Zhang
- 58 **Highly Effective Lead Ion Adsorption by Manganese-Dioxide-Supported Core-Shell Structured Magnetite**
Haipeng Zhang, Shiyong Chen, Yuhua Shan, Xiaoqing Qian, Yanju Yang and Juanjuan Wang
- 69 **Performance of ozonation on bisphenol a degradation: Efficiency, mechanism and toxicity control**
Qi Han, Wenyi Dong, Hongjie Wang, Boping Yu, Zijun Dong, Mu Li, Linshen Xie and Zhiguang Dai
- 83 **Application of iron–carbon microbial galvanic activated sludge combined with MBR process in the treatment of wastewater from comprehensive railway station**
Qi Zhang, Zheng Liang, Xiaotao Guan, Jingwen Liang and Pan Gao
- 91 **Contamination of per- and polyfluoroalkyl substances in the water source from a typical agricultural area in North China**
Xiaowei Wang, Hongwei Zhang, Xiaosong He, Jianfei Liu, Zhiliang Yao, Hongbin Zhao, Dayang Yu, Baosen Liu, Tianfu Liu and Weilong Zhao



OPEN ACCESS

EDITED AND REVIEWED BY

Paolo Perona,
Platform of Hydraulic Constructions (PL-
LCH), IIC, ENAC, EPFL, Switzerland

*CORRESPONDENCE

Jiangyong Hu,
✉ hujiangyong@nus.edu.sg

RECEIVED 15 March 2023

ACCEPTED 14 April 2023

PUBLISHED 19 April 2023

CITATION

Deng S, Hu J, Ong S-L, Li Q and Han J
(2023), Editorial: Advanced technologies
for industrial wastewater reclamation.
Front. Environ. Sci. 11:1187335.
doi: 10.3389/fenvs.2023.1187335

COPYRIGHT

© 2023 Deng, Hu, Ong, Li and Han. This is
an open-access article distributed under
the terms of the [Creative Commons
Attribution License \(CC BY\)](#). The use,
distribution or reproduction in other
forums is permitted, provided the original
author(s) and the copyright owner(s) are
credited and that the original publication
in this journal is cited, in accordance with
accepted academic practice. No use,
distribution or reproduction is permitted
which does not comply with these terms.

Editorial: Advanced technologies for industrial wastewater reclamation

Shihai Deng^{1,2}, Jiangyong Hu^{2*}, Say-Leong Ong², Qilin Li³ and
Jie Han¹

¹School of Human Settlements and Civil Engineering, Xi'an Jiaotong University, Xi'an, China, ²Centre for
Water Research, Department of Civil and Environmental Engineering, National University of Singapore,
Singapore, Singapore, ³Department of Civil and Environmental Engineering, Rice University, Houston, TX,
United States

KEYWORDS

industrial wastewater, pollutants disposal, resource reclamation, effluent reuse, energy
generation, nutrient and mineral recovery

Editorial on the Research Topic

Advanced technologies for industrial wastewater reclamation

Humankind is facing the significant challenge of water scarcity (Martins et al., 2020). Since 1950, the world population has doubled, and global water consumption has increased by more than 600% (Martins et al., 2020). A report by the United Nations demonstrated that two-thirds of the world's population would face water stress by the year 2025 (Ahmed, 2006). A significant fraction of the increased water consumption was attributed to the rapid growth in the industrial developments (Sathya et al., 2022). Nearly all water consumed in industries ends up as industrial wastewater (IWW). The release of IWW into the environment may adversely affect the environment and pose a health threat to humans and our ecosystem (Martins et al., 2020).

Innovative solutions are therefore needed to provide adequate treatment of IWW to meet the increasingly stringent discharge standards and explore options to obtain sufficient water to support industrial developments (Cai et al., 2021). Treating and reclaiming treated industrial effluent can be an effective option to meet both challenges. Nonetheless, IWW is far more complex than domestic sewage, containing numerous organic and inorganic pollutants and exhibiting much greater variability in wastewater characteristics (Sathya et al., 2022). As a result, employing state-of-the-art biological treatment technologies alone is often inadequate for meeting stringent discharge standards, not to mention the ability to meet water reclamation requirements (Samaei et al., 2018; Sathya et al., 2022). Alternatives such as advanced oxidation processes (AOPs, e.g., ozonation (Deng et al., 2021a; Jothinathan et al., 2021), Fenton (Cai et al., 2020a; Cai et al., 2021; Sathya et al., 2022) and photocatalytic oxidation (Thiruvengkatachari et al., 2008; Autin et al., 2013) and separation processes (e.g., membrane filtration (Deng et al., 2021b; Liu et al., 2021) and adsorption (Ambaye et al., 2020) have been used for treating recalcitrant organics. However, AOPs typically require high energy (e.g., O₃-generation in the ozonation process and UV-irradiation in the photocatalytic process) and chemical (e.g., oxidants and catalysts in the Fenton process and persulphate-based oxidation process) consumptions and therefore are expensive options (Loh et al., 2021; Wu et al., 2021; Jothinathan et al., 2022). Separation processes, on the other hand, have been used for pollutant removal and resource recovery, but innovative strategies

are still needed to reduce their costs (Ambaye et al., 2020; Liu et al., 2021). Thus, there is a need to develop innovative technologies and build upon our knowledge of existing technologies for IWW treatment and reclamation.

Beyond the development of innovative technologies, combinations of the existing technologies could also obtain considerable performance with reduced energy and chemical consumption. Deng et al. (2021b) combined catalytic ozonation processes with a membrane bioreactor (MBR) for the treatment of phenolic wastewater produced by the petrochemical industry. This combination achieved total organic carbon (TOC) and phenolic compounds removals of 98.0% and 99.4%, respectively, and decreased the membrane fouling rate of MBR by 88.2%. The pretreatment by catalytic ozonation in the combined process reduced the acute biotoxicity of the wastewater by 79.2% and increased the 5-day biochemical oxygen demand to chemical oxygen demand ratio (BOD₅/COD) by 2.45-folds, which significantly contributed to the performance enhancement and membrane fouling mitigation of MBR (Deng et al., 2021b). Tong et al. (2018) combined the adsorption processes by lignite-activated coke (LAC-adsorption) and immobilized biological filter (IBF) in the treatment of heavy oil wastewater on a pilot-scale system. The combined process obtained a dissolved organic carbon (DOC) removal of 85.9%, where most biorefractory compounds were removed by the pre-LAC-adsorption process and benefitted the subsequent IBF, and the post-LAC-adsorption process contributed to amides removal (Tong et al., 2018). Cai et al. (2020b) combined the fluidized bed reactor-based Fenton processes (FBR-Fenton) with a biological activated carbon (BAC) system for the reclamation of reverse osmosis concentrate and obtained a COD removal of 69% with a low average effluent COD of 26 mg/L. In the combined process, the FBR-Fenton processes markedly contributed to the degradation of humic acid and fulvic acid and improved the BOD₅/COD ratio by 4.2–10.0 times, which strengthened the performance of the BAC system (Cai et al., 2020b).

In addition to the IWW treatment and effluent reuse, the recovery of valuable resources is also essential under the global trends of the circular economy (Goglio et al., 2019; Soltangheisi et al., 2019; Cheng et al., 2022). Wastewater is a rich source of organic carbon, nutrients (e.g., nitrogen N) and phosphorus P) and metals (e.g., potassium K), copper (Cu) and silver (Ag). Concerning energy generation, Heidrich et al. precisely determined the energy content of domestic wastewater (DWW) through freeze-drying samples to minimize the loss of volatiles and organic matters. Their results indicated that DWW contains an energy generation potential of 7.6 kJ/L (Heidrich et al., 2011). Wang et al. also estimated that the energy content of DWW related to COD was 23 W per capita (Wang et al., 2017). Similar assessments on IWW are lacking, but a significant energy recovery potential of organic IWW can be estimated due to their normally much higher organic carbon concentration. In terms of nutrients, it has been estimated that more than 20% of consumed P from minerals is excreted by human activities (Cordell et al., 2009). Robles et al. estimated that the global resource recovery from waste streams could essentially retrieve 50% of the P consumed by humans. Additionally, an N to P mass ratio of over 3 has been widely observed in research done on various waste streams, which indicated that more N than P is lost during

the wastewater treatment (Batstone et al., 2015; Robles et al., 2020). Some kinds of IWW contain extremely high concentrations of N and P compared to DWW (Bokun et al., 2020; Deng et al., 2022). For example, in coking wastewater, the ammonia concentration is usually in a high range of 500–2,000 mg N/L, and it could further research the range of 3,500–10,000 mg N/L in the semi-coking wastewater when the pyrolytic temperature of coal was reduced to 600°C–800°C (Ma et al., 2017; Bokun et al., 2020; Huang et al., 2021). P concentration is usually high in the waste streams, such as fertilizer production wastewater, paper pulping and making wastewater and some of the chemical industry wastewater (Bian et al., 2011; Hutnik et al., 2013; Gentili & Sveriges, 2014). Specifically, the P concentration in the wastewater from the phosphorus mineral fertilizers industry (Hutnik et al., 2013) and the wastewater from PolyTH production industry (Bian et al., 2011) could reach 445 mg P/L and 15,000–18,000 mg P/L, respectively. Metal ions are also rich in IWW, such as K and Mg are rich in dairy wastewater and manure wastewater (Goglio et al., 2019), and Ag and Cu are rich in deplating wastewater (Gu et al., 2020). Based on the abovementioned information, IWW is an abundant source of energy, nutrients and metals to be recovered and reused, which could significantly contribute to the circular economy. Furthermore, the worldwide increase in consumption and the gradual depletion of natural resources have emphasized the need for resource recovery from waste streams (Goglio et al., 2019; Soltangheisi et al., 2019). Therefore, instead of releasing resource-rich waste streams into the water bodies increasing the environmental risk, this resource recovery can lead to multiple benefits, such as generating valuable products, greatly improving wastewater treatment processes, reclaiming wastewater, maintaining the ecological balance of aquatic environments and reducing the carbon footprint in wastewater disposal. In order to fulfill this vision, novel technologies for resource recovery from IWW need to be developed by the research community.

This Research Topic focuses on novel technologies for IWW treatment for the purpose of resource reclamation. This includes the dissemination of knowledge generated from studies regarding the development, optimization, and applications of advanced technologies aiming at the treatment and resource recovery of IWW. It also aims to address an important aspect of sustainable water management with an emphasis on meeting the needs of the industrial sector from a global perspective.

We hope this Research Topic can contribute significantly to both the research and the engineering communities for managing IWW treatment and reclamation.

Author contributions

All authors listed have made a substantial, direct and intellectual contribution to the work, and approved it for publication.

Conflict of interest

The authors declare that the research was conducted in the absence of any commercial or financial relationships that could be construed as a potential conflict of interest.

Publisher's note

All claims expressed in this article are solely those of the authors and do not necessarily represent those of their affiliated

References

- Ahmed, A. M. (2006). UNDP, 2006, beyond scarcity: Power, poverty and global water circles human development report. *Ahfad J.* 23 (2), 150.
- Ambaye, T. G., Vaccari, M., van Hullebusch, E. D., Amrane, A., and Rtimi, S. (2020). Mechanisms and adsorption capacities of biochar for the removal of organic and inorganic pollutants from industrial wastewater. *Int. J. Environ. Sci. Technol. (Tehran)* 18 (10), 3273–3294. doi:10.1007/s13762-020-03060-w
- Autin, O., Hart, J., Jarvis, P., MacAdam, J., Parsons, S. A., and Jefferson, B. (2013). The impact of background organic matter and alkalinity on the degradation of the pesticide metaldehyde by two advanced oxidation processes: UV/H₂O₂ and UV/TiO₂. *Water Res. Oxf.* 47 (6), 2041–2049. doi:10.1016/j.watres.2013.01.022
- Batstone, D. J., Hulsen, T., Mehta, C. M., and Keller, J. (2015). Platforms for energy and nutrient recovery from domestic wastewater: A review. *Chemosphere* 140, 2–11. doi:10.1016/j.chemosphere.2014.10.021
- Bian, D., Ai, S., Liu, J., Zuo, Y., and Tian, X. (2011). Treatment of phosphorus waste water using crystallization method. *J. Environ. Sci.* 23, S106–S109. doi:10.1016/S1001-0742(11)61088-7
- Bokun, C., Siyu, Y., Yangyang, W., Miyangzi, S., and Yu, Q. (2020). Intensified phenols extraction and oil removal for industrial semi-coking wastewater: A novel economic pretreatment process design. *J. Clean. Prod.* 242, 118453. doi:10.1016/j.jclepro.2019.118453
- Cai, Q. Q., Jothinathan, L., Deng, S. H., Ong, S. L., Ng, H. Y., and Hu, J. Y. (2021). “11 - Fenton- and ozone-based AOP processes for industrial effluent treatment,” in *Advanced oxidation processes for effluent treatment plants*. Editor M. P. Shah (Elsevier), 199–254.
- Cai, Q. Q., Wu, M. Y., Hu, L. M., Lee, B. C. Y., Ong, S. L., Wang, P., et al. (2020a). Organics removal and *in-situ* granule activated carbon regeneration in FBR-Fenton/GAC process for reverse osmosis concentrate treatment. *Water Res. Oxf.* 183, 116119. doi:10.1016/j.watres.2020.116119
- Cai, Q. Q., Wu, M. Y., Li, R., Deng, S. H., Lee, B. C. Y., Ong, S. L., et al. (2020b). Potential of combined advanced oxidation – biological process for cost-effective organic matters removal in reverse osmosis concentrate produced from industrial wastewater reclamation: Screening of AOP pre-treatment technologies. *Chem. Eng.* 389, 123419. doi:10.1016/j.cej.2019.123419
- Cheng, D., Ngo, H. H., Guo, W., Chang, S. W., Nguyen, D. D., Zhang, S., et al. (2022). Impact factors and novel strategies for improving biohydrogen production in microbial electrolysis cells. *Bioresour. Technol.* 346, 126588. doi:10.1016/j.biortech.2021.126588
- Cordell, D., Drangert, J.-O., and White, S. J. G. e. c. (2009). The story of phosphorus: Global food security and food for thought. *Glob. food Secur. food thought* 19 (2), 292–305. doi:10.1016/j.gloenvcha.2008.10.009
- Deng, S., Jothinathan, L., Cai, Q., Li, R., Wu, M., Ong, S. L., et al. (2021a). FeOx@GAC catalyzed microbubble ozonation coupled with biological process for industrial phenolic wastewater treatment: Catalytic performance, biological process screening and microbial characteristics. *Water Res. Oxf.* 190, 116687. doi:10.1016/j.watres.2020.116687
- Deng, S., Peng, S., Ngo, H. H., Oh, S. J.-A., Hu, Z., Yao, H., et al. (2022). Characterization of nitrous oxide and nitrite accumulation during iron (Fe(0))- and ferrous iron (Fe(II))-driven autotrophic denitrification: Mechanisms, environmental impact factors and molecular microbial characterization. *Chem. Eng. J.* 438, 135627. doi:10.1016/j.cej.2022.135627
- Deng, S., Wang, Q., Cai, Q., Ong, S. L., and Hu, J. (2021b). Efficient bio-refractory industrial wastewater treatment with mitigated membrane fouling in a membrane bioreactor strengthened by the micro-scale ZVI@GAC galvanic-cells-initiated radical generation and coagulation processes. *Water Res.* 209, 117943. doi:10.1016/j.watres.2021.117943
- Gentili, F. G., and Sveriges, I. (2014). Microalgal biomass and lipid production in mixed municipal, dairy, pulp and paper wastewater together with added flue gases. *Bioresour. Technol.* 169, 27–32. doi:10.1016/j.biortech.2014.06.061
- Goglio, A., Marzorati, S., Rago, L., Pant, D., Cristiani, P., and Schievano, A. (2019). Microbial recycling cells: First steps into a new type of microbial electrochemical technologies, aimed at recovering nutrients from wastewater. *Bioresour. Technol.* 277, 117–127. doi:10.1016/j.biortech.2019.01.039
- Gu, J. N., Liang, J., Chen, C., Li, K., Zhou, W., Jia, J., et al. (2020). Treatment of real depleting wastewater through an environmental friendly precipitation-electrodeposition-oxidation process: Recovery of silver and copper and reuse of wastewater. *Sep. Purif. Technol.* 248, 117082. doi:10.1016/j.seppur.2020.117082
- Heidrich, E. S., Curtis, T. P., and Dolfing, J. (2011). Determination of the internal chemical energy of wastewater. *Environ. Sci. Technol.* 45 (2), 827–832. doi:10.1021/es103058w
- Huang, H., Li, B., Dai, J., Wang, W., Zhang, M., and Ou, Y. (2021). Ammonia nitrogen removal from coking wastewater and high quality gypsum recovery by struvite recycling by using calcium hydroxide as decomposer. *J. Environ. Manag.* 292, 112712. doi:10.1016/j.jenvman.2021.112712
- Hutnik, N., Kozik, A., Mazieniczuk, A., Piotrowski, K., Wierzbowska, B., and Matynia, A. (2013). Phosphates (V) recovery from phosphorus mineral fertilizers industry wastewater by continuous struvite reaction crystallization process. *Water Res.* 47 (11), 3635–3643. doi:10.1016/j.watres.2013.04.026
- Jothinathan, L., Cai, Q. Q., Ong, S. L., and Hu, J. Y. (2022). Fe-Mn doped powdered activated carbon pellet as ozone catalyst for cost-effective phenolic wastewater treatment: Mechanism studies and phenol by-products elimination. *J. Hazard. Mater.* 424, 127483. doi:10.1016/j.jhazmat.2021.127483
- Jothinathan, L., Cai, Q. Q., Ong, S. L., and Hu, J. Y. (2021). Organics removal in high strength petrochemical wastewater with combined microbubble-catalytic ozonation process. *Chemosphere Oxf.* 263, 127980. doi:10.1016/j.chemosphere.2020.127980
- Liu, Y., Liu, H., and Shen, Z. (2021). Nanocellulose based filtration membrane in industrial waste water treatment: A review. *Materials* 14 (18), 5398. doi:10.3390/ma14185398
- Loh, W. H., Cai, Q. Q., Li, R., Jothinathan, L., Lee, B. C. Y., Ng, O. H., et al. (2021). Reverse osmosis concentrate treatment by microbubble ozonation-biological activated carbon process: Organics removal performance and environmental impact assessment. *Sci. total Environ.* 798, 149289. doi:10.1016/j.scitotenv.2021.149289
- Ma, X., Wang, X., Liu, Y., Gao, J., and Wang, Y. (2017). Variations in toxicity of semi-coking wastewater treatment processes and their toxicity prediction. *Ecotoxicol. Environ. Saf.* 138, 163–169. doi:10.1016/j.ecoenv.2016.09.031
- Martins, R. C., Quinta-Ferreira, R. M., Rasteiro, M. G., Dantas, R., and Gmurek, M. (2020). Editorial: Advanced processes for wastewater treatment and water reuse. *Front. Environ. Sci.* 8. doi:10.3389/fenvs.2020.611159
- Robles, A., Aguado, D., Barat, R., Borrás, L., Bouzas, A., Gimenez, J. B., et al. (2020). New frontiers from removal to recycling of nitrogen and phosphorus from wastewater in the Circular Economy. *Bioresour. Technol.* 300, 122673. doi:10.1016/j.biortech.2019.122673
- Samaei, S. M., Gato-Trinidad, S., and Altaee, A. (2018). The application of pressure-driven ceramic membrane technology for the treatment of industrial wastewaters – a review. *Sep. Purif. Technol.* 200, 198–220. doi:10.1016/j.seppur.2018.02.041
- Sathya, K., Nagarajan, K., Carlin Geor Malar, G., Rajalakshmi, S., and Raja Lakshmi, P. (2022). A comprehensive review on comparison among effluent treatment methods and modern methods of treatment of industrial wastewater effluent from different sources. *Appl. water Sci.* 12 (4), 70–27. doi:10.1007/s13201-022-01594-7
- Soltangheisi, A., Withers, P. J. A., Pavinato, P. S., Cherubin, M. R., Rossetto, R., Do Carmo, J. B., et al. (2019). Improving phosphorus sustainability of sugarcane production in Brazil. *Glob. change Biol. Bioenergy* 11 (12), 1444–1455. doi:10.1111/gcbb.12650
- Thiruvengkatachari, R., Vigneswaran, S., and Moon, I. S. (2008). A review on UV/TiO₂ photocatalytic oxidation process (Journal Review). *Korean J. Chem. Eng.* 25 (1), 64–72. doi:10.1007/s11814-008-0011-8
- Tong, K., Zhang, Z., Lin, A., Song, Q., Ji, G., Wang, D., et al. (2018). Treatment of super heavy oil wastewater by a combined process of lignite-activated coke adsorption and immobilized biological filter degradation: Performance and the relevant microbial community analysis. *J. Chem. Technol. Biotechnol.* 93 (10), 2942–2951. doi:10.1002/jctb.5650
- Wang, K., Sheng, Y., Cao, H., Yan, K., and Zhang, Y. (2017). Impact of applied current on sulfate-rich wastewater treatment and microbial biodiversity in the cathode chamber of microbial electrolysis cell (MEC) reactor. *Chem. Eng. J.* 307, 150–158. doi:10.1016/j.cej.2016.07.106
- Wu, M. Y., Cai, Q. Q., Xu, H. P., Ong, S. L., and Hu, J. Y. (2021). Simulation of FBR-Fenton/GAC process for recalcitrant industrial wastewater treatment with a computational fluid dynamics-kinetic model framework. *Water Res. Oxf.* 203, 117504. doi:10.1016/j.watres.2021.117504



Cultivation of *Chlorella vulgaris* in Membrane-Treated Industrial Distillery Wastewater: Growth and Wastewater Treatment

Feng Li[†], David Kwame Amenorfenyo[†], Yulei Zhang, Ning Zhang, Changling Li and Xianghu Huang^{*}

College of Fisheries, Guangdong Ocean University, Zhanjiang, China

OPEN ACCESS

Edited by:

Shihai Deng,
Xi'an Jiaotong University, China

Reviewed by:

Binghan Xie,
Harbin Institute of Technology, Weihai,
China
Xu Zhou,
Harbin Institute of Technology,
Shenzhen, China
Pengfei Cheng,
Ningbo University, China
Vineet Kumar,
Guru Ghasidas Vishwavidyalaya, India

*Correspondence:

Xianghu Huang
huangxh@gdou.edu.cn

[†]These authors have contributed
equally to this work and share first
authorship

Specialty section:

This article was submitted to
Water and Wastewater Management,
a section of the journal
Frontiers in Environmental Science

Received: 04 September 2021

Accepted: 08 October 2021

Published: 21 October 2021

Citation:

Li F, Amenorfenyo DK, Zhang Y,
Zhang N, Li C and Huang X (2021)
Cultivation of *Chlorella vulgaris* in
Membrane-Treated Industrial Distillery
Wastewater: Growth and
Wastewater Treatment.
Front. Environ. Sci. 9:770633.
doi: 10.3389/fenvs.2021.770633

The alcohol industry discharges large quantities of wastewater, which is hazardous and has a considerable pollution potential. Cultivating microalgae in wastewater is an alternative way of overcoming the current high cost of microalgae cultivation and an environmentally friendly treatment method for industrial effluents. The study analyzed the growth and biochemical composition of *Chlorella vulgaris* cultivated in membrane-treated distillery wastewater (MTDW) and nutrients removal efficiency. The results showed biomass productivity of $0.04 \text{ g L}^{-1} \text{ d}^{-1}$ for MTDW with the contents of content of protein, carbohydrate, and lipid at $49.6 \pm 1.4\%$, $26.1 \pm 0.6\%$, and $10.4 \pm 1.8\%$, respectively. The removal efficiencies of TN, TP, and COD were 80, 94, and 72.24% in MTDW, respectively. In addition, removal efficiencies of 100, 85.37, and 42.86% for Ca^{2+} , Mg^{2+} , and Mo^{2-} were achieved, respectively. The study added to our growing knowledge on the cultivation of *Chlorella* with wastewater, suggesting that it was feasible to cultivate *Chlorella* with MTDW and represented an economical and environmentally friendly strategy for microalgae biomass production and reuse of wastewater resources.

Keywords: wastewater treatment, microalgae, *Chlorella*, distiller wastewater, biomass production

INTRODUCTION

Industrial wastewater is one of the main sources of pollution of the water environment, and its production has a serious negative impact on the ecosystem and human life. Therefore, the fight against wastewater has become a major issue in terms of health, environment, and economy (Abdel-Raouf et al., 2012). The quality and quantity of industrial wastewater vary according to the type of industry. The metal processing industry emits chromium, nickel, zinc, cadmium, lead, iron, and titanium compounds. The printing plant releases inks and dyes (Hanchang, 2009). Wastewater from paper mills contains chloride organics and dioxins, as well as suspended solids and organic wastes (Lindholm-Lehto et al., 2015). The petrochemical industry discharges a large number of phenols and mineral oil (Évertson et al., 2018). The content of suspended solids and organic matter in wastewater from food processing plants is very high (Qasim and Mane, 2013). In contrast, distilleries produce large amounts of acidic, stubborn, and colored wastewater with high organic content (Sanjay and Jamaluddin, 2018), which may lead to the destruction of the aquatic environment causing eutrophication, affecting human health and recreational activities (Sanjay and Jamaluddin, 2018; Stutter et al., 2018; Thoré et al., 2021). The alcohol industry discharges up to 0.3 billion m^3 of high-concentration wastewater each year in China (Guo et al., 2006), which has become the second largest

source of organic pollution. Cassava alcohol wastewater is widely produced in cassava-based bioethanol industries (Quan et al., 2014). In general, about 12 tons of wastewater would be generated to produce 1 ton of cassava ethanol (Lin et al., 2016). Industrial wastewater with high organic and acidic substances many contain as high as 40,000~130,000 mg L⁻¹ chemical oxygen demand (COD) concentration (Gang et al., 2008).

The source of industrial wastewater comes with different characteristics. Hence, the treatment of industrial wastewater should be specifically designed for specific wastewater. Recently, several technologies such as photocatalysis (Al-Mamun et al., 2019), electrodialysis (Deng et al., 2020; Liu et al., 2020), iron-oxides-doped granular activated carbon catalyst (Deng et al., 2021), and Fe/C galvanic cells strengthened A2O process (Fe/C-A2O) (Peng et al., 2020) have been developed with significant effects for industrial wastewater treatment. Presently, distilleries use a multi-stage strategy in wastewater treatment, including pretreatment, secondary treatment, and tertiary treatment. Pretreatment reduces temperature of the wastewater as well as removes suspended solids of large particles in the wastewater (Yang and Wyman, 2007), while an anaerobic wastewater treatment system removed most of the organic matter in the wastewater (Sanjay and Jamaluddin, 2018). Finally, most of the N and P in the wastewater is removed through advanced treatment such as anaerobic and aerobic processes and membrane bioreactor (MBR) (Noor et al., 2013). However, the wastewater after membrane treatment still contains some amount of organic matter, nutrients, and other substances, which may be harmful to the environment. Conventional treatment methods are extensively used, they are however characterized by excessive use of chemicals, high operational and maintenance cost. These methods also generate huge amounts of sludge, thereby making conventional treatment methods environmentally and economically unfavorable (Amenorfenyo et al., 2020).

The microalgae-based wastewater treatment is an environmentally friendly wastewater treatment method, which is often used to treat secondary or tertiary wastewater and is considered one of the promising technologies for wastewater treatment. As a kind of eukaryotic green microalgae with strong photosynthesis ability, *Chlorella* is considered as one of the easily cultivated microalgae that contains high-quality protein, carotenoids, vitamins, and minerals, it has long been proposed as a healthy food substitute for humans and animals (Liu et al., 2013; Liu et al., 2014; Znad et al., 2018). The use of *Chlorella* for wastewater treatment and nutrient recovery reduces cost of wastewater treatment, and production of useful biomass (Sánchez-Zurano et al., 2021). In recent years, cultivation of microalgae especially *Chlorella vulgaris* in wastewater have attracted more and more attention. According to previous studies, *Chlorella* could remove organic contaminants, and heavy metals from as urban wastewater (Tercero et al., 2014), domestic wastewater (Aziz and Ng, 1992), textile wastewater (Chu et al., 2009), and piggery wastewater (Ji et al., 2012). However, little is known about cultivation of *Chlorella* in membrane-treated distillery wastewater (MTDW) for nutrient recovery and biomass production, and its feasibility.

In this study, we performed the biomass production of *Chlorella* coupled with the treatment of MTDW, which seeks to explore the nutrient removal efficiency, biomass production and productivity, and biochemical content of *C. vulgaris* grown in MTDW. The work sought to give useful information that will lead to the understanding of the cost-effective method of wastewater treatment and microalgae biomass production.

MATERIALS AND METHODS

Collection and Pre-Inoculation of Microalgae

Freshwater algae *C. vulgaris* was acquired from the laboratory of Ecology of Water Area and Aquaculture Environment of Fisheries College, Guangdong Ocean University, South China. The vegetative cells were grown photoautotrophically at 2000 lx (white light). The 7-day-old algal cells were collected and inoculated into 2 L Erlenmeyer flasks filled with 1 L of BG11 medium at an initial optical density of 0.2 (OD₆₈₀) in FDFF illuminated incubator 2000 lx (white light) and 25°C for 9 days.

Wastewater Collection and Analysis

The wastewater used in this study, MTDW was collected from SDIC Guangdong Bio-Energy Co., Ltd., Zhanjiang, South China. The wastewater sample was collected in a 5 L plastic container that was thoroughly pre-washed with the wastewater from the company. To reduce the decomposition of a substrate, MTDW sample was stored at 4°C before the wastewater characteristics analysis. Then wastewater was pretreated by means of filtration using a glass microfiber filter (934-AH, Whatman, United States) to remove turbidity and large particles. The filtered sample was autoclaved at 121°C for 30 min to eliminate bacteria and other algal growth inhibitors.

Determination of Dry Weight and Chlorophyll *a*

Microalgae biomass concentration were measured every 72 h. Dry weight (DW) was determined by filtering a 10 ml samples of the algal suspension through pre-weighed (m_1) filters (47 mm, 1.2 µm, Whatman). Then drying the filters (105°C, overnight) to a constant weight and weighing with microbalance (m_2). The DW (g L⁻¹) was calculated with Eq. 1.

$$DW = (m_2 - m_1) \times 10^3 / 10. \quad (1)$$

Biomass productivity (g L⁻¹ day⁻¹) was calculated with Eq. 2.

$$\text{Biomass productivity} = (DW_i - DW_0) / (t_i - t_0), \quad (2)$$

where DW_i and DW_0 represent the dry biomass (g L⁻¹) at time t_i and t_0 (day).

The pigment contents of the microalgae thus chlorophyll *a* was analyzed after extraction in 95% ethanol (w/v). Briefly, 5 ml of the suspensions were filtered and freeze-dried at -20°C for 12 h; the dried biomass was suspended in ethanol for 4 h in dark.

The suspensions were later centrifuged at 5,000 rpm for 10 min and the pigment contents of the supernatant were spectrophotometrically measured at 665 and 649 nm. The Eq. 3 was used to calculate the pigment contents (Hartmut and Alan, 1983).

$$\text{Chlorophyll } a = (13.95 \times A_{665}) - (6.88 \times A_{649}). \quad (3)$$

Carbohydrate, Protein and Lipid Quantification

Protein extractions were determined according to the modified method described in Barbarino and Lourenço (2005) and Ge et al. (2018). As follows: weigh 30 mg powder of *Chlorella*, and then add 8 ml of distillery water. After soaking for 12 h, centrifuge at 15,000 rpm (4°C) for 20 min to collect the supernatant. Then use 2.0 ml 0.1 N (or 2 M) NaOH to re-extract the concentrated pellets. After centrifugation at 15,000 rpm (21°C) for 20 min, the supernatant was collected and mixed with the previous supernatant. 10 ml of the extract was taken to determine protein concentration with the aid of Bio-Rad DC protein assay (Cat. 500-0111, Bio-Rad Laboratories, Hercules, United States). Anthrone colorimetric approach was used to assess carbohydrate and protein content of the supernatants using a Hach model DR 2800 spectrophotometer, glucose, and serum albumin were used as the standard for carbohydrate and protein.

Ge and Champagne (2016) methods were used to assess lipid content. Briefly, the microalgal suspension was harvested via centrifugation (4°C, 5000 rpm, 10 min), the bio-mass was washed twice with distillery water, and then oven-dried overnight at 60°C. A 0.1 g dry biomass of *Chlorella* was immersed in 3 ml of distillery water and vortexed at 3,000 rpm for 30 s, then placed in a water bath at 90°C for 20 min. Methanol/chloroform (extraction solution) of a proportion of 1:2 v/v was added after it attained room temperature. The lipids of sample were extracted overnight at room temperature after which, 1 ml of distillery water was added. The organic phase was collected by centrifugation (20°C, 10 min) and transferred into a pre-weighted dish. The chloroform was evaporated at 50°C, and then the extracted lipids were subjected to gravimetric analysis.

Nutrients Concentration and Removal Efficiency

All samples were filtered through filter paper (0.22 µm, Whatman) and analyzed for nutrients, TN, TP, and COD. Macro and Micronutrients were tested by Qingdao Sci-tech Innovation Quality Testing Co., Ltd. (China). Total Nitrogen (TN), Total phosphorus (TP), and COD were determined every 3 days starting from the day of inoculation. Persulfate digestion method and acid-persulfate digestion method were used for analyzing TN and TP, respectively. COD concentration was measured with a multi-functional water quality analyzer (LIANHUA, 5B-3B, China).

Nutrient removal efficiency (%) is calculated by the Eq. 4.

$$\text{Nutrient removal efficiency} = \frac{(C_0 - C_1)}{C_0} \times 100\%, \quad (4)$$

where C_0 is the nutrient concentration of the influent and C_1 is the nutrient concentration of the effluent.

FAMES Test and GC Analysis

A 0.1 g wet sample of *Chlorella* was hydrolyzed and methylated with 2 ml of 100% acetyl chloride in 20 ml of methanol solution at 90°C (Ge et al., 2018). Then, filter the sample with filter paper (90 mm, Whatman) by washing it with 10 ml of methanol. Next, use a rotary evaporator to evaporate the methanol, and then add 10 ml of hexane and vortex the sample for 5 min. Use a glass pipette (Fisherbrand™ Pasteur) to remove the hexane layer and evaporate the hexane, and then analyze the recovered FAME by gas chromatography (GC). Helium was used as a carrier gas. The temperature of the injector and detector is 260°C. The FAME peaks in the samples were identified by comparing their retention times with those of the standards (Supelco TM 37 component FAME mix, Sigma-Aldrich).

RESULTS

Microalgae Growth

C. vulgaris was cultivated in MTDW and BG11 (control) under 30°C, 4,000 lx, 40% Vinoculation/Vmedia growth condition for 15 days to assess biomass and biomass productivity. The growth curve of *C. vulgaris* was shown in Figure 1A. The algal biomass in MTDW and control are 0.65 g L⁻¹ and 0.26 g L⁻¹ with biomass productivity of 0.04 g L⁻¹ d⁻¹ (MTDW) and 0.02 g L⁻¹ d⁻¹ (control) respectively, after 15 days. This result was totally higher than the results obtained by Tan et al. (2018). The study showed maximum Chl-*a* (see Figure 1B) content in both the MTDW and the control with 6.48 ± 0.67 mg L⁻¹ and 1.80 ± 0.65 mg L⁻¹ on day 14 and day 8 respectively. However, both media showed a decreasing trend in Chl-*a*, with 5.73 ± 0.94 mg L⁻¹ and 0.76 ± 0.16 mg L⁻¹ at the end of the cultivation period. Both treatments showed totally different growth patterns. The MTDW experienced a lag phase between day 1 and 2, and the exponential growth phase was experienced in day 3 and lasted for 14 days. The stationary phase set in toward the end of the cultivation period as the nutrient concentration diminished. The control showed steady growth throughout the cultivation period. The lag phase lasted for a day while exponential growth begun on the third day and lasted up to day 14.

Biochemical Composition of *C. vulgaris* Cultivated in MTDW and BG11 Media

Table 1 depicts the biochemical composition of *C. vulgaris* biomass cultivated in MTDW and control (BG11) at the end of the treatment. As the results showed, MTDW demonstrated 2-fold higher protein content than the control. The MTDW recorded 49.6 ± 1.4% protein content compared to 22.4 ± 2.3% of the control medium. And 26.1 ± 0.6% and 29.9 ± 1.1%, and 10.4 ± 1.8% and 16.2 ± 0.4% of carbohydrate and lipids for MTDW and the control respectively. Compared with the control, the reason for the lower

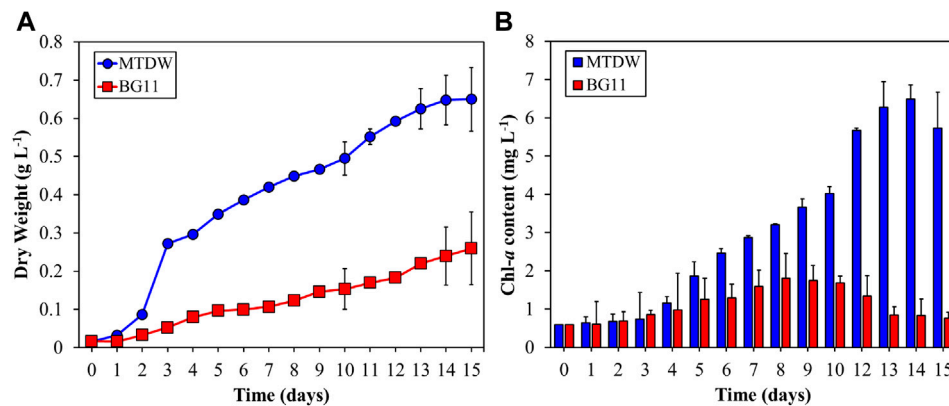


FIGURE 1 | The dry weight (A) and Chl-a content (B) of *C. vulgaris* in the MTDW group and BG11 group.

TABLE 1 | Biochemical compositions of *C. vulgaris* cultivated in MTDW and BG11.

Composition (%)	MTDW	Control
Protein	49.6 ± 1.4	22.4 ± 2.3
Carbohydrate	26.1 ± 0.6	29.9 ± 1.1
Lipid	10.4 ± 1.8	16.2 ± 0.4

TABLE 2 | Amino acids compositions and contents (g/100 g dry biomass) of *C. vulgaris* cultivated in MTDW and BG11.

Amino acids	MTDW	BG11
Aspartate	3.30	2.535
Threonine	1.15	0.75
Serine	1.55	0.85
Glutamate	6.90	4.67
Glycine	3.16	2.31
Alanine	4.16	3.350
Valine	2.89	2.30
Isoleucine	2.12	1.40
Leucine	4.25	3.48
Tyrosine	1.29	0.50
Phenylalanine	2.14	1.35
Lysine	4.46	3.345
Histidine	1.04	0.61
Arginine	5.92	3.900
Proline	2.49	1.21

carbohydrate and lipid content in MTDW may be related to the light intensity. This is in agreement with a similar result obtained by Qiu et al. (2019). It is however clear that MTDW can promote protein production in *C. vulgaris* than BG11 medium. This result was slightly higher than that of Miao et al. (2016). It is documented that higher nitrogen content induces algae growth that could lead to accumulation of amino acid (Martínez et al., 2000). *C. vulgaris* showed higher biomass growth in MTDW than BG11 which translated into higher protein production.

The amino acid content and composition were analyzed in MTDW and BG11 at the end of the cultivation. As shown in

TABLE 3 | Fatty acid compositions and contents (g/100 g dry biomass) of *C. vulgaris* cultivated in MTDW and BG11.

Fatty acid	MTDW	BG 11
Myristic Acid (14:0)	0.11	0.14
Pentadecanoic Acid (15:0)	0.001	0.001
Palmitic Acid (16:0)	0.139	0.312
Palmitoleic Acid (16:1)	0.012	0.03
Margaric Acid (17:0)	0.001	0.031
Oleic Acid (18:1)	0.43	0.80
Stearic Acid (18:0)	0.016	0.013
Linoleic Acid (18:2, ω-6)	0.137	0.169
Arachidonic Acid (20:0)	0.044	0.036
γ-Linolenic Acid (18:2)	0.003	0.003
α-Linolenic Acid (18:3)	0.249	0.218
Behenic Acid (22:0)	0.004	0.004
Erucic Acid	0.068	0.078
11,14,17-Eicosatrienoic Acid (20:5 ω-3)	0.043	0.053
Arachidonic Acid	0.002	0.002
13-16-Docosadienoic Acid (22:6, ω-3)	0.003	0.003
Lignoceric Acid	0.004	0.004
15-Tetracosenoic Acid	0.002	0.002

Table 2, all tested amino acids in the MTDW group were higher than those in the control group.

GC analysis of fatty acid composition *C. vulgaris* in both MTDW and the control are shown in **Table 3**. The contents of Myristic Acid, Palmitic Acid, Margaric Acid, Oleic Acid, Linoleic Acid, Erucic Acid, and 11,14,17-Eicosatrienoic Acid in the MTDW group were lower than those in the control group, and the contents of Palmitoleic Acid, Stearic Acid, Arachidonic Acid, and α-Linolenic Acid were higher than those in the control group. Pentadecanoic Acid, γ-Linolenic Acid, Behenic Acid, Arachidonic Acid, 13-16-Docosadienoic Acid, Lignoceric Acid, and 15-Tetracosenoic Acid were similar in both MTDW and the control.

MTDW Treatment Using *C. vulgaris*

TN, TP, and COD Removal

The concentration of TN, TP, and COD were presented in **Figure 2**. Nitrogen, is the main component of algal proteins and enzymes catalyst, and are responsible for microalgae

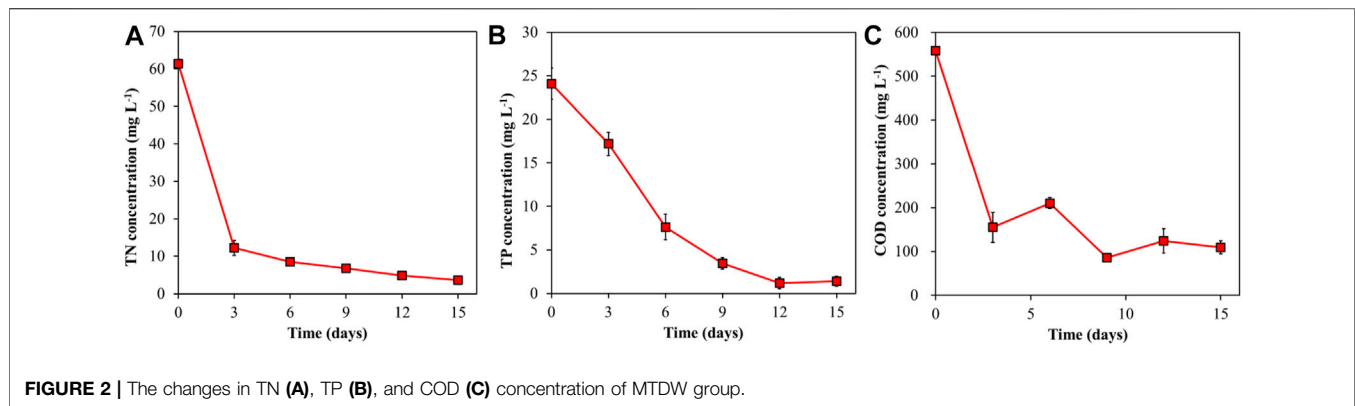


TABLE 4 | Macro/micro nutrient concentrations and RE values in MTDW.

Nutrient	Initial concentration (mg L ⁻¹)	Final concentration (mg L ⁻¹)	Removal efficiency (%)
Macro			
Na ⁺	269	253	5.23
K ⁺	1,020	980	3.92
Ca ²⁺	0.01	0.00	100
Mg ²⁺	18.8	2.75	85.37
Micro			
Fe ³⁺	1.8	1.52	15.56
Zn ²⁺	nd	nd	
Mn ²⁺	nd	nd	
As ³⁺	0.03	0.02	33.33
B ⁻	0.3	0.2	33.33
Mo ²⁻	0.07	0.04	42.86
Pb ²⁺	0.03	0.02	33.33
Cu ²⁺	0.18	0.13	27.78

nd: not detected.

growth, photosynthesis and metabolism (Kong et al., 2021). The study showed 80% TN removal efficiency. However, the highest removal rate was observed on the exponential growth phase. This coincides with a study reported by Iasimone et al. (2018).

Phosphorus is another key element for microalgae growth and other cellular activities (energy transfer and biosynthesis of nucleic acids) (Kong et al., 2021). Affected by the utilization of *C. vulgaris*, TP concentration decreased steadily within the first 12 days until stable on day 15. Affected by *C. vulgaris*, 94% TP removal efficiency was recorded at the end of cultivation period. Based on the results, phosphorus (TP) removal could directly be affected by *C. vulgaris* growth due to culture conditions. Asian and Kapdan (2006) reported 78% phosphate removal efficiency for *C. vulgaris* cultivation at 7.7 mg L⁻¹ initial concentration, less than 30% removal efficiency at higher concentration, this is clear that cultivation conditions of microalgae could affect phosphorus removal efficiency.

COD concentration (Figure 2C) varied during the period of measurement. There was a slide increase in concentration on day 6 and day 9. Again, the highest COD removal was recorded at the exponential growth phase of *C. vulgaris* with 72.24% removal efficiency. It was observed from the results that COD in MTDW was effectively utilized by *C. vulgaris*.

Macro and Micronutrient Removal

As shown in Table 4, at the end of the cultivation period, removal efficiency obtained for macronutrients ranged between 3.92 and 100% compared to 15.56–42.86% for micronutrients. Ca²⁺ reduced from the initial concentration of 0.01 mg L⁻¹ to 0.00 mg L⁻¹ in MTDW with a removal efficiency of 100%. The concentration of Mg²⁺ reduced from 18.8 mg L⁻¹ to 2.75 mg L⁻¹, and the removal efficiency reached 85.37%. The concentration of Na⁺ and K⁺ decreased from 269 mg L⁻¹ to 1,020 mg L⁻¹–253 mg L⁻¹ and 980 mg L⁻¹, and the corresponding removal efficiencies were 5.59 and 3.92%, respectively. For micronutrients, Mo²⁻ had the highest removal efficiency of 42.86%, and the concentration reduced from 0.07 mg L⁻¹ to 0.04 mg L⁻¹. Followed by As³⁺, B⁻, and Pb²⁺, their concentrations were reduced from 0.03 mg L⁻¹, 0.30 mg L⁻¹, and 0.03 mg L⁻¹ to 0.02 mg L⁻¹, 0.20 mg L⁻¹, and 0.02 mg L⁻¹, respectively, and the corresponding removal efficiencies were all 33.3%. The concentration of Cu²⁺ and Fe³⁺ in MTDW decreased from the initial 0.18 mg L⁻¹ and 1.80 mg L⁻¹ to 0.13 mg L⁻¹ and 1.52 mg L⁻¹, and the removal efficiency reached 27.78 and 15.56%, which were lower than other micronutrients. In

addition, Zn^{2+} and Mn^{2+} were not detected in this experiment.

DISCUSSION

Microalgae is a single-cell bioreactor driven by sunlight that converts carbon dioxide into potential proteins, lipids, carbohydrates, and high-value biological compounds, in the presence of a sufficient amount of nitrogen, phosphorous, and some trace elements. By 2024, the overall market potential of algae-based products expected to reach approximately USD 1.143 billion (Mehta et al., 2018). Meanwhile, the viable market potential of microalgae in the phytoremediation of wastewater and biofuels is currently increasing (Mustafa et al., 2021). Wastewater treatment with microalgae has been considered an environmentally sound bioremediation method and applied for more than 60 years (Jing et al., 2007). Many microalgae can grow effectively under wastewater conditions by utilizing the rich inorganic nitrogen and phosphorus in wastewater, such as *Desmodesmus* sp. (Benítez et al., 2018), *Scenedesmus* sp. (Han et al., 2020), *Acutodesmus dimorphus* (Chokshi et al., 2016), *C. vulgaris* (Lv et al., 2018; Mujtaba et al., 2018), and so on. Due to its rich in protein and other nutrients, bio-safety, and the feasibility of large-scale outdoor cultivation and maintenance, *Chlorella* has become one of the most in-depth studies of microalgae in biomass production and wastewater treatment (Liu and Chen, 2014). Previous studies have shown that *Chlorella* can grow and produce biomass in wastewater such as urban wastewater (Tercero et al., 2014), domestic wastewater (Aziz and Ng, 1992), textile wastewater (Chu et al., 2009), piggy wastewater (Ji et al., 2012), etc. Our study showed that cultivating *Chlorella* with MTDW was also a feasible strategy.

Although *Chlorella* is easily adaptable to different wastewater media, the nutrients in the wastewater significantly affect the growth of microalgae and the production of biomass (Cai et al., 2013). When wastewater is used as a nutrient source for wastewater-based microalgae cultivation, carbon: nitrogen (C: N) and carbon: phosphorus (C:P) ratios could be considered (Chiu et al., 2015). Lee and Lee (2002) pointed out that *Chlorella kessleri* culture could successfully remove high concentrations of nitrogen from wastewater supplemented with glucose, indicating that sufficient carbon source supply was beneficial to the utilization of nitrogen and phosphorus. Chui et al. (2015) suggested that the carbon limitation in wastewater could be overcome by adding waste CO_2 , such as flue gas. In addition, the typical N/P ratio for the optimal conditions for microalgal biomass production is 8:1 (Chui et al., 2015). However, the N/P ratio of MTDW is close to 5:2, which means that the nitrogen source in the wastewater would be another limiting factor for microalgae growth. According to Chiu et al. (2015), the biomass productivity of *Chlorella* in different wastewater ranged from $0.029 \text{ g L}^{-1} \text{ d}^{-1}$ to $0.64 \text{ g L}^{-1} \text{ d}^{-1}$. In contrast, $0.04 \text{ g L}^{-1} \text{ d}^{-1}$ biomass productivity of *Chlorella* cultured in MTDW is not high, indicating that the use of MTDW to

cultivate *Chlorella* to produce biomass still has much room for improvement.

Due to microalgae can use nutrients in wastewater to promote their growth, microalgal are particularly useful for reducing the concentration of inorganic nitrogen and phosphorus of wastewater (Ahluwalia and Goyal, 2007). Previous studies have shown that *Chlorella* has a very significant removal effect on nitrogen, phosphorus, and COD in different wastewater (Lam et al., 2017; Benítez et al., 2018; Lv et al., 2018; Mujtaba et al., 2018). However, the nutrient concentration of wastewater from different sources is different, which has a direct impact on the removal of nutrients. Kumar et al. (2019) reported that the nitrogen removal efficiency of *Chlorella* in sewage wastewater (38%) was lower than that of kitchen wastewater (67%), while the removal efficiency of phosphorus (88%) is higher than that of kitchen wastewater (75%). In this study, the removal rate of TP in MTDW by *Chlorella* reached 94%, the removal rate of TN was 80%, and the removal rate of COD exceeded 70%. These results indicate that *Chlorella* was very effective in MTDW treatment to reduce the organic and inorganic nutrients released into natural water, thereby preventing eutrophication problems.

Many studies have shown that utilizing microalgae could effectively remove metal elements from wastewater (Cabanelas et al., 2013; Cho et al., 2013; Zhu et al., 2013). Some metal ions can be attached to the cell surface through one or more surface complexation, ion exchange, and redox (Sheng et al., 2004; Vinod et al., 2010). Biosorption also involves cell metabolism and other processes, during which metal ions enter the cell through metal transporters, and are finally stored in vacuoles or organelles (Mehta and Gaur, 2005; Flórez-Miranda et al., 2017). *Chlorella* has been reported to remove many metals from wastewater, including Al, Ca, Cd, Cu, Fe, Mg, Mn, Ni, Ur, and Zn (Sandau et al., 1996; Lau et al., 1999; Chong et al., 2000; Mehta and Gaur, 2001; Mehta and Gaur, 2005; Wang et al., 2009). Similar to previous studies' conclusions, our study shown that *Chlorella* could effectively remove Ca, Mg, Mo, Fe, As, B, Pb, and Cu in distillery wastewater.

Cultivation of microalgae in large quantities is challenged by the high cost of nutrients and freshwater. According to (Kadir et al., 2018), the cultivation of microalgae in wastewater is an alternative way of overcoming the current high cost of microalgae cultivation. Slade and Bauen (2013) estimated more than 50% reduction in production cost by cultivation microalgae in wastewater as a nutrient, CO_2 and freshwater source. The composition of MTDW is stable and could be used for *Chlorella* cultivation without complicated treatment, which can effectively reduce the cost of *Chlorella* cultivation. On the other hand, *Chlorella* can remove nutrients, organic matter, and metals from MTDW. These substances may lead to the destruction of the aquatic environment causing eutrophication, affecting human health and recreational activities (Stutter et al., 2018). In addition, because biomass is rich in protein and fatty acids, *C. vulgaris* could be cultivated in MTDW as a high-quality protein source in aquaculture.

CONCLUSION

The growth and biochemical composition of *C. vulgaris* cultivated in MTDW and nutrients removal efficiency from the wastewater were analyzed. After cultivated 15 days in MTDW, 0.65 g L⁻¹ algal biomass with biomass productivity of 0.04 g L⁻¹ d⁻¹ were obtained. The protein content, carbohydrate, and lipids reached 49.6 ± 1.4%, 26.1 ± 0.6%, and 10.4 ± 1.8%, respectively. 94% of phosphorus and 80% of nitrogen were removed from MTDW, and the removal efficiency of COD reached 72.24%. In addition, there was the highest removal efficiency of Ca²⁺ in MTDW with recording a 100%. Followed by Mg²⁺, an 85.37% removal efficiency was reached. The removal efficiency of other nutrients Na⁺, K⁺, Fe³⁺, As³⁺, B⁻, Mo²⁻, and Cu²⁺ obtained ranged 3.92–42.86%. This study proved that it was feasible to cultivate *Chlorella* with MTDW and represented an economical and environmentally friendly *Chlorella* cultivation strategy. There appears to be a great potential for *Chlorella* in the

area of tertiary distillery wastewater treatment. The feasibility of applying it to full-scale requires further research in culture strategy to maximize biomass production and improve the removal efficiency of nutrients in wastewater.

DATA AVAILABILITY STATEMENT

The original contributions presented in the study are included in the article/Supplementary Material, further inquiries can be directed to the corresponding author.

AUTHOR CONTRIBUTIONS

FL: Data curation, methodology, writing-original draft, writing-review and editing; DA: Data curation, investigation, writing-original draft; YZ: Methodology; NZ: Methodology; CL: Project administration; XH: Project administration, resources.

REFERENCES

- Abdel-Raouf, N., Al-Homaidan, A. A., and Ibraheem, I. B. M. (2012). Microalgae and Wastewater Treatment. *Saudi J. Biol. Sci.* 19 (3), 257–275. doi:10.1016/j.sjbs.2012.04.005
- Ahluwalia, S. S., and Goyal, D. (2007). Microbial and Plant Derived Biomass for Removal of Heavy Metals from Wastewater. *Bioresour. Techn.* 98, 2243–2257. doi:10.1016/j.biortech.2005.12.006
- Al-Mamun, M. R., Kader, S., Islam, M. S., and Khan, M. Z. H. (2019). Photocatalytic Activity Improvement and Application of UV-TiO₂ Photocatalysis in Textile Wastewater Treatment: A Review. *J. Environ. Chem. Eng.* 7 (5), 103248–103437. doi:10.1016/j.jece.2019.103248
- Amenorfenyo, D. K., Huang, X., Li, C., Li, F., Zeng, Q., Zhang, N., et al. (2020). A Review of Microalgae and Other Treatment Methods of Distillery Wastewater. *Water Environ. J.* 34, 988–1002. doi:10.1111/wej.12552
- Aslan, S., and Kapdan, I. K. (2006). Batch Kinetics of Nitrogen and Phosphorus Removal from Synthetic Wastewater by Algae. *Ecol. Eng.* 28 (1), 64–70. doi:10.1016/j.ecoleng.2006.04.003
- Aziz, M. A., and Ng, W. J. (1992). Feasibility of Wastewater Treatment Using the Activated-Algae Process. *Bioresour. Techn.* 40, 205–208. doi:10.1016/0960-8524(92)90143-L
- Barbarino, E., and Lourenço, S. O. (2005). An Evaluation of Methods for Extraction and Quantification of Protein from Marine Macro- and Microalgae. *J. Appl. Phycol.* 17 (5), 447–460. doi:10.1007/s10811-005-1641-4
- Benítez, M. B., Champagne, P., Ramos, A., Torres, A. F., and Ochoa-Herrera, V. (2018). Wastewater Treatment for Nutrient Removal with Ecuadorian Native Microalgae. *Environ. Techn.* 40, 2977–2985. doi:10.1080/09593330.2018.1459874
- Cabanelas, I. T. D., Ruiz, J., Arbib, Z., Chinalia, F. A., Garrido-Pérez, C., Rogalla, F., et al. (2013). Comparing the Use of Different Domestic Wastewaters for Coupling Microalgal Production and Nutrient Removal. *Bioresour. Techn.* 131, 429–436. doi:10.1016/j.biortech.2012.12.152
- Cai, T., Park, S. Y., and Li, Y. (2013). Nutrient Recovery from Wastewater Streams by Microalgae: Status and Prospects. *Renew. Sust. Energ. Rev.* 19, 1364–1371. doi:10.1016/j.rser.2012.11.030
- Chiu, S., Kao, C., Chen, T., Chang, Y., Kuo, C., and Lin, C. (2015). Cultivation of Microalgal *Chlorella* for Biomass and Lipid Production Using Wastewater as Nutrient Resource. *Bioresour. Techn.* 184, 179–189. doi:10.1016/j.biortech.2014.11.080
- Cho, S., Lee, N., Park, S., Yu, J., Luong, T. T., Oh, Y. K., et al. (2013). Microalgae Cultivation for Bioenergy Production Using Wastewaters from A Municipal WWTP as Nutritional Sources. *Bioresour. Techn.* 131, 515–520. doi:10.1016/j.biortech.2012.12.176
- Chokshi, K., Pancha, I., Ghosh, A., and Mishra, S. (2016). Microalgal Biomass Generation by Phycoremediation of Dairy Industry Wastewater: An Integrated Approach towards Sustainable Biofuel Production. *Bioresour. Techn.* 221, 455–460. doi:10.1016/j.biortech.2016.09.070
- Chong, A. M. Y., Wong, Y. S., and Tam, N. F. Y. (2000). Performance of Different Microalgal Species in Removing Nickel and Zinc from Industrial Wastewater. *Chemosphere* 41, 251–257. doi:10.1016/S0045-6535(99)00418-X
- Chu, W. L., See, Y. C., and Phang, S. M. (2009). Use of Immobilised *Chlorella Vulgaris* for the Removal of Colour from Textile Dyes. *J. Appl. Phycol.* 21, 641–648. doi:10.1007/s10811-008-9396-3
- Deng, S., Jothinathan, L., Cai, Q., Li, R., Wu, M., Ong, S. L., et al. (2021). FeOx@GAC Catalyzed Microbubble Ozonation Coupled with Biological Process for Industrial Phenolic Wastewater Treatment: Catalytic Performance, Biological Process Screening and Microbial Characteristics. *Water Res.* 190, 116687–121354. doi:10.1016/j.watres.2020.116687
- Deng, S., Peng, S., Xie, B., Yang, X., Sun, S., Yao, H., et al. (2020). Influence Characteristics and Mechanism of Organic Carbon on Denitrification, N₂O Emission and NO₂⁻ Accumulation in the Iron [Fe(0)]-Oxidizing Supported Autotrophic Denitrification Process. *Chem. Eng. J.* 393, 124736–128947. doi:10.1016/j.cej.2020.124736
- Flórez-Miranda, L., Cañizares-Villanueva, R. O., Melchy-Antonio, O., Martínez-Jerónimo, F., and Flores-Ortiz, C. M. (2017). Two Stage Heterotrophy/Photoinduction Culture of *Scenedesmus Incrassatus*: Potential for Lutein Production. *J. Biotechnol.* 262, 67–74. doi:10.1016/j.biortec.2017.09.002
- Gang, L., Li, X., Qi, Z., and Sun, J. (2008). Status Quo and Development of the Resource Recycling Treatment Technologies of Cassava Ethanol Wastewater. *Ind. Water Treat.* 4 (08), 1–5. (In Chinese).
- Ge, S., and Champagne, P. (2016). Nutrient Removal, Microalgal Biomass Growth, Harvesting and Lipid Yield in Response to Centrate Wastewater Loadings. *Water Res.* 88, 604–612. doi:10.1016/j.watres.2015.10.054
- Ge, S., Qiu, S., Tremblay, D., Viner, K., Champagne, P., and Jessop, P. G. (2018). Centrate Wastewater Treatment with *Chlorella Vulgaris*: Simultaneous Enhancement of Nutrient Removal, Biomass and Lipid Production. *Chem. Eng. J.* 342, 310–320. doi:10.1016/j.cej.2018.02.058
- Guo, H. C., Chen, B., Yu, X. L., Huang, G. H., Liu, L., and Nie, X. H. (2006). Assessment of Cleaner Production Options for Alcohol Industry of China: A Study in the Shouguang Alcohol Factory. *J. Clean. Prod.* 14 (1), 94–103. doi:10.1016/j.jclepro.2004.07.006
- Han, J., Thomsen, L., Pan, K., Wang, P., Wawilow, T., Osundeko, O., et al. (2020). Treating Wastewater by Indigenous Microalgae Strain in Pilot Platform Located inside a Municipal Wastewater Treatment Plant. *Environ. Techn.* 41, 3271. doi:10.1080/09593330.2019.1604816
- Hanchang, S. H. I. (2009). Industrial Wastewater-Types, Amounts and Effects. *Point Sourc. Pollut. Local Effects Their Control.* 2, 191–203.

- Hansen, É., Rodrigues, M. A. S., Aragão, M. E., and de Aquim, P. M. (2018). Water and Wastewater Minimization in A Petrochemical Industry through Mathematical Programming. *J. Clean. Prod.* 172, 1814–1822. doi:10.1016/j.jclepro.2017.12.005
- Hartmut, K., and Alan, R. W. (1983). Determinations of Total Carotenoids and Chlorophylls a and B of Leaf Extracts in Different Solvents. *Analysis* 4, 142–196. doi:10.1042/bst0110591
- Iasimone, F., Felice, V. D., Fantasma, F., Iorizzi, M., and Pirozzi, F. (2018). Effect of Light Intensity and Nutrients Supply on Microalgae Cultivated in Urban Wastewater: Biomass Production, Lipids Accumulation and Settability Characteristics. *J. Environ. Manage.* 223, 1078–1085. doi:10.1016/j.jenvman.2018.07.024
- Ji, M. K., Kim, H. C., Sapireddy, V. R., Yun, H. S., Abou-Shanab, R. A. I., Choi, J., et al. (2012). Simultaneous Nutrient Removal and Lipid Production from Pretreated Piggery Wastewater by *Chlorella Vulgaris* YSW-04. *Appl. Microbiol. Biotechnol.* 97, 2701–2710. doi:10.1007/s00253-012-4097-x
- Jing, S., Podola, B., and Melkonian, M. (2007). Removal of Nitrogen and Phosphorus from Wastewater Using Microalgae Immobilized on Twin Layers: An Experimental Study. *J. Appl. Phycol.* 19, 417–423. doi:10.1007/s10811-006-9148-1
- Kadir, W. N. A., Lam, M. K., Uemura, Y., Lim, J. W., and Lee, K. T. (2018). Harvesting and Pre-treatment of Microalgae Cultivated in Wastewater for Biodiesel Production: A Review. *Energ. Convers. Manage.* 171, 1416–1429. doi:10.1016/j.enconman.2018.06.074
- Kong, W., Kong, J., Ma, J., Lyu, Hong, Feng, S., Wang, Z., et al. (2021). *Chlorella Vulgaris* Cultivation in Simulated Wastewater for the Biomass Production, Nutrients Removal and CO₂ Fixation Simultaneously. *J. Environ. Manage.* 284, 112070. doi:10.1016/j.jenvman.2021.112070
- Kumar, P. K., Krishna, S. V., Naidu, S. S., Kavita, V., Bhagawan, D., and Himabindu, V. (2019). Biomass Production from Microalgae *Chlorella* Grown in Sewage, Kitchen Wastewater Using Industrial CO₂ Emissions: Comparative Study. *Carbon Resour. Convers.* 2 (2), 126–133. doi:10.1016/j.crccon.2019.06.002
- Lam, M. K., Yusoff, M. I., Uemura, Y., Lim, J. W., Khoo, C. G., Lee, K. T., et al. (2017). Cultivation of *Chlorella Vulgaris* Using Nutrients Source from Domestic Wastewater for Biodiesel Production: Growth Condition and Kinetic Studies. *Renew. Energ.* 103, 197–207. doi:10.1016/j.renene.2016.11.032
- Lau, P. S., Lee, H. Y., Tsang, C. C. K., Tam, N. F. Y., and Wong, Y. S. (1999). Effect of Metal Interference, pH and Temperature on Cu and Ni Biosorption by *Chlorella Vulgaris* and *Chlorella Miniata*. *Environ. Technol.* 20, 953–961. doi:10.1080/09593332008616890
- Lee, K., and Lee, C. G. (2002). Nitrogen Removal from Wastewaters by Microalgae without Consuming Organic Carbon Sources. *J. Microbiol. Biotechnol.* 12 (6), 979–985.
- Lin, R., Cheng, J., Yang, Z., Ding, L., Zhang, J., Zhou, J., et al. (2016). Enhanced Energy Recovery from Cassava Ethanol Wastewater through Sequential Dark Hydrogen, Photo Hydrogen and Methane Fermentation Combined with Ammonium Removal. *Bioresour. Technol.* 214, 686–691. doi:10.1016/j.biortech.2016.05.037
- Lindholm-Lehto, P. C., Knuutinen, J. S., AhkolaHerve, H. S. J. S. H., and Herve, S. H. (2015). Refractory Organic Pollutants and Toxicity in Pulp and Paper Mill Wastewaters. *Environ. Sci. Pollut. Res.* 22, 6473–6499. doi:10.1007/s11356-015-4163-x
- Liu, J., and Chen, F. (2014). “Biology and Industrial Applications of *Chlorella*: Advances and Prospects,” in *Microalgae Biotechnology*. Editors C Posten and F Chen (Springer. Part of the Advances in Biochemical Engineering/Biotechnology book series), 1–35. doi:10.1007/10_2014_286
- Liu, J., and Hu, Q. (2013). “*Chlorella*: Industrial Production of Cell Mass and Chemicals,” in *Handbook of Microalgal Culture: Applied Phycolgy and Biotechnology*. Editors A Richmond and Q Hu (Wiley), 329–338. doi:10.1002/9781118567166.ch16
- Liu, Y., Ke, X., Zhu, H., Chen, R., Chen, X., Zheng, X., et al. (2020). Treatment of Raffinate Generated via Copper Ore Hydrometallurgical Processing Using a Bipolar Membrane Electrodialysis System. *Chem. Eng. J.* 382, 122956–128947. doi:10.1016/j.cej.2019.122956
- Lv, J. P., Liu, Y., Feng, J., Liu, Q., Nan, F. R., and Xie, S. L. (2018). Nutrients Removal from Undiluted Cattle Farm Wastewater by the Two-Stage Process of Microalgae-Based Wastewater Treatment. *Bioresour. Technol.* 264, 311–318. doi:10.1016/j.biortech.2018.05.085
- Martínez, M. E., Sánchez, S., Jimenez, J. M., El Yousfi, F., and Munoz, L. (2000). Nitrogen and Phosphorus Removal from Urban Wastewater by the Microalga *Scenedesmus Obliquus*. *Bioresour. Technol.* 73 (3), 263–272. doi:10.1016/S0960-8524(99)00121-2
- Mehta, P., Singh, D., Saxena, R., Rani, R., Gupta, R. P., Puri, S. K., et al. (2018). “High-Value Coproducts from Algae—An Innovative Way to Deal with Advance Algal Industry,” in *Waste to Wealth*. Editors R Singhania, R Agarwal, R Kumar, and R Sukumaran Springer. Part of the Energy, Environment, and Sustainability Book Series, 343–363. doi:10.1007/978-981-10-7431-8_15
- Mehta, S. K., and Gaur, J. P. (2001). Removal of Ni and Cu from Single and Binary Metalsolutions by Free and Immobilized *Chlorella Vulgaris*. *Eur. J. Protistology* 37, 261–271. doi:10.1078/0932-4739-00813
- Mehta, S. K., and Gaur, J. P. (2005). Use of Algae for Removing Heavy Metal Ions from Wastewater: Progress and Prospects. *Crit. Rev. Biotechnol.* 25, 113–152. doi:10.1080/07388550500248571
- Miao, M. S., Yao, X. D., Shu, L., Yan, Y. J., Wang, Z., Li, N., et al. (2016). Mixotrophic Growth and Biochemical Analysis of *Chlorella Vulgaris* Cultivated with Synthetic Domestic Wastewater. *Int. Biodeterioration Biodegradation* 113, 120–125. doi:10.1016/j.ibiod.2016.04.005
- Mujtaba, G., Rizwan, M., Kim, G., and Lee, K. (2018). Removal of Nutrients and COD through Co-culturing Activated Sludge and Immobilized *Chlorella Vulgaris*. *Chem. Eng. J.* 343, 155–162. doi:10.1016/j.cej.2018.03.007
- Mustafa, H. M., Hayder, G., and Jagaba, A. H. (2021). Microalgae: A Renewable Source for Wastewater Treatment and Feedstock Supply for Biofuel Generation. *Biointerface Res. Appl. Chem.* 11, 7431–7444. doi:10.33263/BRIAC111.74317444
- Mutamim, N. S. A., Noor, Z. Z., Hassan, M. A. A., and Yuniarto, A. (2013). Membrane Bioreactor: Applications and Limitations in Treating High Strength Industrial Wastewater. *Chem. Eng. J.* 225, 109–119. doi:10.1016/j.cej.2013.02.131
- Peng, S., Deng, S., Li, D., Xie, B., Yang, X., Lai, C., et al. (2020). Iron-Carbon Galvanic Cells Strengthened Anaerobic/Anoxic/Oxic Process (Fe/C-Azo) for High-Nitrogen/Phosphorus and Low-Carbon Sewage Treatment. *Sci. Total Environ.* 722, 137657–139697. doi:10.1016/j.scitotenv.2020.137657
- Qasim, W., and Mane, A. V. (2013). Characterization and Treatment of Selected Food Industrial Effluents by Coagulation and Adsorption Techniques. *Water Resour. Industry* 4, 1–12. doi:10.1016/j.wri.2013.09.005
- Qiu, S., Wang, L., Pascale, C., Gao, G., Chen, Z., Wang, S., et al. (2019). Effects of Crystalline Nanocellulose on Wastewater-Cultivated Microalgal Separation and Biomass Composition. *Appl. Energ.* 239, 0306–2619. doi:10.1016/j.apenergy.2019.01.212
- Quan, X., Tao, K., Mei, Y., and Jiang, X. (2014). Power Generation from Cassava Alcohol Wastewater: Effects of Pretreatment and Anode Aeration. *Bioproc. Biosyst Eng* 37 (11), 2325–2332. doi:10.1007/s00449-014-1210-9
- Sánchez-Zurano, A., Guzmán, J. L., Acién, F. G., and Fernández-Sevilla, J. M. (2021). An Interactive Tool for Simulation of Biological Models into the Wastewater Treatment with Microalgae. *Front. Environ. Sci.* 9, 298. doi:10.3389/fenvs.2021.721324
- Sandau, E., Sandau, P., and Pulz, O. (1996). Heavy Metal Sorption by Microalgae. *Acta Biotechnologica* 16, 227–235. doi:10.1002/abio.370160402
- Sanjay, P., and Janmaluddin (2018). Treatment of Distillery Waste Water: A Review. *Int. J. Theor. Appl. Sci.* 10 (1), 117–139.
- Sheng, P. X., Ting, Y. P., Chen, J. P., and Hong, L. (2004). Sorption of Lead, Copper, Cadmium, Zinc, and Nickel by Marine Algal Biomass: Characterization of Biosorptive Capacity and Investigation of Mechanisms. *J. Colloid Interf. Sci.* 275, 131–141. doi:10.1016/j.jcis.2004.01.036
- Slade, R., and Bauen, A. (2013). Micro-algae Cultivation for Biofuels: Cost, Energy Balance, Environmental Impacts and Future Prospects. *Biomass and Bioenergy* 53, 29–38. doi:10.1016/j.biombioe.2012.12.019
- Stutter, M. I., Graeber, D., Evans, C. D., Wade, A. J., and Withers, P. J. A. (2018). Balancing Macronutrient Stoichiometry to Alleviate Eutrophication. *Sci. Total Environ.* 634, 439–447. doi:10.1016/j.scitotenv.2018.03.298
- Tan, X. B., Zhao, X. C., Zhang, Y. L., Zhou, Y. Y., Yang, L. B., and Zhang, W. W. (2018). Enhanced Lipid and Biomass Production Using Alcohol Wastewater as Carbon Source for *Chlorella Pyrenoidosa* Cultivation in Anaerobically Digested Starch Wastewater in Outdoors. *Bioresour. Technol.* 247, 784–793. doi:10.1016/j.biortech.2017.09.152
- Tercero, E. A. R., Sforza, E., Morandini, M., and Bertucco, A. (2014). Cultivation of *Chlorella Protothecoides* with Urban Wastewater in Continuous Photobioreactor: Biomass Productivity and Nutrient Removal. *Appl. Biochem. Biotechnol.* 172, 1470–1485. doi:10.1007/s12010-013-0629-9
- Thoré, E. S. J., Schoeters, F., De Cuyper, A., Vleugels, R., Noyens, I., Bleyen, P., et al. (2021). Waste Is the New Wealth - Recovering Resources from Poultry Wastewater for Multifunctional Microalgae Feedstock. *Front. Environ. Sci.* 9, 253. doi:10.3389/fenvs.2021.679917

- Vinod, V. T. P., Sashidhar, R. B., and Sreedhar, B. (2010). Biosorption of Nickel and Total Chromium from Aqueous Solution by Gum Kondagogu (*Cochlospermum Gossypium*): A Carbohydrate Biopolymer. *J. Hazard. Mater.* 178, 851–860. doi:10.1016/j.jhazmat.2010.02.016
- Wang, L., Min, M., Li, Y. C., Chen, P., Chen, Y. F., Liu, Y. H., et al. (2009). Cultivation of Green Algae *Chlorella* Sp. In Different Wastewaters from Municipal Wastewater Treatment Plant. *Appl. Biochem. Biotechnol.* 162, 1174–1186. doi:10.1007/s12010-009-8866-7
- Yang, B., and Wyman, C. E. (2008). Pretreatment: The Key to Unlocking Low-Cost Cellulosic Ethanol. *Biofuels, Bioprod. Bioref.* 2 (1), 26–40. doi:10.1002/bbb.49
- Zhu, L., Wang, Z., Takala, J., Hiltunen, E., Qin, L., Xu, Z., et al. (2013). Scale-up Potential of Cultivating *Chlorella Zofingiensis* in Piggery Wastewater for Biodiesel Production. *Bioresour. Techn.* 137, 318–325. doi:10.1016/j.biortech.2013.03.144
- Znad, H., Al Ketife, A. M. D., Judd, S., AlMonmani, F., and Vuthaluru, H. B. (2018). Bioremediation and Nutrient Removal from Wastewater by *Chlorella Vulgaris*. *Ecol. Eng.* 110, 1–7. doi:10.1016/j.ecoleng.2017.10.008

Conflict of Interest: The authors declare that the research was conducted in the absence of any commercial or financial relationships that could be construed as a potential conflict of interest.

Publisher's Note: All claims expressed in this article are solely those of the authors and do not necessarily represent those of their affiliated organizations, or those of the publisher, the editors and the reviewers. Any product that may be evaluated in this article, or claim that may be made by its manufacturer, is not guaranteed or endorsed by the publisher.

Copyright © 2021 Li, Amenorfenyo, Zhang, Zhang, Li and Huang. This is an open-access article distributed under the terms of the Creative Commons Attribution License (CC BY). The use, distribution or reproduction in other forums is permitted, provided the original author(s) and the copyright owner(s) are credited and that the original publication in this journal is cited, in accordance with accepted academic practice. No use, distribution or reproduction is permitted which does not comply with these terms.



Catalytic Oxidation of Methylene Blue by Attapulgite/TiO₂

Jianping Shang*, Yu Jiang, Xiaoping Qin, Bin Zhao and Xuefei Li

College of Chemical Engineering, Sichuan University of Science and Engineering, Zigong, China

Methylene blue (MB) is a common pollutant in wastewater of printing and dyeing industry. At present, ozone oxidation is commonly used in the treatment of printing and dyeing wastewater. Ozone is used for oxidation reaction directly and indirectly. However, the reaction rate is not fast enough. In this study, the attapulgite (ATP) was modified by tetrabutyl titanate-ethanol solution. The TiO₂/ATP nanocomposite with high catalytic activity was prepared. The synthesized samples were subjected to characterized by X-ray diffraction (XRD) and Fourier Transform infrared spectroscopy (FTIR). The morphology and particle size of the particles were observed by scanning electron microscopy (SEM). The TiO₂/ATP nanocomposite was calcined at 300°C for 2 h, and the degradation rate of 80 mg/L methylene blue was 99.8%. The experimental results show that the ozone, temperature and mass transfer factors are excluded, and the effects of temperature, MB concentration and pH on the degradation of methylene blue are investigated. The optimal reaction conditions are as follows: The ozone concentration is 0.067 g/min; the ozone flow rate is 0.15 NL/min; the stirrer rotation speed is 550 r/min; the catalyst is 0.1 g; the temperature is 50°C; Based on the results, the reaction mechanism was derived and the kinetic study of the experiment was carried out.

Keywords: titanium dioxide, attapulgite, methylene blue, catalytic ozonation, kinetics

OPEN ACCESS

Edited by:

Shihai Deng,
Xi'an Jiaotong University, China

Reviewed by:

Zhongyu Li,
Changzhou University, China
Zhifeng Hu,
Beijing Jiaotong University, China

*Correspondence:

Jianping Shang
welsons@126.com

Specialty section:

This article was submitted to
Water and Wastewater Management,
a section of the journal
Frontiers in Environmental Science

Received: 26 September 2021

Accepted: 28 October 2021

Published: 15 November 2021

Citation:

Shang J, Jiang Y, Qin X, Zhao B and
Li X (2021) Catalytic Oxidation of
Methylene Blue by Attapulgite/TiO₂.
Front. Environ. Sci. 9:783313.
doi: 10.3389/fenvs.2021.783313

INTRODUCTION

At present, the discharge of dye industry wastewater has reached 2 billion tons per year (Xue 2021). Considered as environmental pollutant, there are over 30,000 kinds of synthetic dyes used worldwide. Among them, the wide application of methylene blue in the printing and dyeing industries has resulted in the alarming pollution of industrial wastewater containing methylene blue to other pure water bodies (Zhang et al., 2008).

The current approaches of wastewater treatment containing organic dye include biological method, coagulation method, oxidation method, adsorption method and membrane separation method. The most commonly used methods for treating dyeing wastewater at home and abroad are biochemical method, flocculation precipitation method and catalytic oxidation with activated as catalyst where later two approaches have been the common practice (Song et al., 2003; Li, 2007; Chen et al., 2009). The activated carbon is expensive and the regeneration process is complicated, which limits its wide application.

Because of its unique crystal structure, large specific surface area, high chemical and mechanical stability, attapulgite is suitable for catalyst carrier. Especially for the low price, attapulgite has practical significance in wastewater treatment. Meanwhile the slag can be reused, where the photocatalyst can be prepared with TiO₂. Studies showed that activated attapulgite is resistant to

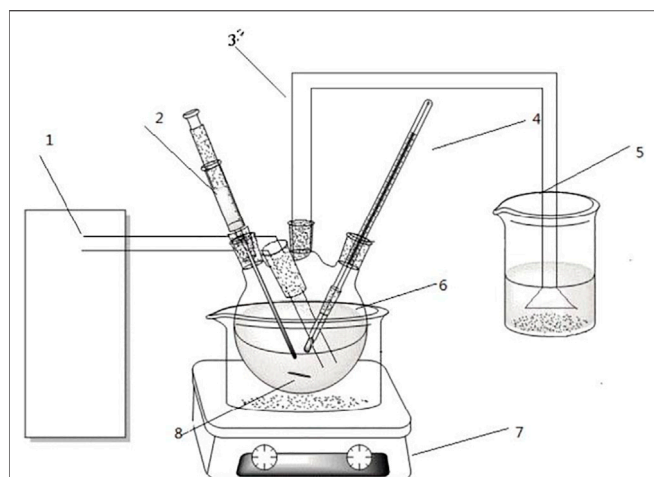


FIGURE 1 | Diagram of experimental devices. 1-Ozone generator, 2-colloidal sampler, 3-thermometer, 4-exhaust pipe, 5-tail gas recovery cup, 6-four-necked flask, 7-magnetic stirring heater, 8-stirring rotor.

organophosphorus pesticides such as trichlorfon and dichlorvos (Peng et al., 2006; Zhang et al., 2013; Yang et al., 2014). In the wastewater treatment process, the transitional metallic, as a catalytic, can speed up the reaction, and improve the reaction efficiency. The results of previous experiments showed that the homogenous catalysis of Zn, Ti, Mn, Ni. Sometimes, the same element can be not only used as a catalyst in the solution, but also in the solid phase accelerator as an active component (Yin et al., 2003). TiO₂ has been widely studied for the degradation of various organic compounds because it is nontoxic, highly efficient, stable, environmentally friendly, and inexpensive (Virukyte and Varma, 2012; Yin et al., 2013; Fang et al., 2014; Yu et al., 2019; Qiao et al., 2021). So, TiO₂ was used as the active component of multiphase catalyst in this paper. Oxygen atoms in ozone have strong electron-philicity or proton-philicity, so they show strong oxidizability. Ozone molecules decompose into highly active oxygen atoms, and part of ozone decompose into hydroxyl radical •OH with strong oxidizing effect in water. Strong oxidation of oxygen atoms and •OH in water can sterilize, destroy the organic structure, degrade the organic matter, make the organic matter mineralization (Masschelein, 1992). The process has the characteristics of non-toxic, low secondary pollution, low selectivity, quick action time and high efficiency. ATP is a very good catalyst carrier, where TiO₂ was loaded on as the active component can promote the conversion of ozone oxide into hydroxyl radical which can accelerates the decomposition of MB.

In this paper, TiO₂/attapulgite nanocomposite were successfully prepared. The catalytic process, with ozone-assisted oxidation was investigated, including the effects of temperature, MB concentration and pH on the degradation of methylene blue. Moreover the property and microstructure of the catalyst were measured. And the degradation mechanism of MB was derived and the reaction kinetic was proposed.

EXPERIMENTAL

Experimental Set-Up

The experimental set-up used in the experiment are a 4 flask with 250 ml volume, 101-1AB electric blast drying oven (Beijing Zhongxing Weiye Century Instrument Co., Ltd.) for drying sample, a constant temperature magnetic stirrer (Shanghai Lichen Bangxi Instrument Technology Co., Ltd.) for reaction, HY-010 type ozone generator (Chengdu Yifeng Hongyuan Environmental Protection Technology Co., Ltd.), I3 type UV-visible spectrophotometer (Jinan Haineng Instrument Co., Ltd.) for analysis sample concentration and OTL1200 type tube furnace for modifying catalyst with high temperature. The experiment set-up is shown in **Figure 1**:

Experimental Reagents

The chemical reagents used in the experiment are methylene blue C₁₆H₁₈ClN₃S·3H₂O, attapulgite (ATP) Mg₅Si₈O₂₀(OH)₂(OH₂)₄·3H₂O, tetrabutyl titanate (C₁₆H₃₆O₄Ti), anhydrous ethanol (C₂H₅OH), hydrochloric acid (AR), ammonia (AR), sodium diethyldithio carbamate (AR), hydroxylamine hydro-chloride (AR), ammonium citrate (AR), ethylenediamine (AR), trichlorome -thane (AR).

Preparation of ATP/TiO₂

About 40 g of attapulgite with a particle size of about 180 mesh was screened and immersed in 200 ml of 4 mol/L dilute hydrochloric acid for 8 h, and then filtered by suction to neutrality and dried in an oven at a temperature of 80°C for 4 h. A tetrabutyl titanate-ethanol impregnation solution with a volume ratio of 1:4 was placed for use. The water absorption of 31.8 g acid-modified attapulgite was measured to be 24.5 ml, and it was dried in an oven for 3 h. Subsequently, 24.5 ml of tetrabutyl titanate-ethanol impregnation solution was added to 31.8 g of attapulgite, sealed with a plastic wrap, and immersed for 13.5 h. The impregnated attapulgite was hydrolyzed in a water bath for 1 h, hydrolyzed to Ti(OH)₄, dried in an oven and oxidized to TiO₂, and dried for 3 h. The attapulgite was placed in a tube furnace and calcined at 500°C for 2 h, and sealed in a bag.

Characterization

The X-ray diffractometer (XRD) was used for the physical phase and purity analysis of all samples on the DX-2600 instrument with Cu Kα as the radiation source with an operating voltage of 30 kV and a current of 10 mA. The morphology of the particles was observed by transmission electron microscopy (SEM), and the working voltage was 15 kV. The composition and functional groups of all catalysts were qualitatively analyzed via infrared spectroscopy (FTIR) with spectral scanning range: 4000-4000 cm⁻¹.

Catalytic Oxidation of Methylene Blue Wastewater

An analytical balance was used to weight 0.1 g of modified attapulgite from section 2.3 for later use. A certain amount of

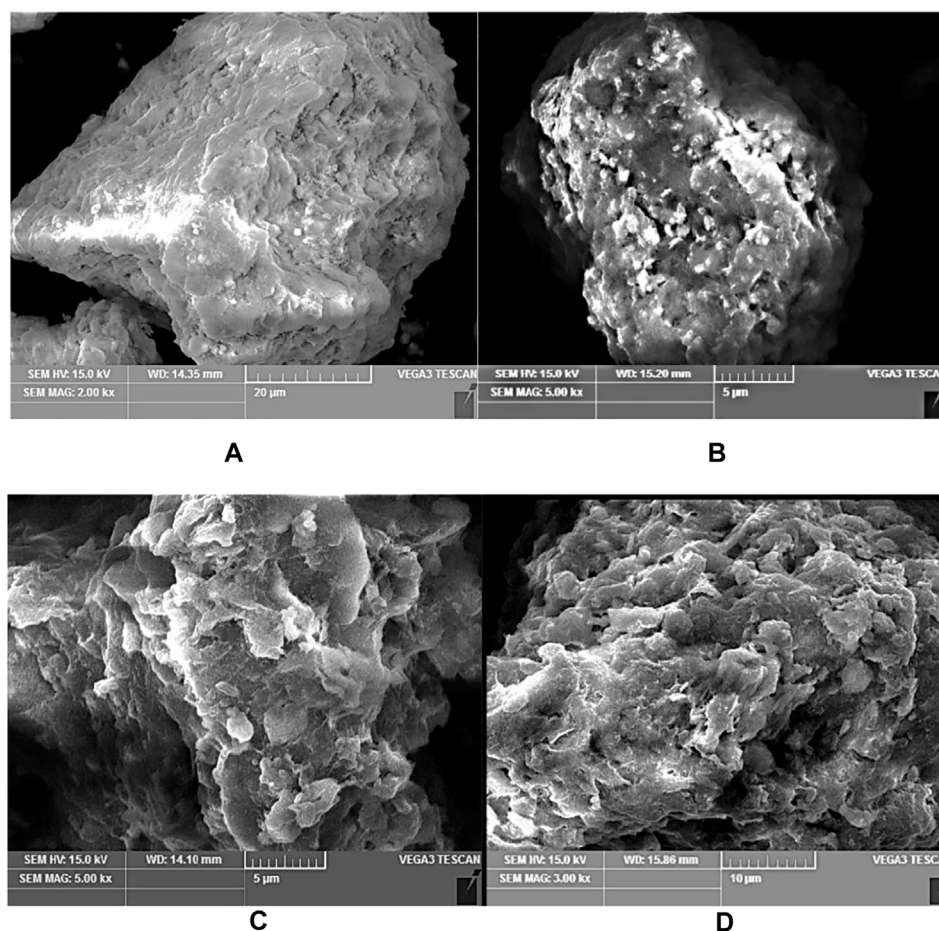


FIGURE 2 | (A) SEM image of Original soil, (B) Calcination at 300°C, (C) Calcination at 400°C, (D) Calcination at 500°C.

methylene blue stock solution was removed from the 1000 mg/L methylene blue mother liquor to prepare a methylene blue reaction solution of the desired concentration. The prepared MB solution was poured into a dry four-necked flask, with a magnetic stirrer; the four-necked flask containing the solution was placed in a water bath where the MB solution below the water. The speed and temperature of the magnetic stirrer were set; the bottom of the meter and the bottom of the trachea were at the same level as the stirrer; when the reaction temperature of the MB solution reached the specified temperature, it would pass through the four ports. After the modified attapulgite catalyst was added into the flask, the ozone generator switch was turned on and the timer was started. The sampler was used to take 5 ml of sample liquid through the sampling port every time. The residue was filtered through the disposable filter head and then put into the sample tube for testing. The temperature was controlled during the reaction so that the temperature difference was lower than $\pm 1^{\circ}\text{C}$. After the reaction was completed, the solution with a constant volume was measured by an ultraviolet spectrophotometer at its maximum wavelength of 665 nm. The degradation rate is calculated according to the following formula:

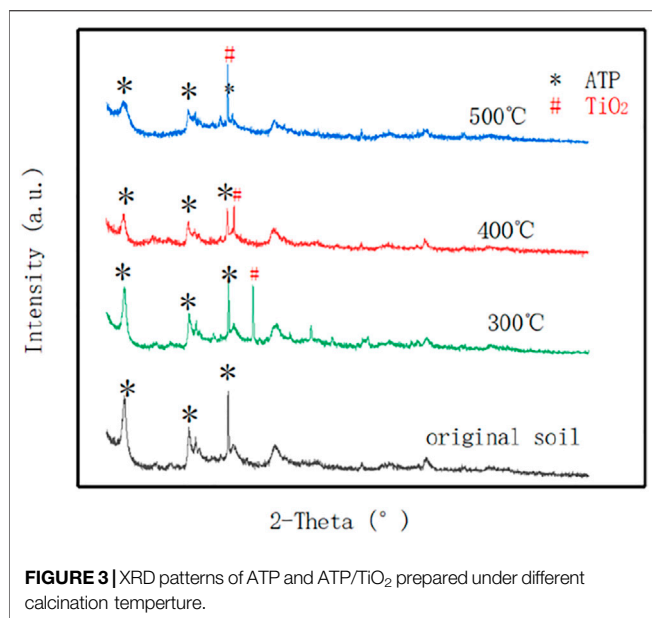
$$D = \left(1 - \frac{A}{A_0}\right) \times 100\% \quad (1)$$

Where D is the degradation rate (%), and A and A₀ are the absorbance before and after degradation, respectively.

RESULTS AND DISCUSSION

SEM of the Sample

The SEM is employed to study the morphology of the attapulgite/TiO₂ composite materials. The SEM images of three composite samples, calcined at 300°C, 400°C, and 500°C for 2 hours were shown in **Figure 2**. One can see that the attapulgite has a loose structure as well as a large surface area and specific surface area, so it has a good adsorption effect. The TiO₂ nanoparticles with a particle size of less than 10 nm are more uniformly distributed on the surface of the attapulgite clay, and the morphology and size of the TiO₂ and the attapulgite clay change little after loading. Nevertheless, the TiO₂ nanoparticles are not fully attached to the surface of the attapulgite clay. With a small amount of TiO₂, the crystal form has anatase transformed into rutile type, and a small amount of spherical-like particles appear on the surface. A



small portion is dispersed around the TiO₂/attapulgite powder, which indirectly increases the specific surface area and surface area. When the temperatures are 300°C and 400°C, the structure changes little, but the crystal structure of TiO₂ on the surface will change. At 500°C, the catalyst has a loose structure. Although the surface area has increased, the pore structure of the crystal will collapse, thereby reducing the specific surface area.

As shown in **Figure 2A**, the surface of the original attapulgite without heating has a layered structure with a smooth surface, which has a large surface area and specific surface area.

Figure 2B is the SEM of the modified attapulgite that was calcined at 300°C, one can see that the surface of the heated attapulgite becomes porous, and the internal structure changes. The small white spheres on the surface are TiO₂ particles which increase the surface area and the adsorption efficiency.

Figure 2C shows the SEM of attapulgite calcined at 400°C, which showed a more fluffy porous structure with a dense layers, the shapes of TiO₂ particles become irregular than those in **Figure 2B**.

When the attapulgite is calcined at 500°C, its surface becomes fluffier and more porous as shown in **Figure 2D**. Meanwhile the pores collapse, the surface is sintered, and the growth of TiO₂ crystals is hindered.

XRD Characterization of the Sample

In order to further investigate the coating condition of the sample, the X-ray diffraction spectrum of sample was collected. The range is 5–90°. The XRD results were analyzed by Jade software to obtain the phase analysis and the results. ATP/TiO₂ calcined at 300, 400, and 500°C are shown in **Figure 3**.

It can be seen from that the XRD patterns of four ATP samples have a strong diffraction peak where the 2θ is at 8.495°. For the ATP/TiO₂ sample with a calcination temperature of 300°C, a strong diffraction characteristic peak of TiO₂ appears when 2θ is 25.339 and 30.807, respectively. For the ATP/TiO₂ sample

calcined at 400°C, a strong diffraction characteristic peak of TiO₂ appears when 2θ is 27.446, 36.085, and 54.322, respectively. At the calcination temperature of 500°C, a strong diffraction characteristic peak of TiO₂ show at 25.27 and 48.049. The higher the temperature, the more TiO₂ is loaded in the ATP. In the four graphs, the diffraction peak of ATP decreases with the rising temperature. This is ascribed to the reduction of the ATP diffraction peak intensity caused by the hydroxyl group on the attapulgite clay's surface as well as the separation of adsorbed water, crystal water and structural water. When the temperature is too high, the internal channel collapses. Other peaks in the graph are caused by the presence of impurities in the sample itself. The overall crystal lattice of the catalyst is intact and not destroyed. The product has obvious diffraction peaks, and the interlayer spacing fluctuates. The diffraction peaks remain orderly after calcination, and the crystal lattice is intact.

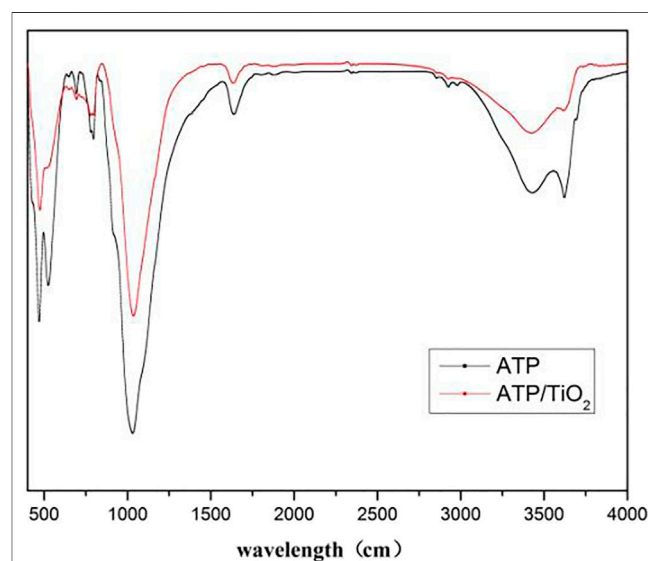
In order to further investigate the coating condition of the sample, the FTIR of sample was collected.

Figure 4 was the FTIR patterns of ATP and ATP/TiO₂. The absorption peaks at 470 and 1032 cm⁻¹ corresponded to the stretching vibration of the Si-O-Si bond in amorphous SiO₂. The absorption band of modified attapulgite near 700 cm⁻¹ is produced by asymmetric stretching vibration of Ti-O. The absorption peak at 1639 cm⁻¹ is produced by N-H. The absorption peak in the range of 3000 to 3800 cm⁻¹ is generated by the surface hydroxyl group of SiO₂. The absorption peaks of ATP/TiO₂ were weakened because other chemical bonds were formed after the modification.

Catalytic Oxidation of Methylene Blue by ATP/TiO₂

Effect of Ozone

In 150 ml MB solution, the experimental condition as follows: the concentration is 60 mg/L, the flow rate of ozone is 0.15 NL/min,



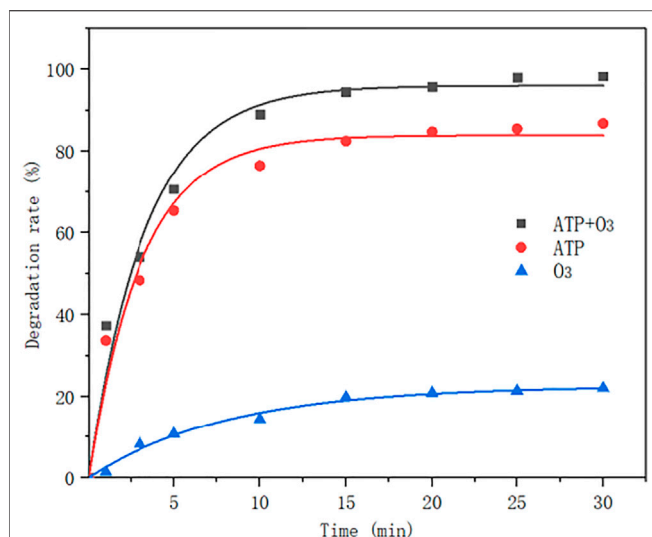


FIGURE 5 | Comparative experimental results of ozone and catalyst.

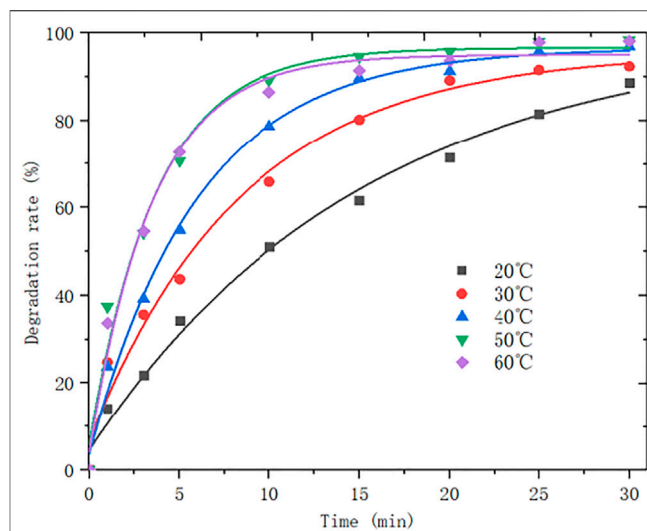


FIGURE 7 | Effect of reaction temperature on MB degradation rate.

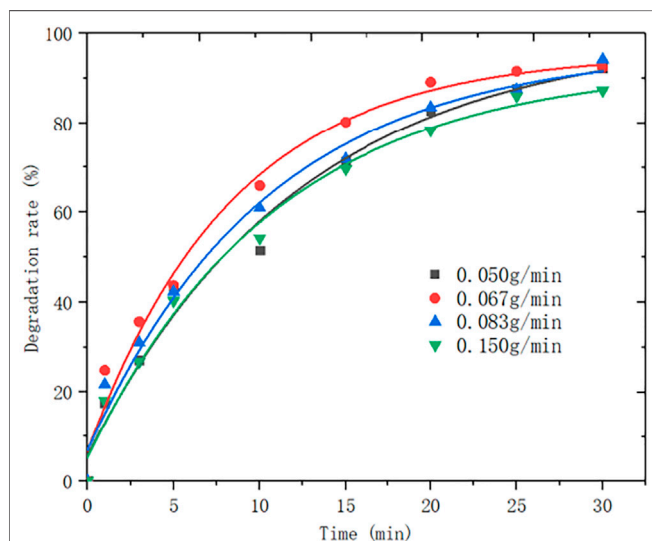


FIGURE 6 | Effect of ozone concentration on degradation rate.

the concentration of ozone is 0.067 g/L, pH is 5.5, the amount of attapulgite is 0.1 g, the stirring speed is 55 r/min, and the reaction temperature is 50°C. The reaction results are as shown in the figure below:

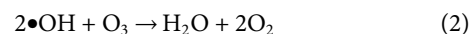
It can be seen from **Figure 5**, when the same modified attapulgite is added, the ozone ratio is different, and the degradation rate of methylene blue increases to some extent. In the absence of ozone, the degradation rate can reach 90% or so. After the introduction of ozone, the rate can reach 98%. This indicates that the catalyst has a certain adsorption capacity, but the degradation rate can be further improved under the indirect oxidation of ozone. The addition of catalyst significantly improves the efficiency, indicating that

the catalyst plays a critical role in the degradation of methylene blue.

The effect of ozone concentration was also considered, and the results are as shown in **Figure 6**:

It can be seen from **Figure 6** that the degradation rate of MB decreases with the increasing ozone flow rate. When the ozone concentration is above 0.067 g/L, the degradation rate of MB decreases with the increase of ozone concentration. Nevertheless, when the ozone concentration is below 0.067 g/L, the degradation rate of MB decreases as the ozone concentration declines. Thus, it can be concluded that the optimal ozone concentration is 0.067 g/L.

The reason is that during the reaction, the ozone content in the solution is affected by the dissolution, reaction and decomposition of ozone (Chen et al., 2015; Zhang et al., 2015). Within a certain ozone flow range, as the ozone flow rate increases, the solubility of ozone in water increases, and the yield of $\bullet\text{OH}$ also increases, resulting in a faster degradation of MB. For a certain volume of reaction system, the solubility of ozone in the solution is constant. After the solution is saturated with ozone, the ozone in the reaction system is excessive, in which case, the impact of the amount of ozone on the reaction is negligible. When the ozone flow exceeds a certain value, excessive ozone will participate in the quenching reaction of OH (see **Equation 1**), which reduces the amount of $\bullet\text{OH}$ involved in the reaction and thus impacts the degradation of MB.



The gas-liquid mass transfer factor is eliminated, so that the reaction system is controlled by reaction and non-mass transfer control. In this experiment, in order to make the degradation rate of MB as high as possible, the ozone flow rate was chosen to be 6 L/min. If applied to industrial production, the economic efficiency of unit ozone removal MB should be evaluated to determine the optimal ozone flow.

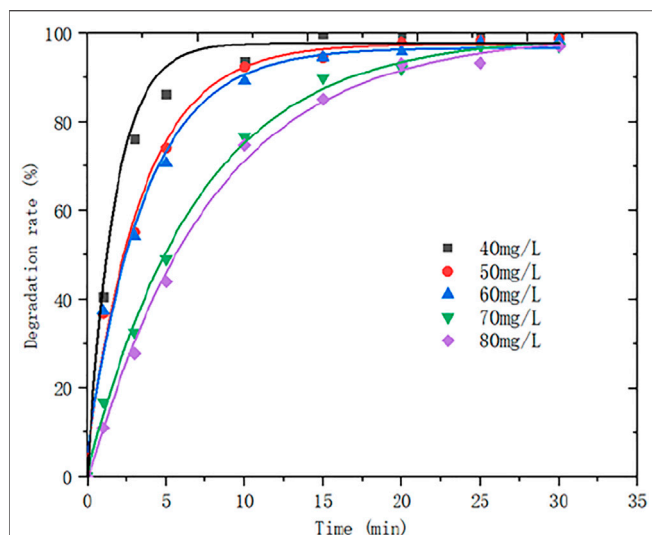


FIGURE 8 | Effect of MB solution concentration on MB degradation rate.

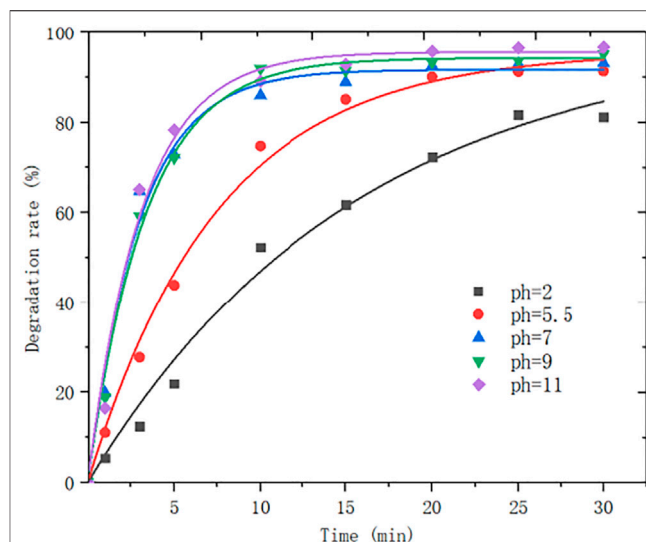
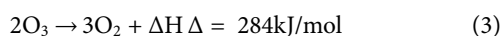


FIGURE 9 | Effect of pH on MB degradation rate.

Effect of Reaction Temperature

The experimental condition as follows: At a rotational speed of 550 r/min, the ozone flux is 0.15 NL/min, the ozone concentration is 0.067 g/L, and the pH is 5.5. The amount of attapulgite is 0.1 g, the initial concentration of 150 ml of MB solution is 60 mg/L. The reaction was carried out under the conditions of 20°C, 30°C, 40°C, 50°C, and 60°C, respectively. The change curve of MB degradation rate over time is shown in Figure 7.

It can be seen from Figure 7 when the reaction temperature is lower than 50°C, the degradation rate of MB gradually increases with the rising reaction temperature; when the reaction temperature is 50°C, the change in reaction temperature has little effect on the degradation of MB. Therefore, with the increase of reaction temperature, the degradation rate of MB first increases and then remains unchanged. According to the study by Masschelein (1992), ozone is quite poor in stability and is easy to decompose at even room temperature (see Eq. 2). The half-life of ozone decomposition in water is related to temperature. When the temperature is below 50°C, the decomposition rate will increase accordingly as it rises, and more •OH will be produced in the solution, and increasing temperature will enhance the activation in the reaction system (Li, 2007). The ratio of molecules increases the probability of effective collision and accelerates the degradation rate. Nevertheless, when the temperature rises to a certain value, the solubility of ozone in water will be greatly reduced. Because •OH can be decomposed by ozone in water, the degradation rate is reduced accordingly.



The optimum reaction temperature is 50°C, at which neither the solubility of ozone in water is not too low nor the degradation rate is not too slow, thus the reaction rate can be maintained at a suitable temperature. Furthermore, this is also the temperature

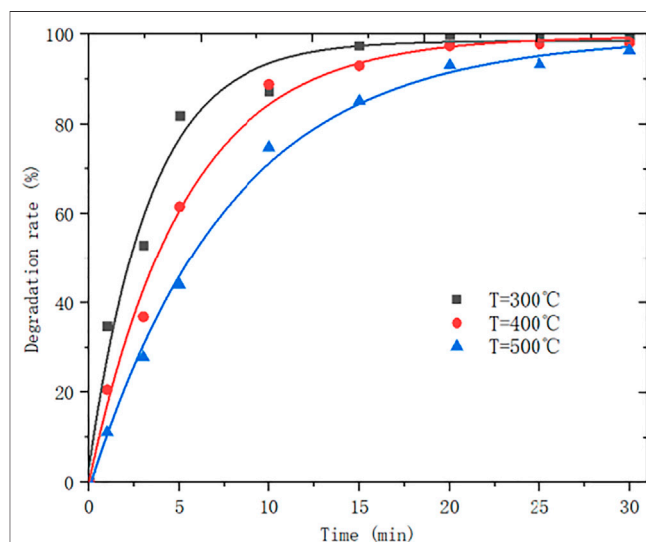


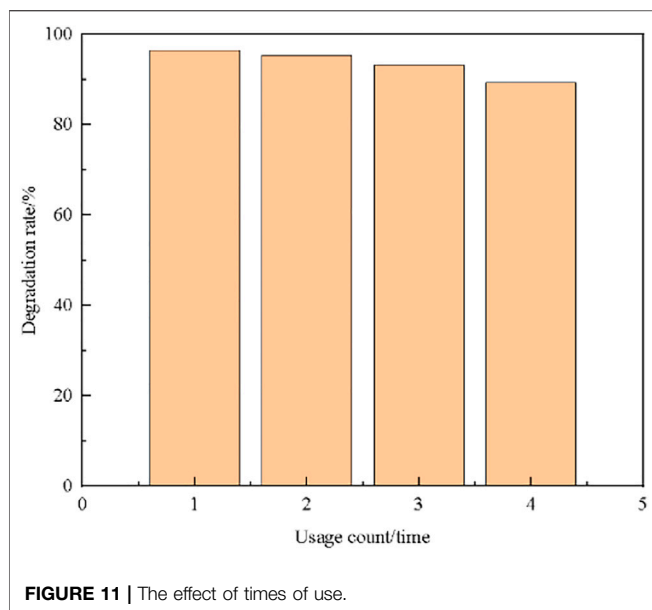
FIGURE 10 | Effect of calcination temperature on methylene blue wastewater.

that is easier to control, so the temperature of subsequent experiments is set to 50°C as well.

Effect of MB Solution Concentration

The experimental condition as follows: the reaction temperature is 50°C, the rotation speed is 550 r/min, the ozone flux is 0.15 L/min, the ozone concentration is 0.067 g/L, the attapulgite dosage is 0.1 g, pH is 5.5, the initial concentration of 150 ml MB solution is 40 mg/L. The experiment was performed under the conditions of 50 mg/L, 60 mg/L, 70 mg/L and 80 mg/L. The variation curve of MB degradation rate over time is shown in Figure 8.

The gas-liquid-solid heterogeneous reaction is a complex process. As can be seen from Figure 8, under the above



optimal experimental conditions, the initial concentration of MB was changed to observe the degradation of MB. The results showed that the degradation rate is faster as the initial concentration of MB is lower. Because of the heterogeneous catalysis, the reactants are adsorbed before the catalytic reaction, and adsorbed in the catalyst pores for catalytic oxidation. Due to the limited adsorption sites, the higher the MB concentration, the lower the adsorption efficiency. In addition, because the molecular weight of the adsorbed reactants is also limited, the degradation rate declines as the increasing concentration.

Effect of pH

The experimental condition as follows: the reaction temperature is 50°C, the rotational speed is 550 r/min, an ozone flux is 0.15 L/min, the ozone concentration is 0.067 g/L, attapulgite dosage is 0.1 g, an initial concentration of 150 ml of MB solution is 80 mg/L. The change curve of MB degradation rate over time is shown in **Figure 9**.

The results showed that the decolorization rate of MB increases along with the pH. Under acidic conditions, the decolorization rate is lower than that under alkaline conditions. By analyzing the principle of ozone oxidation, it is found that the oxidation intensity of ozone enhances with the rising pH. The above experimental phenomenon indicates that the hydroxyl radical generated by ozone decomposition by itself is the main driving force for MB degradation. Under acidic conditions, the direct reaction between ozone and MB molecules is much slower. Therefore, the degradation process of MB can be expressed by a continuous quasi-first-order equation.

Effect of Catalyst Calcination Temperature

The tetrabutyl titanate-ethanol impregnation liquid has a volume ratio of 1:4. After intermediate treatment, it is calcined by a nitrogen atmosphere in a tube furnace, and calcined at 300°C,

400°C, and 500°C, respectively. The effect of calcination temperature on the degradation rate of 80 mg/L MB solution was investigated. The experimental results are as shown in **Figure 10**.

When the calcination temperature is too high, the catalyst pores collapse and the specific surface area of adsorption is reduced, so the degradation rate will be slowed down, whereas, the temperature increases TiO₂ and ATP load better, so the final degradation rate will tend to a close value.

Recycle and Re-Use

Collect the used composite catalyst, wash it several times with deionized water, dry it and grind it. Obtain the relationship between the number of times the composite catalyst is used and the degradation rate, as shown in **Figure 11**:

From **Figure 11**, it can be seen that the recovered attapulgite/TiO₂ composite photocatalyst still exhibits high catalytic activity, and the degradation effect can reach 89% even if it is used for the fourth time. This shows that attapulgite as a carrier can give full play to its characteristics of strong adsorption and high thermal stability. The composite catalyst solves the problem of secondary pollution while processing methylene blue, and enhances the utilization rate of titanium dioxide.

Ozone Reaction Kinetics

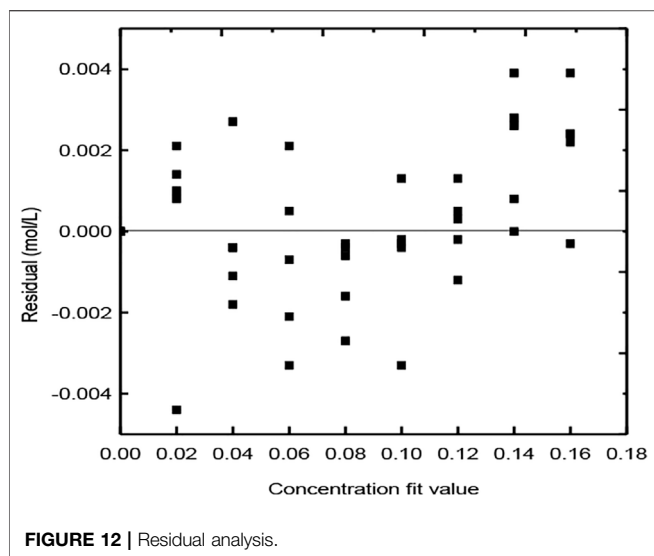
Ozone enters the aqueous solution through aeration, in which the gas-liquid contact mass transfer is involved, and the gas is diffused in the water. According to classical dual-mode theory (Achari et al., 2021; Wu et al., 2021), ozone oxidation of organic matter may exist in two forms: the form of ozone gas diffuses into the liquid, reacts with organic matter at the gas-liquid interface or liquid film before entering the liquid phase, and the selectivity of ozone for such substances Strong results; another portion of unreacted ozone reacts with the organic matter through the liquid membrane into the liquid phase.

$$-\frac{d[D]}{dt} = k_{O_3}[O_3][D] + k_{OH}[\cdot OH][D] \quad (4)$$

Where [O₃] and [D] are the concentrations of ozone molecules and organic matter, respectively, and the ozone concentration and OH are deemed to be constant values. In the unbuffered MB solution, a quasi-stable condition for hydroxyl radicals is assumed. The concentration of hydroxyl radicals can be estimated by Benitez and Beltran from **Eq. 5**:

$$[OH\cdot] = \frac{3[O_3][OH^-]}{[D]} \cdot \frac{KHOO\cdot}{KHO\cdot} \quad (5)$$

In the formula, [HO·] and [HOO·] are the concentrations of hydroxyl radicals and hydroxide ions, respectively. [O₃] is the dissolved ozone concentration, [D] is the concentration of the MB solution, and k_{HO·} is the second-order rate constant of the [·OH] reaction path. k_{HOO·} is a kinetic constant for the decomposition of ozone to form a free radical HOO· under high pH conditions. At higher pH, the ozone molecules decompose more hydroxyl radicals, resulting in a large amount of hydroxide ions. Substituting [OH] in **Eq. 5** into **Eq. 6**, yields **Eq. 7**:



$$-\frac{d[D]}{dt} = k_{O_3}[O_3][D] + k_{OH}[\cdot OH][D] \quad (6)$$

$$-\frac{d[D]}{dt} = k_{O_3}[O_3][D] + 3k_{OOH}[OH^-][O_3] \quad (7)$$

Since the concentration of O₃ is excessive, the ozone oxidation process of MB molecules is an apparent quasi-first-order kinetic reaction. Therefore, the formulas $k_{O_3}[O_3]$ and $3k_{OOH}[OH^-]$ are assumed to be constant.

Under acidic conditions, the MB solution in deionized water has a PH of 5.5. In weakly acidic solution, because the MB solution is a non-buffered solution, [OH⁻] is 0 in the solution. The kinetic formula is the apparent first-order kinetics:

$$-\frac{d[D]}{dt} = k \cdot [O_3]^n [D]^m \quad (8)$$

With the standard curve of MB solution, the molar concentration at time *t* at *T* = 50°C, *C*_{MB} = 80 mg/L, and pH = 5.5 is obtained. Because ozone is continuously and excessively introduced during the reaction, $k[O_3]$ in the formula can be used as a constant. MATLAB software is used to theoretically model the formula. The kinetic equation is:

$$-\frac{d[D]}{dt} = 7.0525 \times [D]^{1.92} \quad (9)$$

The following results are obtained by fitting the experimental data, as shown in **Figure 12**.

As shown in the figure, the residuals of the experiments are evenly distributed on the upper and lower sides of the zero line, indicating a good fitting degree.

The *k* values with different temperatures were obtained as shown in **Table 1**.

According to Arrhenius formula.

$$k = k_0 \exp(-E_a/RT) \quad (10)$$

E_a was obtain by plotting $\ln k$ 1/*T*.

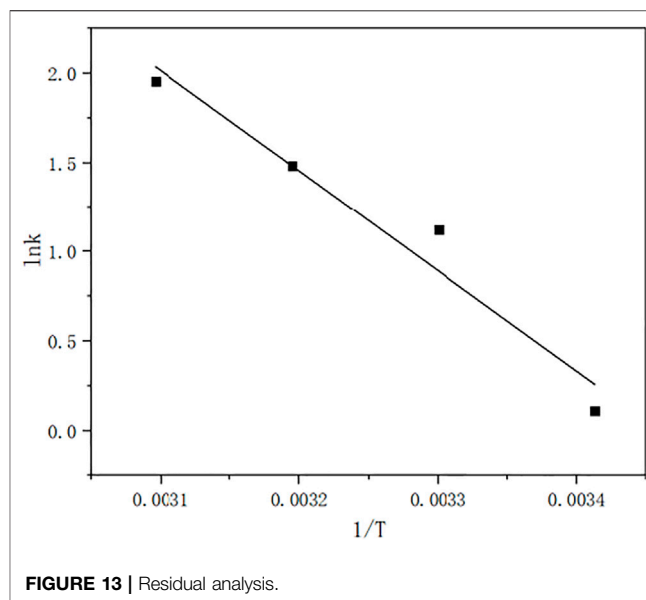


TABLE 1 | *k* values fitted at different temperatures.

Temperature (°C)	<i>k</i>
20	1.1148
30	3.0672
40	4.4077
50	7.0525
60	5.5701

From **Figure 13**, the slope is -5610.59, so the *E_a* is 46.646 kJ/mol. The results show that when the ozone is excessive, the ozone concentration is constant, and the degradation kinetics of the MB solution is the apparent first-order kinetics. Under acidic conditions, MB degradation is carried out by direct ozone oxidation, whereas under alkaline conditions, MB degradation is carried out by indirect ozone oxidation. In terms of the relative degradation rate, the higher the pH, the faster the degradation rate. For the final degradation rate, the weak acidity, neutrality and alkalinity can reach 99% degradation rate. This indicates that the above kinetic equation is suitable for most reactions, except for strongly acidic reactions. The degradation rate of MB in this process is 99.8% greater than 73.8% obtained by some researchers (Yin et al., 2003) under the optimum condition.

CONCLUSION

In this work, the experimental scheme is to impregnate the attapulgite with a volume of tetrabutyl titanate-ethanol solution. After drying, the tetrabutyl titanate was hydrolyzed to TiO₂ under the action of water vapor, and calcined at a low temperature of 300°C to obtain a uniform distribution of surface anatase TiO₂. The TiO₂ attapulgite nanocomposite was loaded, and the material had high catalytic activity.

The attapulgite modified with TiO₂ was calcined at 300°C for 2 h, and the degradation rate of 80 mg/L methylene blue was 99.8%. The experimental results show that the ozone, temperature and mass transfer factors are excluded, so the effects of temperature, MB concentration and pH on the degradation of methylene blue are investigated. The optimal reaction conditions are as follows: The ozone concentration is 0.067 g/min; the ozone flow rate is 0.15 NL/min; the stirrer rotation speed is 550 r/min; catalyst is 0.1 g; the temperature is 50°C.

The decolorization process of MB is quasi-first-order kinetics, and the kinetic equation is obtained with E_a 46.646 kJ/mol.

DATA AVAILABILITY STATEMENT

The original contributions presented in the study are included in the article/supplementary material, further inquiries can be directed to the corresponding author.

REFERENCES

- Achari, V. S., Lopez, R. M., Rajalakshmi, A. S., Jayasree, S., Shibin, O. M., John, D., et al. (2021). Microporous Carbon with Highly Dispersed Nano-Lanthanum Oxide (La₂O₃) for Enhanced Adsorption of Methylene Blue. *Separat. Purif. Tech.* 279, 119626. doi:10.1016/j.seppur.2021.119626
- Chen, R., Zhang, G., and Yi, C. (2015). Experimental Study on the Degradation of oilfield Wastewater Containing polymer by Microwave Enhanced Ozone Oxidation. *Ind. Water Treat.* 3, 90–92.
- Chen, Z., Guo, T., Li, X., Chen, F., Lu, X., and Zhang, Y. (2009). Catalytic Oxidation Treatment of Methylene Blue Dye Wastewater by Attapulgite-Loaded CeO₂. *Kinetic Energ. Mater.* 10 (40), 122–137. doi:10.1016/j.catcom.2008.12.055
- Fang, Y., Li, Z., Yang, B., Xu, S., Hu, X., Liu, Q., et al. (2014). Effect of Dye Structure on Optical Properties and Photocatalytic Behaviors of Squaraine-Sensitized TiO₂ Nanocomposites. *J. Phys. Chem. C* 118, 16113–16125. doi:10.1021/jp502208y
- Fei Yin, Z., Wu, L., Gui Yang, H., and Hua Su, Y. (2013). Recent Progress in Biomedical Applications of Titanium Dioxide. *Phys. Chem. Chem. Phys.* 15, 4844–4858. doi:10.1039/c3cp43938k
- Li, X. (2007). Application of Attapulgite Clay in Wastewater Treatment. *J. Gansu United Univ.* 21 (3), 12–18. doi:10.3969/j.issn.1672-691X.2007.03.015
- Masschelein, W. (1992). *Unit Processes in Drinking Water Treatment*. New York: Marcel Dekker.
- Peng, S., Xie, J., Qing, C., Chen, T., Xu, H., Chen, J., et al. (2006). Treatment of Acid Fuchsin Dye Wastewater by TiO₂ Attapulgite Photocatalytic Oxidation Process. *J. Chin. Ceram. Soc.* 34 (10), 55–57. doi:10.3321/j.issn:0454-5648.2006.10.010
- Qiao, X. X., Liu, X. J., Zhang, W. Y., Cai, Y. L., Zhong, Z., Li, Y. F., et al. (2021). Superior Photo-Fenton Activity towards Chlortetracycline Degradation over Novel G-C₃N₄ Nanosheets/schwertmannite Nanocomposites with Accelerated Fe(III)/Fe(II) Cycling. *Separat. Purif. Tech.* 279, 119760. doi:10.1016/j.seppur.2021.119760
- Song, R., Yang, L., and Sheng, J. (2003). Surface Modification and Characterization of Nano Attapulgite. *Bull. Silicate* 22 (3), 36–39. doi:10.3969/j.issn.1001-1625.2003.03.009
- Virkutyte, J., and Varma, R. S. (2012). Visible Light Activity of Ag-Loaded and Guanidine Nitrate-Doped Nano-TiO₂: Degradation of Dichlorophenol and Antibacterial Properties. *RSC Adv.* 2, 1533–1539. doi:10.1039/c1ra00990g
- Wu, H., Liu, Y., Chen, B., Yang, F., Wang, L., Kong, Q., et al. (2021). Enhanced Adsorption of Molybdenum(VI) from Aquatic Solutions by Chitosan-Coated Zirconium-Iron Sulfide Composite Enhanced Adsorption of Molybdenum(VI) from Aquatic Solutions by Chitosan-Coated Zirconium-Iron Sulfide Composite. *Separat. Purif. Tech.* 279, 119736. doi:10.1016/j.seppur.2021.119736
- Xue, G. (2021). Technology Progress of Dyeing Wastewater Treatment. *Ind. Water Treat.* 41 (9), 10–17. doi:10.19965/j.cnki.iwt.2021-0433
- Yang, J., Wang, G., Guan, Z., Zhang, N., Tong, Y., and Li, J. (2014). Preparation and Characterization of Nano-TiO₂ Loaded with Attapulgite Clay and its Adsorption of Ni(II). *New Chem. Mater.* 7, 24–29.
- Yin, L., Lu, X., and Ai, F. (2003). Effect of Ti-Attapulgite Catalyst on Ozonation Degradation of Dye Wastewater. *J. Chin. Ceram. Soc.* 31 (1), 66–69. doi:10.3321/j.issn:0454-5648.2003.01.014
- Yu, C., He, H., Fan, Q., Xie, W., Liu, Z., and Ji, H. (2019). Novel B-Doped BiOCl Nanosheets with Exposed (001) Facets and Photocatalytic Mechanism of Enhanced Degradation Efficiency for Organic Pollutants. *Sci. Total Environ.* 694, 133727. doi:10.1016/j.scitotenv.2019.133727
- Zhang, D., Xu, B., and Zhu, P. (2013). Study on the Mechanism of Photocatalytic Degradation of Methylene Blue by TiO₂. *J. East China Normal University(Natural Science)* (9), 35–42. doi:10.3969/j.issn.1000-5641.2013.05.005
- Zhang, L., Liu, H., and Zhang, B. (2015). Mechanism of Enhancement Ozonation by Ultrasound for Degradation of Polyacrylamide in ASP Produced. *CIESC Journal* 6, 2242–2247. doi:10.11949/j.issn.0438-1157.20150085
- Zhang, W., Li, W., and Sun, W. (2008). Preparation and Characterization of Cobalt-Supported Attapulgite Catalysts Catalytic Oxidation Performance. *Mol. Catal.* 22 (4), 302–307. doi:10.16084/j.cnki.issn.1001-3555.2008.04.001

AUTHOR CONTRIBUTIONS

JS contributed to the conception of the study, experiment, data analyses and wrote the manuscript; YJ performed the experiment; XQ contributed significantly to analysis and manuscript preparation; BZ performed the data analyses; XL helped perform the analysis with constructive discussions.

ACKNOWLEDGMENTS

The authors gratefully acknowledge the Program of Key Laboratories of Fine Chemicals and Surfactants in Sichuan Provincial Universities (No. 2020JXY03), the Scientific Research Fund of Sichuan Provincial Education Department (No. 17ZA0273), and the Talent Introduction Fund of Sichuan University of Science and Engineering (No. 2015RC53).

Conflict of Interest: The authors declare that the research was conducted in the absence of any commercial or financial relationships that could be construed as a potential conflict of interest.

Publisher's Note: All claims expressed in this article are solely those of the authors and do not necessarily represent those of their affiliated organizations, or those of the publisher, the editors and the reviewers. Any product that may be evaluated in this article, or claim that may be made by its manufacturer, is not guaranteed or endorsed by the publisher.

Copyright © 2021 Shang, Jiang, Qin, Zhao and Li. This is an open-access article distributed under the terms of the Creative Commons Attribution License (CC BY). The use, distribution or reproduction in other forums is permitted, provided the original author(s) and the copyright owner(s) are credited and that the original publication in this journal is cited, in accordance with accepted academic practice. No use, distribution or reproduction is permitted which does not comply with these terms.



Decomplexation Performance of Cu-EDTA and Parameter Optimization by Three-Dimensional Electro-Fenton

Yameng Ma^{1†}, Xiao Huang^{1†*}, Qi Han², Jianghua Yu¹, Fengjiao Yu³ and Jia Zhu^{3*}

¹Collaborative Innovation Center of Atmospheric Environment and Equipment Technology, Jiangsu Key Laboratory of Atmospheric Environment Monitoring and Pollution Control, School of Environmental Science and Engineering, Nanjing University of Information Science and Technology, Nanjing, China, ²Shenzhen Academy of Environmental Sciences, Shenzhen, China, ³School of Materials and Environmental Engineering, Shenzhen Polytechnic, Shenzhen, China

OPEN ACCESS

Edited by:

Shihai Deng,
Xi'an Jiaotong University, China

Reviewed by:

Zacharias Frontistis,
University of Western Macedonia,
Greece
Zhirong Sun,
Beijing University of Technology,
China

*Correspondence:

Xiao Huang
huangxiao901231@126.com
Jia Zhu
zhujia@szpt.edu.cn

[†]These authors have contributed
equally to this work and share first
authorship

Specialty section:

This article was submitted to
Water and Wastewater Management,
a section of the journal
Frontiers in Environmental Science

Received: 19 November 2021

Accepted: 04 January 2022

Published: 25 January 2022

Citation:

Ma Y, Huang X, Han Q, Yu J, Yu F and
Zhu J (2022) Decomplexation
Performance of Cu-EDTA and
Parameter Optimization by Three-
Dimensional Electro-Fenton.
Front. Environ. Sci. 10:818142.
doi: 10.3389/fenvs.2022.818142

The strong stability of Cu-ethylenediaminetetraacetic acid (Cu-EDTA) results in the low decomplexation efficiency by the traditional Fenton process. For breaking this limitation, a three-dimensional electro-Fenton (3D-EF) system was constructed to study the decomplexation of Cu-EDTA at different pH, and the effects of Fe²⁺ concentration, particle electrode dosage, current density, and coexisting ions on decomplexation performance were investigated. The results showed that 3D-EF exhibited high pollutant removal efficiency in a wide pH range compared with the traditional electro-Fenton process. The optimal conditions for the removal of Cu-EDTA were as follows: the pH was 7, Fe²⁺ was 1 mmol L⁻¹, granular activated carbon was 2 g L⁻¹, and current density was 10 mA cm⁻², and the optimum Cu-EDTA removal efficiency reached 90.95%. In addition, the presence of Cl⁻ slightly improved the decomplexation efficiency, whereas NO₃⁻ and HPO₄²⁻ inhibited the removal of Cu-EDTA. The kinetics of Cu-EDTA decomplexation in all experimental groups followed the first-order kinetic equation.

Keywords: Cu-EDTA, three-dimensional electro-Fenton, decomplexation, parameter optimization, electrochemical

INTRODUCTION

The chelator ethylenediaminetetraacetic acid (EDTA) is widely used in electroplating, metallurgical, and chemical cleaning industries to form stable complexes with heavy metals of different structures (Wang et al., 2019; Wang Y. et al., 2020). Their efficient removals remain a key challenge in the field of wastewater treatment. Cu-ethylenediaminetetraacetic acid (Cu-EDTA), a strong stability complex compound in wide pH range of wastewater, poses potential hazards to water, soil environments, and human health (Song et al., 2021), and it is difficult to remove from wastewater by chemical precipitation and other processes. Therefore, appropriate methods should be taken to overcome this problem (Hu et al., 2021; Wang and Chen, 2021; Wang and Tang, 2021).

Some promising treatment methods for removing the stable complex from wastewater have received extensive attention, such as electro-coagulation (Xie et al., 2020), nonthermal plasma oxidation (Wang et al., 2019; Liu et al., 2021), photo-electrocatalytic oxidation (He et al., 2021; Shah and Patel, 2021), ozone-based oxidation (Zhao et al., 2018a; Guan et al., 2022), and microwave-assisted Fenton reaction (Wang H. et al., 2020; Xia et al., 2021). Electrochemical advanced oxidation processes (EAOPs) are sought-after for many researchers due to their high degradation efficiency, versatility, and environmental friendliness (Wang and Zhuan, 2020; Wang and Chen, 2021; Wang

and Wang, 2021). The hydroxyl radical ($\cdot\text{OH}$) produced from the electro-Fenton (EF) process by the reaction of Fe^{2+} and H_2O_2 solution owns the characteristics of strong oxidation, high reactivity, easy formation, non-selectivity, and harmlessness, which has been proved to have perfect removal performance for the stable complex in wastewater (Wang and Wang, 2018; Chen and Wang, 2021). Chu et al. (2022) prepared several composite cathodes using graphite, carbon nanotube, and polytetrafluoroethylene, and the degradation efficiency of cefepime reached nearly 100% at pH 3.0. Zhang et al. (2022) synthesized a novel core-shell $\text{Fe@Fe}_2\text{O}_3\text{-CeO}_2$ composite for effective degradation of the tetracycline (TC) pollutant, and TC removal efficiency reached 90.7% within 1 h at the optimum pH of 3.85. Midassi et al. (2020) used the carbon-felt cathode and boron-doped diamond anode to completely remove chloroquine at pH 3.0. Hence, three-dimensional electro-Fenton (3D-EF) is appropriate for refractory organics removal, and whether it owns the same decomplexation efficiency on Cu-EDTA needs to be further studied.

The EF reaction could produce high activity only in a narrow pH range (may be in pH 2.5–3.5), which greatly limits the application of EF technology. In order to solve the problems, the 3D-EF system has been constructed by adding particle electrodes between the anode and cathode. It was reported that the rhodamine B removal reached 91.6% in the 3D-EF system in the presence of Fe-Cu/kaolin particle electrodes (Zhang et al., 2019). Iron foam was used as the particle electrode in a 3D-EF system in the study of Zheng et al. (2019) and found that the chemical oxygen demand (COD) and total nitrogen (TN) removal percentage in folic acid wastewater reached 43.5 and 70.4%, respectively, under the following optimal conditions: the initial COD concentration of 10 g L^{-1} , applied current of 0.3 A, initial pH of 3, and particle electrode of 4 g. It is noteworthy that the Long's team reported that the diclofenac removal rate reached 96.3% in the presence of manganese slag-loaded active substance as a particle electrode (Long et al., 2019). Among them, it can be noted the work of Li M. et al. (2021), who prepared Cu-Fe bimetallic aerogel-like carbon as a catalytic particle electrode based on sodium alginate to remove 81.1% of fulvic acids at pH 5.4, voltage 2.5, and catalyst dosage of 4 g L^{-1} .

In the 3D-EF system, the electrode plate, pH, Fe^{2+} , particle electrodes, current density, and coexisting ions could affect the efficiency of pollutant removal. Among them, the electrode material plays a decisive role in the generation of OH, which is a key factor in the wastewater treatment by EF (Ou et al., 2019). According to the reports, graphite electrode plates (carbon materials) have been widely examined and regarded as the most efficient electrode plates (Zhang et al., 2019; Zhang B. et al., 2019; Song et al., 2020). Graphite material plates showed better removal effect for some refractory organics, but less research was carried out on Cu-EDTA using graphite polar plates. Due to the unique functional group structure on the surface of graphite (carbon materials), organics decompose through free radical-induced pathways (Duan et al., 2018). Compared with other electrodes, graphite electrodes are easier to obtain, low-cost, nontoxic, and own a high specific surface

area, which will be cost-effective in electrochemical analysis (Le et al., 2017; Zhao K. et al., 2018). In addition, the excellent electrical conductivity of graphite makes it an ideal candidate for electrodes (Pan et al., 2020; Tasić et al., 2021).

In this study, a 3D-EF system with granular-activated carbon (GAC) as the particle electrode was used to remove Cu-EDTA. The effects of main parameters (the pH value of initial solution, Fe^{2+} concentration, particle electrode dosage, current density, and coexisting ions) on the decomplexation performance of Cu-EDTA were optimized. In addition, the reaction kinetics for all optimization processes were fitted. This study provides a new idea for the decomplexation of Cu-EDTA and other complexes, and provides a suitable way for the treatment of complex heavy metal complexes.

MATERIALS AND METHODS

Chemicals

All the reagents used in this study were of analytical grade. Ethylenediaminetetraacetic acid disodium salt ($\text{C}_{10}\text{H}_{14}\text{N}_2\text{Na}_2\text{O}_8 \cdot 2\text{H}_2\text{O}$) was purchased from Shanghai Macklin Biochemical Co., Ltd. (Shanghai, China). Copper sulfate ($\text{CuSO}_4 \cdot 5\text{H}_2\text{O}$), sodium chloride (NaCl), sodium nitrate (NaNO_3), disodium hydrogen phosphate ($\text{Na}_2\text{HPO}_4 \cdot 12\text{H}_2\text{O}$), and sodium sulfate (Na_2SO_4) were purchased from Tianjin Damao Chemical Reagent Factory. (Tianjin, China). Sodium hydroxide (NaOH) was purchased from Shantou Xilong Scientific Co., Ltd. (Shantou, China). Sulfuric acid (H_2SO_4) was purchased from Hengyang Kaixin Chemical Reagent Co., Ltd. (Hengyang, China). GAC was obtained from Shanghai Aladdin Inc. (Shanghai, China). The particle size of GAC is approximately 0.6–2 mm. Solutions were prepared with Milli-Q water.

Experimental Setup

In this study, the experimental device consists of a 5 A, -30 V DC-regulated power supply (HXD-305DM), 500-ml beaker, and magnetic stirrer (IKA). The polar plates were dual graphite electrode plates ($100 \times 50 \times 5\text{ mm}$) with a 70-mm plate spacing and GAC particle electrode. The graphite electrode plate and GAC were boiled in dilute acid and alkali for 30 min, ultrasonic cleaned for 20 min, and dried in an oven at 105°C for 10 h.

Experimental Procedure

The Cu-EDTA reserve solution of 50 mg L^{-1} was added into a 500-ml breaker with a volume of 300 ml solution for each experiment. Besides, 0.2 mol L^{-1} NaOH and H_2SO_4 were used to adjust the initial pH, and 0.047 mol L^{-1} Na_2SO_4 was used as the electrolyte. The reaction time was 120 min, and the samples were taken three times at 10, 30, 60, 90, and 120 min. After that, sample's pH were adjusted to 11 with H_2SO_4 or NaOH to form hydroxide precipitates of heavy metal ions to remove from the supernatant and diluted 500 times for further detection. The concentration of the remaining heavy metal complex in samples was determined by inductively coupled plasma mass

spectrometry (ICP-MS) after being filtered by a 0.22- μm membrane.

Cu-EDTA Degradation by 3D-EF

In order to prove the advantage of the 3D-EF system for the decomplexation of Cu-EDTA, a GAC system ($\text{pH} = 3$ and $\text{Fe}^{2+} = 1 \text{ mmol L}^{-1}$), EF system ($\text{pH} = 3$, $\text{Fe}^{2+} = 1 \text{ mmol L}^{-1}$, and current density 4 mA cm^{-2}), and 3D-EF system ($\text{pH} = 3$, $\text{Fe}^{2+} = 1 \text{ mmol L}^{-1}$, GAC 2 g L^{-1} , and current density 4 mA cm^{-2}) were set up. Three samples were taken at 10, 30, 60, 90 and 120 min to detect the Cu concentration.

Parameter Optimization of 3D-EF Degradation

The relevant factors include pH , Fe^{2+} , particle electrodes, and current density to assess the efficiency in removing Cu-EDTA via the 3D-EF. For investigating the effect of pH on the decomplexation of Cu-EDTA, the changes of Cu-EDTA removal efficiency in different pH ($\text{pH} = 3, 5, 7$, and 9) were investigated. Different amounts of Fe^{2+} ($0.5, 1.0, 1.5$, and $2.0 \text{ mmol L}^{-1} \text{ Fe}^{2+}$) were put into the solution to study the effect of Fe^{2+} dosages on Cu-EDTA decomplexation. This was followed up by using the most suitable pH solution obtained from the previous experiment. Subsequently, different doses of the particle electrode (doses of $1, 2, 3, 4, 5$, and 6 g L^{-1}) were added to discuss the effect of the particle electrode on the decomplexation of Cu-EDTA. The most suitable conditions such as pH , Fe^{2+} dosages, and particle electrode were prepared. A certain current density ($2, 4, 6, 8, 10$, and 12 mA cm^{-2}) was added to study its effect on Cu-EDTA decomplexation.

Effect of Coexisting Ions on Cu-EDTA Removal

The effects of coexisting ions (Cl^- , NO_3^- , and HPO_4^{2-}) were studied in terms of the most suitable conditions such as solution pH of 7 , $1 \text{ mmol L}^{-1} \text{ Fe}^{2+}$, 4 g L^{-1} GAC, and current density of 10 mA cm^{-2} .

Chemical Analytical Methods

The solution pH was measured by a pH meter (PB-10, Sartorius). During the electrolysis, samples were collected at specific time intervals for copper ion determination. If not noted otherwise, each experiment was repeated three times to ensure the repeatability of experimental results. The concentrations of copper ions were determined by inductively coupled plasma mass spectrometry (ICP-MS, NexION 2000). The conditions for the detection of copper ions were as follows: a radio frequency power of 1500 W , plasma gas flow of 15 L min^{-1} , and auxiliary gas flow of 1.0 L min^{-1} and nebulization gas flow of 1.0 L min^{-1} .

Statistical Analysis

Three replicates were conducted for each sample, and average values were calculated and shown in charts. Origin 8.6 software was used for drawing figures.

The Cu-EDTA removal rate was calculated by Eq. 1.

$$R(\%) = \left(1 - \frac{C_t}{C_0}\right) \times 100\%, \quad (1)$$

where R is the removal efficiency at time (t), C_0 is the initial concentration, and C_t is the copper ion concentration at time (t).

The term removal rate refers to the kinetic process; the Cu-EDTA decay is followed by the first-order reaction kinetics with reaction rate constants (K_{obs}) determined in min^{-1} according to Eq. 2.

$$\ln\left(\frac{C_0}{C_t}\right) = kt, \quad (2)$$

where t is the electrolysis time (min).

RESULTS AND DISCUSSION

Removal of Cu-EDTA by 3D-EF

Three different reaction systems, i.e., GAC adsorption system, EF reaction system, and 3D-EF reaction system were studied to prove the advantage of the 3D-EF process for the decomplexation of Cu-EDTA, and the results were demonstrated in Figure 1. The decomplexation efficiency of Cu-EDTA increased with the reaction time extended in all experience groups (Figure 1A), and the removal rates of Cu-EDTA were $11.37, 75.46$, and 86.81% in three groups, respectively. The 3D-EF reaction system owned higher removal efficiency than that of GAC adsorption and EF processes. From Figure 1B; Table 1, it is noted that the degradation of Cu-EDTA in all systems conformed to the first-order kinetic model, and the reaction rate constant K_{obs} of the 3D-EF, GAC, and EF were $0.0175, 0.0126$, and 0.0012 , respectively, which indicated that the 3D-EF reaction system owns a good application prospect for Cu-EDTA decomplexation. Hu et al. (2021) prepared the Ni/GO-PAC particle electrode, and Cu-EDTA degradation reached 99% at 1 mmol L^{-1} Cu-EDTA, current density of 1.6 mA cm^{-2} , and $\text{pH} = 3.15$. Also, Song et al. (2021) used $\text{RuO}_2\text{-IrO}_2/\text{Ti}$ and Al electrodes to treat Cu-EDTA wastewater, and the Cu removal efficiency reached 99.85% . Zhao et al. (2018b) explored the application of the EF technique by using iron-sacrificing electrodes, and the effluent could meet discharge standard (0.3 mg L^{-1} for Cu in China) under the initial pH of 2.0 , H_2O_2 dosage of $6 \text{ mL L}^{-1} \text{ h}^{-1}$, current density of 20 mA cm^{-2} , and sulfate electrolyte concentration of 2 g L^{-1} .

In the 3D-EF process, the additional particle electrode adsorbed pollutants, and the contaminated materials underwent electrochemical degradation on the surface of the particle electrode to achieve the efficient removal. The lower current was able to enhance the removal efficiency of pollutants, which could greatly improve the chemical reaction rate and treatment effect. Therefore, the 3D-EF reaction system exhibited better performance than the conventional EF reaction system. Theoretically, using activated carbon as the particle electrode in the EF reaction system was able to enhance Cu-EDTA removal, which was related to the particle electrode increasing the electrode specific surface area, increasing the utilization of the whole space, and improving the mass transfer effect (Zhang et al., 2018; Li H. et al., 2021), and a

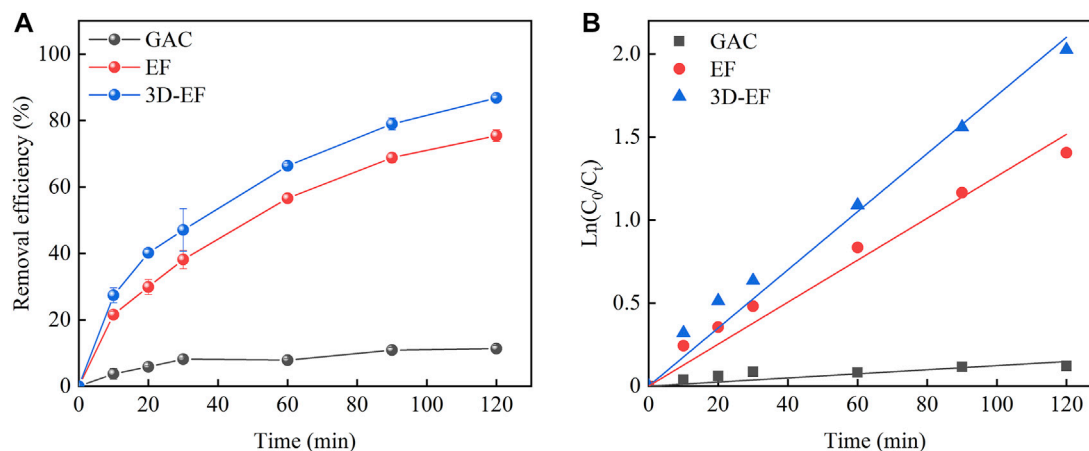


FIGURE 1 | (A) Removal efficiency of Cu-EDTA in different reaction systems and **(B)** kinetics fitting of Cu-EDTA removal in different reaction systems. (pH = 3 and $\text{Fe}^{2+} = 1 \text{ mmol L}^{-1}$).

TABLE 1 | Pseudo-first-order kinetics of Cu-EDTA removal in different reaction systems.

Reaction system	$K_{obs} (\text{min}^{-1})$	Correlation coefficient R^2
GAC	0.0012	0.8722
EF	0.0126	0.9860
3D-EF	0.0175	0.9907

synergistic strengthening effect should appear with the combination of the activated carbon and electrochemical process. However, this synergy was not obvious in this study. It might be because that the adsorption of Cu-EDTA by activated carbon was presented and occupied the active sites of the particle electrodes, and with the reaction extending, the Fe^{2+} and $\cdot\text{OH}$ on the surface of the particle electrode formed the Fenton reaction, whose products (Fe^{3+} and Cu^{2+}) took the place of these sites to inhibit the synergistic strengthening performance.

pH Application Window for Cu-EDTA Decomplexation by 3D-EF

Different initial pH conditions could affect the degradation efficiency of Cu-EDTA and is illustrated in Figure 2A. The removal efficiency of Cu-EDTA reached more than 80% at different initial pH conditions, and the removal rates of Cu-EDTA were 84.22, 88.04, 90.19, and 87.74%, when the pH ranged from 3 to 9. Among them, the Cu-EDTA removal rate reached the maximum when the pH was 7. The experimental results proved that using GAC particles as the particle electrode in a 3D-EF system broke a limitation of pH conditions, which enabled the 3D-EF reaction system to better treat various types of water quality and greatly broadened the application window of pH. The kinetics of Cu-EDTA removal at different pH conditions were fitted as shown in Figure 2B. The reaction rate constant K_{obs} of Cu-EDTA reaches maximum at pH 7 and reaction time 120 min. The reaction rate constant K_{obs} showed a tendency of increasing at first and then decreasing with the

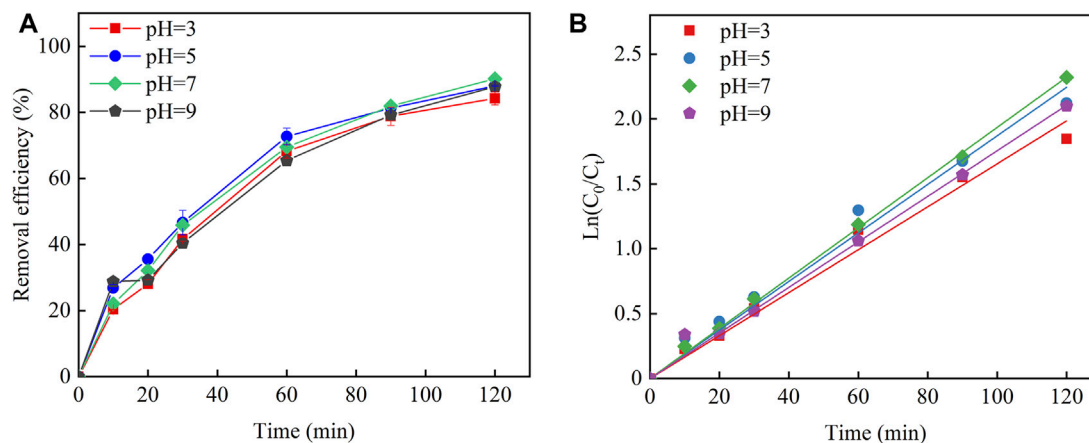


FIGURE 2 | (A) Effects of pH application on the Cu-EDTA complex-breaking removal effect of Cu-EDTA and **(B)** kinetic fitting of Cu-EDTA removal effect.

TABLE 2 | Pseudo-first-order kinetics of Cu-EDTA removal at different pH.

pH	K_{obs} (min ⁻¹)	Correlation coefficient R^2
3	0.0166	0.9920
5	0.0187	0.9916
7	0.0194	0.9993
9	0.0176	0.9963

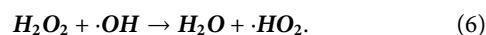
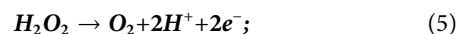
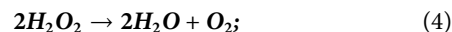
increase of the initial pH, which was the same as the removal effect of Cu-EDTA (Table 2).

The lower pH values tend to have higher pollutant removal rates in many EF studies. Shi et al. (2021) demonstrated that the removal rate of ibuprofen could reach 90.2% in 120 min at pH 3.0 and current density of 10 mA cm⁻². Also, for aniline, ciprofloxacin, and cefazolin, their removal efficiencies were more than 99, 91.30, and 95.8% under acid condition, respectively (Ma et al., 2021; Yao et al., 2021; Ghasemi et al., 2020). GAC particles, particle electrodes used in a 3D-EF system, made this system remove Cu-EDTA better under neutral conditions. The reason could be explained as follows: low pH value contributed to higher oxygen evolution potential and direct oxidation played the dominant role. However, there would be a certain side reaction of hydrogen forming in the negative area, which inevitably occupied some of the active spots (Eq. 3) (Guan et al., 2018). Under acidic conditions, the Fenton reaction occurred between Fe²⁺ and ·OH on the electrode surface of GAC particles, which could improve the oxidation ability of the whole reaction system and enhance the removal effect of Cu-EDTA. On the contrary, with the pH increase, the side effect of oxygen forming would occur in the positive area. The decomposition of H₂O₂ into H₂O and O₂ under alkaline conditions was also occurred in a certain scavenging reaction with ·OH. In turn, the ·OH on the particle electrode surface decreased and the oxidation capacity was somewhat diminished, so that the treatment efficacy decreased at high pH values (Eqs 4–6) (Zheng et al., 2019; Zhang M.-h. et al., 2019). Therefore, the operation of the 3D-EF system with GAC particles at neutral or

TABLE 3 | Pseudo-first-order kinetics parameters of removal effect of Cu-EDTA by Fe²⁺ dosage.

Fe ²⁺ (mmol L ⁻¹)	K_{obs} (min ⁻¹)	Correlation coefficient R^2
0	0.0182	0.9988
0.5	0.0204	0.9930
1.0	0.0215	0.9856
1.5	0.0169	0.9924
2.0	0.0157	0.9965

near neutral pH reduced the chemical requirements for pH regulation and reduced operating costs to achieve optimal treatment performance.

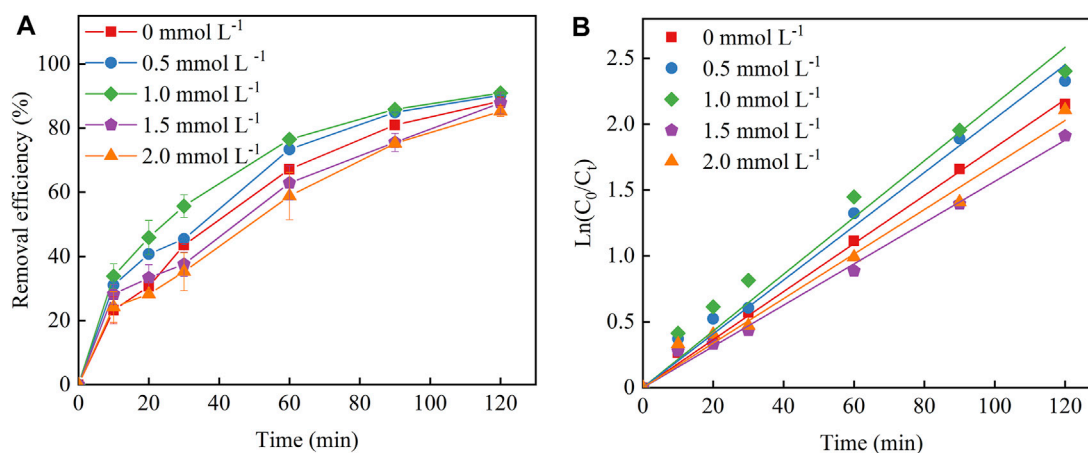


Influencing Factors of Cu-EDTA Removal by 3D-EF

Fe²⁺ Dosage

The Fe²⁺ dosage has certain influence on Cu-EDTA removal in a 3D-EF process. As shown in Figure 3A, the removal rate of Cu-EDTA presented an increasing trend first and then decreased with the increase of Fe²⁺ dosage. The highest removal efficiency could reach up to 90.95%, which was achieved at a Fe²⁺ dosage of 1 mmol L⁻¹ after 120 min reaction. Kinetic fitting of Fe²⁺ dosage for Cu-EDTA removal is shown in Figure 3B with the increase of Fe²⁺ concentration. The reaction rate constant K_{obs} also showed a trend of increasing first and then decreasing, and the reaction rate constant K_{obs} peaked at the Fe²⁺ dosage of 1 mmol L⁻¹. The reaction rate constant K_{obs} reached a maximum of 0.0215 at 1 mmol L⁻¹ Fe²⁺ (Table 3).

Fe²⁺ was the core of the 3D-EF reaction system. The removal of Cu-EDTA depended mainly on the reaction of the plate and

**FIGURE 3** | (A) Effects of Fe²⁺ dosage on the removal effect of Cu-EDTA and (B) kinetic fitting of removal effect of Cu-EDTA.

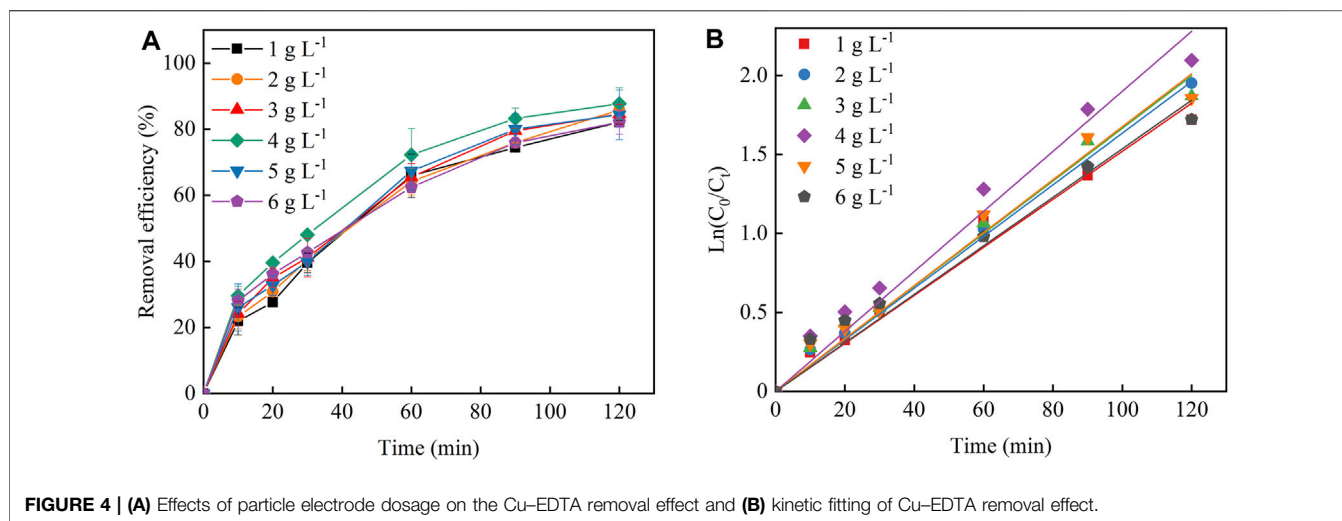
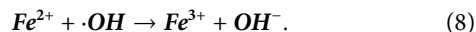
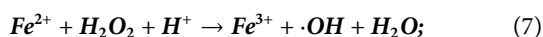


TABLE 4 | Pseudo-first-order kinetics parameters of Cu-EDTA removal with different particle electrode dosages.

Particle electrode (g L ⁻¹)	K_{obs} (min ⁻¹)	Correlation coefficient R^2
1	0.0152	0.9910
2	0.0164	0.9973
3	0.0167	0.9923
4	0.0190	0.9874
5	0.0168	0.9897
6	0.0154	0.9857

the particles without Fe²⁺ adding into this reaction system. The activity of microelectrolysis was weak with low-dosage Fe²⁺ addition, and the Cu-EDTA removal rate gradually increased with increasing Fe²⁺ dosage to generate more $\cdot\text{OH}$ through the system reaction (Eq. 7) (Feng et al., 2010; Chu et al., 2021). Too high Fe²⁺ concentration increased the contact probability of Fe²⁺ and H₂O₂ and also subsequently increased the $\cdot\text{OH}$ production. However, too much of Fe²⁺ and $\cdot\text{OH}$ produced side effects and formed Fe³⁺, which consumed a large amount of $\cdot\text{OH}$, resulting in the decline of the Cu-EDTA removal rate in the 3D-EF reaction system (Eq. 8) (Huang et al., 2020; Zhang et al., 2020).



Particle Electrode Dosage

Particle electrode loading was also another key factor affecting the 3D-EF reaction system to treat Cu-EDTA. As seen in the inset of Figure 4A, the removal rate of Cu-EDTA was similar with that of the Fe²⁺ dosage experiment group, and the highest removal rate of Cu-EDTA was 87.71% after 120 min of reaction when the particle electrode was 4 g L⁻¹ Figure 4B; Table 4 showed that the removal efficiency of the Cu-EDTA reaction rate constant K_{obs} reached a maximum value of 0.0190 at the particle electrode dosage of 4 g L⁻¹.

The particle electrode was distributed throughout the reaction system and formed microelectrode particles under the action of an electric field, which increased the specific surface area of the electrode, shortened the electrode spacing, greatly improved the mass transfer rate and current utilization efficiency, and improved the treatment capacity of pollutants (Dargahi et al., 2021). As the particle electrode increased, the surface area and the adsorption sites on the electrode increased, and then the Cu-EDTA removal efficiency increased accordingly (Wang et al., 2021). With the continuous increase of the particle electrode, the excess particle electrode occupied more space in the reaction system, which made the reaction system overloaded. In turn, the current and mass efficiencies will also be affected, such as leading to the short circuiting of the particle electrode and inhibiting the removal of contaminants (Zheng et al., 2016; Ghanbarlou et al., 2020).

Current Density

Figure 5A shows the removal effect of Cu-EDTA at different current densities. The worst removal effect of Cu-EDTA was 71.52% after 120 min at a current density of 2 mA cm⁻². With the increase of current density to 10 mA cm⁻², the best removal efficiency of Cu-EDTA was obtained with the removal rate of 87.26%. However, Cu-EDTA removal efficiency showed a decreasing trend as the current density continued to increase to 12 mA cm⁻² within the reaction system. In Figure 5B, the reaction rate constants K_{obs} at a current density of 10 mA cm⁻² were much larger than those at other current densities. From Table 5, the reaction rate constant K_{obs} reached a maximum of 0.0180 at a current density of 10 mA cm⁻².

As the current density increased within the reaction system, the electron density and H₂O₂ production on the electrode also gradually increased, and Fe²⁺ reacted with H₂O₂ to generate $\cdot\text{OH}$ (Eq. 9). Moreover, the removal of Cu-EDTA gradually increased because the electron transfer between electrodes increased and accelerated the progress of its direct oxidation reaction on the electrode surface (Barhoumi et al., 2016; Moreira et al., 2019). Further increasing current density did not significantly improve

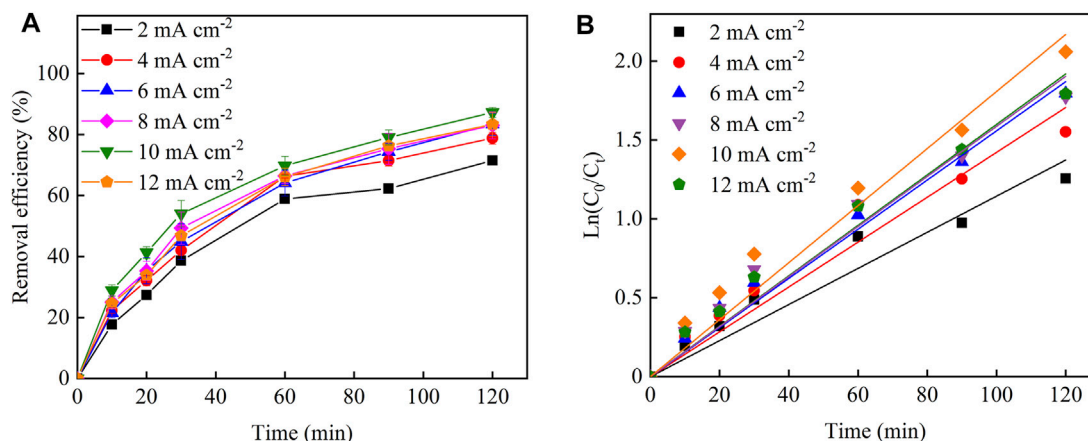
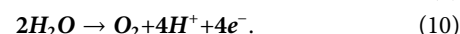


FIGURE 5 | (A) Effects of current density on the removal efficiency of Cu-EDTA and (B) kinetic fitting of removal effect of Cu-EDTA.

TABLE 5 | Pseudo-first-order kinetics parameters of Cu-EDTA removal with different current density.

Current density (mA cm ⁻²)	K_{obs} (min ⁻¹)	Correlation coefficient R^2
2	0.0115	0.9706
4	0.0142	0.9759
6	0.0156	0.9905
8	0.0159	0.9817
10	0.0180	0.9823
12	0.0160	0.9872

the removal efficiency of Cu-EDTA because excess H_2O_2 was a scavenger of $\cdot OH$. The high current density would accelerate the decomposition of H_2O_2 and promote the occurrence of competitive side reactions such as hydrogen evolution (Eq. 3) and oxygen evolution (Eq. 10) resulting in the decrease of the concentration of $\cdot OH$ (Zhang et al., 2020; Zhang et al., 2022).



Coexisting Ions

The efficiency of the 3D-EF reaction system was affected by all kinds of ions in wastewater, which could accelerate the decomposition rate of H_2O_2 through competitive adsorption. The images as shown in Figure 6A further supported that the coexistent Cl^- could promote the removal of pollutions in the 3D-EF reaction system. After 120 min, the Cu-EDTA removal rate reached 87% in the control group, and the experiment group after adding Cl^- could achieve 87.55% removal efficiency, which was slightly improved by 0.55% compared with that of the control group. Hence, it can be concluded that Cl^- owned a certain promoting effect on the removal of Cu-EDTA by the 3D-EF process. However, the removal efficiency of Cu-EDTA was 85.45 and 82.90%, respectively, when NO_3^- and HPO_4^{2-} were added into the reaction system for 120 min, which was 1.55 and 4.1%

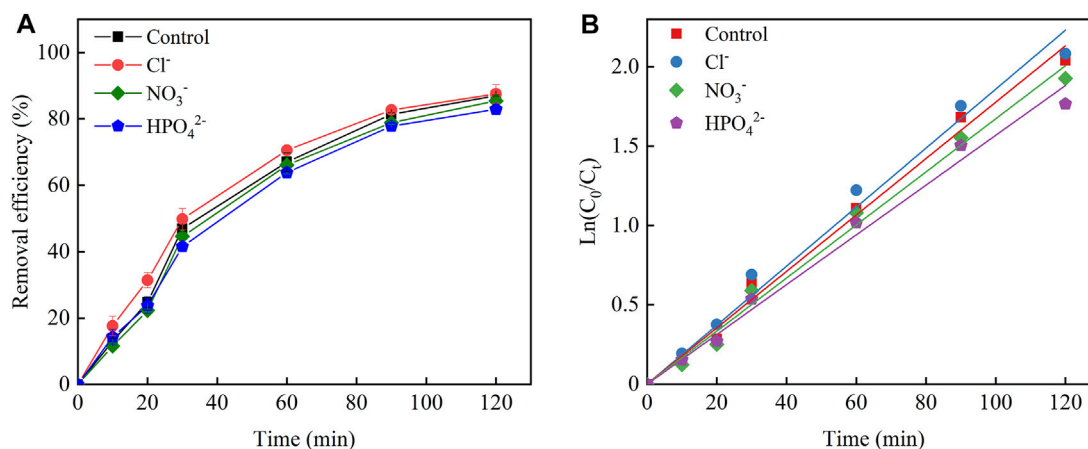


FIGURE 6 | (A) Effects of coexisting ions on the removal efficiency of Cu-EDTA and (B) kinetic fitting of removal effect of Cu-EDTA.

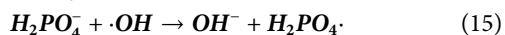
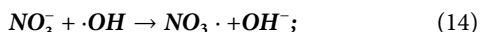
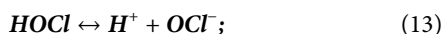
TABLE 6 | Pseudo-first-order kinetics parameters of Cu-EDTA removal with coexisting ions.

Coexisting ions	K_{obs} (min ⁻¹)	Correlation coefficient R^2
Control group	0.0178	0.9955
Cl ⁻	0.0186	0.9930
NO ₃ ⁻	0.0167	0.9953
HPO ₄ ²⁻	0.0157	0.9942

lower than that of the control group. This phenomenon reflected that NO₃⁻ and HPO₄²⁻ could inhibit the removal of Cu-EDTA.

From **Figure 6B**, the slope of the reaction system with the addition of the Cl⁻ group was larger than that of the control group, while the slopes of the reaction system with the addition of NO₃⁻ and HPO₄²⁻ groups were smaller than those of the control group. The reaction rate constant K_{obs} of 0.0186 for the addition of the Cl⁻ group was larger than that of the control group (0.0178) and so as the addition of NO₃⁻ and HPO₄²⁻ groups (0.0167 and 0.0157, respectively) (**Table 6**).

It was noticed that a certain promotion of Cu-EDTA removal was found after the addition of Cl⁻, which was related to the reactive chlorine species generated in this reaction system. Because the active species generated after the addition of Cl⁻ exhibited a higher lifetime than ·OH, the diffusion of active species played a promoting role for Cu-EDTA removal (Rommozzi et al., 2020; Mandal et al., 2020). Cl⁻ involved in the hydrogen evolution reaction in the anode region to form Cl₂ and underwent further hydrolysis to form highly oxidized ClO⁻ promoting the removal of Cu-EDTA (**Eqs 11–13**). NO₃⁻ and HPO₄²⁻ would have a competitive electronic effect with Cu-EDTA, and NO₃⁻ and HPO₄²⁻ were also able to scavenge a certain ·OH, which in turn generated more reactive NO₃· and H₂PO₄· leading to a decrease in Cu-EDTA removal effect (**Eqs 14, 15**) (Cheng et al., 2017; Teng et al., 2021). Therefore, NO₃⁻ and HPO₄²⁻ would inhibit Cu-EDTA removal in the 3D-EF reaction system.



REFERENCES

- Barhoumi, N., Oturan, N., Olvera-Vargas, H., Brillas, E., Gadri, A., Ammar, S., et al. (2016). Pyrite as a Sustainable Catalyst in Electro-Fenton Process for Improving Oxidation of Sulfamethazine. Kinetics, Mechanism and Toxicity Assessment. *Water Res.* 94, 52–61. doi:10.1016/j.watres.2016.02.042
- Chen, H., and Wang, J. (2021). Degradation and Mineralization of Ofloxacin by Ozonation and Peroxone (O₃/H₂O₂) Process. *Chemosphere* 269, 128775. doi:10.1016/j.chemosphere.2020.128775
- Cheng, T.-H., Huang, C.-P., Huang, Y.-H., and Shih, Y.-J. (2017). Kinetic Study and Optimization of Electro-Fenton Process for Dissolution and Mineralization of Ion Exchange Resins. *Chem. Eng. J.* 308, 954–962. doi:10.1016/j.cej.2016.09.142

CONCLUSION

In this study, the 3D-EF reaction system using GAC particles as particle electrodes could effectively achieve the goal of Cu-EDTA decomplexation. The performance of Cu-EDTA decomplexation by 3D-EF was better than that by the GAC and EF with a decomplexation efficiency of 90.95%, which broke the pH limit of the traditional EF reaction system and widened the application window of pH. Cu-EDTA was optimally treated at an initial pH of 7, 1 mmol L⁻¹ Fe²⁺, 4 g L⁻¹ GAC, and current density of 10 mA cm⁻². In addition, Cl⁻ promoted the removal of Cu-EDTA in the 3D-EF reaction system; however, NO₃⁻ and HPO₄²⁻ inhibited Cu-EDTA removal.

DATA AVAILABILITY STATEMENT

The original contributions presented in the study are included in the article/supplementary material, further inquiries can be directed to the corresponding authors.

AUTHOR CONTRIBUTIONS

YM contributed to data curation, methodology, writing—original draft, and writing—review and editing; XH designed all experiments and revised and examined the manuscript; JY contributed to review and editing; FY contributed to data curation and investigation; and JZ interpreted the data and resources. All authors read and approved the final manuscript.

FUNDING

This work was supported by a project grant from the National Natural Science Foundation of China (421078064), Urban Smart Water Pollution Prevention and Control Technology Development Center, Project Source: Department of Education of Guangdong Province (2019GGCZX007), Project of Shenzhen Science and Technology Plan (KJYY20180206180737010), University-Level Supporting Projects by Shenzhen Polytechnic (6020320003K), Startup Foundation for Introducing Talent of NUIST, and Natural Science Fund Project of Colleges in Jiangsu Province (20KJB610010).

- Chu, Y., Su, H., Liu, C., and Zheng, X. (2022). Fabrication of sandwich-like Super-hydrophobic Cathode for the Electro-Fenton Degradation of Cefepime: H₂O₂ Electro-Generation, Degradation Performance, Pathway and Biodegradability Improvement. *Chemosphere* 286, 131669. doi:10.1016/j.chemosphere.2021.131669
- Chu, Y., Su, H., Lv, R., and Zhang, X. (2021). Enhanced Electro-Reduction of Fe³⁺ to Fe²⁺ by Acidified Carbon Nanotube-Modified Graphite Cathode and its Application in a Novel Fenton Process for P-Nitrophenol Degradation. *J. Water Process Eng.* 40, 101912. doi:10.1016/j.jwpe.2020.101912
- Dargahi, A., Hasani, K., Mokhtari, S. A., Vosoughi, M., Moradi, M., and Vaziri, Y. (2021). Highly Effective Degradation of 2,4-Dichlorophenoxyacetic Acid Herbicide in a Three-Dimensional Sono-Electro-Fenton (3D/SEF) System Using Powder Activated Carbon (PAC)/Fe₃O₄ as Magnetic Particle Electrode. *J. Environ. Chem. Eng.* 9 (5), 105889. doi:10.1016/j.jece.2021.105889

- Duan, X., Sun, H., Shao, Z., and Wang, S. (2018). Nonradical Reactions in Environmental Remediation Processes: Uncertainty and Challenges. *Appl. Catal. B: Environ.* 224, 973–982. doi:10.1016/j.apcatb.2017.11.051
- Feng, C.-H., Li, F.-B., Mai, H.-J., and Li, X.-Z. (2010). Bio-electro-Fenton Process Driven by Microbial Fuel Cell for Wastewater Treatment. *Environ. Sci. Technol.* 44, 1875–1880. doi:10.1021/es9032925
- Ghanbarlou, H., Nasernejad, B., Nikbakht Fini, M., Simonsen, M. E., and Muff, J. (2020). Synthesis of an Iron-Graphene Based Particle Electrode for Pesticide Removal in Three-Dimensional Heterogeneous Electro-Fenton Water Treatment System. *Chem. Eng. J.* 395, 125025. doi:10.1016/j.cej.2020.125025
- Ghasemi, M., Khataee, A., Gholami, P., Soltani, R. D. C., Hassani, A., and Orooji, Y. (2020). In-situ Electro-Generation and Activation of Hydrogen Peroxide Using a CuFeNLDH-CNTs Modified Graphite Cathode for Degradation of Cefazolin. *J. Environ. Manage.* 267, 110629. doi:10.1016/j.jenvman.2020.110629
- Guan, W., Zhang, B., Tian, S., and Zhao, X. (2018). The Synergism between Electro-Fenton and Electrocoagulation Process to Remove Cu-EDTA. *Appl. Catal. B: Environ.* 227, 252–257. doi:10.1016/j.apcatb.2017.12.036
- Guan, Z., Guo, Y., Huang, Z., Liao, X., Chen, S., Ou, X., et al. (2022). Simultaneous and Efficient Removal of Organic Ni and Cu Complexes from Electroless Plating Effluent Using Integrated Catalytic Ozonation and Chelating Precipitation Process in a Continuous Pilot-Scale System. *Chem. Eng. J.* 428, 131250. doi:10.1016/j.cej.2021.131250
- He, S., Li, T., Zhang, L., Zhang, X., Liu, Z., Zhang, Y., et al. (2021). Highly Effective Photocatalytic Decomplexation of Cu-EDTA by MIL-53(Fe): Highlight the Important Roles of Fe. *Chem. Eng. J.* 424, 130515. doi:10.1016/j.cej.2021.130515
- Hu, X., Yang, S., You, X., Zhang, W., Liu, Y., and Liang, W. (2022). Electrocatalytic Decomplexation of Cu-EDTA and Simultaneous Recovery of Cu with Ni/GO-PAC Particle Electrode. *Chem. Eng. J.* 428, 131468. doi:10.1016/j.cej.2021.131468
- Huang, A., Zhi, D., Tang, H., Jiang, L., Luo, S., and Zhou, Y. (2020). Effect of Fe²⁺, Mn²⁺ Catalysts on the Performance of Electro-Fenton Degradation of Antibiotic Ciprofloxacin, and Expanding the Utilizing of Acid Mine Drainage. *Sci. Total Environ.* 720, 137560. doi:10.1016/j.scitotenv.2020.137560
- Le, T. X. H., Bechelany, M., and Cretin, M. (2017). Carbon Felt Based-Electrodes for Energy and Environmental Applications: A Review. *Carbon* 122, 564–591. doi:10.1016/j.carbon.2017.06.078
- Li, H., Yang, H., Cheng, J., Hu, C., Yang, Z., and Wu, C. (2021). Three-dimensional Particle Electrode System Treatment of Organic Wastewater: A General Review Based on Patents. *J. Clean. Prod.* 308, 127324. doi:10.1016/j.jclepro.2021.127324
- Li, M., Qin, X., Cui, J., Guo, R., Guo, C., Wang, Z., et al. (2021). Three-dimensional Electro-Fenton Degradation for Fulvic Acids with Cu-Fe Bimetallic Aerogel-like Carbon as Particle Electrode and Catalyst: Electrode Preparation, Operation Parameter Optimization and Mechanism. *J. Environ. Chem. Eng.* 9, 105573. doi:10.1016/j.jece.2021.105573
- Liu, Y., Wang, D., Xue, M., Song, R., Zhang, Y., Qu, G., et al. (2021). High-efficient Decomplexation of Cu-EDTA and Cu Removal by High-Frequency Non-thermal Plasma Oxidation/alkaline Precipitation. *Sep. Purif. Tech.* 257, 117885. doi:10.1016/j.seppur.2020.117885
- Long, Y., Feng, Y., Li, X., Suo, N., Chen, H., Wang, Z., et al. (2019). Removal of Diclofenac by Three-Dimensional electro-Fenton-persulfate (3D electro-Fenton-PS). *Chemosphere* 219, 1024–1031. doi:10.1016/j.chemosphere.2018.12.054
- Ma, B., Lv, W., Li, J., Yang, C., Tang, Q., and Wang, D. (2021). Promotion Removal of Aniline with Electro-Fenton Processes Utilizing Carbon Nanotube 3D Morphology Modification of an Ag-Loaded Copper Foam Cathode. *J. Water Process Eng.* 43, 102295. doi:10.1016/j.jwpe.2021.102295
- Mandal, P., Gupta, A. K., and Dubey, B. K. (2020). Role of Inorganic Anions on the Performance of Landfill Leachate Treatment by Electrochemical Oxidation Using graphite/PbO₂ Electrode. *J. Water Process Eng.* 33, 101119. doi:10.1016/j.jwpe.2019.101119
- Midassi, S., Bedoui, A., and Bensalah, N. (2020). Efficient Degradation of Chloroquine Drug by Electro-Fenton Oxidation: Effects of Operating Conditions and Degradation Mechanism. *Chemosphere* 260, 127558. doi:10.1016/j.chemosphere.2020.127558
- Moreira, J., Bocalon Lima, V., Athie Goulart, L., and Lanza, M. R. V. (2019). Electrosynthesis of Hydrogen Peroxide Using Modified Gas Diffusion Electrodes (MGDE) for Environmental Applications: Quinones and Azo Compounds Employed as Redox Modifiers. *Appl. Catal. B: Environ.* 248, 95–107. doi:10.1016/j.apcatb.2019.01.071
- Ou, B., Wang, J., Wu, Y., Zhao, S., and Wang, Z. (2019). A Highly Efficient Cathode Based on Modified Graphite Felt for Aniline Degradation by Electro-Fenton. *Chemosphere* 235, 49–57. doi:10.1016/j.chemosphere.2019.06.144
- Pan, Z., Yu, F., Li, L., Liu, M., Song, C., Yang, J., et al. (2020). Low-cost Electrochemical Filtration Carbon Membrane Prepared from Coal via Self-Bonding. *Chem. Eng. J.* 385, 123928. doi:10.1016/j.cej.2019.123928
- Rommozzi, E., Giannakis, S., Giovannetti, R., Vione, D., and Pulgarin, C. (2020). Detrimental vs. Beneficial Influence of Ions during Solar (SODIS) and Photo-Fenton Disinfection of E. coli in Water: (Bi)carbonate, Chloride, Nitrate and Nitrite Effects. *Appl. Catal. B: Environ.* 270, 118877. doi:10.1016/j.apcatb.2020.118877
- Shah, B. R., and Patel, U. D. (2021). Mechanistic Aspects of Photocatalytic Degradation of Lindane by TiO₂ in the Presence of Oxalic Acid and EDTA as Hole-Scavengers. *J. Environ. Chem. Eng.* 9, 105458. doi:10.1016/j.jece.2021.105458
- Shi, K., Wang, Y., Xu, A., Zhou, X., Zhu, H., Wei, K., et al. (2021). Efficient Degradation of Ibuprofen by Electro-Fenton with Microtubular Gas-Diffusion Electrodes Synthesized by Wet-Spinning Method. *J. Electroanalytical Chem.* 897, 115615. doi:10.1016/j.jelechem.2021.115615
- Song, D., Li, J., Wang, Z., and Zhao, C. (2020). Performance of Graphite Felt as Anodes in the Electro-Fenton Oxidation Systems: Changes in Catalysis, Conductivity and Adsorption Properties. *Appl. Surf. Sci.* 532, 147450. doi:10.1016/j.apsusc.2020.147450
- Song, P., Sun, C., Wang, J., Ai, S., Dong, S., Sun, J., et al. (2022). Efficient Removal of Cu-EDTA Complexes from Wastewater by Combined Electrooxidation and Electrocoagulation Process: Performance and Mechanism Study. *Chemosphere* 287, 131971. doi:10.1016/j.chemosphere.2021.131971
- Tasić, Z. Z., Petrović Mihajlović, M. B., Simonović, A. T., Radovanović, M. B., and Antonijević, M. M. (2021). Review of Applied Surface Modifications of Pencil Graphite Electrodes for Paracetamol Sensing. *Results Phys.* 22, 103911. doi:10.1016/j.rinp.2021.103911
- Teng, X., Li, J., Wang, J., Liu, J., Ge, X., and Gu, T. (2021). Effective Degradation of Atrazine in Wastewater by Three-Dimensional Electrochemical System Using Fly Ash-Red Mud Particle Electrode: Mechanism and Pathway. *Sep. Purif. Tech.* 267, 118661. doi:10.1016/j.seppur.2021.118661
- Wang, H., Zhao, Z., Zhang, X., Dong, W., Cao, Z., He, L., et al. (2020). Rapid Decomplexation of Ni-EDTA by Microwave-Assisted Fenton Reaction. *Chem. Eng. J.* 381, 122703. doi:10.1016/j.cej.2019.122703
- Wang, J., and Chen, X. (2021). Removal of Antibiotic Resistance Genes (ARGs) in Various Wastewater Treatment Processes: An Overview. *Crit. Rev. Environ. Sci. Tech.* 1, 1–60. doi:10.1080/10643389.2020.1835124
- Wang, J., and Tang, J. (2021). Fe-based Fenton-like Catalysts for Water Treatment: Preparation, Characterization and Modification. *Chemosphere* 276, 130177. doi:10.1016/j.chemosphere.2021.130177
- Wang, J., and Wang, S. (2018). Activation of Persulfate (PS) and Peroxymonosulfate (PMS) and Application for the Degradation of Emerging Contaminants. *Chem. Eng. J.* 334, 1502–1517. doi:10.1016/j.cej.2017.11.059
- Wang, J., and Wang, S. (2021). Effect of Inorganic Anions on the Performance of Advanced Oxidation Processes for Degradation of Organic Contaminants. *Chem. Eng. J.* 411, 128392. doi:10.1016/j.cej.2020.128392
- Wang, J., and Zhuang, R. (2020). Degradation of Antibiotics by Advanced Oxidation Processes: An Overview. *Sci. Total Environ.* 701, 135023. doi:10.1016/j.scitotenv.2019.135023
- Wang, Q., Yu, J., Chen, X., Du, D., Wu, R., Qu, G., et al. (2019). Non-thermal Plasma Oxidation of Cu(II)-EDTA and Simultaneous Cu(II) Elimination by Chemical Precipitation. *J. Environ. Manage.* 248, 109237. doi:10.1016/j.jenvman.2019.07.008
- Wang, Y., Liu, Y., Wu, B., Rui, M., Liu, J., and Lu, G. (2020). Comparison of Toxicity Induced by EDTA-Cu after UV/H₂O₂ and UV/persulfate Treatment: Species-specific and Technology-dependent Toxicity. *Chemosphere* 240, 124942. doi:10.1016/j.chemosphere.2019.124942
- Wang, Z., Song, B., Li, J., and Teng, X. (2021). Degradation of Norfloxacin Wastewater Using Kaolin/steel Slag Particle Electrodes: Performance, Mechanism and Pathway. *Chemosphere* 270, 128652. doi:10.1016/j.chemosphere.2020.128652
- Xia, H., Li, C., Yang, G., Shi, Z., Jin, C., He, W., et al. (2022). A Review of Microwave-Assisted Advanced Oxidation Processes for Wastewater Treatment. *Chemosphere* 287, 131981. doi:10.1016/j.chemosphere.2021.131981

- Xie, S., Shao, W., Zhan, H., Wang, Z., Ge, C., Li, Q., et al. (2020). Cu(II)-EDTA Removal by a Two-step Fe(0) Electrocoagulation in Near Natural Water: Sequent Transformation and Oxidation of EDTA Complexes. *J. Hazard. Mater.* 392, 122473. doi:10.1016/j.jhazmat.2020.122473
- Yao, B., Luo, Z., Yang, J., Zhi, D., and Zhou, Y. (2021). FeII/FeIII Layered Double Hydroxide Modified Carbon Felt Cathode for Removal of Ciprofloxacin in Electro-Fenton Process. *Environ. Res.* 197, 111144. doi:10.1016/j.envres.2021.111144
- Zhang, B., Hou, Y., Yu, Z., Liu, Y., Huang, J., Qian, L., et al. (2019). Three-dimensional Electro-Fenton Degradation of Rhodamine B with Efficient Fe-Cu/kaolin Particle Electrodes: Electrodes Optimization, Kinetics, Influencing Factors and Mechanism. *Sep. Purif. Tech.* 210, 60–68. doi:10.1016/j.seppur.2018.07.084
- Zhang, J., Qiu, S., Feng, H., Hu, T., Wu, Y., Luo, T., et al. (2022). Efficient Degradation of Tetracycline Using Core-Shell Fe@Fe₂O₃-CeO₂ Composite as Novel Heterogeneous Electro-Fenton Catalyst. *Chem. Eng. J.* 428, 131403. doi:10.1016/j.cej.2021.131403
- Zhang, M.-h., Dong, H., Zhao, L., Wang, D.-x., and Meng, D. (2019). A Review on Fenton Process for Organic Wastewater Treatment Based on Optimization Perspective. *Sci. Total Environ.* 670, 110–121. doi:10.1016/j.scitotenv.2019.03.180
- Zhang, Y., Chen, Z., Wu, P., Duan, Y., Zhou, L., Lai, Y., et al. (2020). Three-dimensional Heterogeneous Electro-Fenton System with a Novel Catalytic Particle Electrode for Bisphenol A Removal. *J. Hazard. Mater.* 393, 120448. doi:10.1016/j.jhazmat.2019.03.067
- Zhao, K., Su, Y., Quan, X., Liu, Y., Chen, S., and Yu, H. (2018). Enhanced H₂O₂ Production by Selective Electrochemical Reduction of O₂ on Fluorine-Doped Hierarchically Porous Carbon. *J. Catal.* 357, 118–126. doi:10.1016/j.jcat.2017.11.008
- Zhao, Z., Dong, W., Wang, H., Chen, G., Tang, J., and Wu, Y. (2018b). Simultaneous Decomplexation in Blended Cu(II)/Ni(II)-EDTA Systems by Electro-Fenton Process Using Iron Sacrificing Electrodes. *J. Hazard. Mater.* 350, 128–135. doi:10.1016/j.jhazmat.2018.02.025
- Zhao, Z., Liu, Z., Wang, H., Dong, W., and Wang, W. (2018a). Sequential Application of Fenton and Ozone-Based Oxidation Process for the Abatement of Ni-EDTA Containing Nickel Plating Effluents. *Chemosphere* 202, 238–245. doi:10.1016/j.chemosphere.2018.03.090
- Zheng, T., Wang, Q., Shi, Z., Fang, Y., Shi, S., Wang, J., et al. (2016). Advanced Treatment of Wet-Spun Acrylic Fiber Manufacturing Wastewater Using Three-Dimensional Electrochemical Oxidation. *J. Environ. Sci.* 50, 21–31. doi:10.1016/j.jes.2016.03.020
- Zheng, Y., Qiu, S., Deng, F., Zhu, Y., Li, G., and Ma, F. (2019). Three-dimensional Electro-Fenton System with Iron Foam as Particle Electrode for Folic Acid Wastewater Pretreatment. *Sep. Purif. Tech.* 224, 463–474. doi:10.1016/j.seppur.2019.05.054

Conflict of Interest: The authors declare that the research was conducted in the absence of any commercial or financial relationships that could be construed as a potential conflict of interest.

Publisher's Note: All claims expressed in this article are solely those of the authors and do not necessarily represent those of their affiliated organizations, or those of the publisher, the editors, and the reviewers. Any product that may be evaluated in this article, or claim that may be made by its manufacturer, is not guaranteed or endorsed by the publisher.

Copyright © 2022 Ma, Huang, Han, Yu, Yu and Zhu. This is an open-access article distributed under the terms of the Creative Commons Attribution License (CC BY). The use, distribution or reproduction in other forums is permitted, provided the original author(s) and the copyright owner(s) are credited and that the original publication in this journal is cited, in accordance with accepted academic practice. No use, distribution or reproduction is permitted which does not comply with these terms.



Calcium-Mediated Regulation Promotes the Biofilm Formation of Two Novel Pyridine-Degrading Bacteria

Fuzhong Xiong¹, Donghui Wen^{1*} and Qilin Li²

¹College of Environmental Sciences and Engineering, Peking University, Beijing, China, ²Department of Civil and Environmental Engineering, Rice University, Houston, TX, United States

OPEN ACCESS

Edited by:

Zifu Li,

University of Science and Technology
Beijing, China

Reviewed by:

Yichao Wu,

Huazhong Agricultural University,
China

Hongbo Liu,

University of Shanghai for Science and
Technology, China

*Correspondence:

Donghui Wen
dhw@pku.edu.cn

Specialty section:

This article was submitted to
Water and Wastewater Management,
a section of the journal
Frontiers in Environmental Science

Received: 15 November 2021

Accepted: 10 February 2022

Published: 24 February 2022

Citation:

Xiong F, Wen D and Li Q (2022)
Calcium-Mediated Regulation
Promotes the Biofilm Formation of Two
Novel Pyridine-Degrading Bacteria.
Front. Environ. Sci. 10:815528.
doi: 10.3389/fenvs.2022.815528

In bioaugmented wastewater treatment systems, it is essential for recalcitrant pollutant-degrading bacteria to form biofilms. Inducing biofilm formation in these bacteria, however, is challenging as it involves multiple inter-related regulating pathways and environmental factors. Herein, we report the remarkable promoting effect of Ca^{2+} on biofilm formation of two novel pyridine-degrading bacteria with poor innate biofilm-forming capabilities, *Pseudomonas* sp. ZX01 and *Arthrobacter* sp. ZX07. The roles of Ca^{2+} in different biofilm development stages were investigated. Our data showed strong influences of Ca^{2+} on the initial attachment of the two strains onto positively charged glass surfaces by altering cell surface charge as well as the cation bridging effect. Contrary to many other biofilm promoting mechanisms, Ca^{2+} downregulated the extracellular polymeric substances (EPS) production per cell in both *Pseudomonas* sp. ZX01 and *Arthrobacter* sp. ZX07, while increasing biofilm biomass. This is attributed to the strong cationic bridging between Ca^{2+} and EPS which can elevate the efficiency of the extracellular products in binding bacterial cells. Furthermore, Ca^{2+} increased the protein-to-polysaccharide (PN/PS) ratio in biofilm EPS of both strains, which favored cell aggregation, and biofilm establishment by increasing the hydrophobicity of cell surfaces. More intriguingly, the intracellular c-di-GMP, which can drive the switch of bacterial lifestyle from planktonic state to biofilm state, was also elevated markedly by exogenous Ca^{2+} . Taken together, these results would be of guidance for applying the two strains into bioaugmented biofilm reactors where Ca^{2+} supplement strategy can be employed to facilitate their biofilm formation on the surfaces of engineering carriers.

Keywords: biofilm formation, calcium cation, cell-to-surface attachment, cationic bridging, extracellular polymeric substances (EPS), c-di-GMP

INTRODUCTION

Nitrogenous heterocyclic compounds (NHCs) such as pyridine and quinoline are toxic organic pollutants commonly found in wastewater from coal coking, gasification, and refining processes in coal chemical industries (Bai et al., 2010; Xu et al., 2015). Due to their high polarity, once released into the environment, they can spread quickly, and exert harmful effects on ecological systems and human health (Kaiser et al., 1996; Thomsen and Kilen, 1998; Bi et al., 2006). Furthermore, their stable structures make them highly resistant to conventional biological wastewater treatment employing

common microorganisms (Liang et al., 2018). Therefore, bioaugmentation, which utilizes selected microorganisms capable of degrading these recalcitrant organic pollutants, is getting increasing attention and is regarded as an effective, and economically feasible solution (Herrero and Stuckey, 2015). For example, taken pyridine as a target pollutant, various bacteria belonging to the genus of *Micrococcus* (Sims et al., 1986), *Rhizobium* (Shen et al., 2015), *Shinella* (Bai et al., 2009), *Paracoccus* (Bai et al., 2008), and *Pseudomonas* (Mohan et al., 2003) have been isolated and used for degradation of pyridine in wastewater treatment. However, the application of the bioaugmentation strategy also faces many challenges. In particular, the inoculated bacteria often fail to colonize in the microbial community due to inhospitable conditions or intense competition from indigenous species (Raper et al., 2018). Fu et al. (2009) reported that the inoculated strain disappeared from a biological aerated filter (BAF) within 3 days and attributed it to its poor biofilm-forming ability. On the other hand, strategies that promote the formation of stable biofilms by the inoculated bacteria on carriers have been shown to improve the degradation of target pollutants in bioaugmented systems (Zhao B. et al., 2018; Yue et al., 2018). However, the existing knowledge of efficiently regulating bacterial biofilm formation is obscured especially in the field of wastewater treatment engineering.

Biofilms are well-organized microbial communities, in which cells adhere to biotic or abiotic surfaces and are covered by a self-secreted extracellular polymeric substances (EPS) matrix. They represent the most widespread lifestyle for microbes (Stoodley et al., 2002; Flemming and Wuertz, 2019). Compared to the planktonic lifestyle, biofilms provide a range of advantages for microbial cells to enhance the stability of community structures, and their resistance to unfavorable conditions or environmental shock loads by enhancing intercellular communication and cooperation (Jefferson, 2004; Flemming et al., 2016). Biofilm formation is a complex, multi-step process involving various self-regulated mechanisms, e.g., quorum sensing (QS) (da Silva et al., 2017), bis-(3'-5')-cyclic dimeric guanosine monophosphate (c-di-GMP) signaling (Wu et al., 2015), and flagella and pili mediated motility (Van Houdt and Michiels, 2005), as well as multiple surface properties including hydrophilicity and surface charge (Renner and Weibel, 2011). Moreover, biofilm development is influenced by many environmental factors such as temperature, pH, nutrients, hydraulic shear force, osmotic pressure, and divalent cations (Rinaudi et al., 2006; Zhou et al., 2013; Gomes et al., 2014). Therefore, to promote biofilm formation of the inoculated bacteria in bioaugmented reactors, it is important to identify the most crucial ones from those intricate factors.

Calcium cation (Ca^{2+}) has been widely recognized as the important second messenger in bacterial cells, participating in modulating many cellular activities and metabolic pathways (Dominguez et al., 2015; Parker et al., 2016). Many studies noted that calcium played non-negligible roles in the formation of bacterial biofilms, yet the effects varied widely in different bacterial species. For instance, calcium was found to stimulate cell-to-cell adhesion and

biofilm establishment of *Pseudomonas mendocina* NR802 (Mangwani et al., 2014), *Citrobacter werkmanii* BF-6 (Zhou et al., 2016), *Bacillus* sp. (He et al., 2016), *Flavobacterium columnare* (Cai et al., 2019), and *Vibrio fischeri* (Tischler et al., 2018); but it was also shown to inhibit biofilm formation of *Staphylococcus aureus* (Shukla and Rao, 2013), and *Vibrio cholerae* (Bilecen and Yildiz, 2009). In these previous studies, calcium was found to alter cell surface charge and the electrical double layer (Marcinakova et al., 2010), elevate the production of extracellular proteins and polysaccharides (Mangwani et al., 2014; He et al., 2016), and enhance cationic bridging between bacterial cells via its interactions with EPS components such as extracellular DNA (eDNA) (Das et al., 2014). However, the specific mechanisms through which calcium mediates bacterial adhesion and subsequent biofilm formation remain inconclusive and even a subject of controversy. Moreover, the bacteria species ever studied are mainly model species or from clinical, food-related, plant-related, and marine environments. Thus, it necessitates investigating more bacterial strains from wastewater treatment plants.

In this study, we evaluated the effects of calcium on the biofilm establishment and architecture of two pyridine-degrading bacteria, *Pseudomonas* sp. ZX01 and *Arthrobacter* sp. ZX07. The underlying mechanisms of calcium-mediated regulation were also explored from the perspectives of initial cell-to-surface attachment, EPS production, and c-di-GMP signaling. The purpose of this study was to provide a fundamental understanding of the roles that calcium plays in regulating bacterial biofilm-forming behaviors, and practical guidelines for more efficient application of the two NHC-degrading strains in bioaugmented biofilm reactors.

MATERIALS AND METHOD

Chemicals

Tryptone and yeast extract were purchased from Oxoid (United Kingdom). 1% (w/v) crystal violet solution, phosphate buffered saline (PBS), and BCA Protein Assay Kit were purchased from Solarbio (China). The fluorescent dyes, SYTO9 and tetramethyl-rhodamine conjugates of concanavalin A (conA-T), were obtained from Invitrogen (United States). All the other conventional inorganic or organic chemicals used in the study were of analytical grade.

Bacterial Strains and Medium

Pseudomonas sp. ZX01 and *Arthrobacter* sp. ZX07, isolated from the activated sludge of a coking wastewater treatment plant, were chosen as the representative research objects, for they were Gram-negative and Gram-positive, respectively. The two strains could grow by taking pyridine as the sole carbon and nitrogen source and showed highly efficient pyridine-degrading abilities. Their 16S rRNA gene sequences can be obtained in GenBank database of NCBI with accession numbers MG760359 and MG760365. The main biochemical characteristics of the two strains were also

summarized in **Supplementary Table S1**. Particularly, the motility of the two strains was tested using the method described in **Supplementary Text S1**. The Luria-Bertani (LB) medium (Sezonov et al., 2007) containing 10 g/L tryptone, 5 g/L yeast extract, and 10 g/L NaCl was used for bacteria enrichment and biofilm formation.

Biofilm Cultivation and Quantification

Microtiter plate biofilm formation assay (O'Toole, 2011) was used to culture and quantify biofilm with some modifications, for its advantages in accuracy, repeatability, and batch processing. Firstly, the bacterial strain was grown in LB medium at 37°C to middle exponential phase until $OD_{600} = 1.0$ and washed twice with 0.9% NaCl. Then the harvested cells were resuspended in LB medium with a final OD_{600} of 0.5. Next, 1 ml cell suspension was seeded in each well of 12-well polystyrene plates (Corning, United States) and incubated at 35°C for 24 h with a shaking speed of 150 rpm. The plates containing LB medium only were taken as the negative control. After incubation, the OD_{600} of bacterial suspension in each well was measured to represent the planktonic cell growth. Then the suspension was discarded and each well was washed three times with sterile water to remove non-adherent cells. The 12-well plates were air-dried at 60°C for 1 h and 2 ml 0.1% crystal violet solution was added into each well to stain the attached biofilm cells for 25 min. Subsequently, the excess dye was rinsed off with sterile water. After drying at 35°C for 1 h again, 4 ml 95% ethanol was added into each well to redissolve the cell-bound crystal violet. Finally, 125 μ l solution from each well was transformed to 96-well plates and OD_{595} was determined using a microplate reader (BioTek Synergy, United States) to represent the biofilm biomass.

In the experiments studying the effects of Ca^{2+} on biofilm formation of the two strains, different concentrations of $CaCl_2$ (i.e., 1, 2, 4, 8, 16, 32, and 64 mM) were added into the medium. For each of the experimental conditions, the assay was performed in triplicate.

Bacterial Initial Attachment Assay

To investigate the effects of Ca^{2+} on bacterial initial attachment, the attachment of the two strains to the glass slides under different Ca^{2+} concentrations were analyzed according to Ramsey and Whiteley (2004) with modifications. Briefly, the bacterial cells in the middle exponential phase were diluted in 15 ml LB medium to a final OD_{600} of 0.5; different concentrations of $CaCl_2$ (i.e., 1, 4, 16, 32, and 64 mM) were also added into the medium. The prepared bacterial culture was then poured into a 90 × 14 mm Petri dish in which a glass slide (75 × 25 mm; Jingan, China) was placed and incubated at 35°C for 1 h with a shaking speed of 90 rpm. After incubation, the glass slide was taken out and rinsed twice with PBS to remove non-adherent cells. Then the glass slide was put into a centrifuge tube with 25 ml 0.9% NaCl and vibrated intensely with a vortex mixer for 30 min to detach the cells. The number of the bacterial cells in the solution was determined using a standard plate counting method and normalized to the area of glass slides as the initial attachment index. All the assays were performed in triplicate.

EPS Extraction and Analysis

EPS was extracted from both planktonic cells and biofilms using a heating method following Bourven et al. (2011) with certain adjustments. The bacterial strain was firstly inoculated in 12-well plates as previously described. Then the suspension in each well was collected and centrifuged. The cell pellets were resuspended in 15 ml 0.9% NaCl and heated in 85°C water bath for 35 min. After filtration with 0.22 μ m filters, the filtrate was collected as EPS from planktonic cells. The 12-well plate with biofilms was rinsed gently twice with sterile water and 1 ml 0.9% NaCl was added into each well of the plate. Then the plate was heat-treated and the suspensions in each well were combined. The resulting filtrate was considered EPS from the biofilms. Moreover, planktonic cells and biofilm cells on the filter were also dried and weighed.

The polysaccharide (PS) and protein (PN) content of the EPS were determined using the phenol-sulfuric acid method (Dubois et al., 1956) and the bicinchoninic acid (BCA) protein assay (Redinbaugh and Turley, 1986), respectively. The final concentrations of PN and PS were normalized by the weight of the planktonic or biofilm cells. The experiments for each condition were conducted in triplicate and each measurement was performed at least 3 times. Furthermore, the fluorescence excitation-emission matrix (EEM) analysis of the EPS from both biofilms and planktonic cells was performed using a HORIBA Aqualog spectrofluorometer. The details of EEM analysis were described in **Supplementary Text S2**.

Biofilm Observation by Confocal Scanning Laser Microscopy

The architecture and composition of biofilms formed by the two strains under different Ca^{2+} concentrations were analyzed using CLSM combined with a double staining method (Yu et al., 2016). Briefly, 700 μ l of the bacterial suspension ($OD_{600} = 0.5$) were inoculated in a μ -Slide chambered coverslip with four wells (ibidi, Germany) and cultured at 35°C at 90 rpm in a rotary shaker for 24 h. After incubation, the chambered coverslip was rinsed twice with PBS to remove planktonic cells. Then the cells and polysaccharides in the biofilms were stained with 10 μ M SYTO9 and 200 μ g/ml conA-T in the dark for 30 min, respectively. After washing with PBS, the chambered coverslip was observed by a CLSM system (Leica TCS SP8, Germany) and Z-stack two-dimensional images (scanned every 0.5 μ m) were obtained from at least three random areas for each sample. The 3-D images were rebuilt using IMARIS software (V9.2.1; Bitplane, Switzerland) and analyzed using COMSTAT (Heydorn et al., 2000).

Intracellular c-di-GMP Extraction and Analysis

The intracellular c-di-GMP was extracted according to the method reported by Spangler et al. (2010). Briefly, the bacterial cells were cultured in 12-well plates to the late exponential growth phase under the same conditions as described above and harvested (5 ml culture volume) by

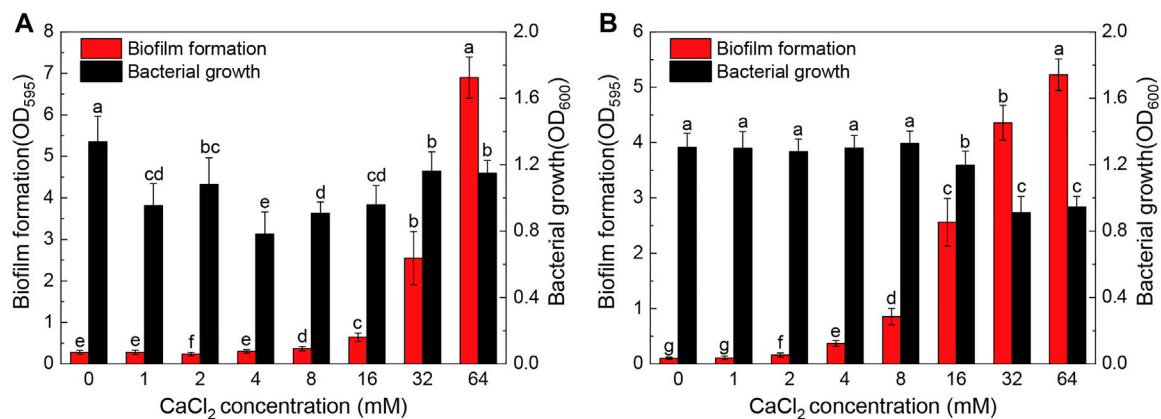


FIGURE 1 | Biofilm formation and bacterial growth of *Pseudomonas* sp. ZX01 (A) and *Arthrobacter* sp. ZX07 (B) in 12-well microtiter plates when adding different concentrations of CaCl₂ into the medium. Bars represented mean \pm standard deviation. Different lowercase letters labeled on the bars represented the significant difference ($p < 0.05$) according to the one-way ANOVA and multiple comparisons.

immediate centrifugation at 4°C for the subsequent extraction. For each culture, the extraction was performed in triplicate. The relative quantitative analysis of c-di-GMP was conducted using a Dionex Ultimate 3000 UPLC system coupled to a TSQ Quantiva Ultra triple-quadrupole mass spectrometer (Thermo Scientific, United States). Moreover, 1 ml of the bacterial culture was collected and the cell pellet obtained by centrifugation was dissolved in 800 μ l of 0.1 M NaOH. After being heat-treated at 95°C for 15 min, the protein content in the solution was determined using a BCA Protein Assay Kit. The final concentration of c-di-GMP (relative content) was normalized as peak area per mg of bacterial protein and presented as the ratio to the control group.

Statistical Analysis

All the experimental data in figures or tables were presented in the form of mean \pm standard deviation. One-way ANOVA and multiple comparisons were also performed using SPSS software (V19.0; IBM, United States) to illustrate the results of different experimental conditions (i.e., Ca²⁺ concentrations). The appropriate statistical test method was selected from Fisher's LSD test and Tamhane's T2 test for multiple comparisons according to the homogeneity of variance. In general, a p -value of <0.05 was regarded as significantly different.

RESULTS

Effects of Calcium on Biofilm Formation

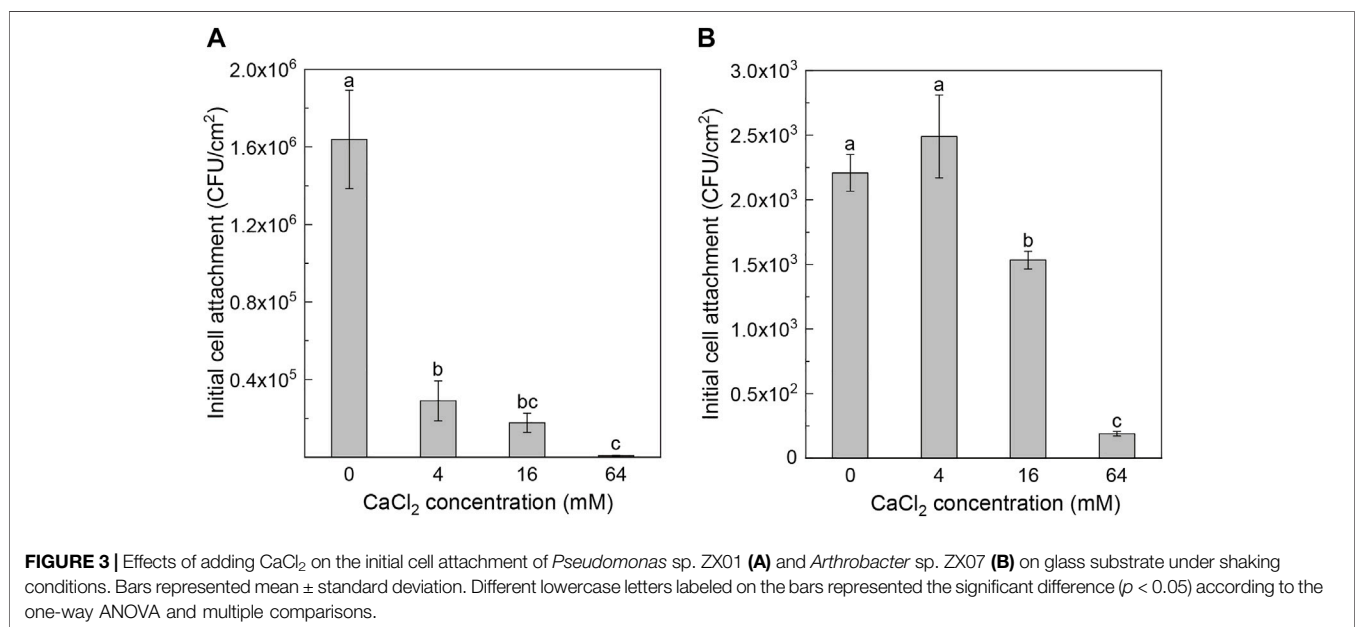
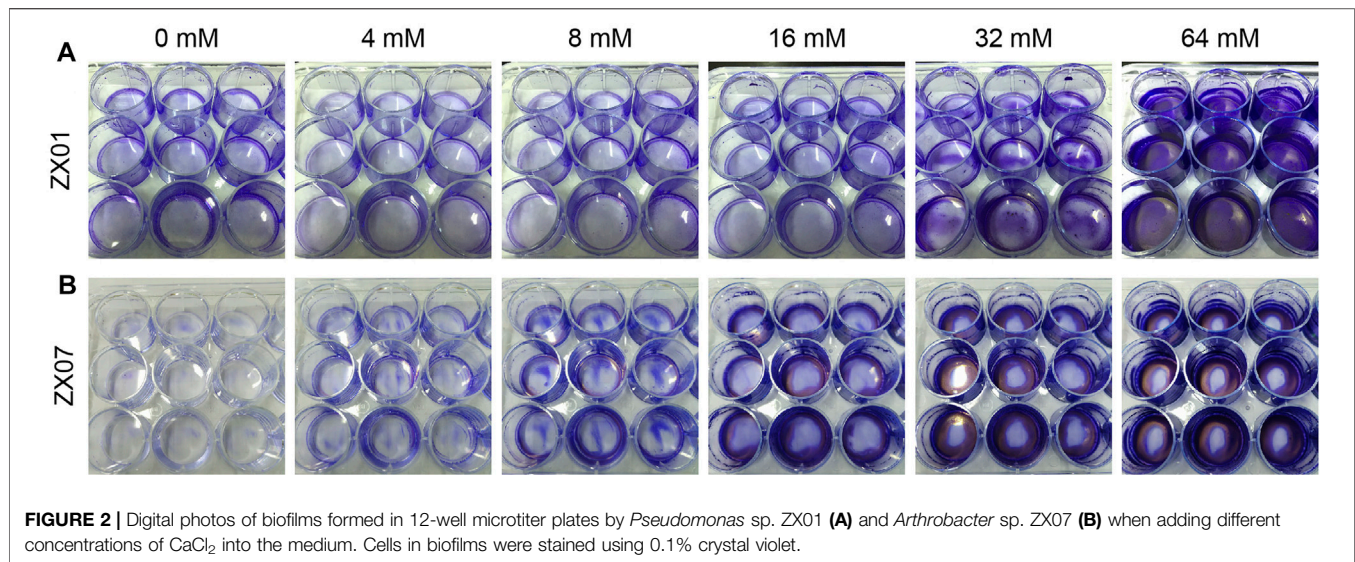
The biofilm formation and planktonic bacterial growth in the presence of different concentrations of Ca²⁺ (0–64 mM) were monitored using the microtiter plate assay. As shown in **Figure 1A**, calcium, when added at sufficient concentration, and significantly promoted biofilm formation of *Pseudomonas* sp. ZX01. In the range of 0–8 mM, Ca²⁺ had little effect on the biofilm formation; while in the range of 16–64 mM, the biofilm biomass was

increased sharply in a concentration-dependent manner. The maximum amount of biofilm biomass was observed in the presence of 64 mM Ca²⁺, which was 24.7 times that of the control (0 mM Ca²⁺). However, the addition of Ca²⁺ reduced the planktonic bacterial growth of ZX01 by 13.3–41.6%, and the minimum bacterial density was found in the presence of 4 mM Ca²⁺. Significantly increased biofilm formation by *Arthrobacter* sp. ZX07 was observed in the presence of exogenous calcium at a much lower Ca²⁺ concentration (2 mM) (**Figure 1B**); in addition, when Ca²⁺ concentration increased from 2 to 64 mM, the biofilm biomass increased in a more even manner; the biofilm biomass of ZX07 at 16, 32, and 64 mM Ca²⁺ was 24.4, 42.2, and 50.8 times as that of the control. These results indicated that calcium had a stronger promoting effect on ZX07 than ZX01. Furthermore, Ca²⁺ did not affect the planktonic growth of ZX07 at concentrations up to 8 mM but repressed planktonic growth by 8.4–30.2% at higher concentrations (16–64 mM).

The effect of Ca²⁺ on biofilm formation can be clearly seen in digital photos of the 12-well microtiter plates (**Figure 2**). **Figure 2A** shows that ZX01 formed more biofilms at the center of the well bottom surface in the presence of 32 mM Ca²⁺; when Ca²⁺ concentration increased to 64 mM, the biofilms occupied the whole bottom of the wells, and the liquid/air/well wall 3-phase interface. Unlike ZX01, in the presence of 16, 32, and 64 mM Ca²⁺, the biofilms of ZX07 mainly appeared at the edge of the well bottom rather than the center (**Figure 2B**).

Effects of Calcium on Bacterial Initial Attachment

The effects of calcium on bacterial initial attachment were determined by measuring cell attachment on glass slides. **Figure 3** presents the number of viable bacterial cells attached to the surface of the glass slide in 1 h. For *Pseudomonas* sp. ZX01, the highest initial attachment was



found in the absence of Ca^{2+} , which was $1.64 \times 10^6 \text{ CFU/cm}^2$ (Figure 3A). With increasing concentration of Ca^{2+} , the initial attachment of ZX01 was significantly repressed; the initial cell attachment in the presence of 64 mM Ca^{2+} ($8.36 \times 10^3 \text{ CFU/cm}^2$) was two orders of magnitude lower than that of the control. As shown in Figure 3B, the initial attachment of *Arthrobacter* sp. ZX07 at 0 and 4 mM Ca^{2+} was significantly higher than that at 16 and 64 mM Ca^{2+} . The lowest initial attachment was observed at a Ca^{2+} concentration of 64 mM ($1.89 \times 10^2 \text{ CFU/cm}^2$), which was an order of magnitude lower than that of the control ($2.21 \times 10^3 \text{ CFU/cm}^2$). These results indicated that Ca^{2+} can inhibit the initial

attachment of the two bacterial strains to positive-charged glass surfaces.

Effects of Calcium on EPS Expressions of Biofilm Cells and Planktonic Cells

The EPS composition of biofilm cells and planktonic cells in the presence of different concentrations of calcium was chemically analyzed. As presented in Figure 4A, both PN and PS content in the biofilm EPS of *Pseudomonas* sp. ZX01 responded to exogenous Ca^{2+} in a significant decreasing trend. Compared with the control, 16 and 32 mM Ca^{2+} could reduce the PN

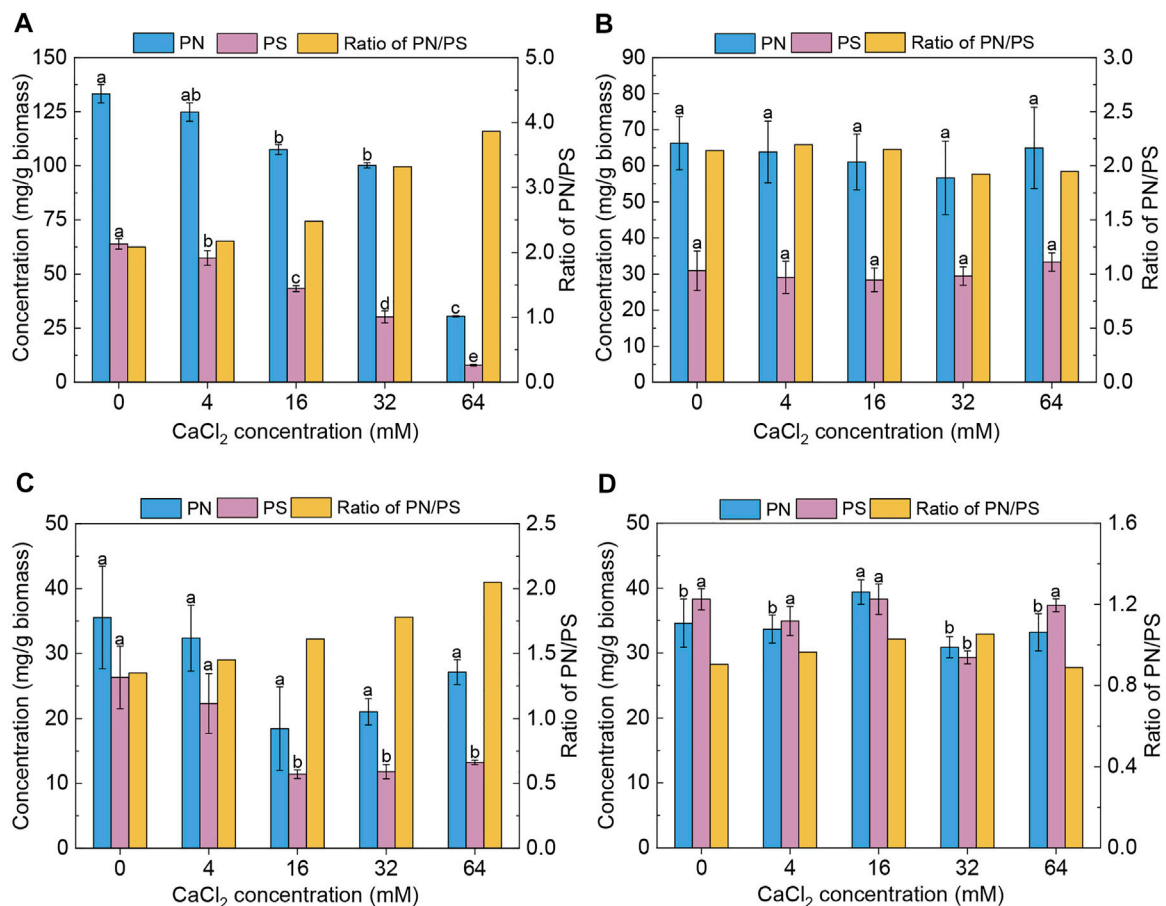


FIGURE 4 | Effects of adding CaCl_2 on protein (PN) content, polysaccharide (PS) content, and the ratio of protein to polysaccharide (PN/PS) in the EPS of both biofilms and planktonic cells. **(A,B)** Biofilms and planktonic cells of *Pseudomonas* sp. ZX01 **(C,D)** Biofilms and planktonic cells of *Arthrobacter* sp. ZX07. Bars represented mean \pm standard deviation of three replicates. Different lowercase letters labeled on the bars represented the significant difference ($p < 0.05$) according to the one-way ANOVA and multiple comparisons.

content by 19.4 and 24.8%, respectively; while in the presence of 64 mM Ca^{2+} , the PN content (i.e., 30.5 mg/g biomass) was reduced even more sharply by 77.1%. Similarly, the PS content was decreased by 10.2–87.7% in a monotonic manner with the addition of Ca^{2+} . The PN/PS ratio of biofilm EPS increased notably (from 2.08 to 3.87) in response to exogenous calcium. Nevertheless, the PN and PS content in the EPS of planktonic bacterial cells were practically unaffected by the addition of Ca^{2+} , staying at around 65 and 30 mg/g biomass, respectively (Figure 4B). Regarding *Arthrobacter* sp. ZX07, the change in PN content in biofilm EPS (Figure 4C) was not statistically significant. However, high Ca^{2+} concentrations (16, 32, and 64 mM) reduced the PS content by 49.8–56.5%. Consequently, the PN/PS ratio of ZX07 biofilm EPS increased from 1.35 (the control) to 2.04 (64 mM Ca^{2+}) with increasing Ca^{2+} concentrations. Like ZX01, the EPS components of planktonic ZX07 cells were not influenced by Ca^{2+} (Figure 4D).

EEM fluorescence spectra were obtained to characterize the EPS composition. In general, EEM spectra could be divided into five regions: Regions I and II represent aromatic protein-like

compounds; Region III represents fulvic acid-like compounds; Region IV represents microbial products such as tyrosine-like, tryptophan-like, and protein-like compounds; Region V represents humic acid-like compounds (Chen et al., 2003). Interestingly, the EEM peaks of the biofilm EPS and planktonic EPS in the absence or presence of Ca^{2+} are similar (Figures 5A–D), indicating that Ca^{2+} did not affect the compounds in EPS of *Pseudomonas* sp. ZX01. Specifically, the two peaks identified from the EEMs were EX/EM = 225/325 nm (Region I) and EX/EM = 275/325 nm (Region IV). In contrast, Ca^{2+} had remarkable influences on the EPS composition of *Arthrobacter* sp. ZX07. Without adding Ca^{2+} , there were 3 peaks in the EEMs of both biofilm and planktonic EPS (Figures 5E,G): EX/EM = 220/350 nm (Region II), EX/EM = 280/350 nm (Region IV), and EX/EM = 325/390 nm (Region V). However, despite sharing the same two peaks in Region II and Region IV, the EEMs of biofilm EPS in the presence of 64 mM Ca^{2+} presented two different peaks locating at EX/EM = 360/450 nm (Region V), and EX/EM = 270/450 nm (Region V) (Figure 5F). Additionally, a different peak at EX/EM = 350/

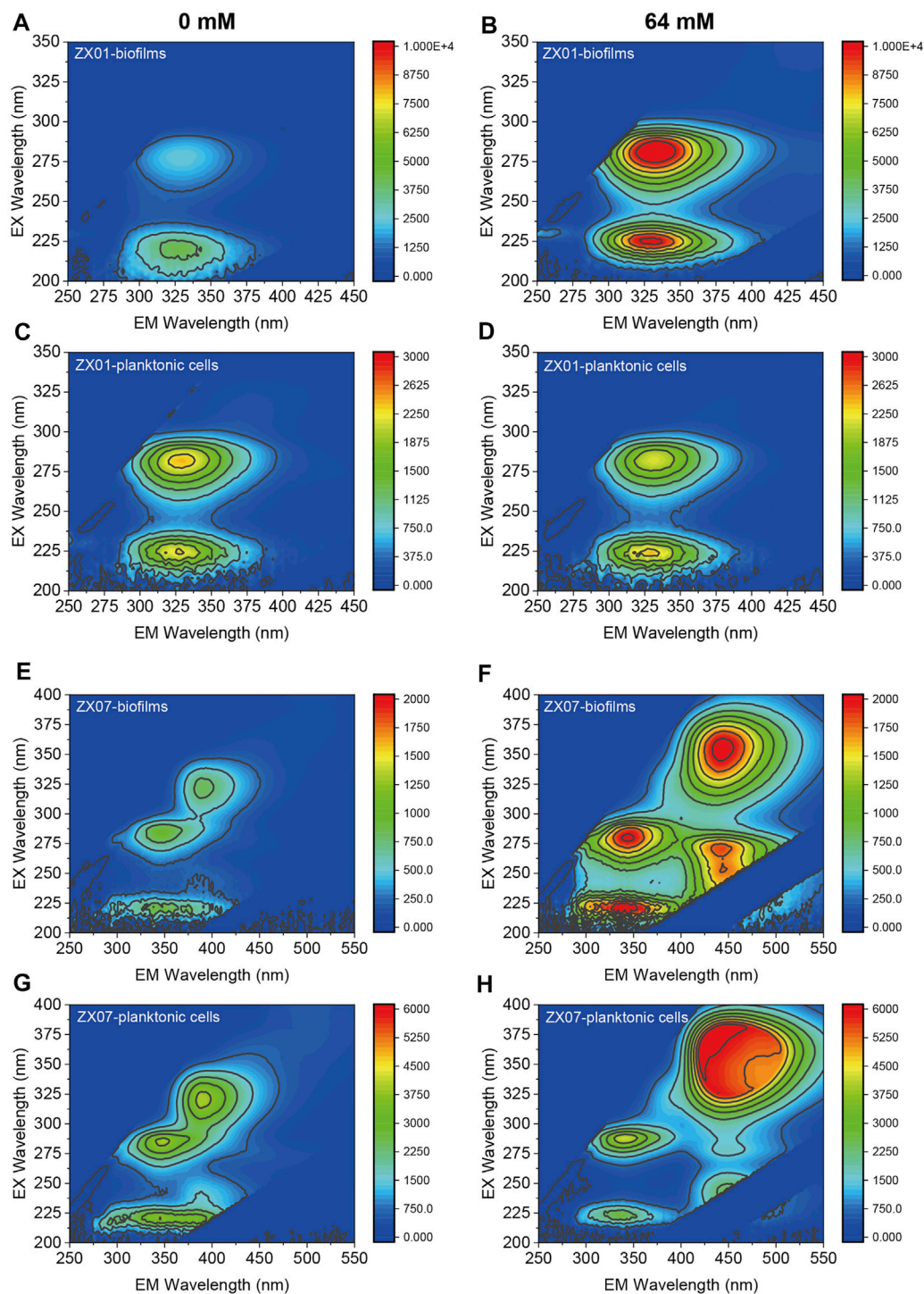


FIGURE 5 | EEM fluorescence spectra of the EPS produced by both biofilms and planktonic cells. **(A,B)** Biofilms of *Pseudomonas* sp. ZX01 in the presence of 0 and 64 mM of CaCl_2 **(C,D)** Planktonic cells of *Pseudomonas* sp. ZX01 in the presence of 0 and 64 mM of CaCl_2 . **(E,F)** Biofilms of *Arthrobacter* sp. ZX07 in the presence of 0 and 64 mM of CaCl_2 **(G,H)** Planktonic cells of *Arthrobacter* sp. ZX07 in the presence of 0 and 64 mM of CaCl_2 .

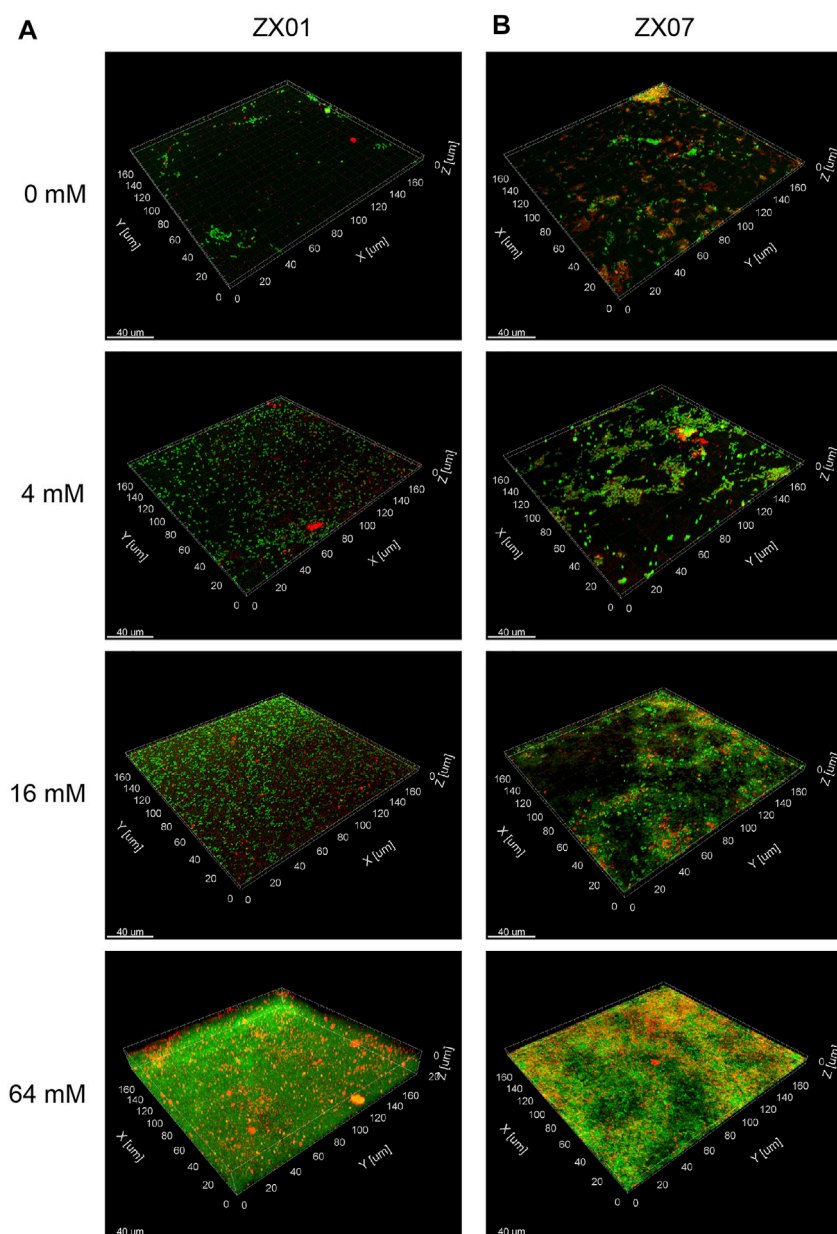


FIGURE 6 | CLSM 3-D images of the biofilms formed by *Pseudomonas* sp. ZX01 (A) and *Arthrobacter* sp. ZX07 (B) in the presence of 0, 4, 16, and 64 mM of CaCl_2 . The cells were stained green with SYTO9; the polysaccharides were stained red with conA-T; the yellow fluorescence represented the combination of cells and polysaccharides.

450 nm (Region V) appeared in the EEMs of planktonic EPS at 64 mM Ca^{2+} (Figure 5H). The above results suggested that exogenous calcium promoted ZX07 to produce certain humic acid-like compounds.

Effects of Calcium on Biofilm Architecture

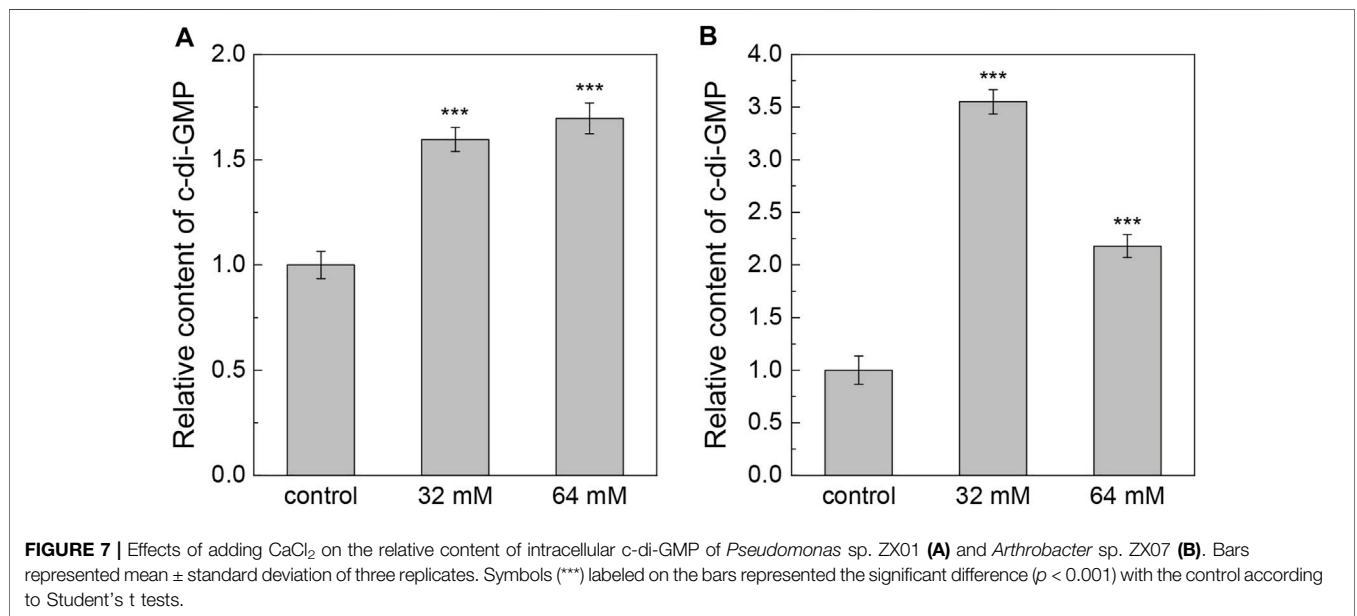
The architecture and topography of the biofilms of the two pyridine-degrading bacteria, formed on μ -Slide surfaces in 24 h, were examined by CLSM 3-D imaging (Figure 6). The green fluorescence signal represents bacterial cells, and the red

signal represents PS in EPS. In the absence of Ca^{2+} , few ZX01 cells adhered to the substrate and formed small aggregates (Figure 6A). Quantitative analysis of CLSM images (Table 1) showed very low average thickness and coverage of ZX01 biofilms at $2.06 \pm 0.29 \mu\text{m}$ and 12.64%, respectively. At Ca^{2+} concentrations of 4 and 16 mM, many more ZX01 cells adhered to the surfaces and the cells were uniformly distributed; PS became clearly visible in biofilms. As a result, the surface coverage of ZX01 biofilms at 4 and 16 mM Ca^{2+} went up to 25.17 and 42.09%, respectively (Table 1). Intriguingly, when

TABLE 1 | Characteristics of biofilms formed by ZX01 and ZX07 under different calcium concentrations calculated from the CLSM images using COMSTAT.

Groups	Total biomass ($\mu\text{m}^3/\mu\text{m}^2$)	Average thickness (μm)	Average coverage (%)	Surface to biovolume ratio ($\mu\text{m}^2/\mu\text{m}^3$)	Roughness coefficient	Average colony size (μm^2)
ZX01-0 mM	0.57 ± 0.06^b	2.06 ± 0.29^c	12.64 ± 0.26^d	12.39 ± 0.66^a	0.44 ± 0.08^a	10.92 ± 3.53^b
ZX01-4 mM	0.97 ± 0.25^b	2.41 ± 0.36^{bc}	25.17 ± 6.38^c	8.10 ± 1.05^b	0.23 ± 0.09^b	12.37 ± 2.82^b
ZX01-16 mM	1.68 ± 0.44^b	3.17 ± 0.41^b	42.09 ± 7.40^b	5.31 ± 0.78^c	0.13 ± 0.03^c	14.41 ± 2.96^b
ZX01-64 mM	16.49 ± 0.63^a	19.56 ± 1.90^a	75.75 ± 3.42^a	1.07 ± 0.11^d	0.02 ± 0.01^d	217.30 ± 55.09^a
ZX07-0 mM	0.40 ± 0.21^c	0.78 ± 0.35^c	9.13 ± 3.26^c	7.86 ± 1.81^a	1.25 ± 0.24^a	13.40 ± 3.73^d
ZX07-4 mM	0.65 ± 0.27^{bc}	1.17 ± 0.34^{bc}	15.47 ± 5.62^{bc}	5.21 ± 2.42^b	1.19 ± 0.24^a	28.13 ± 4.64^c
ZX07-16 mM	0.97 ± 0.11^b	1.73 ± 0.18^b	20.40 ± 3.99^b	3.87 ± 0.68^{bc}	0.58 ± 0.03^b	39.60 ± 2.38^b
ZX07-64 mM	3.75 ± 0.40^a	6.06 ± 0.92^a	52.09 ± 7.93^a	2.02 ± 0.32^c	0.13 ± 0.02^c	84.11 ± 7.93^a

Note: The data were presented as mean \pm standard deviation ($n = 6$). Different lowercase letters labeled on the data represented the significant difference ($p < 0.05$) according to the one-way ANOVA, and Tamhane's T_2 or LSD, post-tests.



64 mM Ca^{2+} was added, ZX01 formed dense and thick biofilms, in which the cells and EPS were distributed in a well-structured mode. The total biomass, average thickness, average coverage, and average colony size of ZX01 biofilms in this condition were all elevated by several times; and the sharp reduction of surface to biovolume ratio and roughness coefficient also suggest that more bacterial cells were aggregated in the form of biofilms. Similar trends were observed in the biofilms of *Arthrobacter* sp. ZX07 (Figure 6B): when the concentration of exogenous Ca^{2+} increased from 0 to 16 mM, more ZX07 cells were attached to the surfaces and the microcolonies became larger, but the distribution of the cells was not uniform; in the presence of 64 mM Ca^{2+} , ZX07 developed extensive and mature biofilms, in which the cells were covered by large amounts of EPS. However, there was a notable difference in the influences of calcium on the biofilm architecture of ZX01 and ZX07. In the range of 0–16 mM, the average colony size of ZX01 biofilms was little affected by Ca^{2+} ; and the cells, stimulated by Ca^{2+} , attached to the substrate in a separated pattern. In contrast, a significant increase in the average colony size was found in ZX07 biofilms, indicating that

Ca^{2+} possibly promoted ZX07 cells to attach to those which had already colonized at the substrate. Therefore, it could be speculated that, for these two strains, the mechanisms inherent in the stimulatory effects of Ca^{2+} on biofilm development were different.

Effects of Calcium on c-di-GMP Level

To address whether exogenous calcium influences the expression of the second messenger c-di-GMP, we analyzed the intracellular c-di-GMP level of the two pyridine-degrading bacteria at different Ca^{2+} concentrations. As exhibited in Figure 7A, after culturing for 24 h, the introduction of Ca^{2+} into the medium significantly elevated the c-di-GMP level in *Pseudomonas* sp. ZX01 cells. The relative content of c-di-GMP in the presence of 32 and 64 mM Ca^{2+} was 59.5 and 69.6% higher than that of the control. In regard to *Arthrobacter* sp. ZX07, the elevation of intracellular c-di-GMP level caused by Ca^{2+} was even more remarkable (Figure 7B). The relative content of c-di-GMP in ZX07 cells at 32 and 64 mM Ca^{2+} was 3.55 and 2.18 times that of the control.

DISCUSSION

In this present study, the significant promotion of biofilm formation of two pyridine-degrading bacteria, *Pseudomonas* sp. ZX01 and *Arthrobacter* sp. ZX07, caused by calcium supplementation was clearly observed. Few cells of the two strains attached to the 12-well plates or μ -Slide coverslips in the absence of Ca^{2+} (Figures 1, 6), indicating they harbored very poor biofilm-forming abilities in their natural state. Hence, it might affect their performances in the bioaugmented biofilm reactors. However, when exposed to Ca^{2+} of a certain concentration range (8–64 mM for ZX01 and 2–64 mM for ZX07), the biofilm biomass formed by the two strains increased greatly in a monotonic and dose-dependent pattern. Mangwani et al. (2014) also reported a dose-dependent increase of *P. mendocina* NR802 biofilms due to the Ca^{2+} addition, but the concentration tested was limited in 5–20 mM. The biofilm formation of *Sinorhizobium meliloti* was elevated in a similar manner by the addition of 7–28 mM Ca^{2+} (Rinaudi et al., 2006). While Zhou et al. (2016) found that within a much larger range of Ca^{2+} concentration (3.125–800 mM), the biofilm formation of *Citrobacter werkmanii* BF-6 was enhanced notably, but the enhancement presented a non-monotonic trend (i.e., increasing firstly and decreasing afterward). Similarly, the biofilm-forming ability of the foodborne pathogen *Cronobacter sakazakii* showed an increase and subsequent decrease with the increasing Ca^{2+} concentration from 0 to 135 mM (Ye et al., 2015). These results suggested that the sensitivity of different bacterial species in response to exogenous calcium varied. Thus, when applying the calcium-mediated regulating strategy to control bacterial biofilm formation in medical, marine, agricultural, or environmental cases, it is important to understand the effects of calcium on the specific bacterial strain of interest due to the high diversity of bacteria.

A typical bacterial biofilm formation process can be divided into five steps: 1) initial cell-to-surface attachment, 2) irreversible adhesion via producing EPS, 3) proliferation and microcolony formation, 4) maturation of biofilms with complex structures, 5) biofilm aging with the dispersal of motile cells (Stoodley et al., 2002; Armbruster and Parsek, 2018). In the first step, bacterial cells sense and attach to the surface reversibly with the assistance of cell appendages (e.g., flagellum) after overcoming the electrostatic repulsion between the cell surface and the substratum (Renner and Weibel, 2011). Our results herein revealed that the presence of Ca^{2+} in the surrounding solutions significantly repressed the initial cell attachment of both ZX01 and ZX07 to the positive-charged glass surfaces (Figure 3). As widely known, bacterial cell surfaces are negatively charged (Soni et al., 2008), and thus Ca^{2+} , as a divalent cation, can effectively neutralize the surface charge by interacting with ligands on the cell surfaces (Wang et al., 2019). Furthermore, in the light of electrostatic double layer compression theory, the increasing ionic strength of the solutions caused by exogenous Ca^{2+} will decrease the absolute value of the negative zeta potential of the bacteria cells (Chen and Walker, 2007; Bundeleva et al., 2011). Thus, when adding high concentrations of Ca^{2+} into the medium, the surface charge of the two bacteria would become less negative. This effect could bring both adverse and favorable consequences for initial cell-to-surface

attachment, which depends on whether the surface charge of the substratum is positive or negative. For instance, another divalent cation, Mg^{2+} , was validated to exhibit a stimulatory effect on the adhesion of *Pseudomonas* sp. strain B13 to negative-charged mineral surfaces (Simoni et al., 2000). However, in the case of extremely high ionic strength caused by calcium (e.g. 1,000 mM), the adhesion efficiency of bacterial cells to quartz surfaces, which were negative-charged, and could also be reduced due to the repulsive electrostatic forces (Chen and Walker, 2007). Apart from neutralizing surface charge, Ca^{2+} has been shown to initiate strong cation bridging interactions between high-affinity sites on cell surfaces and the conditioning film of substrata, and thereby facilitating the adhesion of *P. aeruginosa* cells to alginate-conditioned quartz surfaces (de Kerchove and Elimelech, 2008). Combined with our findings in the present study, it can be concluded that the impacts of Ca^{2+} on the initial cell-to-surface attachment were multi-faceted and substantially linked to physicochemical interactions, yet biological factors presumably played a minor role in this step.

During the next steps of biofilm formation, the bacterial self-secreted EPS consisting of PN, PS, nucleic acids, lipids, humic substances, etc., play more important roles in assisting cell-to-cell aggregation, and biofilm structure construction (Vu et al., 2009; Flemming and Wingender, 2010). Previous research regarding the effects of Ca^{2+} on EPS production mostly showed an enhancing impact. For example, adding an additional 10 mM Ca^{2+} in the medium could significantly promote *Bacillus* sp. cells to synthesize more PN and PS in EPS (He et al., 2016). Liu and Sun (2011) also offered evidence that the extracellular PN produced by microbial cells in sequential batch reactors increased notably when Ca^{2+} of 50 and 100 mg/L was added into the reactors, thereby enhancing bacterial aggregation to form granules. However, inconsistent with these findings, our study found that PN and PS content in biofilms formed by the two strains decreased in response to the increasing Ca^{2+} concentration (Figure 4), yet the biofilm biomass increased evidently. It means that in the presence of exogenous Ca^{2+} , the cells of ZX01 and ZX07 could form more biofilms but require lower EPS production for each bacterial cell. In other words, a smaller amount of EPS would support larger biofilm structures with the assistance of Ca^{2+} . This may be attributed to the cation bridge effect, i.e., Ca^{2+} can bind to the negatively charged functional groups in EPS, and consequently forming EPS- Ca^{2+} -EPS bridges, which favors the construction of sophisticated biofilm structures (Sobeck and Higgins, 2002; Liu and Sun, 2011; Wang et al., 2019). In particular, functional groups such as carboxylic acid and phosphates in extracellular PS were known binding sites for Ca^{2+} (Astasov-Frauenhoffer et al., 2017); more recently, cationic bridging by Ca^{2+} between eDNA was also reported, which promoted bacterial aggregation and biofilm development of several strains including *P. aeruginosa* and *S. aureus* (Das et al., 2014). Therefore, the amount of EPS production per cell may not be a good predictor of the resulting biofilm biomass; Ca^{2+} -mediated interactions among microbial cells and EPS can be highly efficient in forming a large biofilm structure.

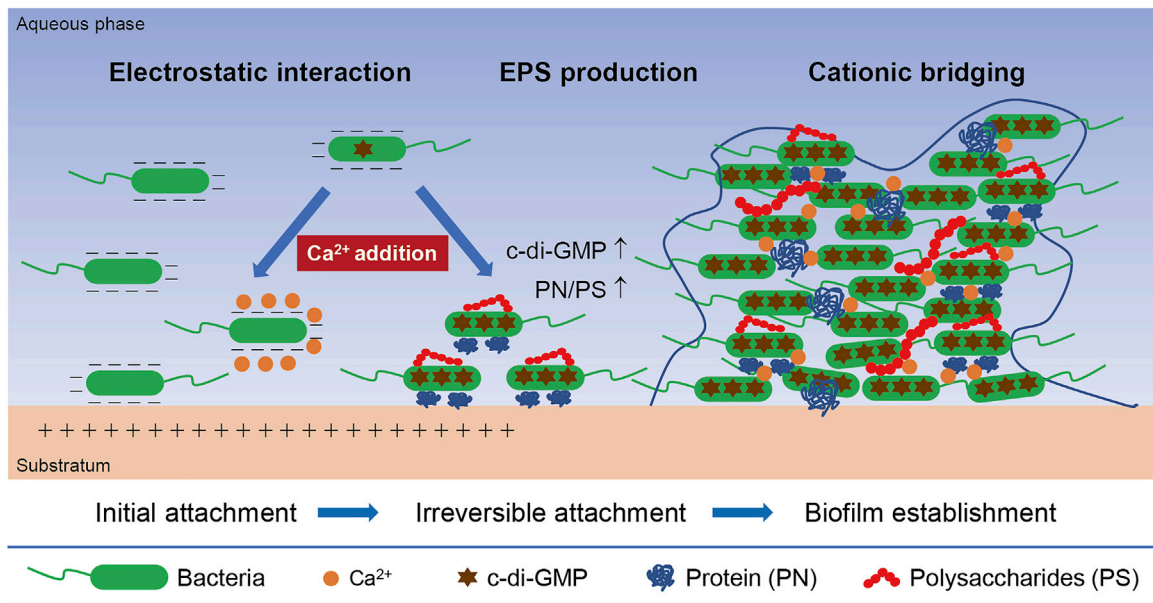


FIGURE 8 | A conceptual illustration of the mechanisms inherent in the calcium-mediated regulation on bacterial biofilm formation.

The ratio of PN/PS in EPS is widely regarded as an important indicator of microbial cell-to-cell aggregating ability in biofilm or granular sludge formation processes. A higher PN content elevates the hydrophobicity of cell surfaces, thereby inducing strong hydrophobic interaction between microbial cells (Hou et al., 2015; Zhao Y. et al., 2018). Our experiments found that the PN/PS ratio in the biofilm EPS of ZX01 and ZX07 increased greatly in the presence of Ca^{2+} (Figure 4). This suggests that calcium-mediated promotion of biofilm formation of these two strains can also be attributed to the higher PN/PS ratio in EPS in addition to the cationic bridging effect of Ca^{2+} . Furthermore, the regulatory effects of Ca^{2+} on multiple gene expressions and metabolic activities have been noted by many studies. Parker et al. (2016) indicated that exogenous Ca^{2+} could induce a substantial transcriptional alteration of the bacterial plant pathogen *Xylella fastidiosa*, including genes encoding cell attachment, motility, and PS secretion, which facilitated biofilm development. The supplementation of 400 mM Ca^{2+} also resulted in a more complex protein expression mode in both biofilms and planktonic cells of *C. werkmanii* BF-6 (Zhou et al., 2016). As demonstrated using EEM fluorescence spectra in our study, 64 mM Ca^{2+} caused a remarkable impact on the EPS expressions in both biofilms, and planktonic cells of ZX07, i.e., the production of humic acid-like compounds, while no significant changes were observed in those of ZX01. Past research has mentioned that due to the abundant ionizable functional groups such as carboxyl and phenolic hydroxyl, humic substances showed high affinities to interact with metal ions (e.g. Cu^{2+} , Ca^{2+}) and form complexes (Wang et al., 2015; Zhao et al., 2020). Hence, the occurrence of humic acid-like compounds in EPS might favor the formation of EPS- Ca^{2+} -EPS bridges and elevate the biofilm-forming ability of ZX07.

The morphological phenotypes of mature biofilms were also altered by Ca^{2+} -mediated regulation. As shown in the CLSM images and the COMSTAT analysis (Figure 6; Table 1), for both ZX01 and ZX07 biofilms, the increase of total biomass, average thickness, and average coverage, and the decrease of roughness coefficient were ascertained in response to the increasing Ca^{2+} concentration, consistent the results in other bacterial strains like *C. werkmanii* and *Shewanella oneidensis* (Zhou et al., 2016; Zhang et al., 2019). Interestingly, the average colony size of ZX01 and ZX07 exhibited quite different responses to the supplementary Ca^{2+} of relatively lower concentrations (i.e., 4 and 16 mM). Specifically, the microcolonies of ZX01 were more dispersed and homogeneous, while ZX07 unevenly developed its microcolonies which were like “rugged mountains”. To the best of our knowledge, this discrepancy might be attributed to the flagella-mediated motility. According to the SEM images of the two strains (Supplementary Figure S1), ZX01 possesses a cellular accessory structure resembling a polar flagellum, while the cell surface of ZX07 is quite smooth without any appendages. In addition, as verified using the motility tests, ZX01 had much stronger swimming motility and swarming motility, both propelled by flagella, than ZX07 (Supplementary Figure S2, S3). Existing evidence demonstrated that bacteria with higher motility tend to be more proficient in moving at the solid-liquid interface and attaching to an abiotic surface (O’Toole and Kolter, 1998; Van Houdt and Michiels, 2005), which was crucial in biofilm development. Therefore, with the assistance of flagella-mediated motility, ZX01 could migrate freely at the substratum and attach onto more sites of the surface, thereby producing more homogeneous biofilms facilitated by Ca^{2+} ; whereas the moving area of ZX07 was limited, and they tended to form microcolonies clinging to the cells that attached randomly to the surface, thus resulting in mountain-like biofilms. Moreover, the biofilm-

forming positions of the two strains were also different (**Figure 2**), which might be still owing to their discrepant motilities. Hence, under the hydraulic shear force in the rotary 12-well plates, ZX01 cells with high motility were able to occupy the whole bottom to form biofilms, yet ZX07 cells with low motility were forced to settle at the periphery of the bottom. Taken together, it was inferred that Ca^{2+} and cell motility might exert a joint regulatory effect on bacterial biofilm formation. Regardless of cell motility, Ca^{2+} can indeed promote the bacteria to form more biofilms, but the motility still exerts influences upon the biofilm architecture.

Recently, the intracellular messenger c-di-GMP was found in many studies to play a global role in regulating the switch of bacterial lifestyle from planktonic state to biofilm-associated state (Valentini and Filloux, 2016; Jenal et al., 2017). By binding to various specific proteins (namely, effectors) in bacterial cells, c-di-GMP controls a wide range of cellular processes including virulence, motility, EPS production, biofilm formation, and dispersion, etc. (Chen et al., 2012). In particular, the intracellular level of c-di-GMP, which is the result of the synthesis by diguanylate cyclases (DGCs) and the degradation by phosphodiesterases (PDEs), is positively associated with the biofilm-forming tendency of bacteria (Ha and O'Toole, 2015). Herein, our study shows elevated intracellular c-di-GMP levels in both ZX01 and ZX07 in the presence of supplementary Ca^{2+} , which was accompanied by enhanced biofilm formation (**Figure 7**). This seems to suggest a potential correlation between Ca^{2+} and c-di-GMP production, although few prior studies have found similar results. Parker et al. (2016) found that the expression of a gene involved in the synthesis of c-di-GMP, *cgsA*, in *X. fastidiosa*, exhibited a weak but non-significant increase in the presence of 4 mM Ca^{2+} . Given the fact that Ca^{2+} is also an essential second messenger in bacterial cells (Dominguez et al., 2015), the little-known interaction of Ca^{2+} and c-di-GMP needs to be further investigated.

In summary, a proposed mechanism of the calcium-mediated regulation on the biofilm formation of the two pyridine-degrading bacteria was illustrated in **Figure 8**. Typically, bacterial cell-to-surface adhesion is driven by the electrostatic interaction, thus the negative-charged bacterial cells tend to adhere to a positive-charged material surface. The divalent Ca^{2+} can neutralize the surface charge of bacterial cells and further weaken their initial attachment to the positive-charged substratum. However, in the presence of Ca^{2+} , the EPS composition of biofilms can be significantly altered, resulting in a higher PN/PS ratio which facilitates the irreversible attachment between bacterial cells. EPS- Ca^{2+} -EPS bridges induced by exogenous calcium also increase the efficiency of EPS in binding cells and constructing biofilm structures. Moreover, the elevated intracellular c-di-GMP level is validated to account for the promotion of biofilm formation.

CONCLUSION

This study comprehensively investigated the effects of Ca^{2+} on different biofilm developing stages of two newly isolated pyridine-degrading bacteria. The main conclusions are as follows:

- 1) the supplemented Ca^{2+} of 16–64 mM markedly promoted the biofilm formation of the two strains with insufficient biofilm-forming capacities;
- 2) by altering cell surface charge, Ca^{2+} influenced the initial cell-to-surface attachment of the two strains in the first step of biofilm formation;
- 3) in the presence of Ca^{2+} , the relatively lower EPS production per cell in biofilms could bind more biofilm biomass, presumably attributed to the cationic bridging between Ca^{2+} and EPS;
- 4) the ratio of PN/PS in biofilm EPS of the two strains showed an increasing tendency in response to exogenous Ca^{2+} , which favored cell aggregation and biofilm formation;
- 5) the intracellular c-di-GMP levels were elevated notably by the supplementary Ca^{2+} , thereby driving the switch of the two strains from planktonic lifestyle to biofilm lifestyle.

Collectively, these findings demonstrated the promising feasibility of facilitating bacterial biofilm formation onto engineering carriers with a Ca^{2+} -based manipulation strategy, which will provide valuable guidance for the application of these pyridine-degrading strains into bioaugmented reactors.

DATA AVAILABILITY STATEMENT

The datasets presented in this study can be found in online repositories. The names of the repository/repositories and accession number(s) can be found in the article/**Supplementary Material**.

AUTHOR CONTRIBUTIONS

Conceptualization: FX and DW; Methodology: FX and QL; Formal analysis and investigation: FX; Writing—original draft preparation: FX; Writing—review and editing: DW and QL; Funding acquisition: DW and QL.

FUNDING

This study was financially supported by the National Natural Science Foundation of China (Grant number 51938001 and 51529801).

ACKNOWLEDGMENTS

The authors would like to acknowledge Institutional Center for Shared Technologies and Facilities, Institute of Microbiology, Chinese Academy of Sciences and Tsinghua University Branch of China National Center for Protein Sciences (Beijing) for infrastructural support.

SUPPLEMENTARY MATERIAL

The Supplementary Material for this article can be found online at: <https://www.frontiersin.org/articles/10.3389/fenvs.2022.815528/full#supplementary-material>

REFERENCES

- Armbruster, C. R., and Parsek, M. R. (2018). New Insight into the Early Stages of Biofilm Formation. *Proc. Natl. Acad. Sci. USA* 115 (17), 4317–4319. doi:10.1073/pnas.1804084115
- Astasov-Frauenhoffer, M., Varganayil, M. M., Decho, A. W., Waltimo, T., and Braissant, O. (2017). Exopolysaccharides Regulate Calcium Flow in Cariogenic Biofilms. *Plos One* 12 (10), e0186256. doi:10.1371/journal.pone.0186256
- Bai, Y., Sun, Q., Xing, R., Wen, D., and Tang, X. (2010). Removal of Pyridine and Quinoline by Bio-Zeolite Composed of Mixed Degrading Bacteria and Modified Zeolite. *J. Hazard. Mater.* 181 (1–3), 916–922. doi:10.1016/j.jhazmat.2010.05.099
- Bai, Y., Sun, Q., Zhao, C., Wen, D., and Tang, X. (2009). Aerobic Degradation of Pyridine by a New Bacterial Strain, *Shinella Zoogloeoides* BC026. *J. Ind. Microbiol. Biotechnol.* 36 (11), 1391–1400. doi:10.1007/s10295-009-0625-9
- Bai, Y., Sun, Q., Zhao, C., Wen, D., and Tang, X. (2008). Microbial Degradation and Metabolic Pathway of Pyridine by a *Paracoccus* Sp. Strain BW001. *Biodegradation* 19 (6), 915–926. doi:10.1007/s10532-008-9193-3
- Bi, E., Schmidt, T. C., and Haderlein, S. B. (2006). Sorption of Heterocyclic Organic Compounds to Reference Soils: Column Studies for Process Identification. *Environ. Sci. Technol.* 40 (19), 5962–5970. doi:10.1021/es060470e
- Bilecen, K., and Yildiz, F. H. (2009). Identification of a Calcium-Controlled Negative Regulatory System Affecting *Vibrio Cholerae* biofilm Formation. *Environ. Microbiol.* 11 (8), 2015–2029. doi:10.1111/j.1462-2920.2009.01923.x
- Bourven, I., Joussein, E., and Guibaud, G. (2011). Characterisation of the Mineral Fraction in Extracellular Polymeric Substances (EPS) from Activated Sludges Extracted by Eight Different Methods. *Bioresour. Technol.* 102 (14), 7124–7130. doi:10.1016/j.biortech.2011.04.058
- Bundeleva, I. A., Shirokova, L. S., Bénézech, P., Pokrovsky, O. S., Kompantseva, E. I., and Balor, S. (2011). Zeta Potential of Anoxygenic Phototrophic Bacteria and Ca Adsorption at the Cell Surface: Possible Implications for Cell protection from CaCO₃ Precipitation in Alkaline Solutions. *J. Colloid Interf. Sci.* 360 (1), 100–109. doi:10.1016/j.jcis.2011.04.033
- Cai, W., De La Fuente, L., and Arias, C. R. (2019). Transcriptome Analysis of the Fish Pathogen *Flavobacterium Columnare* in Biofilm Suggests Calcium Role in Pathogenesis. *BMC Microbiol.* 19, 151. doi:10.1186/s12866-019-1533-4
- Chen, G., and Walker, S. L. (2007). Role of Solution Chemistry and Ion Valence on the Adhesion Kinetics of Groundwater and marine Bacteria. *Langmuir* 23 (13), 7162–7169. doi:10.1021/la0632833
- Chen, W., Westerhoff, P., Leenheer, J. A., and Booksh, K. (2003). Fluorescence Excitation–Emission Matrix Regional Integration to Quantify Spectra for Dissolved Organic Matter. *Environ. Sci. Technol.* 37 (24), 5701–5710. doi:10.1021/es034354c
- Chen, Y., Chai, Y., Guo, J.-h., and Losick, R. (2012). Evidence for Cyclic Di-GMP-Mediated Signaling in *Bacillus Subtilis*. *J. Bacteriol.* 194 (18), 5080–5090. doi:10.1128/Jb.01092-12
- Das, T., Sehar, S., Koop, L., Wong, Y. K., Ahmed, S., Siddiqui, K. S., et al. (2014). Influence of Calcium in Extracellular DNA Mediated Bacterial Aggregation and Biofilm Formation. *PLOS ONE* 9 (3), e91935. doi:10.1371/journal.pone.0091935
- de Kerchove, A. J., and Elimelech, M. (2008). Calcium and Magnesium Cations Enhance the Adhesion of Motile and Nonmotile *Pseudomonas A* on Alginate Films. *Langmuir* 24 (7), 3392–3399. doi:10.1021/la7036229
- Domínguez, D. C., Guragain, M., and Patrauchan, M. (2015). Calcium Binding Proteins and Calcium Signaling in Prokaryotes. *Cell Calcium* 57 (3), 151–165. doi:10.1016/j.ceca.2014.12.006
- Dubois, M., Gilles, K. A., Hamilton, J. K., Rebers, P. A., and Smith, F. (1956). Colorimetric Method for Determination of Sugars and Related Substances. *Anal. Chem.* 28 (3), 350–356. doi:10.1021/ac60111a017
- Fleming, H.-C., Wingender, J., Szewzyk, U., Steinberg, P., Rice, S. A., and Kjelleberg, S. (2016). Biofilms: An Emergent Form of Bacterial Life. *Nat. Rev. Microbiol.* 14, 563–575. doi:10.1038/nrmicro.2016.94
- Fleming, H.-C., and Wingender, J. (2010). The Biofilm Matrix. *Nat. Rev. Microbiol.* 8 (9), 623–633. doi:10.1038/nrmicro2415
- Fleming, H.-C., and Wuerzt, S. (2019). Bacteria and Archaea on Earth and Their Abundance in Biofilms. *Nat. Rev. Microbiol.* 17 (4), 247–260. doi:10.1038/s41579-019-0158-9
- Fu, S., Fan, H., Liu, S., Liu, Y., and Liu, Z. (2009). A Bioaugmentation Failure Caused by Phage Infection and Weak Biofilm Formation Ability. *J. Environ. Sci.* 21 (8), 1153–1161. doi:10.1016/S1001-0742(08)62396-7
- Gomes, L. C., Moreira, J. M. R., Simões, M., Melo, L. F., and Mergulhão, F. J. (2014). Biofilm Localization in the Vertical Wall of Shaking 96-Well Plates. *Scientifica* 2014, 231083. doi:10.1155/2014/231083
- Ha, D.-G., and O'Toole, G. A. (2015). c-di-GMP and its Effects on Biofilm Formation and Dispersion: A *Pseudomonas Aeruginosa* Review. *Microbiol. Spectr.* 3 (2), MB-0003-2014. doi:10.1128/microbiolspec.MB-0003-2014
- He, X., Wang, J., Abdoli, L., and Li, H. (2016). Mg²⁺/Ca²⁺ Promotes the Adhesion of Marine Bacteria and Algae and Enhances Following Biofilm Formation in Artificial Seawater. *Colloids Surf. B: Biointerfaces* 146, 289–295. doi:10.1016/j.colsurfb.2016.06.029
- Herrero, M., and Stuckey, D. C. (2015). Bioaugmentation and its Application in Wastewater Treatment: A Review. *Chemosphere* 140, 119–128. doi:10.1016/j.chemosphere.2014.10.033
- Heydorn, A., Nielsen, A. T., Hentzer, M., Sternberg, C., Givskov, M., Ersbøll, B. K., et al. (2000). Quantification of Biofilm Structures by the Novel Computer Program COMSTAT. *Microbiology* 146 (10), 2395–2407. doi:10.1099/00221287-146-10-2395
- Hou, X., Liu, S., and Zhang, Z. (2015). Role of Extracellular Polymeric Substance in Determining the High Aggregation Ability of Anammox Sludge. *Water Res.* 75, 51–62. doi:10.1016/j.watres.2015.02.031
- Jefferson, K. K. (2004). What Drives Bacteria to Produce a Biofilm? *FEMS Microbiol. Lett.* 236 (2), 163–173. doi:10.1111/j.1574-6968.2004.tb09643.x
- Jenal, U., Reinders, A., and Lori, C. (2017). Cyclic Di-GMP: Second Messenger Extraordinaire. *Nat. Rev. Microbiol.* 15 (5), 271–284. doi:10.1038/nrmicro.2016.190
- Kaiser, J. P., Feng, Y., and Bollag, J. M. (1996). Microbial Metabolism of Pyridine, Quinoline, Acridine, and Their Derivatives under Aerobic and Anaerobic Conditions. *Microbiol. Rev.* 60 (3), 483–498. doi:10.1128/mr.60.3.483-498.1996
- Liang, J., Li, W., Zhang, H., Jiang, X., Wang, L., Liu, X., et al. (2018). Coaggregation Mechanism of Pyridine-Degrading Strains for the Acceleration of the Aerobic Granulation Process. *Chem. Eng. J.* 338, 176–183. doi:10.1016/j.ccej.2018.01.029
- Liu, Y.-J., and Sun, D. D. (2011). Calcium Augmentation for Enhanced Denitrifying Granulation in Sequencing Batch Reactors. *Process Biochem.* 46 (4), 987–992. doi:10.1016/j.procbio.2011.01.016
- Mangwani, N., Shukla, S. K., Rao, T. S., and Das, S. (2014). Calcium-Mediated Modulation of *Pseudomonas Mendocina* NR802 Biofilm Influences the Phenanthrene Degradation. *Colloids Surf. B: Biointerfaces* 114, 301–309. doi:10.1016/j.colsurfb.2013.10.003
- Marciňáková, M., Klingberg, T. D., Lauková, A., and Budde, B. B. (2010). The Effect of pH, Bile and Calcium on the Adhesion Ability of Probiotic Enterococci of Animal Origin to the Porcine Jejunal Epithelial Cell Line IPEC-J2. *Anaerobe* 16 (2), 120–124. doi:10.1016/j.anaerobe.2009.05.001
- Mohan, S. V., Sistla, S., Guru, R. K., Prasad, K. K., Kumar, C. S., Ramakrishna, S. V., et al. (2003). Microbial Degradation of Pyridine Using *Pseudomonas* Sp. and Isolation of Plasmid Responsible for Degradation. *Waste Manage.* 23 (2), 167–171. doi:10.1016/S0956-053x(02)00150-2
- O'Toole, G. A., and Kolter, R. (1998). Flagellar and Twitching Motility Are Necessary for *Pseudomonas Aeruginosa* Biofilm Development. *Mol. Microbiol.* 30 (2), 295–304. doi:10.1046/j.1365-2958.1998.01062.x
- O'Toole, G. A. (2011). Microtiter Dish Biofilm Formation Assay. *J. Vis. Exp.* (47), e2437. doi:10.3791/2437
- Parker, J. K., Chen, H., McCarty, S. E., Liu, L. Y., and De La Fuente, L. (2016). Calcium Transcriptionally Regulates the Biofilm Machinery of *Xylella Fastidiosato* Promote Continued Biofilm Development in Batch Cultures. *Environ. Microbiol.* 18 (5), 1620–1634. doi:10.1111/1462-2920.13242
- Passos da Silva, D., Schofield, M., Parsek, M., and Tseng, B. (2017). An Update on the Sociomicrobiology of Quorum Sensing in Gram-Negative Biofilm Development. *Pathogens* 6 (4), 51. doi:10.3390/pathogens6040051
- Ramsey, M. M., and Whiteley, M. (2004). *Pseudomonas A* Attachment and Biofilm Development in Dynamic Environments. *Mol. Microbiol.* 53 (4), 1075–1087. doi:10.1111/j.1365-2958.2004.04181.x
- Raper, E., Stephenson, T., Anderson, D. R., Fisher, R., and Soares, A. (2018). Industrial Wastewater Treatment through Bioaugmentation. *Process Saf. Environ. Prot.* 118, 178–187. doi:10.1016/j.psep.2018.06.035

- Redinbaugh, M. G., and Turley, R. B. (1986). Adaptation of the Bicinchoninic Acid Protein Assay for Use with Microtiter Plates and Sucrose Gradient Fractions. *Anal. Biochem.* 153 (2), 267–271. doi:10.1016/0003-2697(86)90091-6
- Renner, L. D., and Weibel, D. B. (2011). Physicochemical Regulation of Biofilm Formation. *MRS Bull.* 36 (5), 347–355. doi:10.1557/mrs.2011.65
- Rinaudi, L., Fujishige, N. A., Hirsch, A. M., Banchio, E., Zorreguieta, A., and Giordano, W. (2006). Effects of Nutritional and Environmental Conditions on *Sinorhizobium Meliloti* Biofilm Formation. *Res. Microbiol.* 157 (9), 867–875. doi:10.1016/j.resmic.2006.06.002
- Sezonov, G., Joseleau-Petit, D., and D'Ari, R. (2007). *Escherichia C* Physiology in Luria-Bertani Broth. *J. Bacteriol.* 189 (23), 8746–8749. doi:10.1128/Jb.01368-07
- Shen, J., Zhang, X., Chen, D., Liu, X., and Wang, L. (2015). Characteristics of Pyridine Biodegradation by a Novel Bacterial Strain, *Rhizobium* Sp. NJUST18. *Desalination Water Treat.* 53 (7), 2005–2013. doi:10.1080/19443994.2014.915585
- Shukla, S. K., and Rao, T. S. (2013). Effect of Calcium on *Staphylococcus A* Biofilm Architecture: A Confocal Laser Scanning Microscopic Study. *Colloids Surf. B: Biointerfaces* 103 (0), 448–454. doi:10.1016/j.colsurfb.2012.11.003
- Simoni, S. F., Bosma, T. N. P., Harms, H., and Zehnder, A. J. B. (2000). Bivalent Cations Increase Both the Subpopulation of Adhering Bacteria and Their Adhesion Efficiency in Sand Columns. *Environ. Sci. Technol.* 34 (6), 1011–1017. doi:10.1021/es990476m
- Sims, G. K., Sommers, L. E., and Konopka, A. (1986). Degradation of Pyridine by *Micrococcus Luteus* Isolated from Soil. *Appl. Environ. Microbiol.* 51 (5), 963–968. doi:10.1128/aem.51.5.963-968.1986
- Sobeck, D. C., and Higgins, M. J. (2002). Examination of Three Theories for Mechanisms of Cation-Induced Biofouling. *Water Res.* 36 (3), 527–538. doi:10.1016/S0043-1354(01)00254-8
- Soni, K. A., Balasubramanian, A. K., Beskok, A., and Pillai, S. D. (2008). Zeta Potential of Selected Bacteria in Drinking Water When Dead, Starved, or Exposed to Minimal and Rich Culture Media. *Curr. Microbiol.* 56 (1), 93–97. doi:10.1007/s00284-007-9046-z
- Spangler, C., Böhm, A., Jenal, U., Seifert, R., and Kaever, V. (2010). A Liquid Chromatography-Coupled Tandem Mass Spectrometry Method for Quantitation of Cyclic Di-Guanosine Monophosphate. *J. Microbiol. Methods* 81 (3), 226–231. doi:10.1016/j.jmimet.2010.03.020
- Stoodley, P., Sauer, K., Davies, D. G., and Costerton, J. W. (2002). Biofilms as Complex Differentiated Communities. *Annu. Rev. Microbiol.* 56, 187–209. doi:10.1146/annurev.micro.56.012302.160705
- Thomsen, A. B., and Kilen, H. H. (1998). Wet Oxidation of Quinoline: Intermediates and By-Product Toxicity. *Water Res.* 32 (11), 3353–3361. doi:10.1016/S0043-1354(98)00116-X
- Tischler, A. H., Lie, L., Thompson, C. M., and Visick, K. L. (2018). Discovery of Calcium as a Biofilm-Promoting Signal for *Vibrio Fischeri* Reveals New Phenotypes and Underlying Regulatory Complexity. *J. Bacteriol.* 200 (15), e00016–00018. doi:10.1128/JB.00016-18
- Valentini, M., and Filloux, A. (2016). Biofilms and Cyclic Di-GMP (C-Di-GMP) Signaling: Lessons from *Pseudomonas A* and Other Bacteria. *J. Biol. Chem.* 291 (24), 12547–12555. doi:10.1074/jbc.R115.711507
- Van Houdt, R., and Michiels, C. W. (2005). Role of Bacterial Cell Surface Structures in *Escherichia C* Biofilm Formation. *Res. Microbiol.* 156 (5-6), 626–633. doi:10.1016/j.resmic.2005.02.005
- Vu, B., Chen, M., Crawford, R., and Ivanova, E. (2009). Bacterial Extracellular Polysaccharides Involved in Biofilm Formation. *Molecules* 14 (7), 2535–2554. doi:10.3390/molecules14072535
- Wang, T., Flint, S., and Palmer, J. (2019). Magnesium and Calcium Ions: Roles in Bacterial Cell Attachment and Biofilm Structure Maturation. *Biofouling* 35 (9), 959–974. doi:10.1080/08927014.2019.1674811
- Wang, Y., Qin, J., Zhou, S., Lin, X., Ye, L., Song, C., et al. (2015). Identification of the Function of Extracellular Polymeric Substances (EPS) in Denitrifying Phosphorus Removal Sludge in the Presence of Copper Ion. *Water Res.* 73, 252–264. doi:10.1016/j.watres.2015.01.034
- Wu, Y., Ding, Y., Cohen, Y., and Cao, B. (2015). Elevated Level of the Second Messenger C-Di-GMP in *Comamonas Testosteroni* Enhances Biofilm Formation and Biofilm-Based Biodegradation of 3-Chloroaniline. *Appl. Microbiol. Biotechnol.* 99 (4), 1967–1976. doi:10.1007/s00253-014-6107-7
- Xu, P., Han, H., Zhuang, H., Hou, B., Jia, S., Wang, D., et al. (2015). Anoxic Degradation of Nitrogenous Heterocyclic Compounds by Activated Sludge and Their Active Sites. *J. Environ. Sci.* 31 (5), 221–225. doi:10.1016/j.jes.2014.09.034
- Ye, Y., Ling, N., Jiao, R., Wu, Q., Han, Y., and Gao, J. (2015). Effects of Ca²⁺ and Mg²⁺ on the Biofilm Formation of *Cronobacter Sakazakii* Strains from Powdered Infant Formula. *J. Food Saf.* 35 (3), 416–421. doi:10.1111/jfs.12190
- Yu, H., Liang, H., Qu, F., He, J., Xu, G., Hu, H., et al. (2016). Biofouling Control by Biostimulation of Quorum-Quenching Bacteria in a Membrane Bioreactor for Wastewater Treatment. *Biotechnol. Bioeng.* 113 (12), 2624–2632. doi:10.1002/bit.26039
- Yue, W., Chen, M., Cheng, Z., Xie, L., and Li, M. (2018). Bioaugmentation of Strain *Methylobacterium* Sp. C1 Towards P-Nitrophenol Removal with Broad Spectrum Coaggregating Bacteria in Sequencing Batch Biofilm Reactors. *J. Hazard. Mater.* 344, 431–440. doi:10.1016/j.jhazmat.2017.10.039
- Zhang, Y., Li, C., Wu, Y., Zhang, Y., Zhou, Z., and Cao, B. (2019). A Microfluidic Gradient Mixer-Flow Chamber as a New Tool to Study Biofilm Development under Defined Solute Gradients. *Biotechnol. Bioeng.* 116 (1), 54–64. doi:10.1002/bit.26852
- Zhao, B., Ran, X. C., Tian, M., An, Q., and Guo, J. S. (2018a). Assessing the Performance of a Sequencing Batch Biofilm Reactor Bioaugmented with *P. S* Strain XL-2 Treating Ammonium-Rich Wastewater. *Bioresour. Technol.* 270, 70–79. doi:10.1016/j.biortech.2018.09.015
- Zhao, Q., Goto, R., Saito, T., Kobayashi, T., and Sasaki, T. (2020). Effect of Gamma-Irradiation on Complexation of Humic Substances with Divalent Calcium Ion. *Chemosphere* 256, 127021. doi:10.1016/j.chemosphere.2020.127021
- Zhao, Y., Feng, Y., Li, J., Guo, Y., Chen, L., and Liu, S. (2018b). Insight into the Aggregation Capacity of Anammox Consortia during Reactor Start-Up. *Environ. Sci. Technol.* 52 (6), 3685–3695. doi:10.1021/acs.est.7b06553
- Zhou, G., Li, L.-J., Shi, Q.-S., Ouyang, Y.-S., Chen, Y. B., and Hu, W.-F. (2013). Effects of Nutritional and Environmental Conditions on Planktonic Growth and Biofilm Formation of *Citrobacter Werkmanii* BF-6. *J. Microbiol. Biotechnol.* 23 (12), 1673–1682. doi:10.4014/jmb.1307.0704110.4014/jmb1307.07041
- Zhou, G., Shi, Q.-S., Huang, X.-M., and Xie, X.-B. (2016). Proteome Responses of *Citrobacter Werkmanii* BF-6 Planktonic Cells and Biofilms to Calcium Chloride. *J. Proteomics* 133, 134–143. doi:10.1016/j.jprot.2015.12.019

Conflict of Interest: The authors declare that the research was conducted in the absence of any commercial or financial relationships that could be construed as a potential conflict of interest.

Publisher's Note: All claims expressed in this article are solely those of the authors and do not necessarily represent those of their affiliated organizations, or those of the publisher, the editors and the reviewers. Any product that may be evaluated in this article, or claim that may be made by its manufacturer, is not guaranteed or endorsed by the publisher.

Copyright © 2022 Xiong, Wen and Li. This is an open-access article distributed under the terms of the Creative Commons Attribution License (CC BY). The use, distribution or reproduction in other forums is permitted, provided the original author(s) and the copyright owner(s) are credited and that the original publication in this journal is cited, in accordance with accepted academic practice. No use, distribution or reproduction is permitted which does not comply with these terms.



Oil Load Reduction of Oilfield-Produced Water by Applying Swirl–Cyclonic Flotation: A Pilot-Scale Investigation

Jianfei Liu¹, Huihui Wang¹, Yongfeng Zhao², Yi Zhang³, Hongbing Zhao¹, Weilong Zhao¹, Yongsheng Zhang^{1*}, Xiaowei Wang^{1,4,5*}, Xue Li⁶ and Ming Zhang⁷

¹School of Civil Engineer, Henan Polytechnic University, Jiaozuo, China, ²Henan Institute of Building Science Co., Ltd., Zhengzhou, China, ³Henan Oilfield Engineering Consulting Co., Ltd., Zhengzhou, China, ⁴School of Ecology and Environment, Beijing Technology and Business University, Beijing, China, ⁵State Environmental Protection Key Laboratory of Food Chain Pollution Control, Beijing Technology and Business University, Beijing, China, ⁶Solid Waste and Chemicals Technical Management Centre of Henan Province, Zhengzhou, China, ⁷China Railway Zhengzhou Group Co., Ltd., Zhengzhou, China

OPEN ACCESS

Edited by:

Shihai Deng,
Xi'an Jiaotong University, China

Reviewed by:

Xiao Xu,
East China University of Science and
Technology, China
Helian Li,
University of Jinan, China

*Correspondence:

Yongsheng Zhang
zhongyongsheng@hpu.edu.cn
Xiaowei Wang
xiao_wei_wang@126.com

Specialty section:

This article was submitted to
Water and Wastewater Management,
a section of the journal
Frontiers in Environmental Science

Received: 25 February 2022

Accepted: 30 March 2022

Published: 09 May 2022

Citation:

Liu J, Wang H, Zhao Y, Zhang Y,
Zhao H, Zhao W, Zhang Y, Wang X,
Li X and Zhang M (2022) Oil Load
Reduction of Oilfield-Produced Water
by Applying Swirl–Cyclonic Flotation: A
Pilot-Scale Investigation.
Front. Environ. Sci. 10:883877.
doi: 10.3389/fenvs.2022.883877

A swirl–cyclonic flotation (SCF) apparatus was fabricated by combining hydrocyclone and air flotation separation to reduce the oil droplet load of oilfield-produced water. The apparatus was designed as three concentric cylinders with functions of swirling, air flotation separation, and oil collection. Influencing factors such as influent flow, oil concentration, and aeration rate were investigated in the pilot-scale test. The oil concentration of the effluent was below 100 mg/L during the continuous operation under an influent flow rate of 1.5 m³/h and an aeration rate of 0.4 L/min without addition of any chemicals. Results could be explained by the improvement in the floating velocity of oil droplets, resulting in oil load reduction. The oil and water separation mechanism of the SCF apparatus was determined by analysis of oil droplet size distribution. Compared with other flotation apparatus, the SCF apparatus had the advantages of high oil removal efficiency, low retention time, and stable water treatment quality. The apparatus also had no chemical agents added and had less floor area, leading to reduced chemical cost. The designed SCF apparatus has potential industrial application as pretreatment for oil–water load reduction.

Keywords: oilfield-produced water, swirl–cyclonic flotation, pilot scale, bubble floating velocity, separation

INTRODUCTION

Oil is one of the most important energy sources worldwide and plays a key role in economic development. With the continuous development of oil field exploitation activities, the water content in the liquid produced is constantly rising (Liu, et al., 2021). Moreover, polymer flooding technology has become important in oil fields to improve oil recovery. Compared with traditional flooded water, oilfield-produced water contains higher amounts of organic matter, such as phenols, benzene, petroleum hydrocarbons, and polycyclic aromatic hydrocarbons, which are harmful to humans and the environment (Li, et al., 2021). In addition, treated water is not allowed to be reinjected into ground because of its excessive oil, suspended solid, and complex compound contents. Thus, oilfield-produced water is a major environmental challenge and the current research focus.

Several technologies based on different principles have been used for the treatment of oilfield-produced water. These technologies include coagulation, flocculation, centrifugation, flotation, adsorption, gravity settling, micro-filtration, reverse osmosis, biological method, activated sludge, and electrolytic methods (Yu, et al., 2017; Alammari, et al., 2020; Al-Kaabi, et al., 2021). Flotation is used to separate particulate matter from water or any other liquid (Radzuan, et al., 2016). This method is environmentally friendly because of its high efficiency, easy operation, durability, and lack of moving parts (Kargupta, et al., 2021). However, it needs large-volume equipment and addition of chemicals for emulsion breaking and should be combined with other processes (Feris, et al., 2001). The combination of air flotation and low-intensity cyclonic force is based on the new understanding of the processes of collision, coalescence, fragmentation, adhesion, and migration of microbubbles and oil droplets in a turbulent flow field. The collision adhesion probability of bubbles and oil droplets in the separation area is greatly improved by maximizing the synergistic effect of air flotation separation and low-intensity cyclonic force separation (Wang, et al., 2018). The formation of the body combined with bubbles and oil droplets is thus promoted (Saththasivam, et al., 2016). This method significantly accelerates the separation process compared with traditional air flotation. Equipment for oilfield-produced water treatment has gradually changed from a single type to an integrated apparatus that includes air flotation, swirling flow, and sedimentation instruments (Golestanbagh, et al., 2016). This kind of equipment is becoming popular because of its advantages of simple process, high degree of automation, adjustable working operation, and highly efficient processing.

The literature about the combination of air flotation and low-intensity cyclonic force method presents two issues: First, several studies have investigated the influence of operation condition and geometry parameters on the separation efficiency of apparatus (Prakash, et al., 2018; Feris, et al., 2001; Liu, et al., 2013), and second, some scholars studied separation efficiency by numerical simulation (Wang, et al., 2019; Behin and Bahrani, 2012; Lakghomi, et al., 2015). To our knowledge, the separation efficiency of equipment with various operation parameters in the pilot-scale test remains unclear.

This study aimed to investigate the oil load reduction of oilfield-produced water by swirl-cyclonic flotation (SCF) without using coagulants. Tests were conducted in batch and continuous modes. Factors (flow rate, oil concentration, and aeration rate) were evaluated to obtain the optimum operating conditions. Results can be used to expand flotation technology from a laboratory prototype to a full-scale unit and formulate appropriate control measures.

MATERIALS AND METHODS

Apparatus Description

Different types of flotation apparatus are available. According to the number of cylinders, the preliminary separation zone in existing the flotation apparatus can be divided into three

kinds: one cylinder (**Figure 1A**), two cylinders (**Figure 1B**), and three cylinders (**Figure 1C**). Given the different levels of density and interfacial tension of water and oil, the SCF apparatus contains three concentric cylinders that function in swirling, air flotation separation, and oil collection. The experimental apparatus is shown in **Figure 1D**. **Figure 1C** shows the schematic diagram of **Figure 1D**.

The middle cylinder of 300 mm diameter was used for input of oilfield-produced water including oil and water. The inner cylinder of 75 mm diameter was used to collect oil. The outer cylinder of 500 mm diameter was used to collect wastewater. The height of the whole equipment is 1,000 mm. The center of the three cylinders is in a straight line, and the middle cylinder is sealed. The main body of the experimental apparatus was made of polymethyl methacrylate. The inlet pipe of the apparatus is located at the bottom. The exhaust valve at the top is open to atmosphere during the test to allow the entry of atmospheric pressure. The effluent from the apparatus is connected to a separate tank, which can be adjusted within a suitable height according to flow.

Materials

In the pilot test, oilfield-produced water was obtained from the effluent of the three-phase separator in Nanyang Heavy-oil Plant Co., Ltd., China. It has a total processing capacity of 13,000 m³/d, and its pretreatment process involves “two-stage sedimentation + sand filtration.” During the test, the liquid pressure was set as 0.17 MPa. The liquid temperature was 51–55°C, with an average of 52.2°C. The water content in oilfield-produced water was 95.7–97.2%, with an average of 96.4%.

Tetrachloroethylene was purchased from Tianjin Kemiou Chemical Reagent Co., Ltd., China. This chemical has a melting point of −22.2°C, a boiling point of 121.2°C, and a relative density of 1.63.

Pilot-Scale Test

Oil concentration, aeration rate, and influent flow considerably affect the oil removal efficiency. In the pilot-scale test, influent flow and aeration rate can be adjusted, while the oil concentration of oil-produced water fluctuated and cannot be adjusted.

Tests were conducted with a constant aeration rate of 0.4 L/min and a constant influent flow rate of 1.35 m³/h to investigate the effect of concentration on the removal efficiency. Influent oil concentrations were 273.24, 414.41, 563.94, 773.42, 922.19, and 1,168.1 mg/L, respectively.

Tests were conducted with a constant influent flow of 1.35 m³/h and an influent oil concentration of around 1,100 mg/L to investigate the effect of aeration rate on the removal efficiency. The aeration rates were 0.1, 0.2, 0.3, 0.4, 0.5, 0.6, and 0.7 L/min.

Influent flow rates of 0.9, 1.02, 1.35, 1.5, 1.8, and 2.1 m³/h were used with a constant aeration rate of 0.4 L/min and an influent concentration of around 1,100 mg/L to determine the effect of influent flow on the removal efficiency.

In the batch test, working condition parameters were adjusted. After it became stable, effluent was collected every 20 min. The optimum parameters of oil–water separation were determined, and continuous operation experiment was carried out.

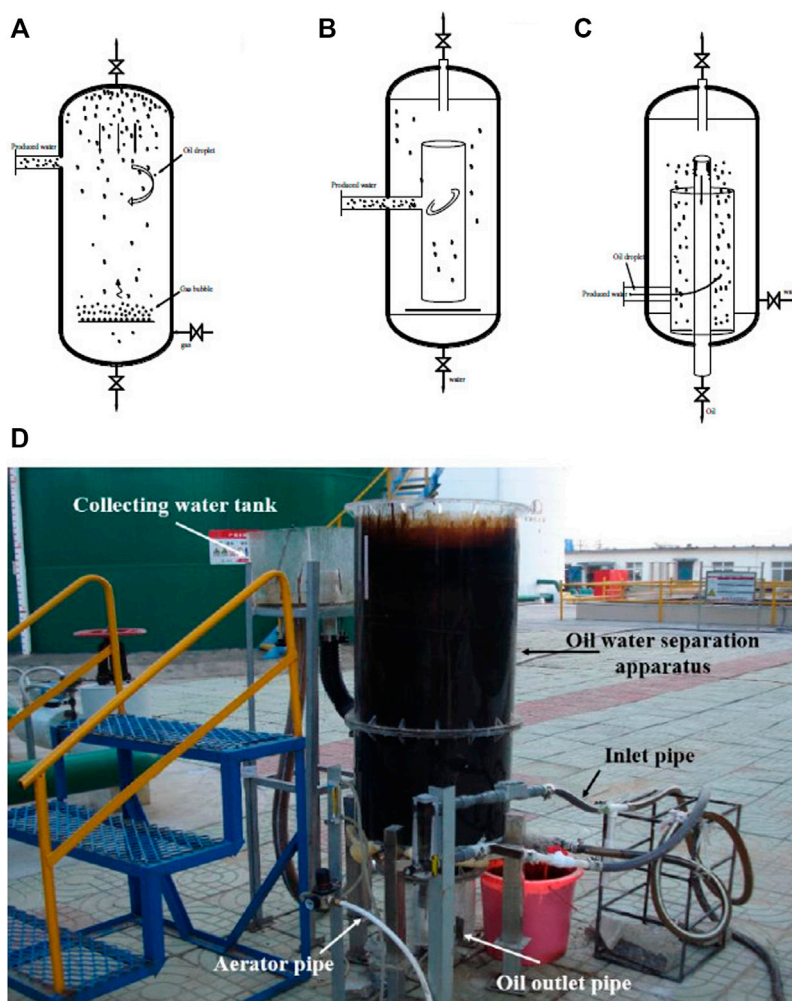


FIGURE 1 | Schematic of (A) single cylinder; (B) double cylinders; (C) triple cylinders; and (D) photo of the swirl-cyclonic flotation apparatus.

Analysis Method

About 0.500 g of heavy oil was weighed on an analytical balance and dissolved in a 100-ml volumetric flask with petroleum ether. The oil content in the solution was 5,000 mg/L. Petroleum ether was used for stepwise dilution to 2,500, 1,000, 500, 100, 50, 10, and 5 mg/L. The oil concentrations were determined by using the JKY-3A infrared oil detector (Jilin Science and Technology Research Institute, China). The specific determination method is based on the *Chinese water quality-Determination of petroleum, animal fats and vegetable oils- Infrared spectrophotometry (HJ637-2018)*. The reagent used in the extraction process was infrared detection reagent tetrachloroethylene. The automatic extractor was used in the extraction process strictly by the calculated residence time, ensuring that the test results more comparative. The linear regression of the test data can reflect the relationship between oil content and absorbance of oil-produced water. The standard curve is as follows:

$$C = 1411.5823A - 33.6358, \quad (1)$$

where A is the absorbance and C is the oil content, mg/L.

A correlation coefficient of 0.9999 was obtained.

The size distribution of oil droplets was analyzed using a laser particle analyzer (BT-9300SE, Dandong Bettersize instruments Ltd., China). The drop visualization of each sample was measured by using the microscope with an objective magnification of 1,000X.

Mechanism

The floating process of oil droplets and bubbles in water is simultaneous. Therefore, the theory of the SCF work can be described by the same set of equations. The oil droplet is taken as an example for the following calculation.

The buoyancy of oil droplet in water is calculated as

$$F_s = \frac{1}{6} \pi d_p^3 (\rho_w - \rho_p) \cdot g, \quad (2)$$

where F_s is the buoyancy of oil droplet, d_p is the particle size of the oil droplet, ρ_w is the density of the water, ρ_p is the density of oil droplet, and g is the acceleration of gravity, respectively.

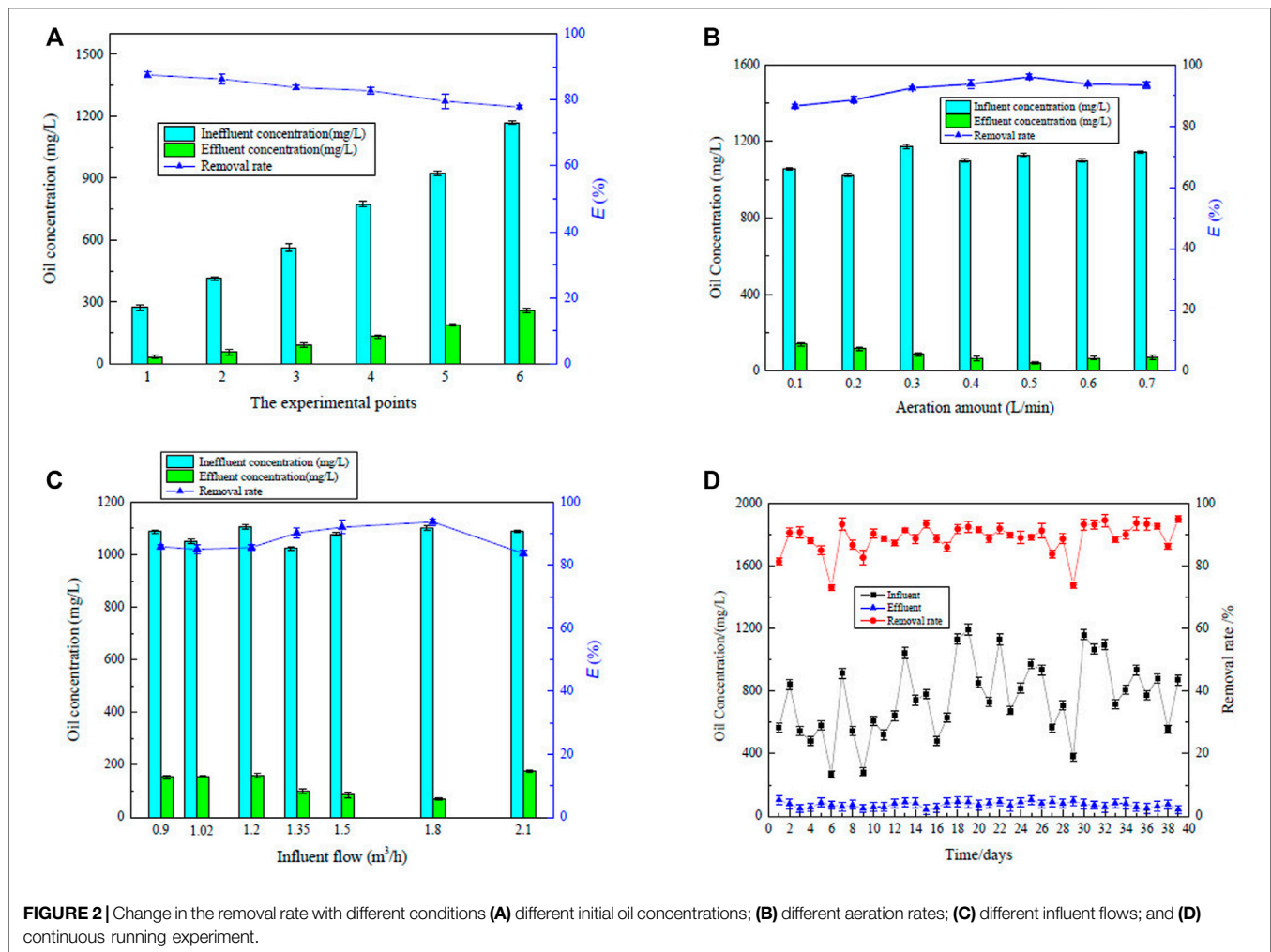


FIGURE 2 | Change in the removal rate with different conditions (A) different initial oil concentrations; (B) different aeration rates; (C) different influent flows; and (D) continuous running experiment.

The resistance of oil droplet in water is calculated as

$$F_f = -\lambda \left(\frac{\pi d_p^2}{4} \right) \left(\frac{u^2 \rho_w}{2} \right), \quad (3)$$

where F_f is the resistance of oil droplets, λ is the resistance coefficient, and u is the floating speed of oil droplets in water, respectively.

When the rising speed of the oil droplet in the water does not change, the acceleration of the oil droplet is 0. At this time, the buoyancy of the oil droplet is the same as the resistance:

$$\frac{1}{6} \pi d_g^3 (\rho_w - \rho_g) \cdot g = -\lambda \left(\frac{\pi d_p^2}{4} \right) \left(\frac{u^2 \rho_w}{2} \right), \quad (4)$$

$$Re = \frac{\rho_w u d_p}{\mu}, \quad (5)$$

$$u = \frac{g d_p^2 (\rho_w - \rho_p)}{18 \mu}, \quad (6)$$

where Re is Reynolds number of oil droplet and μ is the viscosity of water.

RESULTS AND DISCUSSION

Analysis of Factors Affecting Oil–Water Separation

The effects of oil concentration, aeration rate, and influent flow under different working conditions were investigated.

As shown in **Figure 2A**, removal efficiency decreased linearly with increasing influent oil concentration. Higher removal efficiency for oil was achieved at low influent oil concentrations. The frequency of collision and attachment of oil droplet and air bubbles increased at low influent oil concentrations. With increasing oil concentration, the fraction of the oil droplets that did not attach to the air bubbles increased, leading to reduction in removal efficiency (Radzuan, et al., 2016). As the oil concentration of influent oilfield-produced water increased to a certain extent, the oil film became too thick, which blocked the flow of the top oil phase. Beyond the treatment ability, of air flotation, a large oil droplet appeared near the water effluent, thereby decreasing the removal rate.

In the apparatus, the aeration disc has 50- μ m uniform-diameter micropores. Under the action of aeration pump,

bubbles were generated continuously and entered into oil-produced water. The bubble size was affected by increasing velocity, pressure, and surface tension (Leonard, et al., 2021). Some bubbles gathered to form large bubbles, and some of them burst. The bubble particle size is expected to be 10–200 μm . The oil removal rate showed a trend of increasing and then decreasing (Figure 2B). With a low aeration rate, the attachment of the oil droplets to the bubbles might not occur due to the limited number of bubbles. With increasing aeration rate, the number of bubbles increased, and the probability of collision and adhesion between the oil drops and bubbles also increased, thereby increasing the removal efficiency. Higher aeration rate and increasing velocity did not mean higher removal rate. With increasing number of bubbles, bubble–oil droplets dissociated and reduced the separation efficiency of the apparatus. This phenomenon can be explained by the existence of sheets of bubbles that can easily disturb the water flow, thereby reducing the probability of collision and adhesion between the bubbles and oil droplets. In the bubble column reactor, the main influencing parameters of the increasing velocity of bubbles are liquid superficial velocity and gas superficial velocity (Leonard, et al., 2021). Increasing the gas flow rate increased the strength of recirculation, which is expressed by the higher shear rates in the vertical liquid velocity (Panjipour, et al., 2021). Considering the energy saving and treatment effect, the ratio of aeration rate was proposed to be 0.4 L/min.

As shown in Figure 2C, with increasing influent flow from 0.9 m^3/h to 1.8 m^3/h , the corresponding oil removal rate increased first and then decreased. To ensure that the water flow can rotate and rise, the water flow should be maintained at a certain rate. A suitable flow is beneficial to promote the collision, coalescence, migration, and separation between bubbles and oil droplets. If the flow rate is too slow, the hydraulic separation becomes too weak to separate the oil from oilfield-produced water. If the flow rate is too high, the shear stress of the fluid increases, leading to increased breaking ratio of the adhesive body of oil droplets and bubbles. At the same time, a high influent flow results in low hydraulic retention time of oilfield-produced water in the apparatus and low chance of collision and adhesion between the bubbles and oil droplets. In addition, high influent flow means that the high influent rate needs more energy.

A continuous stability experiment was carried out under a influent flow rate of 1.5 m^3/h and aeration rate of 0.4 L/min for 39 days to verify the separation performance and operational stability of the SCF apparatus during operation. The oil concentration was measured 12 times every day, and the average value was taken as the test value. The oil removal rate curve is shown in Figure 2D. When the oil influent concentration of the oilfield-produced water fluctuated within 200–1,200 mg/L during continuous operation, the oil removal rate was 73.09–94.94%, with an average of 92.43%. The minimum effluent concentration appeared at 15th day with the concentration of 41.61 mg/L. In oilfield-produced water with fluctuating concentration, the effluent concentration was stable, indicating that the SCF apparatus presented good adaptability. Compared with the current process in the plant, the removal effect presented no less than the two-stage

sedimentation with less floor area. Hence, the apparatus had high separation efficiency and good operational stability in line with the expected operating indicators.

The effluent oil content exceeded the reinjection standard of China. Considering that low concentration water is conducive to oil–water separation, part of the discharged water can be reinjected to the influent oilfield-produced water to reduce the concentration of the influent water when the concentration is high. Two SCF apparatus can be connected in series to reduce the effluent concentration in actual engineering. In the plant, the discharge water enters the sand filter tank and is finally used for boiler water or groundwater reinjection. SCF has potential industrial application as a pretreatment process for oil–water load reduction.

Oil Separation Mechanism

The oil field-produced water enters tangentially into the middle cylinder and enhances the collision adhesion between the oil droplets and air bubbles, thereby improving the flotation efficiency. When the oil field-produced water enters the SCF apparatus, the separation of the oil phase and water phase occurs. Under the action of SCF, the heavier phase moves to the wall of the cylinder, and the lighter phase moves to the central position. Oil–water separation is a complex process that involves the surface characteristics of oil droplets and their interaction with bubbles (Moosai and Dawe, 2003). Three-phase separation occurs at the liquid/air interface in the SCF apparatus. In the early stage of operation, no film was formed, and the oil concentration in the effluent was high. With the continuous generation, the bubble–oil droplet adhering body floated together and continued to increase at the liquid/air interface. When the experimental conditions are stable, an equilibrium relationship exists between bubble–oil droplet and bubble in the oil–liquid film. The oil droplets are separated from oil-produced water in the oil–liquid film. Three different types of behavior occur in the films when it comes to a stable operation condition. Oil droplets will be skimmed off from the film and flow into the inner cylinder. The heavier water will move to the outside cylinder under cyclonic force, and bubbles will release into the atmosphere. Compared with pure air flotation, the bubble–oil droplet adhering body will rise faster under the action of swirling flow, indicating that the oil–water separation time can be shortened (Edzwald, 2010). Based on Formula 6, the rising velocity of oil droplets can be calculated and shown in Figure 3A. With the oil droplet with 120 μm diameter as example, the floating speed is 9.9 mm/s, and its hydraulic retention time is only about 98 s. Thus, the compact design, low retention time, and high removal rate are the advantages of the SCF apparatus.

The rising velocity of oil droplets gradually increases with increasing oil droplet size. The Reynolds number is a basic parameter used to estimate flow pattern (Xu, et al., 2018). When the oil droplets have particle sizes of 100, 200, and 300 μm , the rising velocities are 0.33, 1.32, and 2.65 mm/s, and the Reynolds numbers are 0.06, 0.47, and 1.43, respectively. All the Reynolds number of oil droplet is below 4.5, which indicate that oil droplets are in the laminar flow area and transition

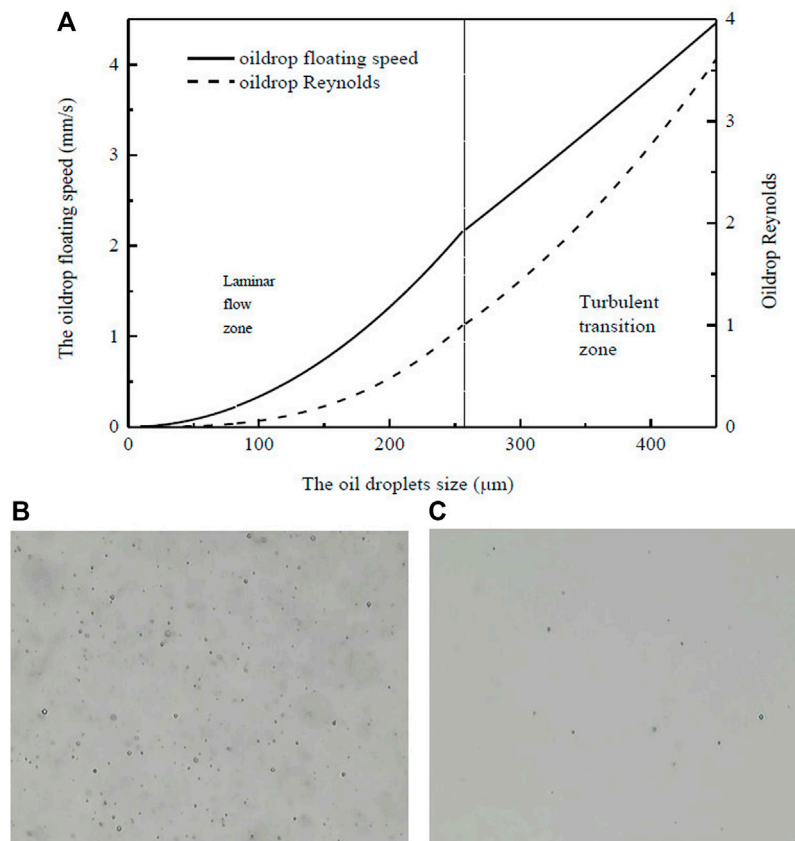


FIGURE 3 | Floating speed (A) and distribution of oil droplets in influent (B) and effluent (C) of oilfield-produced water.

area. The free-floating bubbles has little disturbance to the fluid, and the oil droplets flow under the low-intensity cyclonic force.

The oil droplet distribution in the oilfield-produced water was obtained using a BT-9300SE laser particle size analyzer to clarify the oil and water separation mechanism. When the influent oil concentration was 1,193.26 mg/L, the particle size of the oil droplets in D50 was 250.6 μm , and the maximum particle size of the oil droplets was 900.9 μm . When the effluent oil concentration was 90.32 mg/L, the particle size of D50 oil drops was 13.7 μm and the maximum particle size was 219.3 μm , indicating that part of the emulsified oil with larger particle size was removed by floatation. The removal rates of free oil, dispersed oil, and emulsified oil were 99.98, 80.48, and 61.52%, respectively. Hence, the SCF apparatus is the most effective in removing free oil, and the main form of oilfield-produced water is free oil.

The state of the oil droplets was observed under a Belona biological microscope. As shown in **Figure 3B**, the number of oil droplets is dense and the oil concentration is relatively high. The oil droplets are “ball”-shaped caused by the interface tension between oil and water. **Figure 3C** shows the existing state of oil droplets in the effluent after air floatation. The number of oil droplets in the effluent is sparse, and the particle size of oil

droplets is very small, indicating that air floatation has a good treatment effect on the emulsified oil.

Analysis of Advantages Over Other Flotation Apparatus

The characteristic of the single cylinder is that oil droplets attached to the bubbles move upward with the bubbles, while water moves downward under gravity to the bottom of the apparatus. The main characteristic of the double cylinders is that oil-produced water enters the inner cylinder, which is often installed at the top of the apparatus. Oil droplets attached with the bubbles rise to the oil-phase concentration zone, while the water flows along the wall of the inner cylinder and flows down to the bottom of the vessel. The remarkable characteristic of the three cylinders is that oilfield-produced water enters the middle cylinder. The oil phase can flow into the inner cylinder, and the water phase can flow into the outside cylinder continuously under cyclonic force. **Table 1** summarizes the characteristics of flotation apparatus in the literature. The compact design of the developed apparatus in the present work has three concentric cylinders that function in swirling, air flotation separation, and oil collection.

The removal efficiency can be greatly improved by adding coagulants because coagulated droplets can easily absorb or

TABLE 1 | Characteristics of flotation apparatus.

Oil type	Influent oil concentration (mg/L)	Water inlet position	Cylinder number	Flocculants	Removal efficiency	References
Petroleum	140	Top	2	Chemical	45%	Maelum and Rabe (2015)
Petroleum	100–400	Top	2	3 mg/L PVC	56–85%	Santander et al. (2011)
Motor oil	500	Bottom	1	0.5 wt% C _{14–15} (PO) ₅ SO ₄ Na	60%	Watcharasing et al. (2009)
Cotton oil	100–1,000	Bottom	1	0–200 mg/L aluminum sulfate	65–92%	Hanafy and Nabih (2007)
Petroleum	2000	Bottom	2	48–630 mg/L HPAM	68.5–85%	Qi et al. (2013)
Motor oil	500 ppm	Bottom	1	13.6 mmol/L CTAB	71.2%	Seneesrisakul et al. (2021)
				10 mmol/L MES	77.4%	
				0.62 mmol/L ALF	80.6%	
Petroleum	508	Bottom	1	20 mg/L aluminum sulfate	72%	Al-Shamrani et al. (2002)
Petroleum	2000–2,500	Top	2	150–300 mg/L HPAM	75–88%	Liu et al. (2013)
Personnel care product wastewater	169.7 ± 17	Bottom	1	41 ± 1.7 mg/L ferric chloride	75.8 ± 3.3%	El-Gohary et al. (2010)
Petroleum	212	Top	1	5 mg/L cationic polymer	81%	Multon and Viraraghavan (2008)
	264			5 mg/L nonionic polymer	94%	
petroleum	20% in volume	Bottom	1	5 mg/L MeCS	82%	Maruyama and Seki (2020)
Petroleum	150	Top	1	10 mg/L polyacrylamide	83%	Melo et al. (2003)
Petroleum	475.05	Top	2	30 mg/L PAC	92.19%	Li et al. (2016)
				15 mg/L PAM		
				10 mg/L SDS		
Petroleum	1,193.26	Bottom	3	None	92.43%	This study
Cutting oil	500	Bottom	1	0.1 wt% SDS	98.1%	Buntumpratoomrat et al. (2013)
Petroleum	334–484	Bottom	1	5 mg/L Dismulgan	99%	Etchepare et al. (2017)
Petroleum	300	Bottom	1	250 mg/L of FeCl ₃	99%	Lee et al. (2020)
Cutting oil	10% in volume	Bottom	1	3.6 g/L CaCl ₂	99%	Bensadok et al. (2007)

entrap air bubbles. The oil removal rate can be greatly improved with chemicals (Wang, et al., 2010; El-Gohary, et al., 2010). However, coagulant aid and flocculant in the separation process could produce a large amount of scum, which is not conducive to the recovery and utilization of waste oil. The scum produces mechanical wear and corrosion and causes secondary pollution. The removal rate of the SCF apparatus is higher than that of apparatus in the literature, which can be attributed to the unique compact design of the apparatus. High separation efficiency can be achieved without adding any chemical agents by the apparatus in this work, which also means many chemicals cost could be saved. Therefore, the designed SCF apparatus is suitable for the oil–water load reduction as a pretreatment process.

CONCLUSION

An oil–water separation apparatus with three cylinders was developed by combining hydrocyclone and air flotation separation principle to determine the separation effectiveness of oil and water from oilfield-produced water. Batch and continuous modes were conducted in the pilot test. The optimum operating conditions consisted of an influent flow rate of 1.5 m³/h and an aeration rate of 0.4 L/min by batch test.

In the continuous running mode, the oil removal rate generally was above 90% with fluctuating concentration

under the optimum operating conditions. Compared with other flotation apparatus, the SCF apparatus exhibits the advantages of compact design, lower retention time, and higher removal rate. Two SCF apparatus can be connected in series to reduce the effluent concentration in the actual engineering.

The popularization and application of the designed SCF pretreatment equipment can reduce the oil–water load without using chemicals. As such, the harmful solid oil sludge can be greatly reduced to achieve an environment-friendly and cost-saving operation.

DATA AVAILABILITY STATEMENT

The original contributions presented in the study are included in the article/**Supplementary Material**, further inquiries can be directed to the corresponding authors.

AUTHOR CONTRIBUTIONS

JL: data curation, methodology, writing—original draft; HW: methodology and data curation; YoZ: methodology and data curation; YiZ: methodology and project administration; HZ: methodology; WZ: data curation and investigation; YSZ: methodology and writing—original draft; XW: methodology

and writing—original draft; and XL: project administration and resources.

FUNDING

This study received funding from Key scientific research projects of universities of Henan Provincial Department of Education, China (21B610006), the Fundamental Research Funds for the Universities of Henan Province, China (NSFRF210457), and Henan oilfield Engineering Consulting

Co., Ltd. The funder had the following involvement with the study of oils load reduction of oilfield-produced water application of swirl-cyclonic flotation. All authors declare no other competing interests.

SUPPLEMENTARY MATERIAL

The Supplementary Material for this article can be found online at: <https://www.frontiersin.org/articles/10.3389/fenvs.2022.883877/full#supplementary-material>

REFERENCES

- Al-Kaabi, M. A., Zouari, N., Da'Na, D. A., and Al-Ghouti, M. A. (2021). Adsorptive Batch and Biological Treatments of Produced Water: Recent Progresses, Challenges, and Potentials. *J. Environ. Manage.* 290, 112527. doi:10.1016/j.jenvman.2021.112527
- Al-Shamrani, A. A., James, A., and Xiao, H. (2002). Separation of Oil from Water by Dissolved Air Flotation. *Colloids Surf. A: Physicochem. Eng. Aspects* 209, 15–26. doi:10.1016/S0927-7757(02)00208-X
- Alammar, A., Park, S.-H., Williams, C. J., Derby, B., and Szekely, G. (2020). Oil-in-water Separation with Graphene-Based Nanocomposite Membranes for Produced Water Treatment. *J. Membr. Sci.* 603, 118007. doi:10.1016/j.memsci.2020.118007
- Aliff Radzuan, M. R., Abia-Biteo Belope, M. A., and Thorpe, R. B. (2016). Removal of fine Oil Droplets from Oil-In-Water Mixtures by Dissolved Air Flotation. *Chem. Eng. Res. Des.* 115, 19–33. doi:10.1016/j.cherd.2016.09.013
- Behin, J., and Bahrami, S. (2012). Modeling an Industrial Dissolved Air Flotation Tank Used for Separating Oil from Wastewater. *Chem. Eng. Process. Process Intensif.* 59, 1–8. doi:10.1016/j.cep.2012.05.004
- Bensadok, K., Belkacem, M., and Nezzal, G. (2007). Treatment of Cutting Oil/water Emulsion by Coupling Coagulation and Dissolved Air Flotation. *Desalination* 206, 440–448. doi:10.1016/j.desal.2006.02.070
- Buntungratoomrat, A., Pornsunthorntawe, O., Nitivattananon, S., Chavadej, J., and Chavadej, S. (2013). Cutting Oil Removal by Continuous Froth Flotation with Packing media under Low Interfacial Tension Conditions. *Sep. Purif. Technol.* 107, 118–128. doi:10.1016/j.seppur.2013.01.024
- Edzwald, J. K. (2010). Dissolved Air Flotation and Me. *Water Res.* 44, 2077–2106. doi:10.1016/j.watres.2009.12.040
- El-Gohary, F., Tawfik, A., and Mahmoud, U. (2010). Comparative Study between Chemical Coagulation/precipitation (C/P) versus Coagulation/dissolved Air Flotation (C/DAF) for Pre-treatment of Personal Care Products (PCPs) Wastewater. *Desalination* 252, 106–112. doi:10.1016/j.desal.2009.10.016
- Etchepare, R., Oliveira, H., Azevedo, A., and Rubio, J. (2017). Separation of Emulsified Crude Oil in saline Water by Dissolved Air Flotation with Micro and Nanobubbles. *Sep. Purif. Technol.* 186, 326–332. doi:10.1016/j.seppur.2017.06.007
- Féris, L. A., Gallina, C. W., Rodrigues, R. T., and Rubio, J. (2001). Optimizing Dissolved Air Flotation Design and Saturation. *Water Sci. Technol.* 43, 145–157. doi:10.2166/wst.2001.0486
- Golestanbagh, M., Parvini, M., and Pendashteh, A. (2016). Integrated Systems for Oilfield Produced Water Treatment: The State of the Art. *Energy Sourc. A: Recovery, Util. Environ. Effects* 38, 3404–3411. doi:10.1080/15567036.2016.1154903
- Hanafy, M., and Nabih, H. I. (2007). Treatment of Oily Wastewater Using Dissolved Air Flotation Technique. *Energ. Sourc. Part A: Recovery, Util. Environ. Effects* 29, 143–159. doi:10.1080/009083190948711
- Kargupta, W., Browne, C., Verdugo, L., Hunt, L., Stack, K., Batchelor, W., et al. (2021). Flotation as a Separation Technology for Recovering Pulp Fines and Sustainable Nanocellulose Production. *Sep. Purif. Technol.* 270, 118810. doi:10.1016/j.seppur.2021.118810
- Lakghomi, B., Lawryshyn, Y., and Hofmann, R. (2015). A Model of Particle Removal in a Dissolved Air Flotation Tank: Importance of Stratified Flow and Bubble Size. *Water Res.* 68, 262–272. doi:10.1016/j.watres.2014.09.053
- Lee, J., Cho, W.-C., Poo, K.-M., Choi, S., Kim, T.-N., Son, E.-B., et al. (2020). Refractory Oil Wastewater Treatment by Dissolved Air Flotation, Electrochemical Advanced Oxidation Process, and Magnetic Biochar Integrated System. *J. Water Process Eng.* 36, 101358. doi:10.1016/j.jwpe.2020.101358
- Leonard, C., Ferrasse, J.-H., Lefevre, S., Viand, A., and Boutin, O. (2021). Bubble Rising Velocity and Bubble Size Distribution in Columns at High Pressure and Temperature: From Lab Scale Experiments to Design Parameters. *Chem. Eng. Res. Des.* 173, 108–118. doi:10.1016/j.cherd.2021.07.003
- Li, C., Li, J., Wang, N., Zhao, Q., and Wang, P. (2021). Status of the Treatment of Produced Water Containing Polymer in Oilfields: A Review. *J. Environ. Chem. Eng.* 9, 105303. doi:10.1016/j.jece.2021.105303
- Li, X., Xu, H., Liu, J., Zhang, J., Li, J., and Gui, Z. (2016). Cyclonic State Micro-bubble Flotation Column in Oil-In-Water Emulsion Separation. *Sep. Purif. Technol.* 165, 101–106. doi:10.1016/j.seppur.2016.01.021
- Liu, J., Xu, H., and Li, X. (2013). Cyclonic Separation Process Intensification Oil Removal Based on Microbubble Flotation. *Int. J. Mining Sci. Technol.* 23, 415–422. doi:10.1016/j.ijmst.2013.05.010
- Liu, Y., Lu, H., Li, Y., Xu, H., Pan, Z., Dai, P., et al. (2021). A Review of Treatment Technologies for Produced Water in Offshore Oil and Gas fields. *Sci. Total Environ.* 775, 145485. doi:10.1016/j.scitotenv.2021.145485
- Maelum, M., and Rabe, K. (2015). *Improving Oil Separation from Produced Water Using New Compact Flotation Unit Design*. Oklahoma City, Oklahoma, USA: SPE Publications.
- Maruyama, H., and Seki, H. (2020). Influence of Methylated Milk Casein Flocculant Dosage on Removal Rate of Oil Droplet Removal from O/w in Flotation. *Biochem. Eng. J.* 159, 107584. doi:10.1016/j.bej.2020.107584
- Melo, M. V., Sant'Anna, G. L., and Massarani, G. (2003). Flotation Techniques for Oily Water Treatment. *Environ. Technol.* 24, 867–876. doi:10.1080/09593330309385623
- Moosai, R., and Dawe, R. A. (2003). Gas Attachment of Oil Droplets for Gas Flotation for Oily Wastewater Cleanup. *Sep. Purif. Technol.* 33, 303–314. doi:10.1016/S1383-5866(03)00091-1
- Multon, L. M., and Viraraghavan, T. (2008). Removal of Oil from Produced Water by Dissolved Air Flotation. *Pract. Periodical Hazard. Tox. Radioact. Waste Manage.* 12, 25–29. doi:10.1061/(asce)1090-025x(2008)12:1(25)
- Panjipour, R., Karamoozian, M., and Albijanic, B. (2021). Bubble Size Distributions in Gas-Liquid-Solid Systems and Their Influence on Flotation Separation in a Bubble Column. *Chem. Eng. Res. Des.* 167, 96–106. doi:10.1016/j.cherd.2021.01.001
- Prakash, R., Majumder, S. K., and Singh, A. (2018). Flotation Technique: Its Mechanisms and Design Parameters. *Chem. Eng. Process. - Process Intensif.* 127, 249–270. doi:10.1016/j.cep.2018.03.029
- Qi, W.-K., Yu, Z.-C., Liu, Y.-Y., and Li, Y.-Y. (2013). Removal of Emulsion Oil from Oilfield ASP Wastewater by Internal Circulation Flotation and Kinetic Models. *Chem. Eng. Sci.* 91, 122–129. doi:10.1016/j.ces.2013.01.020
- Santander, M., Rodrigues, R. T., and Rubio, J. (2011). Modified Jet Flotation in Oil (Petroleum) Emulsion/water Separations. *Colloids Surf. A: Physicochem. Eng. Aspects* 375, 237–244. doi:10.1016/j.colsurfa.2010.12.027
- Saththasivam, J., Loganathan, K., and Sarp, S. (2016). An Overview of Oil-Water Separation Using Gas Flotation Systems. *Chemosphere* 144, 671–680. doi:10.1016/j.chemosphere.2015.08.087

- Seneesrisakul, K., Kanokkarn, P., Charoensaeng, A., and Chavadej, S. (2021). Motor Oil Removal from Water by Continuous Froth Flotation: The Influence of Surfactant Structure on Interfacial Adsorption and Foam Properties. *Colloids Surf. A: Physicochem. Eng. Aspects* 618, 126499. doi:10.1016/j.colsurfa.2021.126499
- Wang, C., Wang, Z., Wei, X., and Li, X. (2019). A Numerical Study and Flotation Experiments of Bicyclone Column Flotation for Treating of Produced Water from ASP Flooding. *J. Water Process Eng.* 32, 100972. doi:10.1016/j.jwpe.2019.100972
- Wang, G., Ge, L., Mitra, S., Evans, G. M., Joshi, J. B., and Chen, S. (2018). A Review of CFD Modelling Studies on the Flotation Process. *Minerals Eng.* 127, 153–177. doi:10.1016/j.mineng.2018.08.019
- Wang, L. K., Shammash, N. K., and Wu, B. C. (2010). *Flotation Technology*. London: Humana Press.
- Watcharasing, S., Kongkowitz, W., and Chavadej, S. (2009). Motor Oil Removal from Water by Continuous Froth Flotation Using Extended Surfactant: Effects of Air Bubble Parameters and Surfactant Concentration. *Sep. Purif. Technol.* 70, 179–189. doi:10.1016/j.seppur.2009.09.014
- Xu, X., Ge, X. L., Qian, Y. D., Wang, H. L., and Yang, Q. (2018). Bubble-Separation Dynamics in a Planar Cyclone: Experiments and CFD Simulations. *Aiche J.* 64, 2689–2701. doi:10.1002/aic.16115
- Yu, L., Han, M., and He, F. (2017). A Review of Treating Oily Wastewater. *Arabian J. Chem.* 10, S1913–S1922. doi:10.1016/j.arabjc.2013.07.020

Conflict of Interest: YoZ is employed by the Henan Institute of Building Science Co., Ltd. YiZ is employed by Henan Oilfield Engineering Consulting Co., Ltd. XL is employed by the Solid Waste and Chemicals Technical Management Centre of Henan Province. Author MZ is employed by China Railway Zhengzhou Group Co., Ltd.

The remaining authors declare that the research was conducted in the absence of any commercial or financial relationships that could be construed as a potential conflict of interest.

Publisher's Note: All claims expressed in this article are solely those of the authors and do not necessarily represent those of their affiliated organizations, or those of the publisher, the editors, and the reviewers. Any product that may be evaluated in this article, or claim that may be made by its manufacturer, is not guaranteed or endorsed by the publisher.

Copyright © 2022 Liu, Wang, Zhao, Zhang, Zhao, Zhao, Zhang, Wang, Li and Zhang. This is an open-access article distributed under the terms of the Creative Commons Attribution License (CC BY). The use, distribution or reproduction in other forums is permitted, provided the original author(s) and the copyright owner(s) are credited and that the original publication in this journal is cited, in accordance with accepted academic practice. No use, distribution or reproduction is permitted which does not comply with these terms.



Highly Effective Lead Ion Adsorption by Manganese-Dioxide-Supported Core-Shell Structured Magnetite

Haipeng Zhang, Shiyong Chen, Yuhua Shan, Xiaoqing Qian, Yanju Yang and Juanjuan Wang*

Key Laboratory of Cultivated Land Quality Monitoring and Evaluation, Ministry of Agriculture and Rural Affairs, College of Environmental Science and Engineering, Yangzhou University, Yangzhou, China

OPEN ACCESS

Edited by:

Shihai Deng,
Xi'an Jiaotong University, China

Reviewed by:

Haiqin Wan,
Nanjing University, China
Mazaher Ahmadi,
Bu-Ali Sina University, Iran

*Correspondence:

Juanjuan Wang
wangjuanjuan@yzu.edu.cn

Specialty section:

This article was submitted to
Water and Wastewater Management,
a section of the journal
Frontiers in Environmental Science

Received: 21 April 2022

Accepted: 12 May 2022

Published: 25 May 2022

Citation:

Zhang H, Chen S, Shan Y, Qian X,
Yang Y and Wang J (2022) Highly
Effective Lead Ion Adsorption by
Manganese-Dioxide-Supported Core-
Shell Structured Magnetite.
Front. Environ. Sci. 10:925205.
doi: 10.3389/fenvs.2022.925205

In this research, a magnetic core-shell composite, consisting of a Fe_3O_4 core and a silica shell (called $\text{Fe}_3\text{O}_4@\text{SiO}_2$), was developed and then functionalized via MnO_2 grafting at different MnO_2 deposition levels (termed $\text{Fe}_3\text{O}_4@\text{SiO}_2\text{-MnO}_2$). The resulting materials were characterized by X-ray fluorescence, X-ray diffraction, a vibration sample magnetometer, transmission electron microscopy, N_2 adsorption-desorption, zeta-potential studies and X-ray photoelectron spectroscopy. Visualizations showed that $\text{Fe}_3\text{O}_4@\text{SiO}_2\text{-MnO}_2$ had a magnetite core with size of 100 nm, overlaid by a rough silica shell and a relatively loose MnO_2 deposition. The Pb(II) adsorption onto the composites was also assessed. It was found that MnO_2 deposition on the $\text{Fe}_3\text{O}_4@\text{SiO}_2$ surface enhanced Pb(II) adsorption, and the Pb(II) adsorption amount was highly correlated to the MnO_2 deposition level. The adsorption kinetics of Pb(II) followed pseudo-second-order kinetics, and the adsorption rate could be decreased by increasing the initial concentration of Pb(II) . A higher pH resulted in enhanced Pb(II) adsorption, which slightly increased with the coexistence of Na^+ and Ca^{2+} , along with the presence of dissolved humic acid. The adsorbent could easily be separated and recovered under the action of the external magnetic component and it displayed stable adsorption behaviour over four adsorption-desorption periods. The results emphasize the high potential of $\text{Fe}_3\text{O}_4@\text{SiO}_2\text{-MnO}_2$ materials for the adsorptive removal of Pb(II) in water.

Keywords: lead removal, adsorption, $\text{Fe}_3\text{O}_4@\text{SiO}_2$, MnO_2 grafting, water treatment

INTRODUCTION

Lead (Pb(II)) pollutant in municipal and industrial wastewater poses a serious threat to public health and ecological systems (Liu et al., 2018). Different treatment techniques, involving chemical precipitation (Li et al., 2022), ion exchange (Li et al., 2017), adsorption (Hussain et al., 2021), and membrane separation (Hamid et al., 2020), have been used to eliminate Pb(II) pollution, among which adsorption has the highest removal efficiency and ease of operation. Therefore, the design and preparation of effective adsorbents for aqueous Pb(II) removal are being widely researched.

Some metal oxides—such as Fe_2O_3 , Al_2O_3 , and MnO_2 —have been evaluated for adsorbing Pb(II) from wastewaters, among which MnO_2 has exhibited promising potential for the adsorptive removal of Pb(II) (Zhang et al., 2020b; Yadav et al., 2021; Ghaedi et al., 2022). Zhang et al. (2017a) and Li et al. (2021) found that MnO_2 presented a strong affinity for Pb(II) under acidic conditions and played a significant role in controlling the geochemical cycle of heavy metal ions owing to its high specific surface area and negatively charged surface over an extensive pH range. However, pure nanosized

MnO_2 particles tend to aggregate in water. The separation of MnO_2 nanoparticles requires energy-intensive filtration, increasing the total cost and leading to filter clogging (Zhu et al., 2015).

Magnetic separation is quicker and more efficient than traditional filtration when used to separate suspended magnetic particles (Xia and Liu, 2021). Fe_3O_4 and $\gamma\text{-Fe}_2\text{O}_3$ are common magnetic agents, exhibiting superparamagnetic behaviour and strong magnetization. Combining their magnetic efficacy with that of MnO_2 nanoparticles can help mitigate the limitation of MnO_2 nanoparticles in terms of their slow separation from water. However, magnetic Fe_3O_4 and $\gamma\text{-Fe}_2\text{O}_3$ are not stable under acidic conditions (Bandar et al., 2021). Significant research effort has been devoted to enhancing the stability of magnetic iron oxides by coating them with polymers (Chen et al., 2018), lauric acid (Zhu et al., 2019), carbon (Wang W. et al., 2015), ZrO_2 (Gugushe et al., 2021) and SiO_2 (Vishnu and Dhandapani, 2020). Notably, SiO_2 -based coatings are very stable under acidic conditions and highly resistant to oxidants and reductants (Vishnu and Dhandapani, 2020). Hence, they can act as ideal shell composites to shield the inner magnetic cores. Furthermore, SiO_2 has a high specific surface area and abundant hydroxyl groups, which facilitates facile functionalization. For instance, Huang et al. (2014) used $\text{M-Fe}_3\text{O}_4@\text{SiO}_2/\text{ZnO}$ for the photocatalytic degradation of methyl group, finding that SiO_2 incorporation prevented the agglomeration of the Fe_3O_4 nanoparticles and enhanced the photocatalytic performance. Vishnu and Dhandapani (2020) synthesized an amino-functionalised silica-coated magnetic nanoparticle with high stability under acidic conditions. However, there have been few reports on the incorporation of MnO_2 onto the surface of magnetic core-shell nanoparticles. Zhang et al. (2015) prepared a $\text{Fe}_3\text{O}_4@\text{SiO}_2@\text{MnO}_2$ composite as an adsorbent for the decolouration of methyl orange, which consisted of a magnetic Fe_3O_4 core, SiO_2 shell—with thickness of 40 nm—and MnO_2 nanoparticles adhering to the surface of SiO_2 body, with a diameter of about 10 nm. However, the thick SiO_2 body and large MnO_2 nanoparticles decreased the saturation magnetisation (M_s) of Fe_3O_4 from 82.47 emu g^{-1} – 29.41 emu g^{-1} , which markedly restricted the

efficiency of magnetic separation and recovery of the adsorbent. Hence, we hypothesize that a nanocomposite of Fe_3O_4 core, a thin SiO_2 shell and a monolayer of active MnO_2 will exhibit a high adsorption ability and separability for Pb(II). However, to the best of our knowledge, no such study has been reported to date.

Magnetic nano-adsorbents were synthesized in this study by grafting MnO_2 with various of concentrations onto the surface of $\text{Fe}_3\text{O}_4@\text{SiO}_2$ core-shell nanoparticles. The characterization of the adsorbents included X-ray fluorescence (XRF), powder X-ray diffraction (XRD), transmission electron microscopy (TEM), vibration sample magnetometry (VSM), N_2 adsorption-desorption, X-ray photoelectron spectroscopy (XPS) and zeta-potential tests. The Pb(II) adsorption capabilities of the materials including the adsorption ability, kinetics, the impact of water chemistry on adsorption, and the regeneration of the saturated adsorbents, were investigated to evaluate the performance of the novel adsorptive materials.

MATERIALS AND METHODS

Adsorbent Preparation

The Fe_3O_4 nanoparticles were prepared using the procedure described by Huang et al. (2014) and Shi et al. (2021). In brief, 3.0 g of $\text{FeCl}_3 \cdot 6\text{H}_2\text{O}$, 2.0 g of polyvinylpyrrolidone and 7.2 g of sodium acetate were dissolved in 60 ml ethylene glycol at 50°C . This was followed by transferring the compound to a 100 ml stainless steel autoclave lined with Teflon and heating it to 200°C for 8 h. Once the mixture' temperature dropped to room temperature, the black solid was gathered through magnetic separation, repeatedly washed in ethanol and deionized water, and then dried at 60°C in a vacuum for 12 h.

After dispersing 1.0 g of Fe_3O_4 nanoparticles in 200 ml of deionized water at 80°C , 20 ml of 1.0 mol L^{-1} Na_2SiO_3 solution was added to the suspension with vigorous agitation. The pH was adjusted to 6.0 using 2.0 mol L^{-1} HCl solution within 1 h, followed by 3 h of vigorous agitation at 80°C . It was necessary to utilize magnetic separation to collect the resulting nanoparticles, which were then thoroughly washed with deionized water, and followed by drying for 12 h in a vacuum at 60°C . The material obtained is referred to as $\text{Fe}_3\text{O}_4@\text{SiO}_2$.

KMnO_4 as the source of manganese was used to prepare MnO_2 -functionalized $\text{Fe}_3\text{O}_4@\text{SiO}_2$ nanoparticles. One gram of $\text{Fe}_3\text{O}_4@\text{SiO}_2$ nanoparticles was suspended in 100 ml of deionized water, and the predicted amount of KMnO_4 solution was added. The mixture was then added dropwise to 40 ml of 30% H_2O_2 solution. Within 0.5 h of mechanical stirring, the pH of this solution was adjusted to 7.0 by adding 1.0 mol L^{-1} HNO_3 . Following that, the reaction mixture was agitated at 25°C for 3 h. The final compound was collected through magnetic separation and repeatedly washed with deionized water before drying at 60°C in a vacuum for 12 h. The subsequent components were designated as $\text{Fe}_3\text{O}_4@\text{SiO}_2\text{-MnO}_2(\text{X})$, where X denotes the concentration of MnO_2 (wt. per cent).

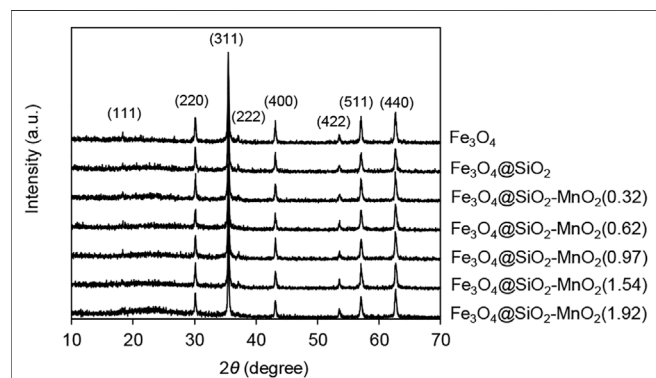
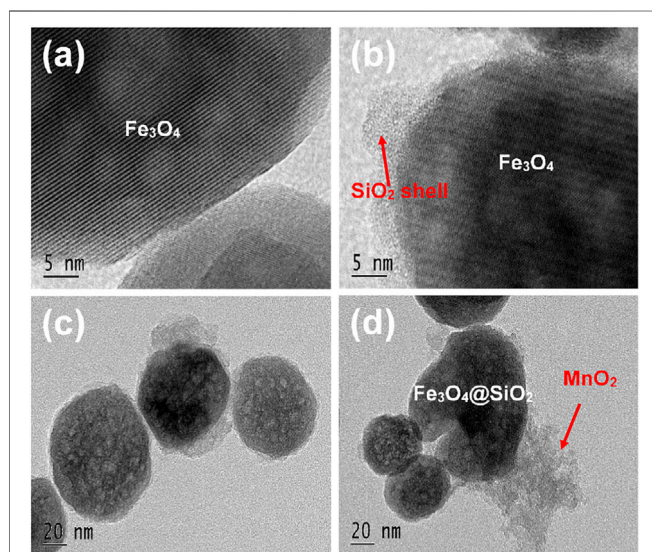


FIGURE 1 | XRD patterns of the samples.

TABLE 1 | BET surface areas and contents of Fe₃O₄, SiO₂ and MnO₂ of the sorbents.

Sample	Content ratio ^a %			S _{BET} (m ² g ⁻¹)
	Fe ₃ O ₄	SiO ₂	MnO ₂	
Fe ₃ O ₄ @SiO ₂	54.24	45.76	—	27.2
Fe ₃ O ₄ @SiO ₂ -MnO ₂ (0.32)	55.15	44.53	0.32	32.1
Fe ₃ O ₄ @SiO ₂ -MnO ₂ (0.62)	54.57	44.81	0.62	36.1
Fe ₃ O ₄ @SiO ₂ -MnO ₂ (0.97)	55.32	43.71	0.97	35.0
Fe ₃ O ₄ @SiO ₂ -MnO ₂ (1.54)	53.66	44.80	1.54	36.6
Fe ₃ O ₄ @SiO ₂ -MnO ₂ (1.92)	54.31	43.77	1.92	38.4

^aDetermined by X-ray fluorescence.**FIGURE 2 |** TEM images of (A) Fe₃O₄, (B) Fe₃O₄@SiO₂, and (C,D) Fe₃O₄@SiO₂-MnO₂(1.54).

Material Characterization

The amount of MnO₂ present in the adsorbents was measured using an ARL9800XP X-ray fluorescence (XRF) spectrometer (Thermo Electron, Switzerland). The X-ray diffraction (XRD) patterns of the materials were recorded using a Rigaku D/max-RA powder diffractometer connected to a Cu K α radiation source over a wide range of angles (10–70°) (Rigaku, Japan). An electron microscopy, the JEM-2100 (JEM-2100, JEOL, Japan), was utilized to analyse the morphology of the adsorbents under investigation. Through the N₂ adsorption-desorption operations performed on a Micromeritics ASAP 2020 analyser (Micromeritics Instrument Co., Norcross, GA, United States), we evaluated the Brunauer–Emmett–Teller (BET) surface area at –196°C (77 K). In this study, an XPS examination was carried out using a PHI5000 VersaProbe equipped with a monochromatized Al K α excitation source ($h\nu = 1,486.6$ eV) (ULVAC-PHI, Japan). The binding energy was calibrated using the C 1s peak (284.6 eV). A vibrating sample magnetometer was used to determine the magnetic characteristics of the sample (Lake Shore VSM 7410,

United States). A Zeta Potential Analyser was utilized to determine the nanoparticles' surface Zeta (ζ) potentials (Zeta PALS, Brookhaven Instruments Co., United States). To ensure proper dispersion 24 h before the zeta potential measurement, 40 mg of the material was spread evenly across 400 ml of 1.0 mmol L⁻¹ NaNO₃ solution, and various solution pH values were obtained by adding 0.1 mol L⁻¹ HNO₃ or NaOH.

Batch adsorption Experiments

We determined the Pb(II) adsorption isotherms by conducting a series of batch adsorption tests. A 40 ml glass vial was filled with 40 ml of Pb(II) solution with various initial concentrations and capped with a screw cap containing 20.0 mg of adsorbent. The pH of the combination was maintained at 4.0 \pm 0.2. The samples were then oscillated in an orbital shaker at 25°C for 24 h. Preliminary kinetic trials (data available upon reasonable request) indicated that the adsorption time (24 h) was sufficient to reach an apparent adsorption equilibrium. Following the equilibrium adsorption, the adsorbent was magnetically isolated from the aqueous solutions. When determining the residual Pb(II) concentrations in aliquots, atomic absorption spectroscopy (AAS) (Hitachi Z-8100, Japan) was utilized. The equilibrium amount (mg g⁻¹) of Pb(II) adsorption was determined as following:

$$q_e = \frac{(C_0 - C_e)V}{M} \quad (1)$$

The initial and equilibrium concentrations of Pb(II) are C_0 and C_e (mg L⁻¹), respectively. The total volume of Pb(II) solution is V (L) and the adsorbent mass M is measured in grams.

The Pb(II) adsorption data were fitted to the Langmuir and Freundlich models, which were often used to describe the interaction between the adsorbate and the adsorbent. The Langmuir and Freundlich models could be expressed as Eqs. 2, 3, respectively:

$$\frac{C_e}{q_e} = \frac{C_e}{q_m} + \frac{1}{q_m b} \quad (2)$$

$$\log q_e = \log K_f + \frac{1}{n} \log (C_e) \quad (3)$$

The maximum adsorption capacity is represented by q_m (mg g⁻¹), and b (L mg⁻¹) is the Langmuir equilibrium constant. K_f (mg g⁻¹) is the Freundlich coefficient, which indicates the adsorbent's adsorption capacity, and n is the linearity index, which indicates the adsorption intensity.

Adsorption Kinetics

To investigate the Pb(II) adsorption kinetics, 250.0 mg of Fe₃O₄@SiO₂-MnO₂(1.54) was put into a round-bottom flask with 500 ml of aqueous solution with different Pb(II) concentrations (10.0 mg L⁻¹ and 25.0 mg L⁻¹) under vigorous stirring. About 5 ml of the solution was sampled using a pipette at preset time separations. The suspended magnetic nanoparticles were fast filtered by a 0.22 μ m filter membrane. AAS was used to determine the concentration of Pb(II) in the filtrate. The

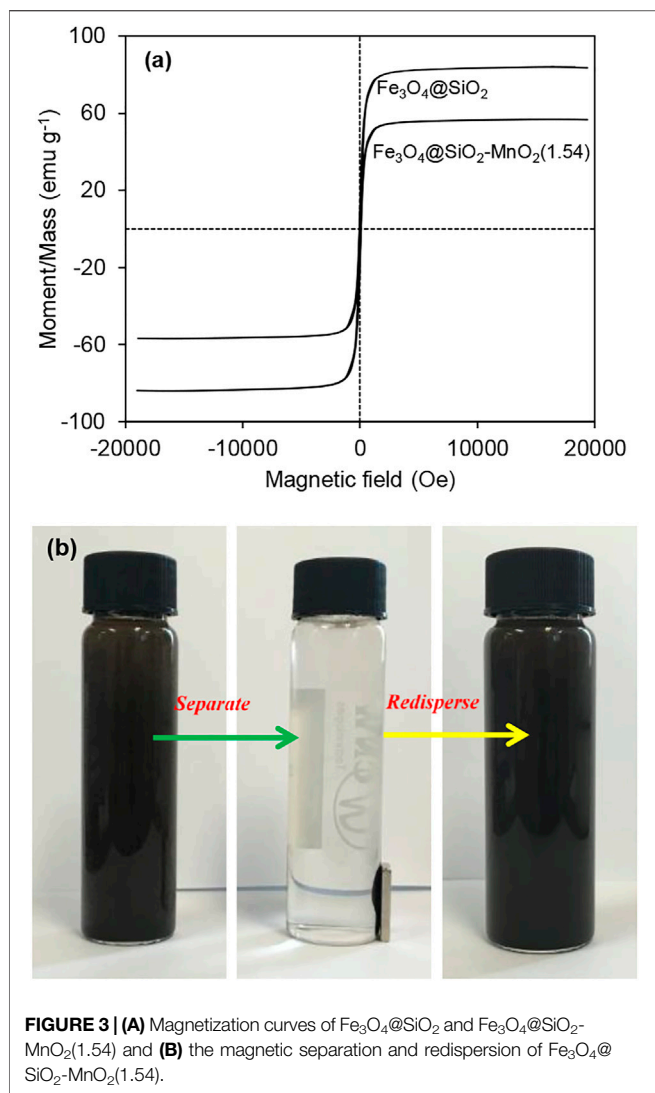


FIGURE 3 | (A) Magnetization curves of Fe₃O₄@SiO₂ and Fe₃O₄@SiO₂-MnO₂(1.54) and **(B)** the magnetic separation and redispersion of Fe₃O₄@SiO₂-MnO₂(1.54).

quantity of Pb(II) adsorption was calculated using the following formula:

$$q_t = \frac{(C_0 - C_t)V}{M} \quad (4)$$

An adsorbing quantity, known as “ q_t ” (mg g⁻¹) is dependent on t (min). C_0 and C_t are the Pb(II) solution concentration (mg L⁻¹) at initial and time t of (mg L⁻¹). The volume of Pb(II) solution is measured by V (L) and the adsorbent mass M is measured in grams.

Effect of Water Chemistry on Pb(II) adsorption

Using Fe₃O₄@SiO₂-MnO₂(1.54) at a temperature of 25°C, the influence of pH on Pb(II) adsorption was investigated. A 25.0 mg L⁻¹ Pb(II) solution with variable pH was added to Teflon-lined, cap-on glass tubes containing 20.0 mg of Fe₃O₄@

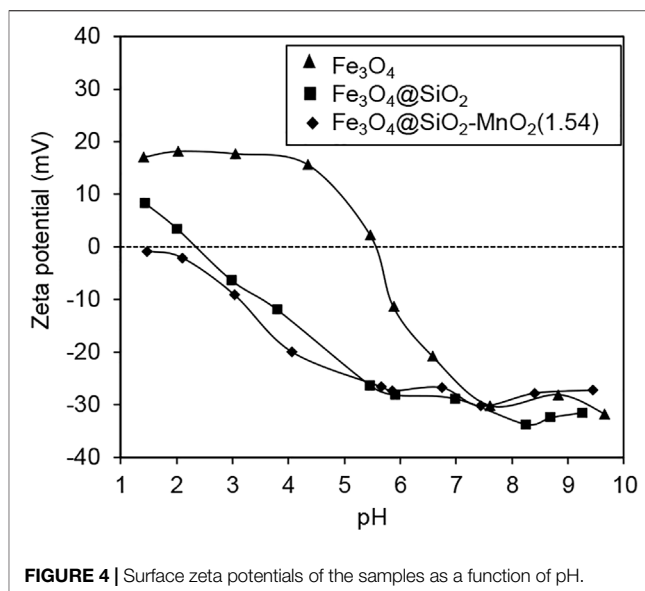


FIGURE 4 | Surface zeta potentials of the samples as a function of pH.

SiO₂-MnO₂(1.54), and the tubes were shaken at 25°C for 48 h. Equation 1 was used to compute the amount of Pb(II) adsorption, and the residual Pb(II) concentration was evaluated by AAS. The effects of co-existing ions on Pb(II)

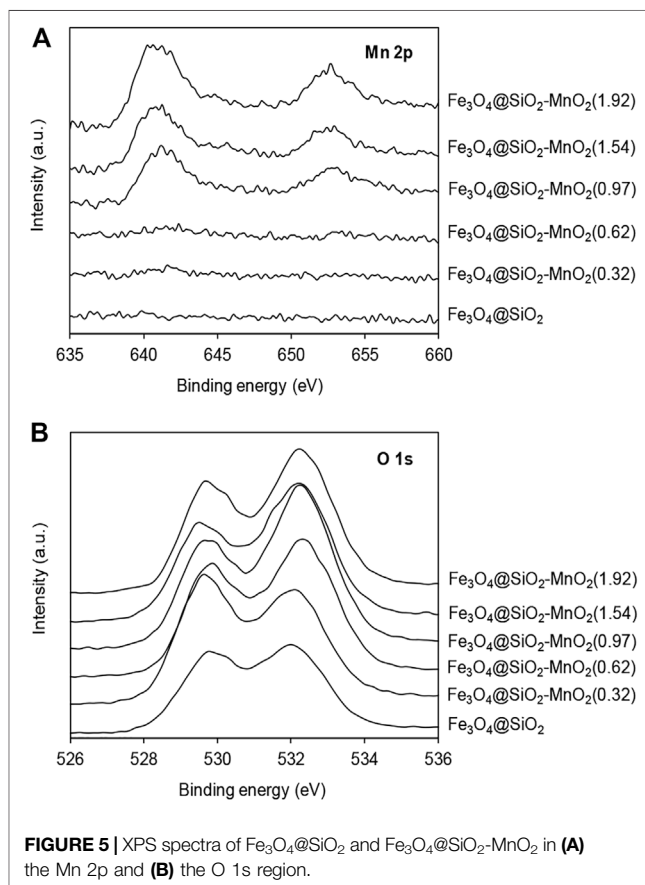
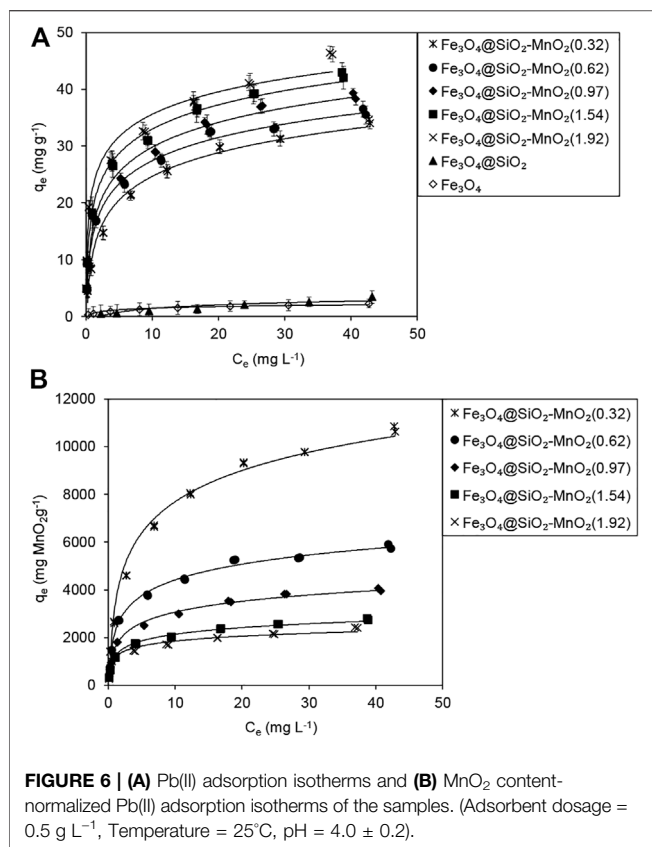


FIGURE 5 | XPS spectra of Fe₃O₄@SiO₂ and Fe₃O₄@SiO₂-MnO₂ in **(A)** the Mn 2p and **(B)** the O 1s region.



adsorption onto Fe₃O₄@SiO₂-MnO₂(1.54) were carried out with the presence of various NaCl or CaCl₂ concentrations (0.01–0.20 mol L⁻¹) at pH 4.0 ± 0.2, and at 25°C. The effect of dissolved humic substances on Pb(II) adsorption was studied by comparing the adsorption isotherms of Pb(II) in the presence and absence of dissolved humic acid (Sigma-Aldrich) at a concentration of 10.2 mg L⁻¹.

Desorption and Regeneration of the Saturated Adsorbent

To determine the reusability of the synthesized sorbent, eight successive periods of Pb(II) adsorption and regeneration on

Pb(II)-saturated Fe₃O₄@SiO₂-MnO₂ (1.54) were conducted. Specifically, 50.0 mg of Fe₃O₄@SiO₂-MnO₂(1.54) was suspended in 100 ml of 25.0 mg L⁻¹ Pb(II) solution and maintained at 25°C for 24 h with vigorous stirring. The Pb(II)-saturated adsorbent was then split magnetically, and the residual Pb(II) concentration was measured by methods described previously. The resultant Pb(II)-saturated adsorbent was regenerated by suspending it in 20 ml of 1.0 mol L⁻¹ HCl solution and keeping it for 24 h. Before the next adsorption-desorption period, the regenerated adsorbent was repeatedly cleaned using deionized water until the pH of the supernatant was almost neutral.

RESULTS AND DISCUSSION

Characterization of the Adsorbents

The XRD diagrams of Fe₃O₄, Fe₃O₄@SiO₂ and Fe₃O₄@SiO₂-MnO₂ with different MnO₂ concentrations are shown in **Figure 1**. The major diffraction peaks of Fe₃O₄ were determined with 2θ of 18.3°, 30.1°, 35.5°, 37.1°, 43.1°, 53.5°, 57.1°, and 62.7°, this indicated the existence of magnetite with a cubic spinel framework (Bandar et al., 2021; Panahandeh et al., 2021). For Fe₃O₄@SiO₂, no prominent and new crystalline peak was observed, revealing that SiO₂ component in Fe₃O₄@SiO₂ was amorphous (Bandar et al., 2021). Upon MnO₂ functionalization, a broad peak at 2θ of 23.7° was detected (except for the diffraction peaks of Fe₃O₄@SiO₂), the intensity of which enhanced with increasing MnO₂ concentration, reflecting the presence of amorphous MnO₂ moieties on the Fe₃O₄@SiO₂ surface (Yin et al., 2011; Zhang et al., 2017b). Additionally, the few diffraction peak features of crystalline MnO₂ reflected the low MnO₂ content in the Fe₃O₄@SiO₂-MnO₂ adsorbents.

The BET surface areas of the adsorbents identified through N₂ adsorption-desorption are summarized in **Table 1**. These specific surface areas of the Fe₃O₄@SiO₂-MnO₂ adsorbents were higher than that of Fe₃O₄@SiO₂, revealing an increase in the surface area upon functionalization. The XRF analysis results of MnO₂ loading amounts are listed in **Table 1**. The MnO₂ contents of Fe₃O₄@SiO₂-MnO₂ adsorbents were 0.32, 0.62, 0.97, 1.54, and 1.92 (wt%), reflecting the successful grafting of MnO₂ onto the Fe₃O₄@SiO₂ surface.

TABLE 2 | Fitting parameters of the Langmuir and Freundlich isotherm models for adsorption of Pb(II) onto the adsorbents.

Adsorbent	Langmuir Model				Freundlich Model		
	<i>b</i> (L mg ⁻¹)	<i>q_m</i> (mg g ⁻¹)	<i>Q_m</i> (mg gMnO ₂ ⁻¹)	<i>Adj. R</i> ²	<i>K_f</i> (mg g ⁻¹)	<i>n</i>	<i>Adj. R</i> ²
Fe ₃ O ₄	1.46	1.59	—	0.963	0.51	0.39	0.994
Fe ₃ O ₄ @SiO ₂	0.55	2.4	—	0.866	0.13	0.85	0.982
Fe ₃ O ₄ @SiO ₂ -MnO ₂ (0.32)	0.78	26.5	8,290.6	0.965	8.91	2.53	0.976
Fe ₃ O ₄ @SiO ₂ -MnO ₂ (0.62)	0.83	32.2	5,185.5	0.991	11.01	2.79	0.961
Fe ₃ O ₄ @SiO ₂ -MnO ₂ (0.97)	0.92	34.0	3,506.2	0.990	11.87	2.75	0.968
Fe ₃ O ₄ @SiO ₂ -MnO ₂ (1.54)	1.84	33.6	2,179.2	0.994	14.33	2.98	0.975
Fe ₃ O ₄ @SiO ₂ -MnO ₂ (1.92)	3.70	35.1	1827.6	0.993	17.23	3.40	0.977

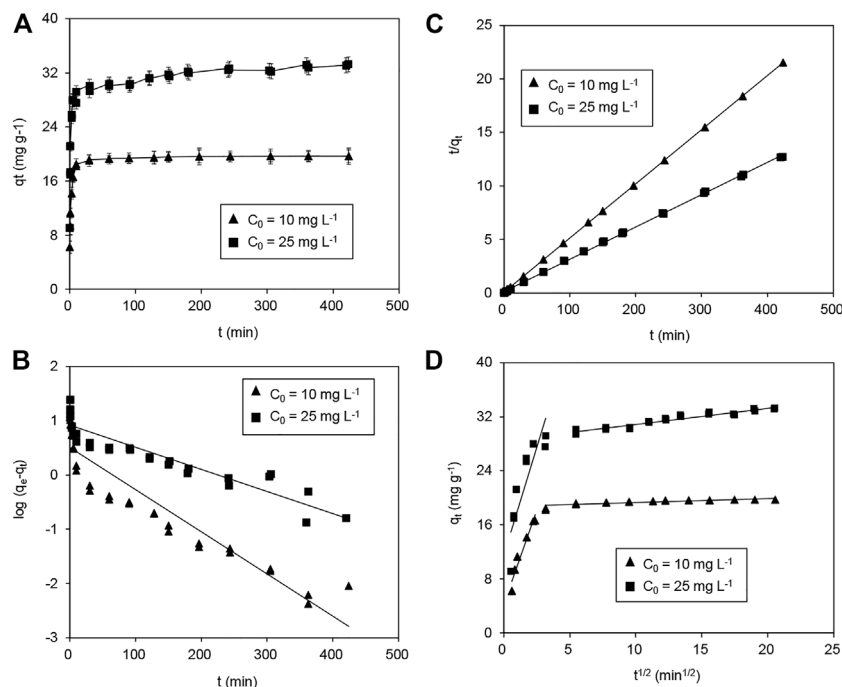


FIGURE 7 | (A) Adsorption of Pb(II) with various initial concentrations on Fe₃O₄@SiO₂-MnO₂(1.54) as a function of the adsorption time, and fitting of Pb(II) adsorption kinetics using the **(B)** pseudo-first-order model, **(C)** pseudo-second-order model and **(D)** Weber-Morris model. (C_0 (Pb(II)) = 10.0 mg L⁻¹ and 25.0 mg L⁻¹, respectively, adsorbent dosage = 0.5 g L⁻¹, Temperature = 25°C, pH = 4.0 ± 0.2).

The TEM images of Fe₃O₄, Fe₃O₄@SiO₂ and Fe₃O₄@SiO₂-MnO₂ are displayed in **Figure 2**. The Fe₃O₄ image (**Figure 2A**) showed the aggregation of spherical clusters with an average diameter of 100 nm. In **Figure 2B**, rough SiO₂ with a thickness of approximately 3 nm outside the Fe₃O₄ core was identified, reflecting that Fe₃O₄@SiO₂ consists of Fe₃O₄ cores and SiO₂ shells. After MnO₂ functionalization (see **Figures 2A,C,D**) relatively loose body was obviously observed on the Fe₃O₄@SiO₂ surface, reflecting the successful deposition of MnO₂ onto the Fe₃O₄@SiO₂ surface.

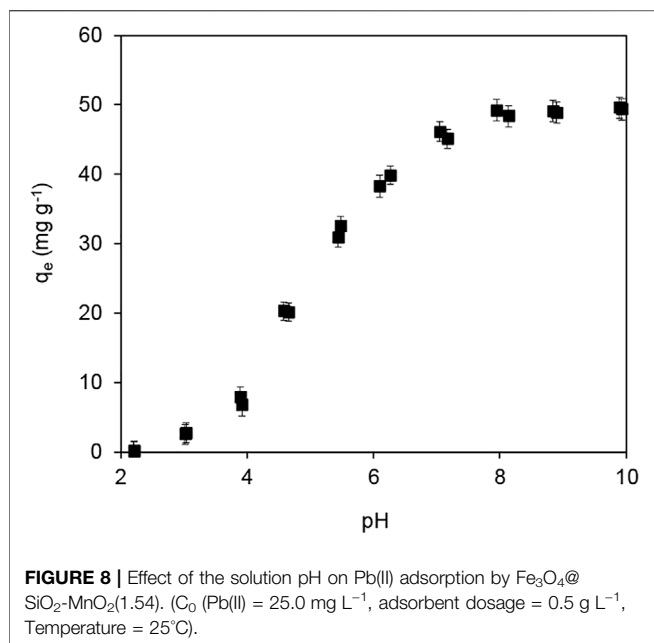
The magnetization curves determined for Fe₃O₄@SiO₂ and Fe₃O₄@SiO₂-MnO₂(1.54) are presented in **Figure 3A**. The saturation magnetisation (M_s) of Fe₃O₄@SiO₂ was determined to be 84.1 emu g⁻¹, whereas the M_s of Fe₃O₄ nanosphere was reported to around 100.3 emu g⁻¹ (Shi et al., 2021). The lower saturation magnetization of Fe₃O₄@SiO₂ than that of Fe₃O₄ could be attributed to the SiO₂ shell. After MnO₂ modification, the saturation magnetization of Fe₃O₄@SiO₂-MnO₂(1.54)

continuously reduced to 56.8 emu g⁻¹, further confirming the successful deposition of MnO₂ onto the Fe₃O₄@SiO₂ surface. VSM results also showed that the samples were superparamagnetic with no remanent coercivity (Xu et al., 2018). As evident in **Figure 3B**, the effective separation and recovery of Fe₃O₄@SiO₂-MnO₂(1.54) could be achieved in seconds with the assistance of an external magnetic field. Further, the nanoparticles quickly redispersed while the magnetic field was removed, reflecting the potential for using MnO₂-functionalized Fe₃O₄@SiO₂ magnetic nanoparticles as recyclable adsorbent in water and wastewater treatment.

The surface zeta potentials of Fe₃O₄, Fe₃O₄@SiO₂ and Fe₃O₄@SiO₂-MnO₂(1.54) are displayed in **Figure 4**, as a function of pH. The surface potential gradually decreased with increases in the pH for all of the samples, likely due to the deprotonated surface hydroxyl groups. The isoelectric point (IEP) of the Fe₃O₄ nanoparticles was found to be 5.8, which was in line with the value found in literature (Bandar et al., 2021). The IEP of Fe₃O₄@

TABLE 3 | Fitting parameters of Pb(II) adsorption kinetics on Fe₃O₄@SiO₂-MnO₂(1.54) using pseudo-first-order, pseudo-second-order, and Weber-Morris models.

C_0 mg L ⁻¹	q_{exp} mg g ⁻¹	Pseudo-first-order			Pseudo-second-order			Weber-Morris Model		
		k_1 min ⁻¹	q_{cal} mg g ⁻¹	Adj. R^2	k_2 g mg ⁻¹ min ⁻¹	q'_{cal} mg g ⁻¹	Adj. R^2	k_d mg g ⁻¹ min ^{-1/2}	I g mg ⁻¹	Adj. R^2
10	19.7	0.018	3.2	0.875	0.049	19.7	0.999	5.49	4.41	0.921
25	33.2	0.011	13.5	0.845	0.006	33.2	0.999	7.53	1.08	0.957

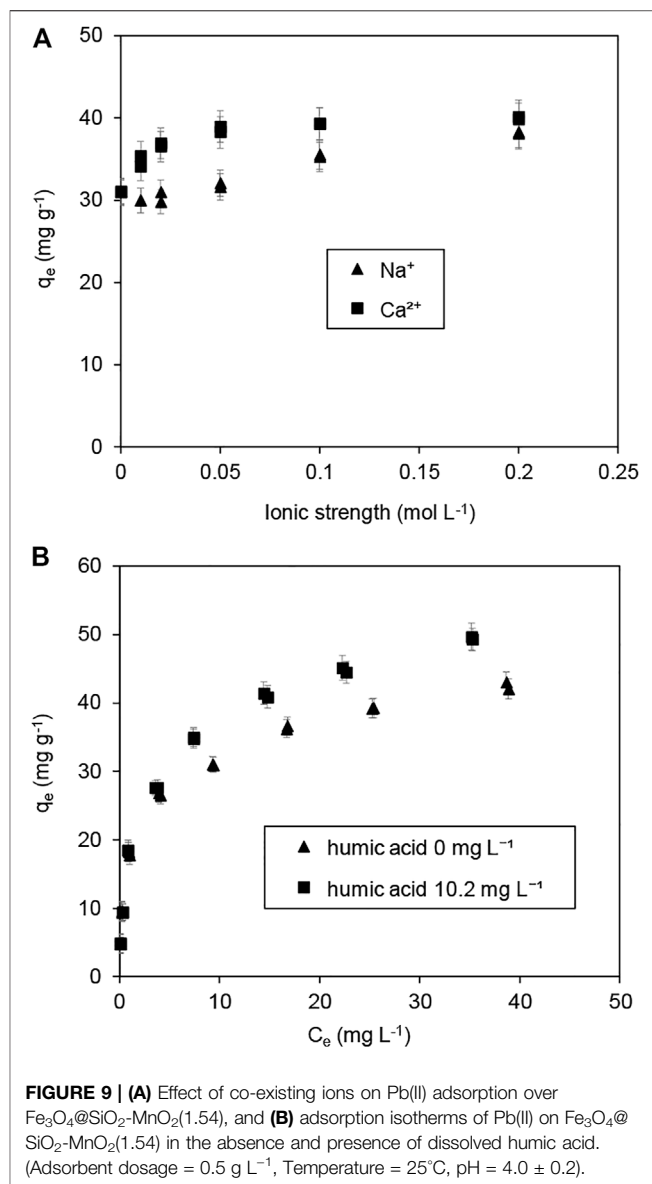


SiO₂ was found to be 2.4, further confirming the successful amorphous silica coating (Wang et al., 2013). More specifically, the IEP of Fe₃O₄@SiO₂-MnO₂(1.54) was found to be approximately 1.4. It is important to note that the IEP of MnO₂ has previously been found to lie within the range of 1–2 (McBride, 1997; Huang et al., 2014). Hence, the lower IEP of Fe₃O₄@SiO₂-MnO₂(1.54) compared with Fe₃O₄@SiO₂ was attributed to the MnO₂ grafting on the Fe₃O₄@SiO₂ surface.

The XPS spectra of Mn 2p and O 1s are presented in **Figures 5A,B**, respectively. In the spectra of Fe₃O₄@SiO₂-MnO₂ adsorbents, Mn 2p peaks were found, reflecting the successful grafting of the MnO₂ functional groups onto the Fe₃O₄@SiO₂ surface. The typical Mn 2p XPS spectrum of Fe₃O₄@SiO₂-MnO₂ nanoparticles revealed a spin-orbit doublet with Mn 2p_{1/2} (653.3 eV) and Mn 2p_{3/2} (641.3 eV), which was separated into a mixed-valent manganese system comprising Mn³⁺ and Mn⁴⁺ (Zhang et al., 2015; Zhang et al., 2017b). Owing to the low MnO₂ content and high MnO₂ dispersion, the intensity of the Mn 2p_{1/2} and Mn 2p_{3/2} peaks of Fe₃O₄@SiO₂-MnO₂(0.32) and Fe₃O₄@SiO₂-MnO₂(0.62), respectively, were not the typical intensities reported for manganese oxides in literature (Zhang et al., 2020a). In the case of the O 1s spectrum (**Figure 5B**), two peaks at 529.8 and 532.1 eV appeared in the spectra of the samples, indicative of the lattice oxygen (*i.e.*, Mn-O, Si-O and Fe-O) and surface oxygen (O-H) (Wan et al., 2020; Minale et al., 2021), respectively. Additionally, the area ratio of surface oxygen increased with increasing MnO₂ deposition levels, which was ascribed to the abundance of hydroxyl groups on the functionalized manganese oxides (Wang et al., 2013).

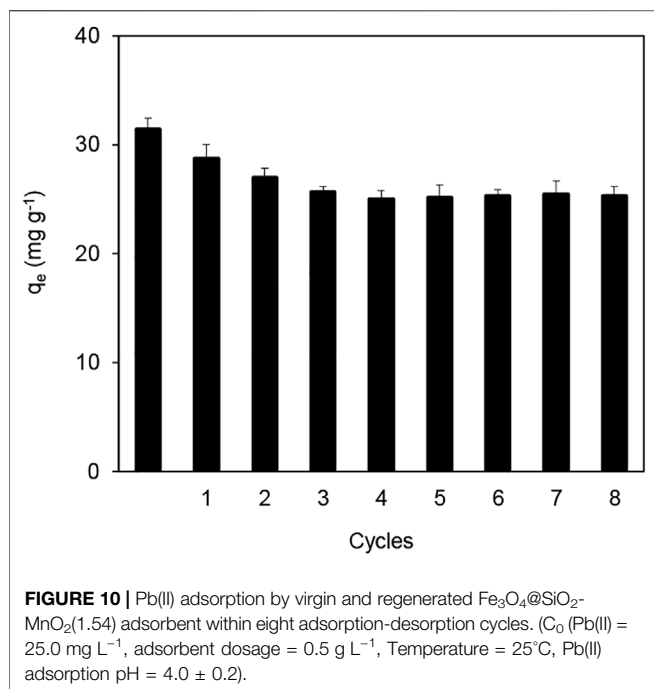
Adsorption Isotherms

Figure 6A shows the isotherms of Pb(II) adsorption onto the adsorbents. Very low quantities of Pb(II) adsorption was detected for Fe₃O₄ and Fe₃O₄@SiO₂, indicating that the Fe₃O₄ and Fe₃O₄@



SiO₂ exhibited a negligible affinity for Pb(II) adsorption. In comparison to Fe₃O₄ and Fe₃O₄@SiO₂, Fe₃O₄@SiO₂-MnO₂ exhibited a significant increase in Pb(II) adsorption, which increased as the MnO₂ deposition level rose, indicating that MnO₂ was the active species for Pb(II) adsorption.

Table 2 summarizes the fitting parameters. For Fe₃O₄@SiO₂-MnO₂(0.32), the *Adj. R*² value (0.976) of the Freundlich model was slightly higher than that of the Langmuir model (0.965), likely because the Fe₃O₄@SiO₂ surface was not entirely covered by MnO₂ at the 0.32% (wt.) deposition level, leading to significant adsorption heterogeneity (Feheem, et al., 2016). In contrast, much higher *R*² values (0.990–0.994) of the Langmuir model were obtained when the MnO₂ deposition levels increased, indicating homogeneous adsorption sites for Pb(II) adsorption at high MnO₂ deposition levels. Additionally, the *b* and *K_f* values increased with increasing



MnO₂ deposition levels, confirming that the active adsorption species was MnO₂.

The calculated q_m of the sorbents suggested that Pb(II) adsorption was not strongly affected by the MnO₂ deposition levels. To obtain deeper insight into the adsorption mechanism, MnO₂-content-normalized adsorption isotherms of Fe₃O₄@SiO₂ with various MnO₂ deposition levels are compared in **Figure 6B**. The calculated maximum adsorption capacities Q_m upon MnO₂ content normalization are listed in **Table 2**. For Fe₃O₄@SiO₂-MnO₂ with various MnO₂ contents, the adsorption capacities Q_m decreased with increasing MnO₂ deposition levels, and the highest Q_m was observed for Fe₃O₄@SiO₂-MnO₂(0.32). This is likely due to the high dispersion of nanosized MnO₂ particles at low deposition levels, and thus, the high utilization of MnO₂ as the active site for Pb(II) adsorption. At higher deposition levels, the MnO₂ particles may aggregate, leading to the partial inaccessibility of the adsorption sites. Notably, almost identical adsorption isotherms were acquired for MnO₂ normalization at deposition levels of 1.54 (wt%) and 1.92 (wt%), reflecting similar structural characteristics (*e.g.*, the content of hydroxyl groups and the particle size) (Zhang et al., 2020a). The nearly identical normalized isotherms implied that the outer surface of SiO₂ shell might be entirely covered at the 1.54% (wt.) MnO₂ deposition, which was in good agreement with the XPS results.

MnO₂ is used as an effective adsorbent for Pb(II) removal in wastewater. Wan et al. (2018) found that the maximum adsorption capacity of biochar-supported hydrated manganese oxide for Pb(II) was 23.8 mg g⁻¹ at a pH of 4.5. Wang S. et al. (2015) investigated Pb(II) adsorption on MnO₂-modified biochar acquired an adsorption capacity of 47.1 mg g⁻¹ at an equilibrium concentration of 40 mg L⁻¹. Note that the adsorption capacity usually increases with the equilibrium concentration of the adsorbate, and these high adsorption capacities reported were

obtained at relatively high Pb(II) equilibrium concentrations. In the current research, the maximum adsorption of Pb(II) on Fe₃O₄@SiO₂-MnO₂(1.54) was 33.6 mg g⁻¹ Fe₃O₄@SiO₂-MnO₂ at an equilibrium concentration of 24.0 mg L⁻¹ and pH of 4.0, showing that the uptake of Pb(II) at low Pb(II) concentrations with the synthesized sorbents was much higher than the reported results and, therefore, a higher efficiency of Pb(II) enrichment was achieved under acidic conditions.

Adsorption Kinetics

The kinetics of Pb(II) adsorption on Fe₃O₄@SiO₂-MnO₂(1.54) with different initial concentrations are depicted in **Figure 7A**. In roughly 30 min, equilibrium was reached at both initial concentrations of 10.0 and 25.0 mg L⁻¹ of Pb(II) on the adsorbent. Adsorption kinetics can be better understood using three kinetic models (Yang et al., 2018): the pseudo-first-order model (Eq. 5), the pseudo-second-order model (Eq. 6), and the Weber-Morris model (Eq. 7).

$$\log(q_e - q_t) = \log q_e - \frac{k_1 t}{2.303} \quad (5)$$

$$\frac{t}{q_t} = \frac{1}{k_2 q_e^2} + \frac{t}{q_e} \quad (6)$$

$$q_t = k_d t^{1/2} + I \quad (7)$$

where the q_t (mg g⁻¹) is the adsorption amount at time t (min), k_1 (min⁻¹) is the pseudo-first-order rate constant, k_2 (g mg⁻¹ min⁻¹) is pseudo-second-order rate constant, k_d and I denote the diffusion constant and the thickness of the boundary layer, respectively.

Figures 7B,C show change curves of $\log(q_e - q_t)$ with t and t/q_t with t ; **Table 3** contains the fitting parameters. The kinetic results for Pb(II) adsorption onto Fe₃O₄@SiO₂-MnO₂(1.54) fit this pseudo-second-order kinetic model very well, showing that Pb(II) adsorption is pseudo-second-order and chemisorption-limited (Panahandeh et al., 2021). Pb(II) adsorbed over Fe₃O₄@SiO₂-MnO₂(1.54) was shown to adhere to pseudo-second-order kinetics when the slopes of the t/q_t against t plots were used. The projected q'_{cal} significant values were very close to the experimental values. There were slower adsorption rates with higher initial Pb(II) concentrations for the Pb(II) adsorption rate constants at 10.0 and 25.0 mg L⁻¹ starting concentrations of Pb(II).

The fitted results of Pb(II) adsorption using Weber-Morris model are shown in **Figure 7D**, and the parameters that best fit the data are listed in **Table 3**. The plots display multilinearity with different initial Pb(II) concentrations, indicating that more than two procedures are involved in the adsorption. In **Figure 7D**, the Weber-Morris plots had two linear portions. The first is assigned to the fast adsorption of Pb(II), and the other to the function of the adsorption equilibrium. According to the model, if the adsorption process is mainly controlled by intraparticle diffusion, the $q_t - t^{1/2}$ plot will be a straight line passing through the origin (Yang et al., 2018). However, the first portion did not pass through initially indicate that external diffusion played a significant role in the adsorption procedure. Additionally, the intercepts decreased at high initial

concentrations, suggesting that the diffusion was not substantially affected by the mass transfer resistance. With initial Pb(II) concentrations of 10.0 and 25.0 mg L⁻¹, respectively, the k_d were 5.5 and 7.5 mg g⁻¹ min^{-1/2}, indicating a higher diffusion constant at a higher initial concentration. This is likely due to the increasing diffusion driving force caused by the increasing concentration gradient.

Impact of Solution Chemistry on Pb(II) adsorption

The impact of the solution pH on Pb(II) adsorption by Fe₃O₄@SiO₂-MnO₂(1.54) is presented in **Figure 8**. The Pb(II) adsorption amount monotonically increased from 0.2 to 48.8 mg g⁻¹ in the pH range from 2.0 to 8.0; subsequently, it remained constant. The pH effect on Pb(II) adsorption could be explained by the electrostatic interaction between the adsorbent and Pb(II), and the precipitation of Pb(II) at high pH conditions (>6.0) (Zhang et al., 2017b). Notably, SiO₂ based shell were not stable against alkaline condition. Although the Pb(II) adsorption capacity of the Fe₃O₄@SiO₂-MnO₂(1.54) was relatively high under high pH conditions, each adsorption performance test in this study was conducted at pH = 4.0 ± 0.2. Generally, the Fe₃O₄@SiO₂-MnO₂(1.54) surface was actively charged at solution pH values under the IEP of 1.4; electrostatic repulsive interaction occurred between Pb(II) and the protonated hydroxyl groups (Wang et al., 2020). In contrast, the adsorption sites were negatively charged at solution pH values above the IEP of 1.4, leading to an electrostatic attraction between deprotonated Mn-OH groups and Pb(II) (Zhang et al., 2020b), enhancing the Pb(II) adsorption.

Alkaline/Earth metal ions in natural water and wastewater may compete against Pb(II) for available adsorption sites of sorbents. The impacts of co-existing Na⁺ and Ca²⁺ on Pb(II) adsorption are shown in **Figure 9A**. These electrolytes resulted in an increase in the Pb(II) adsorption, and Ca²⁺ had a more significant impact on adsorption than Na⁺ did, suggesting that Pb(II) adsorption was controlled mainly by a surface complexation model (Zhang et al., 2020b). Notably, the effects of co-existing Na⁺ and Ca²⁺ on Pb(II) adsorption revealed the presence of a preferable adsorbent, which exhibited great potential for Pb(II) treatment in the presence of co-existing cations at high concentrations.

In aquatic systems, dissolved humic acid may have an effect on the adsorption of Pb(II) (Esfandiar et al., 2022). **Figure 9B** depicts the adsorption isotherms of Pb(II) on Fe₃O₄@SiO₂-MnO₂(1.54) in the absence and presence of dissolved humic acid at a concentration of 10.2 mg L⁻¹. The results indicate the active effect of dissolved humic acid on Pb(II) adsorption at higher equilibrium Pb(II) concentrations under the tested conditions. This positive effect is attributed to the formation of weakly adsorbing complexes between Pb(II) and humic acid (Zhang et al., 2017a).

Regeneration and Reuse of the Adsorbent

Based on the finding that Fe₃O₄@SiO₂-MnO₂ had a poor adsorption capacity at low pH values, the Pb(II)-saturated adsorbent was thought to be regenerated through the acid

treatment. The adsorbent was reused for eight adsorption-regeneration periods and the results are displayed in **Figure 10**. The adsorption capacity reduced from 31.4 to 25.6 mg g⁻¹ during the initial four adsorption-desorption cycles, likely because of partial active species loss during cycle processes or the incomplete desorption of Pb(II) from the surface of Fe₃O₄@SiO₂-MnO₂(1.54). After four cycles, the Fe₃O₄@SiO₂-MnO₂(1.54) adsorption capacity remained constant, and the sorbent could be efficiently separated from the solution within 10 s by an external magnetic field, indicating that the sorbent was stable and recyclable.

Implication for Real-World Application

Efficient removal of Pb(II) in wastewater and rapid separation of adsorbents have always been the difficulties in the practical application of adsorbents. The as-prepared Fe₃O₄@SiO₂-MnO₂ showed high adsorption capacity and good stability for Pb(II) adsorptive removal from acidic Pb(II)-contaminated water, suggesting potential application in wastewater treatment field. Additionally, after adsorbing Pb(II) in wastewater the effective separation and recovery of Fe₃O₄@SiO₂-MnO₂ adsorbent could be accomplished within seconds with an external magnetic field. Furthermore, the Fe₃O₄@SiO₂-MnO₂ adsorbent could be rapidly redispersed while the magnetic field was removed. This means that only one external magnetic field can be used to quickly and efficiently realize the adsorption and desorption of Pb(II) by the adsorbent, which is beneficial to reduce the cost of adsorptive removal of Pb(II) in wastewater.

CONCLUSION

In this research, magnetic core-shell sorbents of Fe₃O₄@SiO₂-MnO₂ with various MnO₂ deposition contents were synthesized through deposition-precipitation and used for Pb(II) adsorption. The characterization results revealed that the Fe₃O₄ core was coated by a rough silica shell and a relatively loose MnO₂ deposition. Accordingly, Fe₃O₄@SiO₂-MnO₂ demonstrated increased Pb(II) adsorption in comparison to Fe₃O₄@SiO₂, and the Pb(II) adsorption amount was positively related to the MnO₂ deposition level. Fe₃O₄@SiO₂-MnO₂ could be easily divided and recovered using an outer magnetic component. The sorbent exhibited stable adsorption and regeneration performance after four consecutive adsorption-desorption periods. This adsorption was contained by surface complexation and slightly enhanced by dissolved humic acid and co-existing cations. These findings highlight that Fe₃O₄@SiO₂-MnO₂ is a promising adsorbent for use in the removal of Pb(II) from water and wastewater.

DATA AVAILABILITY STATEMENT

The original contributions presented in the study are included in the article/Supplementary Material, further inquiries can be directed to the corresponding author.

AUTHOR CONTRIBUTIONS

HZ contributed to data curation, methodology, writing-original draft, and writing-review and editing; SC contributed to data curation and investigation; YS and JW designed all experiments and revised and examined the manuscript; XQ contributed to review and editing; YY contributed to review and editing. All authors have read and agreed to the published version of the manuscript.

REFERENCES

- Bandar, S., Anbia, M., and Salehi, S. (2021). Comparison of MnO₂ Modified and Unmodified Magnetic Fe₃O₄ Nanoparticle Adsorbents and Their Potential to Remove Iron and Manganese from Aqueous Media. *J. Alloys Compd.* 851, 156822. doi:10.1016/j.jallcom.2020.156822
- Chen, Y., Wang, M., Hu, Y., and Han, J. (2018). Poly(2-Aminothiophenol)/MnO₂ Hierarchical Nanocables as Efficient Adsorbents towards Heavy Metal Ions. *Mater. Chem. Phys.* 214, 172–179. doi:10.1016/j.matchemphys.2018.04.076
- Esfandiari, N., Suri, R., and McKenzie, E. R. (2022). Competitive Sorption of Cd, Cr, Cu, Ni, Pb and Zn from Stormwater Runoff by Five Low-Cost Sorbents; Effects of Co-Contaminants, Humic Acid, Salinity and pH. *J. Hazard. Mater.* 423, 126938. doi:10.1016/j.jhazmat.2021.126938
- Faheem Yu, H. X., Liu, J., Shen, J. Y., Sun, X. Y., Li, J. S., et al. (2016). Preparation of MnO_x-Loaded Biochar for Pb²⁺ Removal: Adsorption Performance and Possible Mechanism. *J. Taiwan Inst. Chem. Eng.* 66, 313–320. doi:10.1016/j.jtice.2016.07.010
- Ghaedi, S., Seifpanahi-Shabani, K., and Sillanpää, M. (2022). Waste-to-resource: New Application of Modified Mine Silicate Waste to Removal Pb²⁺ Ion and Methylene Blue Dye, Adsorption Properties, Mechanism of Action and Recycling. *Chemosphere* 292, 133412. doi:10.1016/j.chemosphere.2021.133412
- Gugushe, A. S., Mpupa, A., Munonde, T. S., Nyaba, L., and Nomngongo, P. N. (2021). Adsorptive Removal of Cd, Cu, Ni and Mn from Environmental Samples Using Fe₃O₄-ZrO₂@APS Nanocomposite: Kinetic and Equilibrium Isotherm Studies. *Molecules* 26, 3209. doi:10.3390/molecules26113209
- Hamid, S. A., Azha, S. F., Sellaoui, L., Bonilla-Petriciolet, A., and Ismail, S. (2020). Adsorption of Copper(II) Cation on Polysulfone/zeolite Blend Sheet Membrane: Synthesis, Characterization, Experiments and Adsorption Modelling. *Colloids Surfaces A Physicochem. Eng. Aspects* 601, 124980. doi:10.1016/j.colsurfa.2020.124980
- Huang, S., Gu, L., Zhu, N., Feng, K., Yuan, H., Lou, Z., et al. (2014). Heavy Metal Recovery from Electroplating Wastewater by Synthesis of Mixed-Fe₃O₄@SiO₂/metal Oxide Magnetite Photocatalysts. *Green Chem.* 16, 2696–2705. doi:10.1039/C3GC42496K
- Hussain, T., Hussain, A. I., Chatha, S. A. S., Ali, A., Rizwan, M., Ali, S., et al. (2021). Synthesis and Characterization of Na-Zeolites from Textile Waste Ash and its Application for Removal of Lead (Pb) from Wastewater. *Int. J. Environ. Res. Public Health* 18, 3373. doi:10.3390/ijerph18073373
- Li, Q., Fu, L., Wang, Z., Li, A., Shuang, C., and Gao, C. (2017). Synthesis and Characterization of a Novel Magnetic Cation Exchange Resin and its Application for Efficient Removal of Cu²⁺ and Ni²⁺ from Aqueous Solutions. *J. Clean. Prod.* 165, 801–810. doi:10.1016/j.jclepro.2017.06.150
- Li, W., Li, Y., Liu, J., Chao, S., Yang, T., Li, L., et al. (2021). A Novel Hollow carbon@MnO₂ Electrospun Nanofiber Adsorbent for Efficient Removal of Pb²⁺ in Wastewater. *Chem. Res. Chin. Univ.* 37, 496–504. doi:10.1007/s40242-021-1085-7
- Li, M., Kuang, S., Kang, Y., Ma, H., Dong, J., and Guo, Z. (2022). Recent Advances in Application of Iron-Manganese Oxide Nanomaterials for Removal of Heavy Metals in the Aquatic Environment. *Sci. Total Environ.* 819, 153157. doi:10.1016/j.scitotenv.2022.153157
- Liu, X., Bai, X., Dong, L., Liang, J., Jin, Y., Wei, Y., et al. (2018). Composting Enhances the Removal of Lead Ions in Aqueous Solution by Spent Mushroom Substrate: Biosorption and Precipitation. *J. Clean. Prod.* 200, 1–11. doi:10.1016/j.jclepro.2018.07.182

FUNDINGS

This work was supported by the National Natural Science Foundation of China (31872179, 31901447, 41701093), the Key R&D Plan Program of Jiangsu Province (BE2020319), the Innovation and Entrepreneurship Program of Jiangsu Province (JSSCBS20211062), the Excellent Doctor in Lvyangjinfeng of Yangzhou City (YZLYJFJH2021YXBS155), and the Blue Project of Yangzhou University.

- McBride, M. B. (1997). A Critique of Diffuse Double Layer Models Applied to Colloid and Surface Chemistry. *Clays Clay Minerals* 45, 598–608. doi:10.1346/CCMN.1997.0450412
- Minale, M., Gu, Z., Guadie, A., Li, Y., Wang, Y., Meng, Y., et al. (2021). Hydrous Manganese Dioxide Modified Ploy(sodium Acrylate) Hydrogel Composite as a Novel Adsorbent for Enhanced Removal of Tetracycline and Lead from Water. *Chemosphere* 272, 129902. doi:10.1016/j.chemosphere.2021.129902
- Panahandeh, A., Parvareh, A., and Moraveji, M. K. (2021). Synthesis and Characterization of γ-MnO₂/chitosan/Fe₃O₄ Cross-Linked with EDTA and the Study of its Efficiency for the Elimination of Zinc(II) and Lead(II) from Wastewater. *Environ. Sci. Pollut. Res.* 28, 9235–9254. doi:10.1007/s11356-020-11359-x
- Shi, Y., Han, Z., Yang, J., and Meng, Q. (2021). Influence of the Hallowness and Size Distribution on the Magnetic Properties of Fe₃O₄ Nanospheres. *Langmuir* 37, 9605–9612. doi:10.1021/acs.langmuir.1c01498
- Vishnu, D., and Dhandapani, B. (2020). Integration of *Cynodon Dactylon* and *Muraya Koenigii* Plant Extracts in Amino-Functionalised Silica-Coated Magnetic Nanoparticles as an Effective Sorbent for the Removal of Chromium(VI) Metal Pollutants. *IET Nanobiotechnol.* 14, 449–456. doi:10.1049/iet-nbt.2019.0313
- Wan, S., Wu, J., Zhou, S., Wang, R., Gao, B., and He, F. (2018). Enhanced Lead and Cadmium Removal Using Biochar-Supported Hydrated Manganese Oxide (HMO) Nanoparticles: Behavior and Mechanism. *Sci. Total Environ.* 616–617, 1298–1306. doi:10.1016/j.scitotenv.2017.10.188
- Wan, S., Qiu, L., Li, Y., Sun, J., Gao, B., He, F., et al. (2020). Accelerated Antimony and Copper Removal by Manganese Oxide Embedded in Biochar with Enlarged Pore Structure. *Chem. Eng. J.* 402, 126021. doi:10.1016/j.cej.2020.126021
- Wang, W., Zhou, J., Wei, D., Wan, H., Zheng, S., Xu, Z., et al. (2013). ZrO₂-functionalized Magnetic Mesoporous SiO₂ as Effective Phosphate Adsorbent. *J. Colloid Interface Sci.* 407, 442–449. doi:10.1016/j.jcis.2013.06.053
- Wang, S., Gao, B., Li, Y., Mosa, A., Zimmerman, A. R., Ma, L. Q., et al. (2015a). Manganese Oxide-Modified Biochars: Preparation, Characterization, and Sorption of Arsenate and Lead. *Bioresour. Technol.* 181, 13–17. doi:10.1016/j.biortech.2015.01.044
- Wang, W., Zhang, H., Zhang, L., Wan, H., Zheng, S., and Xu, Z. (2015b). Adsorptive Removal of Phosphate by Magnetic Fe₃O₄@C@ZrO₂. *Colloids Surfaces A Physicochem. Eng. Aspects* 469, 100–106. doi:10.1016/j.colsurfa.2015.01.002
- Wang, B., Yu, J., Liao, H., Zhu, W., Ding, P., and Zhou, J. (2020). Adsorption of Lead(II) from Aqueous Solution with High Efficiency by Hydrothermal Biochar Derived from Honey. *Int. J. Environ. Res. Public Health* 17, 3441. doi:10.3390/ijerph17103441
- Xia, W., and Liu, Y. (2021). Preparation of MnO₂ Modified Magnetic Graphitic Carbon Nitride Composite and its Adsorption toward Pb(II) in Waste Water. *Water Pract. Technol.* 16, 1498–1509. doi:10.2166/wpt.2021.059
- Xu, W., Song, Y., Dai, K., Sun, S., Liu, G., and Yao, J. (2018). Novel Ternary Nanohybrids of Tetraethylenepentamine and Graphene Oxide Decorated with MnFe₂O₄ Magnetic Nanoparticles for the Adsorption of Pb(II). *J. Hazard. Mater.* 358, 337–345. doi:10.1016/j.jhazmat.2018.06.071
- Yadav, P., Farnood, R., and Kumar, V. (2021). HMO-incorporated Electrospun Nanofiber Recyclable Membranes: Characterization and Adsorptive Performance for Pb(II) and As(V). *J. Environ. Chem. Eng.* 9, 106507. doi:10.1016/j.jece.2021.106507

- Yang, Y., Wang, J., Qian, X., Shan, Y., and Zhang, H. (2018). Aminopropyl-functionalized Mesoporous Carbon (APTMS-CMK-3) as Effective Phosphate Adsorbent. *Appl. Surf. Sci.* 427, 206–214. doi:10.1016/j.apsusc.2017.08.213
- Yin, H., Liu, F., Feng, X., Liu, M., Tan, W., and Qiu, G. (2011). Co²⁺-exchange Mechanism of Birnessite and its Application for the Removal of Pb²⁺ and As(III). *J. Hazard. Mater.* 196, 318–326. doi:10.1016/j.jhazmat.2011.09.027
- Zhang, L., Yang, X., and Wu, Y. (2015). Synthesis of Fe₃O₄@SiO₂@MnO₂ Composite Magnetic Submicrospheres as Adsorbent for Methyl Orange Decolouration. *Micro & Nano Lett.* 10, 12–15. doi:10.1049/mnl.2014.0555
- Zhang, H., Gu, L., Zhang, L., Zheng, S., Wan, H., Sun, J., et al. (2017a). Removal of Aqueous Pb(II) by Adsorption on Al₂O₃-Pillared Layered MnO₂. *Appl. Surf. Sci.* 406, 330–338. doi:10.1016/j.apsusc.2017.02.011
- Zhang, H., Wu, A., Fu, H., Zhang, L., Liu, H., Zheng, S., et al. (2017b). Efficient Removal of Pb(II) Ions Using Manganese Oxides: the Role of Crystal Structure. *RSC Adv.* 7, 41228–41240. doi:10.1039/C7RA05955H
- Zhang, H., Xu, F., Xue, J., Chen, S., Wang, J., and Yang, Y. (2020a). Enhanced Removal of Heavy Metal Ions from Aqueous Solution Using Manganese Dioxide-Loaded Biochar: Behaviour and Mechanism. *Sci. Rep.* 10, 6067. doi:10.1038/s41598-020-63000-z
- Zhang, H., Yang, Y., Yuan, L., Liu, G., Shan, Y., Qian, X., et al. (2020b). Improving the Lead Adsorption Performance of Mesoporous MnO₂ by Plasma Surface Modification. *Dwt* 189, 283–295. doi:10.5004/dwt.2020.25607
- Zhu, J., Baig, S. A., Sheng, T., Lou, Z., Wang, Z., and Xu, X. (2015). Fe₃O₄ and MnO₂ Assembled on Honeycomb Briquette Cinders (HBC) for Arsenic Removal from Aqueous Solutions. *J. Hazard. Mater.* 286, 220–228. doi:10.1016/j.jhazmat.2015.01.004
- Zhu, S., Lin, X., Dong, G., Yu, Y., Yu, H., Bian, D., et al. (2019). Valorization of Manganese-Containing Groundwater Treatment Sludge by Preparing Magnetic Adsorbent for Cu(II) Adsorption. *J. Environ. Manag.* 236, 446–454. doi:10.1016/j.jenvman.2019.01.117

Conflict of Interest: The authors declare that the research was conducted in the absence of any commercial or financial relationships that could be construed as a potential conflict of interest.

Publisher's Note: All claims expressed in this article are solely those of the authors and do not necessarily represent those of their affiliated organizations, or those of the publisher, the editors and the reviewers. Any product that may be evaluated in this article, or claim that may be made by its manufacturer, is not guaranteed or endorsed by the publisher.

Copyright © 2022 Zhang, Chen, Shan, Qian, Yang and Wang. This is an open-access article distributed under the terms of the Creative Commons Attribution License (CC BY). The use, distribution or reproduction in other forums is permitted, provided the original author(s) and the copyright owner(s) are credited and that the original publication in this journal is cited, in accordance with accepted academic practice. No use, distribution or reproduction is permitted which does not comply with these terms.



OPEN ACCESS

EDITED BY

Shihai Deng,
Xi'an Jiaotong University, China

REVIEWED BY

Zacharias Frontistis,
University of Western Macedonia,
Greece
Shaohua Wu,
Guangdong University of Petrochemical
Technology, China
Congwei Luo,
Shandong Jianzhu University, China

*CORRESPONDENCE

Zijun Dong,
dongzijun@szu.edu.cn

SPECIALTY SECTION

This article was submitted to Water and
Wastewater Management,
a section of the journal
Frontiers in Environmental Science

RECEIVED 02 August 2022

ACCEPTED 25 August 2022

PUBLISHED 15 September 2022

CITATION

Han Q, Dong W, Wang H, Yu B, Dong Z,
Li M, Xie L and Dai Z (2022),
Performance of ozonation on bisphenol
a degradation: Efficiency, mechanism
and toxicity control.
Front. Environ. Sci. 10:1009499.
doi: 10.3389/fenvs.2022.1009499

COPYRIGHT

© 2022 Han, Dong, Wang, Yu, Dong, Li,
Xie and Dai. This is an open-access
article distributed under the terms of the
Creative Commons Attribution License
(CC BY). The use, distribution or
reproduction in other forums is
permitted, provided the original
author(s) and the copyright owner(s) are
credited and that the original
publication in this journal is cited, in
accordance with accepted academic
practice. No use, distribution or
reproduction is permitted which does
not comply with these terms.

Performance of ozonation on bisphenol a degradation: Efficiency, mechanism and toxicity control

Qi Han^{1,2}, Wenyi Dong², Hongjie Wang², Boping Yu¹,
Zijun Dong^{3*}, Mu Li⁴, Linshen Xie¹ and Zhiguang Dai^{1,2}

¹Shenzhen Academy of Environmental Sciences, Shenzhen, China, ²School of Civil and Environmental Engineering, Harbin Institute of Technology (Shenzhen), Shenzhen, China, ³College of Civil and Transportation Engineering, the Underground Polis Academy, Shenzhen University, Shenzhen, Guangdong, China, ⁴Shenzhen Environmental Science and New Energy Laboratory, Tsinghua-Berkeley Shenzhen Institute, Tsinghua University, Shenzhen, China

In this study, the degradation of bisphenol A (BPA) by ozonation was studied systematically by investigating the effects of different factors, including ozone dosages (0.25–1.50 mg/L), temperatures (10–50°C), initial solution pH (3.0–11.0) and interfering ions. The reaction kinetics were analyzed at the same time. In addition, the generation of intermediates was analyzed and the possible mechanism was proposed by combining with the density functional theory (DFT) calculation. At last, the variation and controlling effect of toxicity was also evaluated. The results showed that ozonation had a stronger degrading ability of BPA (1.0 mg/L). A complete removal efficiency was obtained within 10 min when dosing only 1.0 mg/L ozone. The BPA degradation reactions were well fitted with pseudo-second-order kinetics and could well adapt with the wide range of pH (3.0–9.0), during which over 91% removal of BPA was achieved. The indirect pathway by $\bullet\text{OH}$ oxidation was proved mainly responsible for BPA degradation by the scavenging and electron paramagnetic resonance experiments. HCO_3^- , NH_4^+ and humic acid showed a certain inhibiting effect. Fe^{3+} and Cu^{2+} played a catalytic role on BPA degradation. The DFT calculation has identified that the active regions of BPA was focused at C6, C4, C5 and C1 in terms of radical and electrophilic attack. Thus, combining the results of DFT with GC/MS-MS detection, two degradation pathways of BPA were proposed. Toxicity evaluation showed that, due to the generation and accumulation of more toxic intermediates, values of T% had a sharp increase at initial stage. However, with ozone dosage increasing to 1.50 mg/L, the toxicity could be effectively controlled much lower (5%) than BPA itself (49%).

KEYWORDS

bisphenol A (BPA), ozonation, interfering ions, pathways, toxicity

Highlights

- Ozonation could effectively degrade BPA and control the toxicity of water samples.

- Only 1.0 mg/L of ozone was needed for completely removing of BPA (1.0 mg/L).
- Over 91% removal of BPA was achieved at a wide pH range of 3.0–9.0.
- BPA degradation by ozonation was promoted at the presence of PO_4^{3-} , Cu^{2+} and Fe^{3+} .
- The value of T% could increased significantly up to 68% at initial reaction stage.
- The increase of toxicity was due to the formation of more toxic intermediates.”

1 Introduction

Bisphenol A (2, 2-bis (4-hydroxyphenyl) propane) (BPA) is one of the most important raw material, which has been widely used in plastics and epoxy resins industry (Sharma and MishraDionysioukumar, 2015; Yang, 2015). BPA is also a typical endocrine disrupting chemical (EDC). Due to the strong chemical resistance and stable characteristics of BPA, its estrogenic activity can be exhibited at low concentration levels ($<1 \mu\text{g}/\text{m}^3$) (Wu, 2008). Toxicological data shows that BPA also has adverse effects on aquatic life, animals, and even human health (Ahmadi et al., 2016; Teppala et al., 2012; Bu and WuHeHuang, 2016; Han and Hong 2016). It can affect the brain development and behavioral differentiation of infants, children and adolescents by long-term exposure. Due to its widespread use and moderate water solubility (Hu et al., 2019), BPA could be easily discharged into industrial wastewater, river, lake, groundwater and other natural water bodies (Trojanowicz et al., 2020; Huang et al., 2012). Therefore, it is necessary to apply effective technologies to degrade BPA and control its biotoxicity.

At present, technologies for BPA degradation have included biological degradation, physical adsorption and advanced oxidation processes (AOPs), etc. Conventional biological (Zielin'ska et al., 2016; Ferro Orozco et al., 2013; Schröder, 2006) as well as physical-chemical treatment techniques (Bhatnagar and Anastopoulos, 2016) cannot satisfactorily remove BPA from water as well as reduce the biological toxicity. In order to conquer the limitations of conventional processes, a lot of AOPs have been developed, such as ozonation (Ahmad et al., 2015), photocatalysis (Reddy et al., 2018; Gao et al., 2020; Li et al., 2022; Luo et al., 2022), photoelectrocatalysis (He et al., 2017), Fenton/photo-Fenton (Xiao et al., 2019) and persulfates or sulfite based oxidation (Wu et al., 2018, 2021, 2022). However, due to the stability and catalytic efficiency of catalysts, photocatalytic oxidation was often restricted in application. In Fenton based oxidation process, the yield of sludge was high. In addition, severe reaction conditions (such as solution pH) were required to achieve stable degradation efficiency (Yang et al., 2016). In contrast, owing to the high oxidative potential of ozone

molecule itself (2.08 V) (Kusvuran and Yildirim, 2013) and produced hydroxyl radical ($\bullet\text{OH}$, 2.7 V) (Masten et al., 1994; Garoma et al., 2010), ozonation has been proved as an effective and widely applied method for treating refractory organic pollutants (Quan et al., 2020; Neyens and Baeyens, 2003). It also has the advantages of obvious treatment effect, easy engineering implementation, and easy popularization and application. However, the systematic studies of BPA degradation by ozonation were still limited. It is necessary to apply ozonation for degrading BPA from water.

In the current researches on BPA degradation, most of them have focused on the common influencing factors such as oxidant dosage, initial substrate concentration, pH, temperature, etc (Oguzie et al., 2020; Van Aken et al., 2019; Tay et al., 2012). Since BPA has been widely used in the production of electronic products, the wastewater often contained various complex components such as metal ions and buffer solvents, which were important parameters affecting degradation process. Therefore, it is necessary to investigate the influences of interfering ions in water on BPA degradation. At the same time, most studies have focused on the removal of BPA itself, researches involving the change and control effect of biological toxicity were still relatively insufficient. However, researches have found that more toxic intermediates might be generated during BPA degradation process (Reddy et al., 2018; He et al., 2017; Xiao et al., 2019), which further increased the biological toxicity of the treated wastewater. On the one hand, if the biological toxicity index was ignored, it would be unfavorable for the effective operations of the subsequent biological treatment process. On the other hand, it would pose a threat to the receiving water body and aquatic organisms if the wastewater was directly discharged. Thus, it is of essential to analysis the controlling effect of the toxicity during BPA degradation process. In addition, some possible pathways have been presumed only by identification of the products which was detected through liquid chromatography-mass spectrometry (LC-MS) or gas chromatography-mass spectrometry (GC-MS) [Kusvuran, 2013; Farre et al., 2005], lacking the verification by theoretical analysis and calculations. In recent years, quantum chemical calculation has been verified can explain the reaction from the point of thermodynamic energy. Thus, combining the theory with experiment could comprehensive predict and mutual verify the mechanisms of BPA degrading. In addition, the luminescent bacteria have the advantage of high sensitivity and simple operation during the process of toxicity detecting, which have been applied for testing the integrated and acute toxicity of the reaction samples (Dai et al., 2014; Grimme et al., 2010).

In this study, the performance of ozonation on BPA degradation was systematically investigated under different influencing factors, including ozone dosage, temperature,

initial solution pH and interfering ions. The organic intermediates were detected and identified by GC/MS-MS. The possible degradation pathways were proposed based on the products. At the same time, density functional theory (DFT) calculation was employed to analyze the intermediate products and BPA degradation pathways by ozonation. In addition, the variation and control effect of toxicity during BPA degradation was also analyzed.

2 Material and methods

2.1 Materials

All the chemicals were used as purchased without any further purification. BPA with a purity >99% was purchased from Sigma Aldrich and used as received. Humic acid, sodium phosphate, potassium nitrate, hydroxylammonium chloride, 5,5-dimethyl-1-pyrroline N-oxide (DMPO), methanol (HPLC grade) and dichloromethane (HPLC grade) were obtained from Aladdin Industrial Corporation (China). The freeze-dried bacteria *Vibrio fischeri* (*V. fischeri*, CS234) used for toxicity testing was obtained from SDIX (United States). All solutions were prepared with deionized and ultra pure water (Milli-Q Direct 8, United States). Ozone was produced from purified oxygen by an ozone generator (CF-G-3-10, QingDao GuoLin Co. Ltd., China).

2.2 Degradation experiments

Experiments were performed at room temperature ($25 \pm 1^\circ\text{C}$) in 1000 ml conical flasks with BPA solution of certain concentration. The desired solution pH was adjusted by hydrochloric acid or sodium hydroxide solution. The reaction temperature was controlled with ice bath or water bath. The saturated ozone solution was prepared by putting the ozone generated by the ozone generator into pure water for 2 h. According to the required ozone concentration (0.25, 0.50, 1.00, 1.50 mg/L), the calculated volume of ozone solution was added into the conical flask. Then, the conical flask was stirred slightly to ensure the uniform distribution of ozone in the system. The reaction was sampled periodically (0, 1, 2, 3, 5, 10 min) for 25 ml and quenched immediately by adding 30 μL 0.18 M hydroxylamine hydrochloride solution. The samples were then centrifuged (12,000 r/min) by a centrifugal machine (Centrifuge 5418, Eppendorf, Germany) for 5 min prior to subsequent analysis. All the experiments were carried out in duplicate.

2.3 Analytical methods

The concentration of BPA in the reaction solution was determined using a Ultra Performance Liquid

Chromatography (UPLC, Waters Acquity H-Class, United States) equipped with a TUV detector at the wavelength of 280 nm. The column was BEHC18 (1.7 \times 100 mm, 3.5 μm) with the temperature set at 30°C . The mobile phase, methanol/water (70/30, v/v), was run in an isocratic mode. The flow rate was maintained at 0.2 ml/min for all runs and the injection volume for UPLC analysis was 5 μL . A detection limit of quantitation was 1 $\mu\text{g/L}$ of BPA and a recovery rate of added standard was 91.5% obtained in this study.

The intermediates of BPA degradation were quantified using gas chromatography with mass spectrometry (GC/MS-MS, 7890A-5975C, Agilent, United States). A HP-5 column (5% phenylmethylpolysiloxane) with the dimension of 30 m \times 0.25 mm and 0.25 μm of film thickness was used to separate the organic species with the carrier gas of helium at a flow rate of 1 ml/min. The data for quantitative analysis was acquired in the electron impact mode (70 eV) with scanning in the range of 45–280 m/z. Concentration of dissolved ozone was determined by the indigo colorimetric method (APHA, 2005) using a spectrophotometer (Shimadzu 2450). The solution pH was measured by a portable digital pH meter throughout experiments (pHS-3B, Shanghai, China).

The toxicity of the sample was detected by a DeltaTox II Toxicity Detection System (DeltaTox[®] II, SDIX, United States), which method was according to the ISO standard based on the inhibition of bioluminescence emitted by the luminescent bacteria *V. fischeri* (Laws et al., 2000). In addition, the results of this method have been proved that could comprehensively reflect the toxicity of the water samples, which was caused by the target pollutants and their degradation intermediates (Ding et al., 2015). The luminescence intensities (X) of the water samples to the luminescent bacteria during the reaction were detected after contacting for 15 min. Then, the relative inhibitory rate ($T\%$), which could reflect the integrated toxicity of the water samples, was calculated for each sample relative to the control by Eqs. $T\% = (X_0 - X_t)/X_0 \times 100\%$ (where X_0 and X_t represents the luminescence intensity of the water sample to the luminescent bacteria at 0 and t reaction time, respectively).

2.4 Quantum chemical computation

The quantum chemical computation was carried out by using the density functional theory (DFT) with the Hirshfeld population analysis (Delley, 2000; Kusvuran et al., 2010). The molecule of BPA was initially subjected to geometry optimization relying on the B3LYP level. Then, exchange terms of Hartree, Fock and Becke were combined with the Lee-Yang-Parr correlation function. The standard 6-31G * basis was used at the same time. At last, in order to establish

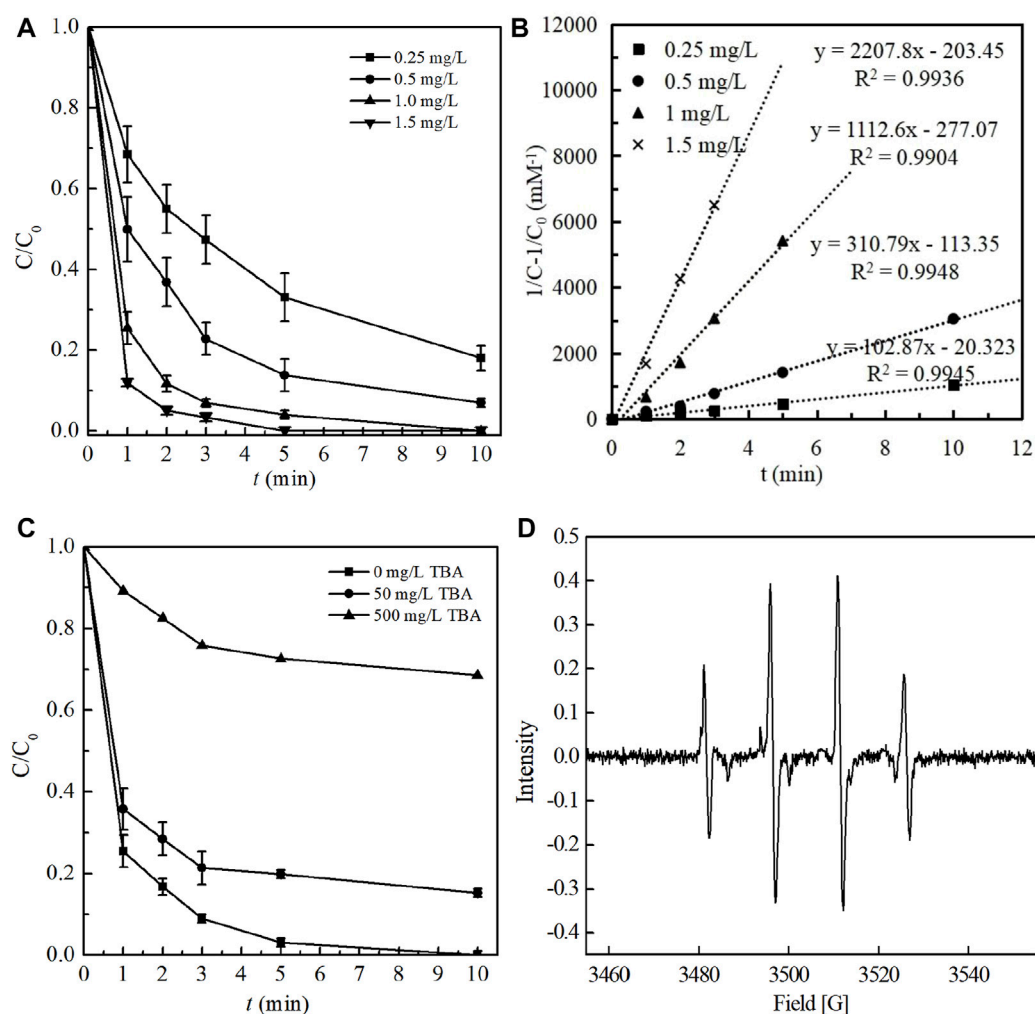


FIGURE 1

(A) Effect of ozone dosage on BPA degradation and (B) Kinetic fitting under different ozone dosage (Experimental conditions: temperature = $25 \pm 1^\circ\text{C}$; initial solution pH = 7.0 $[\text{BPA}]_0 = 1.00 \text{ mg/L}$; ozone dosage of 0.25, 0.5, 1.0, 1.5 mg/L); (C) The free radical scavenging experiments by adding TBA and (D) EPR spectra during ozonation system (Experimental conditions: temperature = $25 \pm 1^\circ\text{C}$; initial solution pH = 7.0 $[\text{BPA}]_0 = 1.00 \text{ mg/L}$; ozone dosage 1.0 mg/L; TBA concentration 0, 50, 500 mg/L).

the active sites as well as the local reactivity of the BPA molecular, the distribution of Frontier molecular orbitals and Fukui indices was determined.

3 Results and discussion

3.1 Performance of ozonation on BPA degradation

This study evaluated the performance of ozonation process for BPA degradation under different ozone dosages (0.25, 0.50, 1.00 and 1.50 mg/L) and the results were shown in Figure 1A. Other experimental parameters, including BPA

concentration, initial solution pH, temperature and oxidation reaction time, were respectively 1.00 mg/L, 7.0, $25 \pm 1^\circ\text{C}$ and 10 min. In general, as depicted in Figure 1A, BPA degradation by ozonation revealed a similar two-stage trend. A rapid degradation was obtained at the initial stage, which was followed by a relatively slow and gradually steady stage. When the dosage of ozone increased from 0.25 to 1.00 mg/L, the degradation efficiency of BPA increased significantly from 81.92% to 100%. As the ozone dosage continued to increase to 1.5 mg/L, the time required to completely degrade BPA was shortened from 10 to 5 min, showing ozonation a rapid and highly efficient method. It has been generally proved that there exist two pathways in the ozonation process for pollutants removal, i.e. the direct

oxidation pathway by molecular ozone (O_3 with a redox potential of 2.08 V) and the indirect one by newly generated radicals ($\bullet OH$ with a redox potential of 2.80 V) (Kusvuran et al., 2010; Wang Y. et al., 2022). Thus, with the increase of ozone dosage, the concentrations of O_3 and $\bullet OH$ in the reaction system increased, increasing the effective collision frequencies with BPA (in particular C=C bond connected by two benzene rings and C-O bond connected by benzene rings (Tay et al., 2012; Pan et al., 1984)) and further promoting the degradation efficiency of BPA.

At the same time, the reactions of BPA with O_3 and $\bullet OH$ during ozonation process could be expressed by the well established pseudo-second-order kinetics under different ozone dosages as follows (as depicted in Figure 3B):

$$-\frac{dC}{C^2} = k_{obs} dt \quad (1)$$

$$\frac{1}{C} - \frac{1}{C_0} = k_{obs} t \quad (2)$$

Where k_{obs} , which equals to $k_{OH}[\bullet OH] + k_{O_3}[O_3]$, is the pseudo-second-order rate constant for BPA degradation during ozonation; C_0 and C is respectively the initial concentration and the residual concentration of BPA at reaction time t . The results exhibited that k_{obs} increased linearly with ozone dosage ($R^2 > 0.98$) (Supplementary Figure S1). With the increase of ozone dosage from 0.25 to 1.50 mg/L, the value of k_{obs} was obviously promoted from 103.9 to 2207.8 $mM^{-1}min^{-1}$, revealing that ozone dosage played a critical role in the BPA degradation process by ozonation.

In order to verify the dominant active species responsible for BPA degradation, the free radical scavenging experiments were conducted by respectively adding 50 and 500 mg/L tert-Butanol (TBA), which is well known as the typical scavenger for $\bullet OH$. The molarity of TBA was 100 and 1000 folds more than BPA and the results were shown in Figure 1C. As the concentration of TBA was 0, 50 and 500 mg/L, the removal efficiencies of BPA after 10 min contacting reaction were respectively 100%, 84.75% and 31.45%, indicating that TBA could significantly inhibit the degradation of BPA in ozonation process. Thus, it could be concluded from the result that $\bullet OH$ was the predominant oxidation species and the indirect pathway was mainly responsible for BPA degradation in ozonation process in this study. The reason might be that in this study, ozone was added in the form of dissolved ozone water, which decomposed more violently and fully, and induced to more free radicals produced.

In addition, to further determine the free radical species produced in the ozonation system, a direct identification analysis was performed using electron paramagnetic resonance (EPR) spectroscopy, which method has been widely used in other similar researches (Wu et al., 2020; Wu et al., 2019). As the existence time of $\bullet OH$ in aqueous solution was very short, DMPO was used to capture $\bullet OH$ so as to form a stable

product DMPO-OH with a specific signal peak (Wang et al., 2022b). As seen from Figure 1D, four characteristic peaks with an intensity ratio of 1:2:2:1 was clearly achieved, corresponding to the characteristic peak of $\bullet OH$. The results further directly proved the existence of $\bullet OH$.

3.2 Effect of temperature on BPA degradation

The effect of reaction temperature on BPA degradation in ozonation process was investigated by varying the temperature in the range of 10–50°C, other operating conditions including BPA, ozone dosage and initial solution pH were respectively as 1 mg/L, 1 mg/L and 7.0. The degradation efficiencies of BPA and the reaction kinetics were illustrated in Figure 2.

As shown in Figure 2A, the removal efficiency of BPA increased sharply from 78.81% to 100% within 10 min as the temperature increased from 10 to 30°C, which reflected that elevating temperature in a certain range could bring an effective improvement of BPA degradation. This phenomenon has also be explained by other reported researches that the effective collision frequencies of oxidants (ozone molecular and newly formed $\bullet OH$) with BPA could be improved with the temperature rise, which further contributed to BPA degradation (Pan et al., 1984). This conclusion was also certificated by the values of k_{obs} , which significantly increased from 83.19 to 2564.4 $mM^{-1}min^{-1}$ as the temperature rose from 10 to 30°C. However, it was worth noting that excessive increase of the temperature would accelerate the decomposition rate of ozone and reduce the amount of oxidants in the solution (Qi et al., 2015), which was unfavorable to BPA degradation. Therefore, as the temperature was 40 and 50°C, the degradation efficiency of BPA was notably decreased to 86.02 and 55.81%. In addition, the corresponding reaction constant k_{obs} was respectively decreased to 136.86 and 26.19 $mM^{-1}min^{-1}$.

In general, the effect of temperature on BPA degradation by ozonation was primarily attributed to its impact on ozone stability and the effective collision frequencies between oxidants and pollutants. Moreover, it could be seen from the results that the optimal reaction temperatures of this system were 25 and 30°C, under which conditions a complete removal of BPA being both obtained. Considering that additional cost and instability generated from the process of temperature control, the room temperature ($25 \pm 1^\circ C$) was adopted in the subsequent experiments.

3.3 Effect of initial solution pH on BPA degradation

Figure 3 presented the effect of initial solution pH on BPA degradation and the reaction constant k_{obs} in the ozonation process. The experiments were carried out by changing the

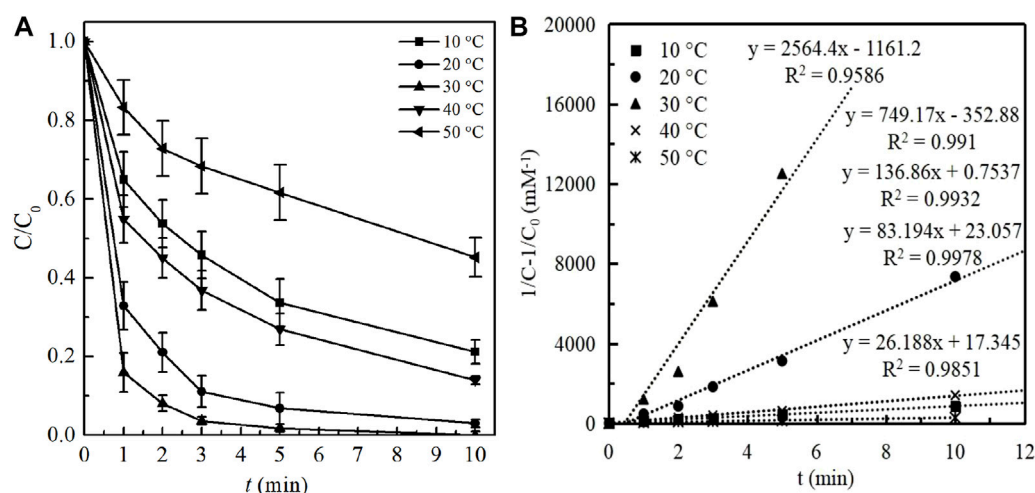


FIGURE 2

(A) Effect of reaction temperature on BPA degradation and (B) Kinetic fitting under different temperature. (Experimental conditions: $[\text{BPA}]_0 = 1.00 \text{ mg/L}$; ozone dosage 1.0 mg/L ; initial solution pH = 7.0; temperature = 10, 20, 30, 40, 50 °C).

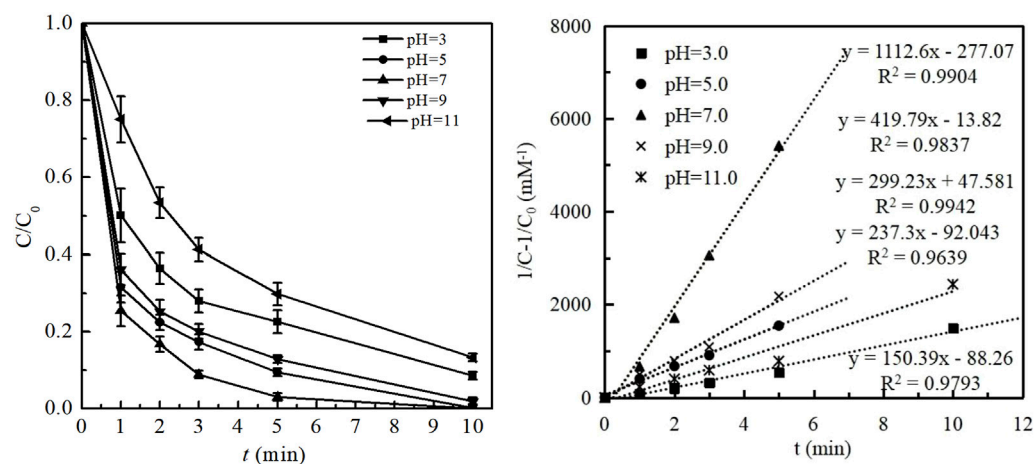


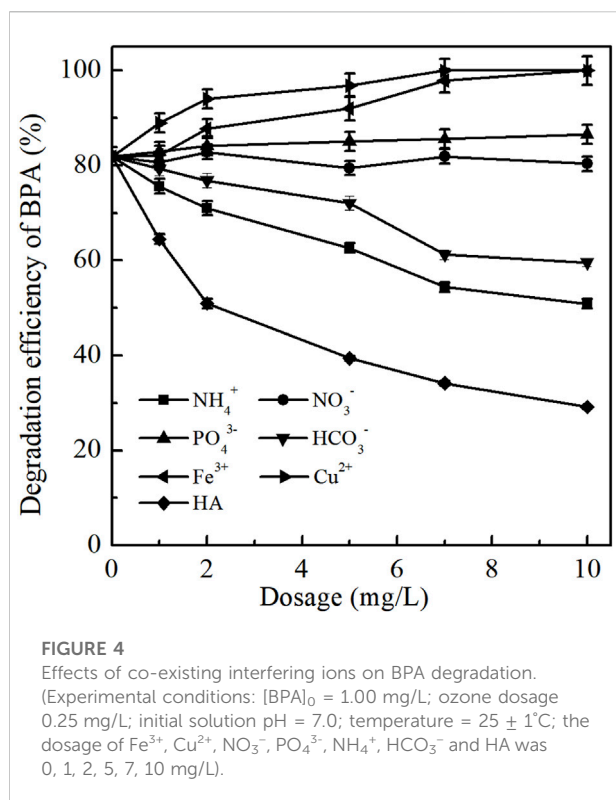
FIGURE 3

(A) Effect of initial solution pH on BPA degradation and (B) Kinetic fitting under different initial solution pH. (Experimental conditions: $[\text{BPA}]_0 = 1.00 \text{ mg/L}$; ozone dosage 1.0 mg/L ; initial solution pH = 3.0, 5.0, 7.0, 9.0, 11.0; temperature = $25 \pm 1^\circ\text{C}$).

initial solution pH in the range of 3.0–11.0, with other conditions of $[\text{BPA}]_0 = 1.00 \text{ mg/L}$; ozone dosage 1.0 mg/L ; temperature = $25 \pm 1^\circ\text{C}$.

Generally, as shown in Figure 3A, over 91% removal of BPA was obtained within 10 min in the ozonation process at a wide pH range of 3.0–9.0, indicating the strong adaptability of ozonation technology to initial solution pH. As the pH value increased from 3.0 to 5.0, the degradation efficiency of BPA

significantly promoted from 91.44% to 99.75%. Correspondingly, as shown in Figure 3B, the reaction constant k_{obs} increased from $150.39 \text{ mM}^{-1}\text{min}^{-1}$ to $299.23 \text{ mM}^{-1}\text{min}^{-1}$. The complete removal of BPA was obtained as the initial pH of 7.0 and the k_{obs} value of $1112.6 \text{ mM}^{-1}\text{min}^{-1}$. As the initial pH further increased to 9.0 and 11.0, the removal efficiency of BPA gradually decreased to 98.16% and 86.74%, respectively, with the value of k_{obs} decreasing to 419.79 and



$237.30 \text{ mM}^{-1}\text{min}^{-1}$. In general, the degradation efficiency of BPA by ozonation under acidic condition was much better than that under alkaline one.

Such pH dependence of degradation performance could be attributed to two reasons, (i) the pattern variation of BPA under different pH based on its pKa; (ii) the self-decomposition of ozone and the generation of $\bullet\text{OH}$ was dependent of solution pH (Zhang et al., 2020). BPA has two dissociation constants, i.e., $\text{pK}_{a1} = 9.6$ and $\text{pK}_{a2} = 10.2$. Thus, the predominant species is the undissociated BPA when pH at the range of 3.0–9.0. With the increase of solution pH ($\text{pH} > 9.6$), more and more BPA molecules existed in the species of BPA^- and BPA^{2-} , which would increase the electron density on the benzene ring and not be beneficial to BPA degradation via direct oxidation pathway. Additionally, it is known that the self-decomposition of ozone would be promoted with the increase of pH, resulting in the more generation of $\bullet\text{OH}$ (Gardoni et al., 2012; Sánchez-Polo et al., 2013) and accelerating BPA degradation by indirect oxidation pathway. As $\bullet\text{OH}$ has been proved as the dominant active species, it played a vital role in BPA degradation in this study. Thus, the removal efficiency of BPA increased with the increase of initial solution pH from 3.0 to 7.0. However, with the initial pH further increasing from 9.0 to 11.0, excessive $\bullet\text{OH}$ would collide with each other and be quenched, resulting in the decrease of available oxidants and the weaken of BPA degradation. In summary, the combined impacts of initial solution pH on BPA degradation by ozonation process

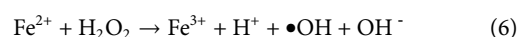
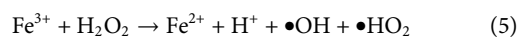
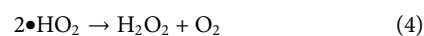
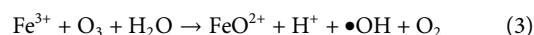
resulted in the effective removal of BPA at a wide pH range of 3.0–9.0. However, compared with the alkaline condition, the removal efficiency of BPA by ozonation was slightly higher under acidic condition, which indicated that as well as the indirect pathway by $\bullet\text{OH}$ oxidation, the direct one by ozone molecular oxidation also played an important role on BPA degradation. In this study, a complete removal of BPA was obtained when the initial pH was 7.0. In addition, increasing solution pH also improved the cost of operation. Therefore, the optimal initial pH of 7.0 without any adjustment was selected in this study from the economic strategy and practical point of view.

3.4 Effects of interfering ions on BPA degradation

Most wastewater normally contains metal ions, inorganic ions and organic matters which coexisting with organic pollutants. Thus, the effects of typical ions, including Fe^{3+} , Cu^{2+} , NO_3^- , PO_4^{3-} , NH_4^+ , HCO_3^- , humic acid (HA) (Tay et al., 2012), on the removal efficiencies of BPA by ozonation were carried out at the concentrations of 0–10 mg/L. Other experimental conditions were as follows $[BPA]_0 = 1.00$ mg/L; ozone dosage 0.25 mg/L; initial solution pH = 7.0; temperature = $25 \pm 1^\circ\text{C}$. The experimental results were presented in Figure 4. In general, with the increase dosing of interfering ions, the degradation efficiency of BPA by ozonation was significantly promoted by the metal ions (Fe^{3+} and Cu^{2+}), slightly enhanced by PO_4^{3-} , obviously weakened by NH_4^+ , HCO_3^- and HA, respectively.

3.4.1 Metal ions

The addition of Fe^{3+} and Cu^{2+} both promoted BPA degradation by ozonation, and the promoting effect was more obvious with the increase of their dosages. Taking Fe^{3+} as an example, when the dosage of Fe^{3+} increased from 0 to 10 mg/L, the degradation efficiency of BPA increased from 81.92% to 100% within 10 min. The reasons mainly include two aspects: on the one hand, the addition of Fe^{3+} might cause the formation of $\text{Fe}(\text{OH})_3$ colloid by hydrolysis of Fe^{3+} in water (Zeng et al., 2012), which has the role of coagulation and flocculation, so that part of BPA can be removed by adsorption. On the other hand, Fe^{3+} has a catalytic effect on ozone, which was conducive to the generation of $\bullet\text{OH}$, thereby strengthening the degradation of BPA by indirect oxidation pathway. The main reactions were shown in Eqs. 3–6 (Kang et al., 2018)



The effect mechanism of Cu^{2+} on BPA degradation in the ozonation process was similar with that of Fe^{3+} . Under neutral conditions, Cu^{2+} mainly existed in the form of $\text{Cu}(\text{OH})_2$ in aqueous solution. $\text{Cu}(\text{OH})_2$ also had coagulation function, and could catalyze ozone-induced chain reactions. In addition, the complete removal of BPA could be achieved within 5 min when Cu^{2+} was dosed, which indicated that the catalytic effect of Cu^{2+} on ozone was more obvious than that of Fe^{3+} .

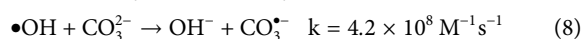
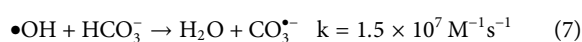
3.4.2 Inorganic ions

As seen from Figure 4, the presence of nitrate ion (NO_3^-) at concentration levels of 0–10 mg/L almost had no influence on BPA degradation in ozonation process. The average removal efficiency of BPA kept fluctuating in the ranges of 79.43%–82.84% before and after the dosing of NO_3^- . This might be due to that NO_3^- does not compete oxidants with BPA.

With the dosage of PO_4^{3-} increasing from 0 to 10 mg/L, the removal efficiency of BPA gradually increased from 81.92% to 86.56%. The addition of PO_4^{3-} could enhance the ionic strength of the reaction system, resulting in a positive ortho-salt effect and being beneficial to BPA degradation by ozonation. In addition, PO_4^{3-} might have a small promoting effect on the ozone decomposition, which facilitated the removal of BPA by generating superoxide radicals and promoting the generation of $\bullet\text{OH}$ (Graham et al., 2004).

The inhibition role of NH_4^+ on BPA degradation in ozonation process was mainly reflected in its reducibility and competition for ozone molecular and hydroxyl radical. Therefore, when the concentration of NH_4^+ increased from 0 to 10 mg/L, the degradation efficiency of BPA significantly decreased from 81.92% to 50.85%.

Meanwhile, the presence of HCO_3^- also inhibited the degradation of BPA by ozonation and this influence was enhanced with the increase of HCO_3^- concentration. The dosing of HCO_3^- could increase the alkalinity of the reaction system, which might increase the solution pH at a slight degree and further promote BPA degradation by indirect oxidation pathway. However, HCO_3^- was also a strong $\bullet\text{OH}$ inhibitor [40], which can capture $\bullet\text{OH}$ to form $\text{CO}_3^{\bullet-}$, thus adversely affecting the degradation efficiency of BPA [41]. The reactions were shown in Eqs. 7, 8.



3.4.3 Organic matter

There are a lot of complex organic compounds in water, many of which have unsaturated structures. Thus, the existence of these organic compounds might have obvious influence on the oxidation reactions. As shown in Figure 4, humic acid (HA) played a great inhibition role on BPA degradation in ozonation

process. With the increase of HA concentration from 0 to 10 mg/L, the removal efficiency of BPA significantly decreased from 81.92% to 29.17%. This was because HA is a natural macromolecular aromatic carboxylic acid with a large number of hydroxyl, carboxyl, and carbonyl functional groups attached to the ring, which was easier to react with the oxidants than BPA (Oguzie et al., 2020; Deborde et al., 2008).

3.5 Identification of products and proposition of mechanism

The identification of products during BPA degradation by ozonation was evaluated by GC/MS-MS. The main fragment ions (m/z) and abundance (%) of reaction products in comparison to the NIST data library are summarized in Table 1. From the GC/MS-MS analysis, nine identified intermediate compounds were 3-methyl-1,4-pentadiene, 1,4-pentadien-3-one, phenol, 1,4-dihydroxy benzene, 4-benzoquinone, cis-butenedioic acid, 4-isopropenylphenol, 4-isopropylphenol and (2E,4Z)-3-(2-(4-Hydroxyphenyl) propan-2-yl)hexa-2,4-dienedioic acid. Four of them have been identified in the earlier reported ozonation process [Kusvuran et al., 2013; Deborde et al., 2008], such as (2E,4Z)-3-(2-(4-Hydroxyphenyl) propan-2-yl)hexa-2,4-dienedioic acid, 4-isopropenylphenol, 4-benzoquinone and 1,4-dihydroxy benzene. The product of 4-isopropenylphenol has also been detected during photocatalytic (Kan et al., 2022; Li et al., 2022) and Fenton-like catalytic (Chu et al., 2021; Xu et al., 2021) degradation of BPA. In addition, phenol, 4-isopropylphenol and even short-chain acids have been found in the electrocatalytic degradation of BPA (Mohammad et al., 2021), which was also similar with this study.

In order to elucidate the degradation pathways of BPA by ozonation, theoretical DFT method was used, during which the regioselectivity for radicals attacking being focused. Supplementary Figure S2 shows the structure of BPA. From the calculations of the Hirshfeld charge distribution and Fukui function of carbon atoms (Table 2), it could be seen that the most positive parts of f -function are localized on C1 (C1'), C4 (C4') and C6 (C6'), which means para and ortho positions of hydroxyl are favourable reactive sites for electrophilic attack. While most positive parts of f^+ function are localized on C2 (C2'), C3 (C3'), C5 (C5') and C6 (C6'), which demonstrated that the C2, C3, C5 and C6 in BPA with high values are the most reactive sites for radical attacks. Then, values of the enthalpy (ΔH , kcal/mol) and the Gibbs free energy (ΔG , kcal/mol) for the reactions between BPA and radicals at SMD/B3LYP/6-311G** level of DFT calculation were calculated, as shown in Figure 5. The values of ΔG at C1, C4, C5, C6 were respectively -7.26 , -8.24 , -4.17 and -9.78 kcal/mol, which were all negative and showed all reactions being thermodynamically exothermic and feasible. In addition, as the ΔH between $\bullet\text{OH}$ and C6 (5.35 kcal/mol) was the lowest,

TABLE 1 Main fragment ions (m/z) and abundance (%) of reaction intermediates identified by GC/MS-MS.

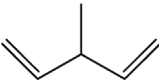
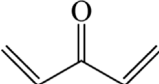
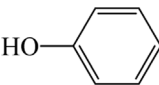
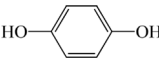

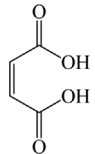
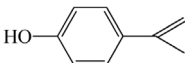
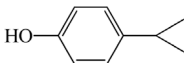
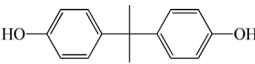
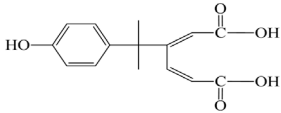
Number	Chemical name	Retention time (min)	Molecular formula	Molecular weight (m/z)	Molecular structure	Detected ions (m/z) (% abundance)
PN1	3-Methyl-1,4-pentadiene	4.4	C ₆ H ₁₀	82		82(22) 67(100) 55(28)
PN2	1,4-Pentadien-3-one	4.99	C ₅ H ₆ O	82		82(59) 81(41) 55(100)
PN3	Phenol	5.99	C ₆ H ₆ O	94		94(86) 66(47)
PN4	1,4-Dihydroxy benzene	6.12	C ₆ H ₆ O ₂	110		110(73) 99(65) 65(78) 55(100)
PN5	4-Benzoquinone	6.87	C ₆ H ₄ O ₂	108		108(100) 82(68) 55(55) 54(81)
PN6	cis-butenedioic acid	9.15	C ₄ H ₄ O ₄	116		99(39) 72(42) 68(54) 55(100)
PN7	4-Isopropenylphenol	12.86	C ₉ H ₁₀ O	134		134(100) 119(83) 91(52)
PN8	4-Isopropylphenol	15.0	C ₉ H ₁₂ O	136		136(32) 121(41) 103(100)
PN9	BPA	21.8	C ₁₅ H ₁₆ O ₂	228		228(21) 213(100) 119(27)
PN10	(2E,4Z)-3-(2-(4-hydroxyphenyl)propan-2-yl)hexa-2,4-dienedioic acid	24.4	C ₁₅ H ₁₆ O ₅	276		276(43) 119(86) 72(67)

TABLE 2 Hirshfield charge distribution and Fukui function of BPA.

No.atom (C)	Charge (0) (e/Å)	Charge (+1) (e/Å)	Charge (-1) (e/Å)	f ⁻	f ⁺	f ⁰
1	0.065	0.122	0.034	0.057	0.031	0.044
2	-0.071	-0.033	-0.141	0.038	0.070	0.054
3	-0.046	-0.007	-0.108	0.039	0.062	0.051
4	-0.012	0.042	-0.030	0.054	0.018	0.036
5	-0.048	-0.013	-0.114	0.035	0.066	0.051
6	-0.072	-0.017	-0.141	0.055	0.069	0.062
7	0.026	0.033	0.023	0.007	0.003	0.005
8	-0.086	-0.075	-0.093	0.011	0.007	0.009

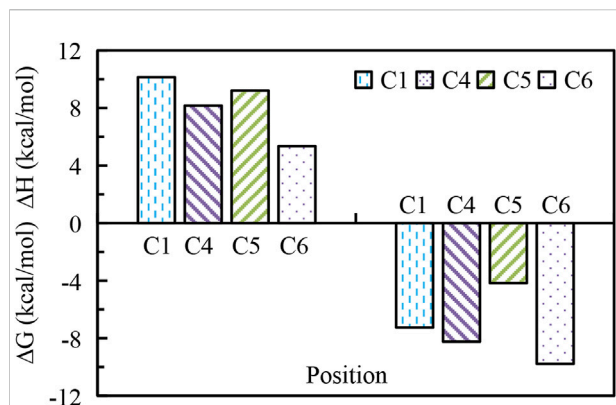


FIGURE 5

Values of ΔH and ΔG for the reactions between BPA and radicals by DFT calculation.

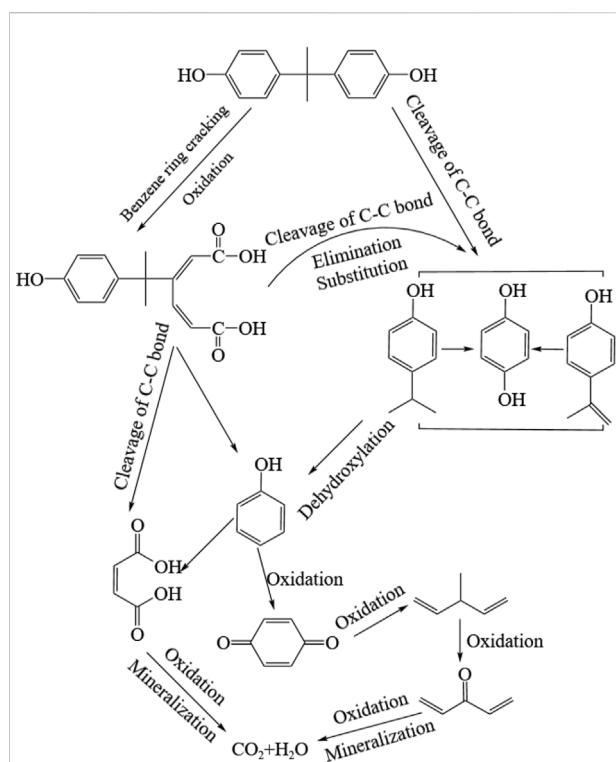


FIGURE 6

The proposed pathways of BPA degradation in ozonation process.

indicating that reactions on the C6 site is easier than on other positions. In general, the reactions between BPA and $\bullet OH$ were sorted from easy to difficult as $C6 > C4 > C5 > C1$.

By combining the results of GC/MS-MS detection and DFT evaluation, the degradation mechanism was proposed and

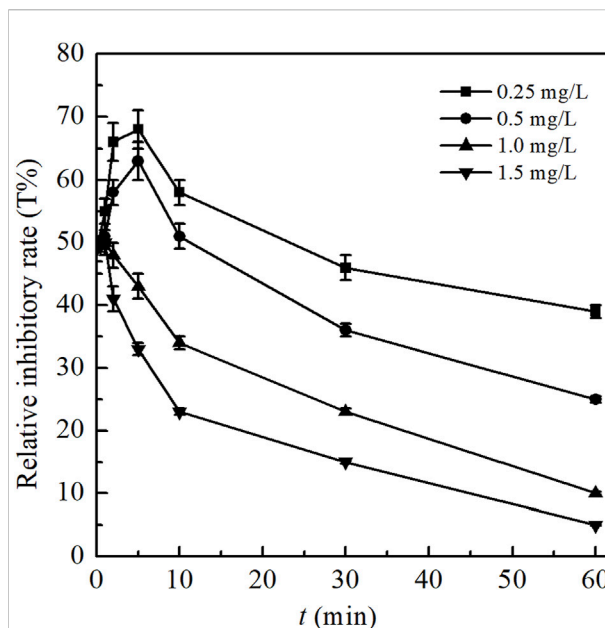


FIGURE 7

Toxicity evolution during BPA degradation by ozonation at different ozone dosages. (Experimental conditions: $[BPA]_0 = 1.00 \text{ mg/L}$; temperature = $25 \pm 1^\circ\text{C}$; initial solution pH = 7.0; O_3 dosage = 0.25, 0.50, 1.00, 1.50 mg/L).

presented in Figure 6. Due to the electrophilic character of BPA, ozone commonly reacts with aromatic rings by electrophilic substitution or 1,3-dipolar cycloaddition (Mvula and Sonntag, 2003; Peternel et al., 2012). However, due to the non-selectively and high-reactivity (10^8 – $10^{10} \text{ L}/(\text{mol}\cdot\text{s})$), the indirect $\bullet OH$ oxidation was chosen as the main pathway for BPA degradation by ozonation system. BPA could be easily attacked by $\bullet OH$ at the sites of C6 and C4 through addition, oxidation and cleavage of the C-C bonds to produce various intermediates then also began to react with these degradation intermediates containing double bonds in their chemical structures [Kusvuran et al., 2013; Wang et al., 2022].

Accordingly, the degradation of BPA by ozonation can be divided into two possible pathways related to the bonds broken. The first pathway was attacking the C-O bond of the benzene ring (C6) by the generated $\bullet OH$, through which the benzene ring was cracked and BPA was oxidized to form PN10. Then, PN10 was transformed into phenol (PN3) and cis-butenedioic acid (PN6) through the cleavage of C-C bond. PN3 was oxidized to PN5 (4-benzoquinone), which was further cracked and oxidized to short-chain products (PN1 and PN2) and even mineralized to CO_2 and H_2O . The second pathway of $\bullet OH$ oxidation started at the C4 site. The C-C bond connecting two benzene rings was attacked, by which the monobenzene ring products was formed (PN4, PN7 and PN8). These three intermediates could be mutual converted through the channels of the addition reactions or hydrogen extraction reactions. Then, they could

also be gradually degraded to PN3, PN5, PN1 and PN2 by a series reactions of dehydroxylation and oxidation. Finally, the products with small molecules were further oxidized and even mineralized into CO_2 and H_2O .

3.6 Variation and controlling effect of the toxicity

As one of the most important ecological parameters, the evolution of the toxicity during BPA degradation by ozonation was estimated on the basis of toxicity tests performed on the luminous bacteria, with which specific method has been explained in the Experimental Section (Freitas et al., 2017; Li et al., 2008). In the experiments, ozone dosages were varied between 0.25 and 1.50 mg/L. The other conditions of initial BPA concentration, temperature and the pH value were 1 mg/L, $25 \pm 1^\circ\text{C}$ and 7.0, respectively. During ozone contacting (0–60 min), the solution samples at different reaction times were orderly inoculated with the bacteria *V. fischeri*. The luminescence relative inhibitory rate (T%) was calculated and evaluated after 15 min. The results obtained were shown in Figure 7.

As can be observed in Figure 7, all the values of the relative inhibitory rate under different ozone dosages increased sharply at the initial stage of reactions, then gradually decreased and finally reached a steady state with the further degradation of BPA and its intermediates, which indicated the toxicity changes of the water samples. BPA is a toxic compound. Its initial bioluminescence inhibition without the presence of ozone was around 49%. Take ozone dosage of 0.25 mg/L as an example, the value of T% rapidly increased to the maximum 68% within 5 min reaction in ozonation process, indicating the significant increase of biotoxicity. This might be attributed to the generation and accumulation of more toxic intermediates of BPA, such as 4-isopropylphenol, cis-butenedioic acid, 4-benzoquinone, 1,4-dihydroxy benzene and phenol (as exhibited in Table 1). Toxicological data have shown that the values of LD50 for these above products were respectively 880, 400, 103, 320, and 530 mg/kg (oral dose, mouse), which were all much lower than that of BPA (4200 mg/kg, oral dose, mouse) and indicated the higher toxicity than BPA itself (Freitas et al., 2017). In addition, as shown in Supplementary Figure S2, the peak area of some intermediates (such as 4-isopropylphenol, 1,4-dihydroxy benzene and phenol) increased sharply to the maximum at the initial stage of the reactions and then gradually decreased as the degradation prolonged, which was consistent with the variation of the toxicity. Due to a series of effects such as ring opening, chain breaking and mineralization in the degradation process, intermediates were continuously oxidized or even mineralized into CO_2 and H_2O , resulting in the gradual reduction of the water samples' biotoxicity (Malik et al., 2020). Thus, the value of T% gradually decreased to 39% after 60 min reaction when dosing 0.25 mg/L of ozone. Similar

findings have been obtained by other researches (Alum et al., 2004; Bertanza et al., 2011; Kim et al., 2008), where more estrogenic intermediates were generated at the initial stage of BPA degradation. However, the level of estrogenicity decreased to below the initial level and subsequently became stable after long contact time and high inlet ozone concentration. It has been reported that more than 98% of the estrogenicity of BPA (initial concentration of 0.10 mg/L) was removed by 1.4 mg/L ozone.

It can also be concluded from Figure 7 that the toxicity of the treated water samples could be effectively controlled with the increase of the ozone dosage. When the dosing of ozone increased from 0.25 to 1.50 mg/L, the maximum values of the relative inhibitory rate obviously decreased from 68% (at 5 min) to 50% (at 1 min), indicating the less formations of more toxic intermediates and less required time for their accumulation. In addition, after reaction for 60 min, the values of T% were significantly decreased from 39% to 5%, which were all below the initial T% of BPA (49%). The complete removal of BPA was achieved when the ozone dosage increased to 1.0 and 1.5 mg/L respectively within 10 and 5 min, which means that the toxic products could be further effectively degraded. From the results obtained, it could be deduced that ozonation is a promising technology for effectively controlling the toxicity of the water samples as well as significantly degrading BPA.

4 Conclusion

The degradation of BPA by ozonation was systematically investigated in this study, and the major conclusions are summarized as follows:

- 1) Ozonation was an effective method for BPA degradation. By dosing 1.0 mg/L of ozone, BPA (1.0 mg/L) was completely removed within 10 min under pH of 7.0 and temperature at $25 \pm 1^\circ\text{C}$. The degradation reactions were well fitted with the pseudo-second-order kinetics and $\bullet\text{OH}$ was proved as the predominant oxidation species.
- 2) Ozonation could effectively adapt the temperature and pH of the reaction solution. A complete removal of BPA was achieved at the optimal reaction temperatures range of $25\text{--}30^\circ\text{C}$. In addition, over 91% of BPA could be removed at a wide pH range of 3.0–9.0.
- 3) The presence of PO_4^{3-} , Fe^{3+} and Cu^{2+} were beneficial to the degradation of BPA, which played the role of ionic enhancer, catalyst, flocculant, etc. However, by competing the reaction active species, BPA degradation was inhibited at the presence of $\bullet\text{OH}$ inhibitors (HCO_3^-), organic compounds (HA) and reducing substance (NH_4^+).
- 4) Results of the DFT calculation revealed that the reaction sites between BPA and $\bullet\text{OH}$ were sorted from easy to difficult as $\text{C6} > \text{C4} > \text{C5} > \text{C1}$.
- 5) The biotoxicity of water samples increased first and then decreased with the reaction time, which was caused by the

generation and accumulation of more toxic intermediates. However, as dosing 1.50 mg/L ozone, the values of T% could be effectively controlled at 5% after 60 min reactions.

Data availability statement

The original contributions presented in the study are included in the article/Supplementary Material, further inquiries can be directed to the corresponding author.

Author contributions

QH performed the data analyses, wrote and revised the manuscript; WD contributed to the conception of the study; HW performed the experiments; BY helped perform the analysis with constructive discussions; PL contributed to the conception of the study and contributed significantly to analysis and manuscript preparation; LX helped perform the revised the manuscript; ZD helped perform the experiments and analysis. All authors have read and agreed to the published version of the manuscript.

Funding

This work was supported by the Project of Shenzhen Science and Technology Innovation Committee (No. KCXFZ202002011006362) and the National Natural Science Foundation of China (Grant No.4217070174).

References

- Ahmad, N. A., Yuzir, M. A., Yong, E. L., Abdullah, N., and Salim, M. R. (2015). Removal of bisphenol A (BPA) in surface water by ozone oxidation process. *Appl. Mech. Mater.* 735, 210–214. doi:10.4028/www.scientific.net/AMM.735.210
- Ahmadi, M., Rahmani, H., Takdastan, A., Jaafarzadeh, N., and Mostoufi, A. (2016). A novel catalytic process for degradation of bisphenol A from aqueous solutions: A synergistic effect of nano-Fe₃O₄@alg-Fe on O₃/H₂O₂. *Process Saf. Environ. Prot.* 104, 413–421. doi:10.1016/j.psep.2016.09.008
- Alum, A., Yoon, Y., Westerhoff, P., and Abbaszadegan, M. (2004). Oxidation of bisphenol A, 17-estradiol, and 17-ethynyl estradiol and byproduct estrogenicity. *Environ. Toxicol.* 19, 257–264. doi:10.1002/tox.20018
- APHA (2005). *Standard methods for the examination of water and wastewater*. 21 th Ed. Washington D.C.
- Bertanza, G., Pedrazzani, R., Dal Grande, M., Papa, M., Zambarda, V., Montani, C., et al. (2011). Effect of biological and chemical oxidation on the removal of estrogenic compounds (NP and BPA) from wastewater: An integrated assessment procedure. *Water Res.* 45, 2473–2484. doi:10.1016/j.watres.2011.01.026
- Bhatnagar, A., and Anastopoulos, I. J. C. (2016). Adsorptive removal of bisphenol A (BPA) from aqueous solution: A review. *Chemosphere* 168, 885–902. doi:10.1016/j.chemosphere.2016.10.121
- Bu, X., and WuHeHuang, X. G. J. (2016). Novel adaptive neural control design for a constrained flexible air-breathing hypersonic vehicle based on actuator compensation. *Acta Astronaut.* 120, 75–86. doi:10.1016/j.actaastro.2015.12.004
- Chu, J., Kang, J., Seong, J., and Chang, G. (2021). Bisphenol A degradation using waste antiviral copper film with enhanced sono-Fenton-like catalytic oxidation. *Chemosphere* 276, 130218. doi:10.1016/j.chemosphere.2021.130218
- Dai, Q., Wang, J., Yu, J., Chen, J., and Chen, J. (2014). Catalytic ozonation for the degradation of acetylsalicylic acid in aqueous solution by magnetic CeO₂ nanometer catalyst particles. *Appl. Catal. B Environ.* 144, 686–693. doi:10.1016/j.apcatb.2013.05.072
- Deborde, M., Rabouan, S., Mazellier, P., Duguet, J. P., and Legube, B. (2008). Oxidation of bisphenol A by ozone in aqueous solution. *Water Res.* 42, 4299–4308. doi:10.1016/j.watres.2008.07.015
- Delley, B. (2000). From molecules to solids with the DMol₃ approach. *J. Chem. Phys.* 113, 7756–7764. doi:10.1063/1.1316015
- Ding, S., Wu, J., Zhang, M., Lu, H., Mahmood, Q., and Zheng, P. (2015). Acute toxicity assessment of ANAMMOX substrates and antibiotics by luminescent bacteria test. *Chemosphere* 140, 174–183. doi:10.1016/j.chemosphere.2015.03.057
- Farre, M. J., Franch, M. I., Malato, S., Aylon, J. A., Peral, J., and Domenech, X. (2005). Degradation of some biorecalcitrant pesticides by homogeneous and heterogeneous photocatalytic ozonation. *Chemosphere* 58, 1127–1133. doi:10.1016/j.chemosphere.2004.09.064
- Ferro Orozco, A. M., Lobo, C. C., Contreras, E. M., and Zaritzky, N. E. (2013). Biodegradation of bisphenol-A (BPA) in activated sludge batch reactors: Analysis of the acclimation process. *Int. Biodeterior. Biodegrad.* 85, 392–399. doi:10.1016/j.ibiod.2013.09.005
- Freitas, E. D., Bubna, G., Brugnari, T., Kato, C., Noll, M., Rauen, T., et al. (2017). Removal of bisphenol A by laccases from *Pleurotus ostreatus* and *Pleurotus pulmonarius* and evaluation of ecotoxicity of degradation products by laccases from *Pleurotus ostreatus* and *Pleurotus pulmonarius*. *Chem. Eng. J.* 330, 1361–1369. doi:10.1016/j.cej.2017.08.051
- Gao, J., Luo, C., GanGan, L., Wu, D., Tan, F., Cheng, X., et al. (2020). A comparative study of UV/H₂O₂ and UV/PDS for the degradation of micro-

Acknowledgments

We acknowledge all the authors for their contributions. We sincerely thank the reviewers and the editor for their effort to review this manuscript.

Conflict of interest

The authors declare that the research was conducted in the absence of any commercial or financial relationships that could be construed as a potential conflict of interest.

Publisher's note

All claims expressed in this article are solely those of the authors and do not necessarily represent those of their affiliated organizations, or those of the publisher, the editors and the reviewers. Any product that may be evaluated in this article, or claim that may be made by its manufacturer, is not guaranteed or endorsed by the publisher.

Supplementary material

The Supplementary Material for this article can be found online at: <https://www.frontiersin.org/articles/10.3389/fenvs.2022.1009499/full#supplementary-material>

- pollutants: Kinetics and effect of water matrix. *Environ. Sci. Pollut. Res.* 27, 24531–24541. doi:10.1007/s11356-020-08794-1
- Gardoni, D., Vailati, A., and Canziani, R. (2012). Decay of ozone in water: A review. *Ozone Sci. Eng.* 34 (4), 233–242. doi:10.1080/01919512.2012.686354
- Garoma, T., Matsumoto, S. A., Wu, Y., and Klinger, R. (2010). Removal of bisphenol A and its reaction-intermediates from aqueous solution by ozonation. *Ozone Sci. Eng.* 32, 338–343. doi:10.1080/01919512.2010.508484
- Graham, N., Jiang, C. C., Li, X. Z., Jiang, J. Q., and Ma, J. (2004). The influence of pH on the degradation of phenol and chlorophenols by potassium ferrate. *Chemosphere* 56, 949–956. doi:10.1016/j.chemosphere.2004.04.060
- Grimme, S., Antony, J., Ehrlich, S., and Krieg, H. (2010). A consistent and accurate *ab initio* parametrization of density functional dispersion correction (DFT-D) for the 94 elements H-Pu. *J. Chem. Phys.* 132, 154104. doi:10.1063/1.3382344
- Han, C., and Hong, Y. C. (2016). Bisphenol A, hypertension, and cardiovascular diseases: Epidemiological, laboratory, and clinical trial evidence. *Curr. Hypertens. Rep.* 18, 11. doi:10.1007/s11906-015-0617-2
- He, L., Liu, H., Lv, B., Liu, P., and Lin, B. (2017). Visible-light-driven photocatalytic performance of nanohybrid incorporating nickel ions into the tetratitanate interlayer. *Vacuum* 138, 64–69. doi:10.1016/j.vacuum.2017.01.024
- Hu, Y., Zhu, Q., Yan, X., Liao, C., and Jiang, G. (2019). Occurrence, fate and risk assessment of BPA and its substituents in wastewater treatment plant: A review. *Environ. Res.* 178, 108732. doi:10.1016/j.envres.2019.108732
- Huang, Y. Q., Wong, C. K., Zheng, J. S., Bouwman, H., Barra, R., Wahlstrom, B., et al. (2012). Bisphenol A (BPA) in China: A review of sources, environmental levels, and potential human health impacts. *Environ. Int.* 42, 91–99. doi:10.1016/j.envint.2011.04.010
- Huang, Y., Yang, T., Liang, M., Wang, Y., Xu, Z., Zhang, D., et al. (2019). Ni-Fe layered double hydroxides catalyzed ozonation of synthetic wastewater containing Bisphenol A and municipal secondary effluent. *Chemosphere* 235, 143–152. doi:10.1016/j.chemosphere.2019.06.162
- Kan, L., Chang, C., Wang, Q., and Wang, X. (2022). Glycol assisted splitting BiOIO₃ into plasmonic bismuth coupled with BiOI co-modified Bi₂WO₆ (BiOI/Bi₂WO₆) to form indirect Z-scheme heterojunction for efficient photocatalytic degradation of BPA. *Sep. Purif. Technol.* 15, 121537. doi:10.1016/j.seppur.2022.121537
- Kang, Y. M., Kim, M. K., and Zoh, K. D. (2018). Effect of nitrate, carbonate/bicarbonate, humic acid, and H₂O₂ on the kinetics and degradation mechanism of Bisphenol-A during UV photolysis. *Chemosphere* 204, 148–155. doi:10.1016/j.chemosphere.2018.04.015
- Kim, S.-E., Park, N.-S., Yamada, H., and Tsuno, H. (2008). Modeling of decomposition characteristics of estrogenic chemicals during ozonation. *Environ. Technol.* 29, 287–296. doi:10.1080/09593330802099643
- Kusvuran, E., Gulnaz, O., Samil, A., and Erbil, M. (2010). Detection of double bond-ozone stoichiometry by an iodimetric method during ozonation processes. *J. Hazard. Mat.* 175, 410–416. doi:10.1016/j.jhazmat.2009.10.021
- Kusvuran, E., and Yildirim, D. (2013). Degradation of bisphenol A by ozonation and determination of degradation intermediates by gas chromatography-mass spectrometry and liquid chromatography-mass spectrometry. *Chem. Eng. J.* 220, 6–14. doi:10.1016/j.cej.2013.01.064
- Laws, S. C., Carey, S. A., Ferrell, J. M., Bodman, G. J., and Cooper, R. L. (2000). Estrogenic activity of octylphenol, nonylphenol, bisphenol A and methoxychlor in rats. *Toxicol. Sci.* 54, 154–167. doi:10.1093/toxsci/54.1.154
- Li, C., Li, X., Graham, N., and Gao, N. (2008). The aqueous degradation of bisphenol A and steroid estrogens by ferrate. *Water Res.* 42, 109–120. doi:10.1016/j.watres.2007.07.023
- Li, Z., Luo, C., Tan, F., Wu, D., Zhai, X., Wang, S., et al. (2022). UV light irradiation combined with nitrate for degradation of bisphenol A: Kinetics, transformation pathways, and acute toxicity assessment. *Environ. Sci. Water Res. Technol.* 8, 586–596. doi:10.1039/d1ew00796c
- Luo, C., Wang, S., Wu, D., Cheng, X., and Ren, H. (2022). UV/Nitrate photocatalysis for degradation of Methylene blue in wastewater: Kinetics, transformation products, and toxicity assessment. *Environ. Technol. Innovation* 25, 102198. doi:10.1016/j.eti.2021.102198
- Malik, S. N., Ghosh, P. C., Vaidya, A. N., and Mudliar, S. N. (2020). Ozone pretreatment of biometanated distillery wastewater in a semi batch reactor: Mapping pretreatment efficiency in terms of COD, color, toxicity and biohydrogen generation. *Biofuels* 11 (7), 801–809. doi:10.1080/17597269.2017.1416521
- Masten, S. J., Davies, S. H. R., Luo, C., Tan, F., Wu, D., Zhai, X., et al. (1994). The use of LiUV light irradiation combined with nitrate for degradation of bisphenol A: Kinetics, transformation pathways, and acute toxicity assessment. *Environ. Sci. Water Res. Technol.* 8, 586–596. doi:10.1039/d1ew00796c
- Mohammad, R., Amin, A., Abdollah, D., Amir, S., Davood, N., Mohammad, K., et al. (2021). Enhanced electrocatalytic degradation of bisphenol A by graphite/β-PbO₂ anode in a three-dimensional electrochemical reactor. *J. Environ. Chem. Eng.* 9 (5), 106072. doi:10.1016/j.jece.2021.106072
- Mvula, E., and Von Sonntag, C. (2003). Ozonolysis of phenols in aqueous solution. *Org. Biomol. Chem.* 1, 1749–1756. doi:10.1039/B301824P
- Neyens, E., and Baeyens, J. (2003). A review of classic Fenton's peroxidation as an advanced oxidation technique. *J. Hazard. Mat.* 98, 33–50. doi:10.1016/S0304-3894(02)00282-0
- Oguzie, K. L., Qiao, M., Zhao, X., Oguzie, E. E., Njoku, V. O., and Obodo, G. A. (2020). Oxidative degradation of Bisphenol A in aqueous solution using cobalt ion-activated peroxymonosulfate. *J. Mol. Liq.* 313, 113569. doi:10.1016/j.molliq.2020.113569
- Pan, G. Y., Chen, C. L., Chang, H. M., and Gratzl, J. S. (1984). Studies on ozone bleaching. I. The effect of pH, temperature, buffer systems and heavy metal-ions on stability of ozone in aqueous solution. *J. Wood Chem. Technol.* 4, 367–387. doi:10.1080/02773818408070655
- Peternel, I., Koprivanac, N., and Grcic, I. (2012). Mineralization of p-chlorophenol in water solution by AOPs based on UV irradiation. *Environ. Technol.* 33, 27–36. doi:10.1080/09593330.2010.504233
- Qi, F., Chu, W., and Xu, B. (2015). Ozonation of phenacetin in associated with a magnetic catalyst CuFe₂O₄: The reaction and transformation. *Chem. Eng. J.* 262, 552–562. doi:10.1016/j.cej.2014.09.068
- Quan, X., Hu, R., Chang, H., Tang, X., Huang, X., Cheng, C., et al. (2020). Enhancing microalgae growth and landfill leachate treatment through ozonation. *J. Clean. Prod.* 248, 119182. doi:10.1016/j.jclepro.2019.119182
- Reddy, P. V. L., Kim, K. H., Kavitha, B., Kumar, V., Raza, N., and Kalagara, S. J. J. o. E. M. (2018). Photocatalytic degradation of bisphenol A in aqueous media: A review. *J. Environ. Manag.* 213, 189–205. doi:10.1016/j.jenvman.2018.02.059
- Sahoo, N., Pakshirajan, K., and Ghosh, P. (2010). Enhancing the biodegradation of 4-chlorophenol by *Arthrobacter chlorophenolicus* A6 via medium development. *Int. Biodeterior. Biodegrad.* 64, 474–480. doi:10.1016/j.ibiod.2010.05.008
- Sánchez-Polo, M., Ocampo-Pérez, R., Rivera-Utrilla, J., and Mota, A. J. (2013). Comparative study of the photodegradation of bisphenol A by HO, SO₄⁻ and CO₃⁻/HCO₃⁻ radicals in aqueous phase. *Sci. Total Environ.* 463, 423–431. doi:10.1016/j.scitotenv.2013.06.012
- Schröder, H. F. (2006). The elimination of the endocrine disruptors 4-nonylphenol and bisphenol A during wastewater treatment - comparison of conventional and membrane assisted biological wastewater treatment followed by an ozone treatment. *Water Pract. Technol.* 1. doi:10.2166/wpt.2006.060
- Sharma, J., and MishraDionysiuKumar, I. M. D. V. (2015). Oxidative removal of Bisphenol A by UV-C/peroxymonosulfate (PMS): Kinetics, influence of co-existing chemicals and degradation pathway. *Chem. Eng. J.* 276, 193–204. doi:10.1016/j.cej.2015.04.021
- Takdastan, A., Kakavandi, B., Azizi, M., and Golshan, M. J. C. E. J. (2018). Efficient activation of peroxymonosulfate by using ferrocenic oxide supported on carbon/UV/us system: A new approach into catalytic degradation of bisphenol A. *Chem. Eng. J.* 331, 729–743. doi:10.1016/j.cej.2017.09.021
- Tay, K. S., Abd Rahman, N., and Abas, M. R. B. (2012). Degradation of bisphenol A by ozonation: Rate constants, influence of inorganic anions, and by-products. *Maejo Int. J. Sci. Technol.* 6 (01), 77–94. doi:10.14456/mijst.2012.7
- Teppala, S., Madhavan, S., and Shankar, A. (2012). Bisphenol A and metabolic syndrome: Results from nhanes. *Int. J. Endocrinol.* 1–5. doi:10.1155/2012/598180
- Trojanowicz, M., Bojanowska-Czajka, A., Szreder, T., Mczyńska-Wielgosz, S., Nichipor, H. J. C. E. J., Fornal, E., et al. (2020). Application of ionizing radiation for removal of endocrine disruptor bisphenol A from waters and wastewaters. *Chem. Eng. J.* 403, 126169. doi:10.1016/j.cej.2020.126169
- Van Aken, P., Lambert, N., Van den Broeck, R., Degreè, J., and Dewil, R. (2019). Advances in ozonation and biodegradation processes to enhance chlorophenol abatement in multisubstrate wastewaters: A review. *Environ. Sci. Water Res. Technol.* 5, 444–481. doi:10.1039/C8EW00562A
- Wang, L., Qi, C., Lu, Y., Arowo, M., and Shao, L. (2022b). Degradation of Bisphenol A by ozonation in a rotating packed bed: Modeling by response surface methodology and artificial neural network. *Chemosphere* 286, 131702. doi:10.1016/j.chemosphere.2021.131702
- Wang, Y., Lin, Y., Yang, C., Wu, S., Fu, X., and Li, X. (2022a). Calcination temperature regulates non-radical pathways of peroxymonosulfate activation via carbon catalysts doped by iron and nitrogen. *Chem. Eng. J.* 451, 138468. doi:10.1016/j.cej.2022.138468

- Wu, C. (2008). Decolorization of C.I. Reactive red 2 in O_3 , fenton-like and O_3 /Fenton-like hybrid systems. *Dyes Pigments* 77, 24–30. doi:10.1016/j.dyepig.2007.03.002
- Wu, S., Li, H., Li, X., He, H., and Yang, C. (2018). Performances and mechanisms of efficient degradation of atrazine using peroxymonosulfate and ferrate as oxidants. *Chem. Eng. J.* 353, 533–541. doi:10.1016/j.cej.2018.06.133
- Wu, S., Lin, Y., Yang, C., Du, C., Teng, Q., Ma, Y., et al. (2019). Enhanced activation of peroxymonosulfate by $LaFeO_3$ perovskite supported on Al_2O_3 for degradation of organic pollutants. *Chemosphere* 237, 124478. doi:10.1016/j.chemosphere.2019.124478
- Wu, S., Liu, H., Yang, C., Li, X., Lin, Y., Yin, K., et al. (2020). High-performance porous carbon catalysts doped by iron and nitrogen for degradation of bisphenol F via peroxymonosulfate activation. *Chem. Eng. J.* 392, 123683. doi:10.1016/j.cej.2019.123683
- Wu, S., Shen, L., Lin, Y., Yin, K., and Yang, C. (2021). Sulfite-based advanced oxidation and reduction processes for water treatment. *Chem. Eng. J.* 414 (15), 128872. doi:10.1016/j.cej.2021.128872
- Wu, S., Yang, C., Lin, Y., and Cheng, J. (2022). Efficient degradation of tetracycline by singlet oxygen-dominated peroxymonosulfate activation with magnetic nitrogen-doped porous carbon. *J. Environ. Sci.* 115, 330–340. doi:10.1016/j.jes.2021.08.002
- Xiao, K., Liang, H., Chen, S., Yang, B., Zhang, J., and Li, J. J. C. (2019). Enhanced photoelectrocatalytic degradation of bisphenol A and simultaneous production of hydrogen peroxide in saline wastewater treatment. *Chemosphere* 222, 141–148. doi:10.1016/j.chemosphere.2019.01.109
- Xu, S., Zhang, Y., Tang, R., Zhang, X., Zhen, H., and Han, Q. (2021). Enhancing Fenton-like catalytic efficiency of Bi_2WO_6 by iodine doping for pollutant degradation. *Sep. Purif. Technol.* 277 (15), 119447. doi:10.1016/j.seppur.2021.119447
- Yang, C. W. (2015). Degradation of bisphenol A using electrochemical assistant $Fe(II)$ -activated peroxydisulfate process. *Water Sci. Eng.* 8, 139–144. doi:10.1016/j.wse.2015.04.002
- Yang, Y., Guo, H., Zhang, Y., Deng, Q., and Zhang, J. (2016). Degradation of bisphenol A using ozone/persulfate process: Kinetics and mechanism. *Water Air Soil Pollut.* 227, 53. doi:10.1007/s11270-016-2746-x
- Zeng, Z., Zou, H., Li, X., Sun, B., Chen, J., and Shao, L. (2012). Ozonation of phenol with $O_3/Fe(II)$ in acidic environment in a rotating packed bed. *Ind. Eng. Chem. Res.* 51, 10509–10516. doi:10.1021/ie300476d
- Zhang, H., He, Y., Lai, L., Yao, G., and Lai, B. (2020). Catalytic ozonation of Bisphenol A in aqueous solution by Fe_3O_4 - MnO_2 magnetic composites: Performance, transformation pathways and mechanism. *Sep. Purif. Technol.* 245, 116449. doi:10.1016/j.seppur.2019.116449
- Zielin'ska, M., Bulowska, K., Cydzik-Kwiatkowska, A., Bernat, K., and Wojnowska-Baryła, I. (2016). Removal of bisphenol A (BPA) from biologically treated wastewater by microfiltration and nanofiltration. *Int. J. Environ. Sci. Technol.* 13, 2239–2248. doi:10.1007/s13762-016-1056-6



OPEN ACCESS

EDITED BY

Shihai Deng,
Xi'an Jiaotong University, China

REVIEWED BY

Zhifeng Hu,
Beijing Academy of Science and
Technology, China
Xiaowei Wang,
Beijing Technology and Business
University, China
Qiang Kong,
Shandong Normal University, China

*CORRESPONDENCE

Qi Zhang,
✉ qzhang@ecjtu.edu.cn
Zheng Liang,
✉ twyliang@126.com

SPECIALTY SECTION

This article was submitted to Water and
Wastewater Management,
a section of the journal
Frontiers in Environmental Science

RECEIVED 31 October 2022

ACCEPTED 12 December 2022

PUBLISHED 22 December 2022

CITATION

Zhang Q, Liang Z, Guan X, Liang J and
Gao P (2022), Application of
iron-carbon microbial galvanic
activated sludge combined with MBR
process in the treatment of wastewater
from comprehensive railway station.
Front. Environ. Sci. 10:1085386.
doi: 10.3389/fenvs.2022.1085386

COPYRIGHT

© 2022 Zhang, Liang, Guan, Liang and
Gao. This is an open-access article
distributed under the terms of the
Creative Commons Attribution License
(CC BY). The use, distribution or
reproduction in other forums is
permitted, provided the original
author(s) and the copyright owner(s) are
credited and that the original
publication in this journal is cited, in
accordance with accepted academic
practice. No use, distribution or
reproduction is permitted which does
not comply with these terms.

Application of iron-carbon microbial galvanic activated sludge combined with MBR process in the treatment of wastewater from comprehensive railway station

Qi Zhang^{1*}, Zheng Liang^{2*}, Xiaotao Guan¹, Jingwen Liang¹ and
Pan Gao¹

¹School of Civil Engineering and Architecture, East China Jiaotong University, Nanchang, China,

²Planning and Standard Research Institute, The National Railway Administration of the Republic of China, Beijing, China

The application of iron-carbon microbial cell activated sludge (ICMC-AS) was carried out in a membrane bioreactor (MBR) processor to treat wastewater from an integrated railway station. Results showed that the chemical oxygen demand (COD), total nitrogen (TN), and total phosphorus (TP) removal efficiencies of the original MBR processor increased from 80%, 30%, and 10% to 92%, 93.5%, and 92%, respectively. Further research showed that the combined sewage treatment system also had a strong impact resistance ability. The combined sewage treatment system ran stably when the COD, TN, and TP concentrations changed greatly. The in-depth analysis of the reaction process and reaction rate of the combined sewage treatment system revealed that the combined system is dominated by COD removal with high nitrogen removal efficiency. The removal rate constants of various pollutants were in the order: K_{COD} (0.647 ± 0.017) > $K_{\text{NO}_3\text{-N}}$ (0.416 ± 0.044) > $K_{\text{NH}_4\text{-N}}$ (0.275 ± 0.014) > K_{TN} (0.258 ± 0.083). Calculations of the energy saving and carbon emission reduction of the combined system showed that the system's annual carbon emission reduction could reach more than 388,203.55 kg CO₂e, which remarkably improves the carbon emission reduction effect and obtains a good green effect. The results indicate that adding ICMC-AS to the MBR processor for combined wastewater treatment can substantially improve the efficiency of wastewater treatment and obtain better energy-saving and emission-reducing effects. This combined application provides an effective way for the transformation and upgrading of small- and medium-scale water treatment systems.

KEYWORDS

railway wastewater, micro-electrolytic, iron-carbon microbial galvanic cell, combined wastewater treatment, MBR, carbon emissions

1 Introduction

The basic principle of wastewater treatment by activated sludge is based on a series of electrochemical and microbial reactions, such as microelectrolysis and electronic exchange (between different microorganisms, between microorganisms and various organic or inorganic substances, and between various substances) in the water formed by iron–carbon galvanic cells. A large number of studies have shown that microelectrolysis has a remarkable degradation effect on refractory substances in sewage treatment (Deng et al., 2020a). However, the application mechanism and removal efficiency of biochemical water treatment under the action of microelectrolysis are not clear because of the complexity of the microelectrolysis process. Current research on microelectrolysis wastewater treatment focuses on iron and carbon microelectric decontamination technologies. For example, Deng et al. developed a microelectrolytic process coupled with microbial nitrogen removal, which is a contact oxidation process based on the loading of microelectrolytic biological carrier formed by mixing Fe^0 and activated carbon. The process removes nitrogen under micro-oxygen condition. The $\text{NH}_4^+\text{-N}$ and TN removal efficiencies of this process were 92.6% and 95.3%, respectively (Deng et al., 2016a). Hu et al. developed an iron-rich substrate (IRS) based on iron–carbon microelectrolysis that can be used for sediment and overlying water remediation. $\text{NH}_4^+\text{-N}$, $\text{PO}_4^{3-}\text{-P}$, organo-N, organo-P, TN, and total phosphorus (TP) in the overlying water were reduced by 48.6%, 97.9%, 34.2%, 67.1%, 53.2%, and 90.4%, respectively, by IRS during the 90 day long-term restoration. Moreover, $\text{NO}_3^-\text{-N}$, $\text{NH}_4^+\text{-N}$, and organic N in sediments were reduced by 98.5%, 26.5%, and 6.3%, respectively (Hu et al., 2020).

Engineering applications are mostly carried out by iron and carbon microelectrolysis combined with biochemical decontamination technology. For example, Qi et al. applied microelectrolysis combined with sequencing batch reactor process to treat oxytetracycline production wastewater. When the influent chemical oxygen demand (COD) was 500 mg/L, the average COD removal rate increased from 76.1% to 94.4% (Qi et al., 2016). Microelectrolysis combined with expanded granular sludge bed and anaerobic/oxic system was used to treat oxytetracycline production wastewater. The oxytetracycline removal rate in the microelectrolysis reaction cell reached more than 95% (Wu et al., 2016).

In this study, iron–carbon microbial cell activated sludge (ICMC-AS) was formed by implanting iron–carbon-based materials into activated sludge microbial mass. ICMC-AS + membrane bioreactor (MBR) process was used for wastewater treatment in an integrated railway station. In order to solve the pollution problem of low nitrogen, phosphorus and other refractory elements in the original MBR reactor. The reaction principle of ICMC-AS is shown in Equations 1–4. The operation law of the combined processing system was obtained by studying its operation efficiency and parameters. The application mechanism of biochemical water treatment under the action of microelectrolysis was clarified through in-depth analysis of the

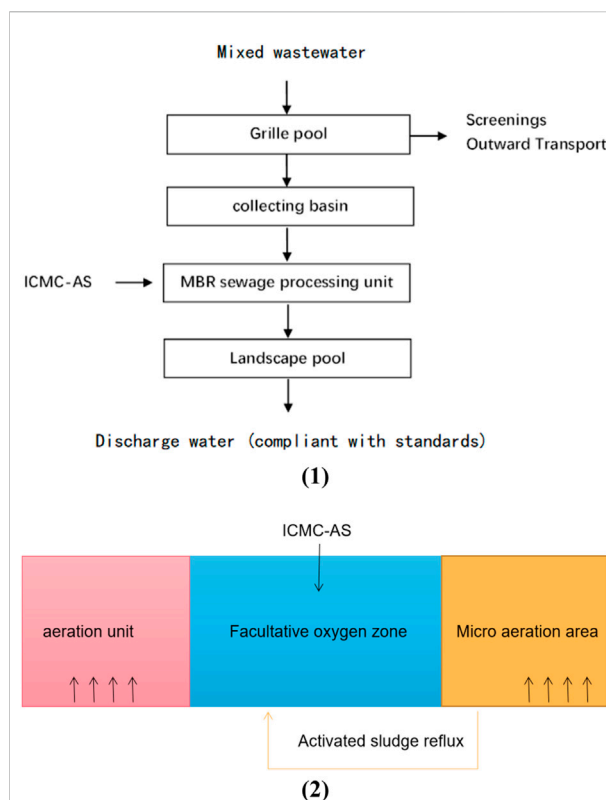
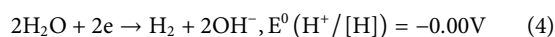
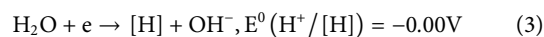
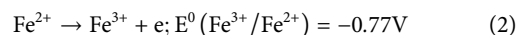
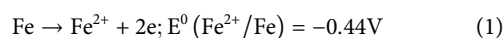


FIGURE 1
ICMC-AS combined MBR device schematic diagram and process flow chart. 1) Flow chart of Fe–C microelectrolysis combined with MBR process. 2) Schematic diagram of ICMC-AS combined MBR device.

reaction process and mechanism of the iron–carbon-based microelectrolysis wastewater treatment system. This study provides an effective way for the transformation and upgrading of small- and medium-scale water treatment systems. It also provides technical support and research data basis for the application of microelectrolysis in sewage treatment technology.



2 Materials and methods

2.1 Sewage treatment equipment and raw sewage main quality

The main body of the sewage treatment equipment is an integrated MBR reactor. Raw sewage was used to discharge

wastewater from a comprehensive railway station, which consists of a railway passenger station, a large warehouse area, and related supporting facilities. The water quality indexes were COD levels of 100–400 mg/L, NH_4^+ -N concentrations of 15–45 mg/L, TN concentrations of 20–60 mg/L, and TP concentrations of 2–6 mg/L.

2.2 Sewage treatment process

As shown in Figure 1 1) sewage from the integrated railway station was collected through the pipeline to the grid pool of the sewage treatment plant. Inorganic suspended matter in the sewage was removed through a thick and fine grid to reduce the wear on the subsequent pipelines and equipment. The effluent enters the catchment pool. As shown in Figure 1 2) A large number of facultative aerobic bacteria are contained in the facultative MBR system and can degrade organic matter in sewage by the dual action of microelectrolysis and facultative bacteria metabolism to degrade macromolecular organic pollutants into small molecular organic matter, which are eventually oxidized and decomposed into stable inorganic substances. Such as carbon dioxide and water. Moreover, power consumption is reduced, because the generation of facultative bacteria does not need the guarantee of dissolved oxygen (DO). The main function of aeration in a sewage treatment system is to scour and shock membrane filaments, and the DO produced can be used to oxidize a part of the small molecular organic matter and maintain the DO value of the effluent to ensure the normal microbial metabolism in the combined MBR system with concurrent oxygen microelectrolysis.

The design scale of the combined treatment system is 400 m³/day, the design total sludge age is infinite, the organic residual sludge discharge is nearly “zero” discharge, the mixed liquid concentration (MLSS) is 8000–20000 mg/L, and the sludge load is 0.02–0.10 kg COD/(kg MLSS-day).

2.3 Preparation of iron–carbon-based materials

The iron–carbon-based material consisted of 40%–50% elemental iron powder (300 mesh), 35%–42% activated carbon powder (200 mesh), 6%–8% metal catalyst (made of various metals), 5%–8% adhesive, and foaming agent, etc. The materials were mixed evenly to prepare 1–2 cm balls, which were dried at 105 °C for about 2 h in a drying oven, preheated at 600 °C for half an hour in a muffle furnace, and heated at 1000 °C for 3 h. After annealing and cooling, the balls were crushed and sifted to retain particles below 150 mesh. The time between production and use should not be too long and should be suitable for real-time production before use to

ensure the activity of iron powder and avoid excessive oxidation.

2.4 Analysis of operation parameters

2.4.1 Water quality index detection and analysis methods

The wastewater treatment efficiency of the new technology was determined by detecting the water quality indexes (COD_{Cr} , NH_4^+ , NO_3^- , NO_2^{2-} , TP, and TN) in and out of the MBR reactor and comparing with the corresponding indexes of the original MBR reactor without ICMC-AS. COD_{Cr} was determined by potassium dichromate method, NH_4^+ was determined by sodium chlorite spectrophotometry, NO_3^- was determined by phenol disulfonic acid spectrophotometry, NO_2^{2-} was determined by N-(1-naphthol)-ethylenediamine spectrophotometry, and TP was determined by potassium persulfate oxidation and ultraviolet spectrophotometry. TN is the sum of the values of NH_4^+ , NO_3^- , and NO_2^{2-} .

2.4.2 Reaction process data detection and reaction rate analysis

Carbon–nitrogen reaction rate was determined and the reaction characteristics of the combined process were defined by detecting the concentration changes of COD, NH_4^+ -N, NO_3^- -N, and NO_2^- -N during the operation of the MBR reactor (sampling every 30 min). The carbon–nitrogen reaction rate was calculated by the Origin software.

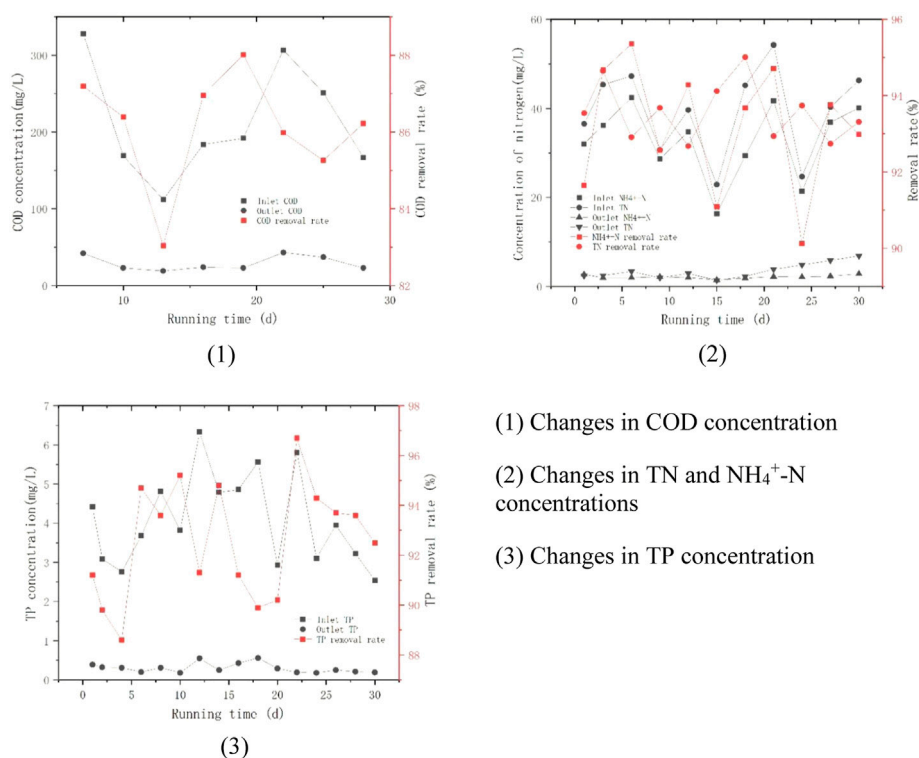
2.4.3 Estimation methods for energy saving and carbon emissions

Energy saving and carbon emission were estimated from three aspects: power consumption, water consumption, and drug consumption. Power consumption was converted according to the removal rate of the major pollutant (TN) and the increase rate. Water consumption only included the backwashing water. Other supporting water was relatively small, and water condition changed greatly; therefore, it was not measured. Carbon emissions were calculated on the basis of CO_2 .

3 Result and discussion

3.1 Variation characteristics of carbon, nitrogen, and phosphorus in the combined sewage treatment system

The data shown in Figure 2 1) show that the COD of the influent municipal sewage varies at 112–328 mg/L without regularity, and a large change in COD value will have a load impact on the water treatment system (Vleeschauwer et al., 2020). Studies have shown that such a load impact will often

**FIGURE 2**

Changes in water quality indicators in the combined sewage treatment system. 1) Changes in COD concentration. 2) Changes in TN and NH₄⁺-N concentrations. 3) Changes in TP concentration.

have a great impact on the water treatment system (Yadu et al., 2019). Experimental data show that the sewage treatment system formed a larger organic shock load, the stable effluent COD value was between 19 and 43 mg/L, and the water COD and effluent COD values had a significant positive correlation. However, the ratio changed, which allowed the sewage treatment system to have a good performance and strong load impact resistance. Compared with the original MBR system without ICMC-AS, the COD removal rate of the combined system increased from 80% to 92%.

As shown in Figure 2 2), the NH₄⁺-N value measured at the inlet in the small test fluctuated greatly between 16 and 42 mg/L, and the TN value was between 2 and 55 mg/L, resulting in the large load impacts of NH₄⁺-N and TN on the sewage treatment system. The load impacts of NH₄⁺-N and TN loads have great influence on water treatment system (Meng et al., 2018). The NH₄⁺-N and TN values measured at the outlet were maintained at about 2–3 mg/L, indicating that the sewage treatment system has a strong ability to resist the load impacts of NH₄⁺-N and TN. In addition, the NH₄⁺-N and TN removal rates were about 93.5% and 94%, respectively, which are not much different from the removal rates in the laboratory. This finding indicates that the removal capacities for NH₄⁺ and TN in the sewage treatment system were strong, and the current concentrations of NH₄⁺ and TN did not

(1) Changes in COD concentration

(2) Changes in TN and NH₄⁺-N concentrations

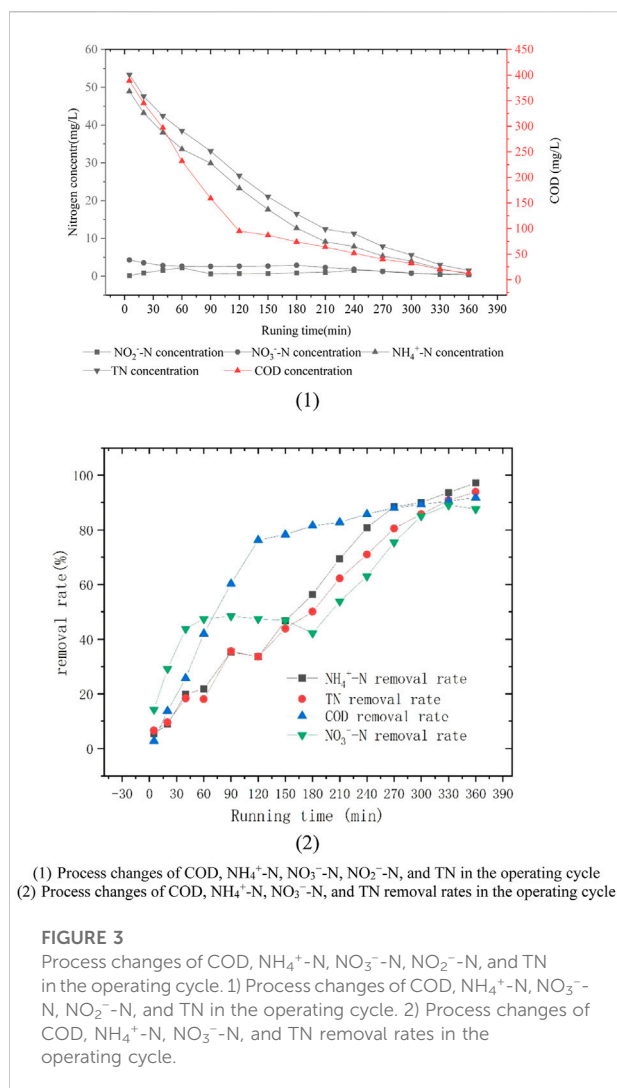
(3) Changes in TP concentration

reach the treatment limits. Additionally, the results show that the sewage treatment system has strong adaptability and adjustment ability and can maintain efficient nitrogen pollutant removal ability under a large load shock. Compared with the original MBR system without ICMC-AS, the NH₄⁺-N and TN removal rates increased from 40% and 30% to 93% and 93.5%, respectively, in the combined system.

As shown in Figure 2 3), the sewage treatment system has a good removal effect. TP values oscillated between 2 and 6 mg/L and were maintained at 0.3 mg/L after being treated by the sewage treatment system. This result indicates that the system had a stable treatment capacity for the TP of municipal sewage between 2 and 6 mg/L (most municipal sewage is within this range), and its removal rate was 92.58% on average. Compared with the original MBR system without ICMC-AS, the TP removal rate of the combined system increased from 10% to 92%.

3.2 Variation characteristics of carbon and nitrogen in the combined sewage treatment system during operation

As shown in Figure 3 1), COD was removed by rapid consumption within the first 120 min, and the value decreased

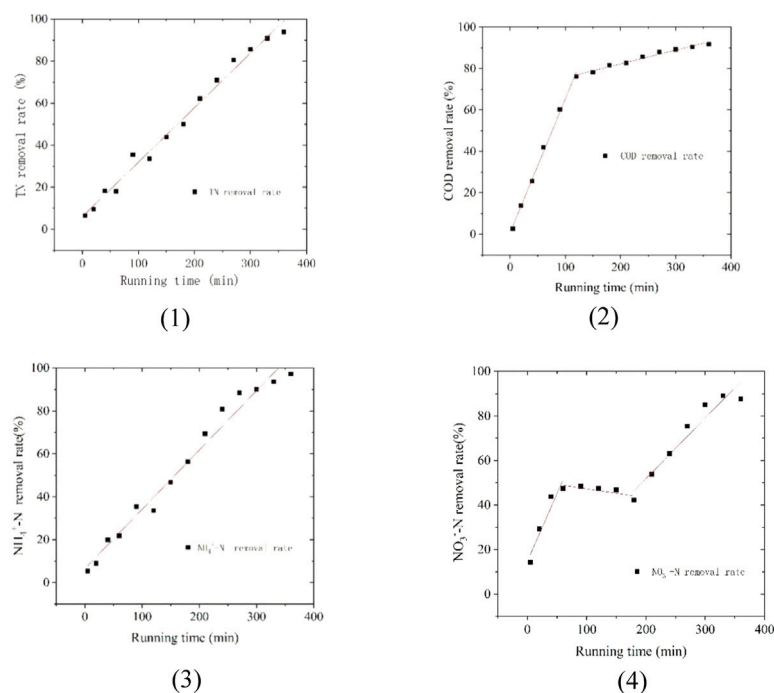


from 400 mg/L to 100 mg/L. NH_4^+ -N decreased from 20 mg/L to 2.32 mg/L within 270 min, and NH_4^+ -N decreased more slowly at 40–60 and 90–120 min. The DO values in these two periods oscillated between 0.2 and 0.3 mg/L, indicating that the biochemical reaction of the system was very violent between 0 and 120 min, which made the DO values hover between 0.2 and 0.3 mg/L and inhibited NH_4^+ -N decomposition. However, NO_3^- -N concentration decreased from 5 mg/L to 2.81 mg/L between 0 and 40 min, increased from 2.58 mg/L to 2.89 mg/L between 40 and 180 min, and gradually decreased to 0.65 mg/L between 180 and 360 min. This finding is because the concentration change of NO_3^- -N is affected by nitrification and denitrification reactions, as well as the biochemical reactions of other elements (such as the biochemical absorption of iron and carbon) (Xing et al., 2016). Therefore, during the first 0–40 min, NO_3^- -N gradually entered the adsorption plane of various reactions and participated in various reactions. Therefore, its value was rapidly reduced to 2.81 mg/L. When these

participating reactions reached saturation or equilibrium state, it reflects the comparison between the rates of nitrification reaction (NO_3^- -N generation) and denitrification reaction (NO_3^- -N transformation and removal) (Deng et al., 2016b). When the rates of nitrification and denitrification reactions reach equilibrium, the value of NO_3^- -N will keep oscillating within a certain numerical range. However, when the denitrification reaction is larger than the nitrification reaction, the value of NO_3^- -N will gradually decrease. In this case, NO_2^- -N is usually seen as an intermediate product in the conversion of NH_4^+ -N to NO_3^- -N (Deng et al., 2020b). NO_2^- -N accumulated gradually from 0 mg/L to 2.21 mg/L at 0–60 min, decreased to 0.61 mg/L at 40–90 min, accumulated gradually accumulated from 0.61 mg/L to 1.57 mg/L at 90–240 min, and then decreased to 0.35 mg/L at 240–360 min. In the whole process, the value of NO_2^- -N experienced two accumulation processes. More complex changes occurred. This change law does not accord with the characteristics of synchronous nitrification and denitrification or short-cut nitrification (Jiaohui et al., 2021; Wang et al., 2021; Tong et al., 2022a; Tong et al., 2022b). Therefore, based on the analysis of the change values of TN and DO, COD, NH_4^+ -N, NO_3^- -N, NO_2^- -N, and DO are co-changing according to a certain correlation. DO showed periodic oscillations and repeated changes during the operation of the system. The changes in DO can be divided into three stages. In the first stage, the operation time of the treatment system was between 0 and 120 min, and the DO value in this period changed between 0.1 and 0.4 mg/L. In the second stage, the operation time of the treatment system was between 120 and 270 min, and the DO value in this period varied between 1.0 and 1.4 mg/L. In the third stage, the operation time of the treatment system was between 270 and 360 min, and the DO value in this period varied between 1.8 and 2.3 mg/L.

3.3 Carbon and nitrogen removal efficiency of the combined sewage treatment system

As shown in Figure 3 2), the change rate of the NO_3^- -N process value was close to that of COD at 0–40 min, indicating that the process of NO_3^- -N reaction during this period was equally dramatic. On the one hand, the reason is that many biochemical reactions of microorganisms in the system require the participation of NO_3^- -N. On the other hand, heterotrophic denitrification bacteria at this stage have sufficient organic carbon sources and a large amount of oxygen to efficiently carry out heterotrophic denitrification and consume NO_3^- -N. At 40–180 min, the NO_3^- -N process value hardly changed and was in a relative equilibrium state because of the lack of relative oxygen and the indomance of the number of relative denitrifiers in the whole system. However, from the analysis of TN removal rate, the overall TN removal rate was maintained at a relatively high growth level. Moreover, the change rates of the decomposition and process values of NH_4^+ -N were also maintained



(1) TN rate fitting; (2) COD rate fitting; (3) $\text{NH}_4^+\text{-N}$ rate fitting; (4) $\text{NO}_3^-\text{-N}$ rate fitting

FIGURE 4

Carbon and nitrogen removal rates of the combined sewage treatment system. 1) TN rate fitting; 2) COD rate fitting; 3) $\text{NH}_4^+\text{-N}$ rate fitting; 4) $\text{NO}_3^-\text{-N}$ rate fitting.

at relatively high levels, which indicates that the nitrification and denitrification reactions were maintained at a relatively high dynamic balance. At 180–360 min, the change rate of the $\text{NO}_3^-\text{-N}$ process value was relatively large, and the COD value dropped to 57 mg/L, which made the organic carbon source become relatively short, and the $\text{NO}_3^-\text{-N}$ reaction process was transferred into the ICMC-AS. At this time, the organic carbon source materials (such as extracellular polymers, etc.) stored in ICMC-AS can be combined with the sufficient aerobic environment outside ICMC-AS to carry out heterotrophic denitrification, and the electron supply of ICMC-AS can be combined with the anoxic, facultative, and aerobic regions of MBR to carry out different degrees of autotrophic denitrification (Adav and Lee 2011; Pellicer-Nacher et al., 2013). Thus, an efficient denitrification reaction with a change rate similar to the process value of $\text{NH}_4^+\text{-N}$ can be achieved.

3.4 Carbon and nitrogen removal rate of combined sewage treatment system

As shown in Figure 4, the reaction rate constants of each substance were obtained by fitting the COD, $\text{NH}_4^+\text{-N}$, $\text{NO}_3^-\text{-N}$, and TN removal efficiencies. Among them, the K_{COD} (0–120 min) was 0.647 ± 0.017 , which is the maximum reaction rate constant of

each substance, and the minimum value of K_{TN} was 0.258 ± 0.083 . If only the conversion of $\text{NH}_4^+\text{-N}$ into $\text{NO}_3^-\text{-N}$ under aerobic condition was considered, the converted $K_{\text{NO}_3^-\text{-N}}$ will be about 0.416 ± 0.044 , but the actual conversion to $\text{NO}_3^-\text{-N}$ is not only the ammonification reaction of $\text{NH}_4^+\text{-N}$. The actual value of $K_{\text{NO}_3^-\text{-N}}$ will be higher than 0.416. Ammonification reaction is the main way to convert $\text{NH}_4^+\text{-N}$ to $\text{NO}_3^-\text{-N}$; thus, other transformation ways are greatly affected by the reaction conditions. Here, we only calculated the $\text{NH}_4^+\text{-N}$ ammonification reaction after weighted estimation. According to the size of the reaction rate constant, the reaction rates were in the order: $K_{\text{COD}} (0.647 \pm 0.017) > K_{\text{NO}_3^-\text{-N}} (0.416 \pm 0.044) > K_{\text{NH}_4^+\text{-N}} (0.275 \pm 0.014) > K_{\text{TN}} (0.258 \pm 0.083)$. Therefore, the combined application system is a wastewater treatment system with high nitrogen removal efficiency dominated by COD removal. The removal rates of various pollutants were in the order of: $\text{COD} > \text{NO}_3^-\text{-N} > \text{NH}_4^+\text{-N} > \text{TN}$.

3.5 Variation of membrane contamination in the combined sewage treatment system

Membrane contamination is inevitable during the operation of the combined system. The system stops the sewage treatment operation and starts the membrane cleaning operation when the

membrane pressure difference reaches 50 kPa. The membrane cleaning system adopts full automatic control. The membrane pressure difference of the original MBR system reached 50 kPa between 5 and 7 days, whereas that of the combined system reached 50 kPa between 7 and 10 days. This finding indicates that the combined system effectively mitigated the membrane contamination. Compared with the original MBR system, the sludge settling performance of the combined system was remarkably improved, and the settling performance of the combined system can reach the settling effect of the original system (30 min) in 5 min.

3.6 Energy saving and carbon emission reduction measurement of the combined sewage treatment system

The sewage treatment scale of the railway station is 3,000 t/day, including six lifting pumps with a total operating power of 9 kW and six MBR wastewater processors with a total operating power of 99 kW. This scale translates into a daily power consumption of 1,903.2 kWh. According to the TN removal rate, which increased by three times conversion, a total of 1268.8 kW h/day energy saving was achieved, and the annual electricity saving was 463,112 kWh. The amount of membrane-cleaning water was 159.6 t/time, and the drug dosage was 1.92 t/day. The average membrane-cleaning volume was reduced from 61 times per year to 43 times, with a reduction of 18 times, saving 2,872.8 t of water and 34.54 t of drug consumption. According to CO₂ conversion, the annual reduction in electricity was 463,112 kWh, which corresponds to the carbon emission reduction of 363,542.92 kg CO₂e; the water saved was 2,872.8 t, which corresponds to the carbon emission reduction of 482.63 kg CO₂e; and the reduction in pharmaceutical dosage was 34.54 t, which corresponds to the comprehensive carbon emission reduction of 24,178 kg CO₂e. Therefore, the annual carbon reduction of the combined system is at least 388,203.55 kg CO₂e.

4 Conclusion

The results showed that ICMS-AS + MBR has a strong ability to resist the impacts of COD, NH₄⁺-N, and TP hydraulic loads. The COD, NH₄⁺-N, and TP values of raw water vary irregularly at 112.0–328.0, 16.0–42.0, and 2.0–6.0 mg/L, respectively, whereas the COD, TN, and TP values of the combined system were all stable in the ranges of 19.2–43.3, 2.1–3.4, and 0.3–0.4 mg/L, respectively. This finding indicates that the combined system has good resistance to hydraulic load impact and has stable effluent quality. Compared with the original MBR system without ICMC-AS, the COD, TN, and TP removal

efficiencies of the combined system increased from 80%, 30%, and 10% to 92%, 93.5%, and 92%, respectively.

The study of the operation efficiency and parameters of the combined system and the in-depth analysis of the reaction process and reaction rate of the iron-carbon microelectrolysis wastewater treatment system revealed that the combined system is a wastewater treatment system dominated by COD removal with high nitrogen removal efficiency. The removal rate constants of various pollutants were in the order: K_{COD} (0.647 ± 0.017) > $K_{\text{NO}_3^--\text{N}}$ (0.416 ± 0.044) > $K_{\text{NH}_4^+-\text{N}}$ (0.275 ± 0.014) > K_{TN} (0.258 ± 0.083).

Compared with the original MBR system, the combined system had a considerably improved sludge settling performance and can reach the settling effect of the original system (30 min) in 5 min. This performance effectively mitigated membrane contamination in the combined system.

The above results indicate that adding iron-carbon microelectrolysis activated sludge to the MBR processor for combined wastewater treatment can enhance the efficiency of wastewater treatment and obtain better energy-saving and emission-reducing effects. This combined application provides an effective way for the transformation and upgrading of small- and medium-scale water treatment systems.

Data availability statement

The original contributions presented in the study are included in the article/supplementary material, further inquiries can be directed to the corresponding authors.

Author contributions

All authors listed have made a substantial, direct, and intellectual contribution to the work and approved it for publication.

Funding

This work was funded by the Science and Technology Research Project of the Education Department of Jiangxi Province, China (No. GJJ200632).

Conflict of interest

The authors declare that the research was conducted in the absence of any commercial or financial relationships that could be construed as a potential conflict of interest.

Publisher's note

All claims expressed in this article are solely those of the authors and do not necessarily represent those of their affiliated

organizations, or those of the publisher, the editors and the reviewers. Any product that may be evaluated in this article, or claim that may be made by its manufacturer, is not guaranteed or endorsed by the publisher.

References

- Adav, S. S., and Lee, D.-J. (2011). Characterization of extracellular polymeric substances (EPS) from phenol degrading aerobic granules. *J. Taiwan Inst. Chem. Eng.* 42 (4), 645–651. doi:10.1016/j.jtice.2010.11.012
- Deng, S., Li, D., Yang, X., Xing, W., Li, J., and Zhang, Q. (2016a). Biological denitrification process based on the Fe(0)-carbon micro-electrolysis for simultaneous ammonia and nitrate removal from low organic carbon water under a microaerobic condition. *Bioresour. Technol.* 219, 677–686. doi:10.1016/j.biortech.2016.08.014
- Deng, S., Li, D., Yang, X., Zhu, S., and Li, J. (2016b). Process of nitrogen transformation and mechanism of organic carbon on denitrification, N₂O emission and NO₂ – accumulation in the iron [Fe(0)]-oxidizing supported autotrophic denitrification process. *Chem. Eng. J.* 393, 124736. doi:10.1016/j.cej.2020.124736
- Deng, S., Peng, S., Xie, B., Yang, X., Sun, S., Yao, H., et al. (2020a). Influence characteristics and mechanism of organic carbon on denitrification, N₂O emission and NO₂ – accumulation in the iron [Fe(0)]-oxidizing supported autotrophic denitrification process. *Chem. Eng. J.* 393, 124736. doi:10.1016/j.cej.2020.124736
- Deng, S., Xie, B., Kong, Q., Peng, S., Wang, H., Hu, Z., et al. (2020b). An oxic/anoxic-integrated and Fe/C micro-electrolysis-mediated vertical constructed wetland for decentralized low-carbon greywater treatment. *Bioresour. Technol.* 315, 123802. doi:10.1016/j.biortech.2020.123802
- Hu, Z., Deng, S., Li, D., Guan, D., Xie, B., Zhang, C., et al. (2020). Application of iron [Fe(0)]-rich substrate as a novel capping material for efficient simultaneous remediation of contaminated sediments and the overlying water body. *Sci. Total Environ.* 748, 141596. doi:10.1016/j.scitotenv.2020.141596
- Jiaohui, X., Dan, C., Cheng, H., Yan, L., Xinbai, J., and Jinyou, S. (2021). Reductive potential from cathode electrode as an option for the achievement of short-cut nitrification in bioelectrochemical systems. *Bioresour. Technol.* 338, 125553. doi:10.1016/j.biortech.2021.125553
- Meng, J., Li, J., Li, J., Antwi, P., Deng, K., Nan, J., et al. (2018). Enhanced nitrogen removal from piggery wastewater with high NH₄⁺ and low COD/TN ratio in a novel upflow microaerobic biofilm reactor. *Bioresour. Technol.* 249, 935–942. doi:10.1016/j.biortech.2017.10.108
- Pellicer-Nacher, C., Domingo-Felez, C., Mutlu, A. G., and Smets, B. F. (2013). Critical assessment of extracellular polymeric substances extraction methods from mixed culture biomass. *Water Res. A J. Int. water Assoc.* 47 (15), 5564–5574. doi:10.1016/j.watres.2013.06.026
- Qi, Y., Wu, S., Xi, F., He, S., Fan, C., Dai, B., et al. (2016). Performance of a coupled micro-electrolysis, anaerobic and aerobic system for oxytetracycline (OTC) production wastewater treatment. *J. Chem. Technol. Biotechnol.* 91 (5), 1290–1298. doi:10.1002/jctb.4719
- Tong, W., Jie, D., Shan-Shan, Y., Le, Z., Bing-Feng, L., Guo-Jun, X., et al. (2022a). A novel cross-flow honeycomb bionic carrier promotes simultaneous nitrification, denitrification and phosphorus removal in IFAS system: Performance, mechanism and keystone species. *Water Res.* 225, 119132. doi:10.1016/j.watres.2022.119132
- Tong, W., Yang, S. S., Zhong, L., Pang, J. W., Zhang, L., Xia, X. F., et al. (2022b). Simultaneous nitrification, denitrification and phosphorus removal: What have we done so far and how do we need to do in the future? *Sci. total Environ.* 856, 158977. doi:10.1016/j.scitotenv.2022.158977
- Vleeschauwer, F. D., Caluwé, M., Dobbeleers, T., Stes, H., Dockx, L., Kiekens, F., et al. (2020). A dynamic control system for aerobic granular sludge reactors treating high COD/P wastewater, using pH and DO sensors. *J. Water Process Eng.* 33, 101065. doi:10.1016/j.jwpe.2019.101065
- Wang, W. Q., Li, D., Gao, X., and Zhang, J. (2021). Combining different aerobic/anoxic durations with zoned sludge discharge to optimize short-cut nitrification denitrifying phosphorus removal granules in domestic sewage. *Huan jing ke xue= Huanjing kexue* 42 (9), 4406–4413. doi:10.13227/j.hjxx.202102182
- Wu, S., Qi, Y., Fan, C., Dai, B., Huang, J., Zhou, W., et al. (2016). Improvement of anaerobic biological treatment effect by catalytic micro-electrolysis for monensin production wastewater. *Chem. Eng. J.* 296, 260–267. doi:10.1016/j.cej.2016.03.140
- Xing, W., Li, D., Li, J., Hu, Q., and Deng, S. (2016). Nitrate removal and microbial analysis by combined micro-electrolysis and autotrophic denitrification. *Bioresour. Technol.* 211, 240–247. doi:10.1016/j.biortech.2016.03.044
- Yadu, A., Sahariah, B. P., and Anandkumar, J. (2019). Novel bioremediation approach for treatment of naphthalene, ammonia-N and sulphate in fed-batch reactor. *J. Environ. Chem. Eng.* 7 (5), 103388. doi:10.1016/j.jece.2019.103388



OPEN ACCESS

EDITED BY

Shihai Deng,
Xi'an Jiaotong University, China

REVIEWED BY

Binghan Xie,
Harbin Institute of Technology, Weihai,
China
Zhifeng Hu,
Beijing Academy of Science and
Technology, China

*CORRESPONDENCE

Zhiliang Yao,
✉ yaozhl@th.btbu.edu.cn

SPECIALTY SECTION

This article was submitted to Water and
Wastewater Management,
a section of the journal
Frontiers in Environmental Science

RECEIVED 15 October 2022

ACCEPTED 01 December 2022

PUBLISHED 23 January 2023

CITATION

Wang X, Zhang H, He X, Liu J, Yao Z,
Zhao H, Yu D, Liu B, Liu T and Zhao W
(2023), Contamination of per- and
polyfluoroalkyl substances in the water
source from a typical agricultural area in
North China.
Front. Environ. Sci. 10:1071134.
doi: 10.3389/fenvs.2022.1071134

COPYRIGHT

© 2023 Wang, Zhang, He, Liu, Yao,
Zhao, Yu, Liu, Liu and Zhao. This is an
open-access article distributed under
the terms of the [Creative Commons
Attribution License \(CC BY\)](https://creativecommons.org/licenses/by/4.0/). The use,
distribution or reproduction in other
forums is permitted, provided the
original author(s) and the copyright
owner(s) are credited and that the
original publication in this journal is
cited, in accordance with accepted
academic practice. No use, distribution
or reproduction is permitted which does
not comply with these terms.

Contamination of per- and polyfluoroalkyl substances in the water source from a typical agricultural area in North China

Xiaowei Wang^{1,2}, Hongwei Zhang³, Xiaosong He⁴, Jianfei Liu⁵,
Zhiliang Yao^{1,2*}, Hongbin Zhao⁵, Dayang Yu^{1,2}, Baosen Liu⁶,
Tianfu Liu⁷ and Weilong Zhao⁵

¹School of Ecology and Environment, Beijing Technology and Business University, Beijing, China,

²State Environmental Protection Key Laboratory of Food Chain Pollution Control, Beijing Technology and Business University, Beijing, China, ³School of Environmental and Municipal Engineering, Lanzhou Jiaotong University, Lanzhou, China, ⁴Chinese Research Academy of Environmental Sciences, Beijing, China, ⁵School of Civil Engineer, Henan Polytechnic University, Jiaozuo, China, ⁶School of Municipal and Environmental Engineering, Shandong Jianzhu University, Jinan, China, ⁷CRRC Environmental Science and Technology Co, Ltd., Beijing, China

There is limited information on contaminations of per- and polyfluoroalkyl substances (PFASs) in the water source affected by agricultural activities. The contamination of PFASs was investigated in the sources of agricultural groundwater and nearby surface water from an important vegetable production base supply for Beijing and Tianjin, located in North China. Σ_{13} PFAS concentrations ranged from 0.321 to 8.285 ng/L, with an average concentration of 2.022 ng/L in the groundwater and 19.673 ng/L in the surface water. With the increase in the carbon chain length, the mean concentrations of PFASs in groundwater generally showed a decreasing trend. The dominated congeners of short-chain perfluorobutanesulfonate and perfluorooctanoate acid (PFOA) were detected in all groundwater samples, with mean concentrations of 0.944 and 0.654 ng/L. The difference was that PFOA and perfluorooctanesulfonate (PFOS) were the dominant congeners in nearby surface water, with concentrations of 7.585 and 3.421 ng/L. Thus, the concentrations of PFOA and PFOS in the surface water were about 8.5 times higher than those in the groundwater, indicating that Σ_{13} PFAS concentrations might decrease with the water migration from the overground to the underground. In addition, significant correlations were observed between PFASs and DOC/TN related to agricultural activities, suggesting a certain relationship existed between PFAS congener distributions and organic carbon/nutrients in water. Health risk assessment indicated that the PFAS exposure caused insignificantly immediate harm to residents in the studied area. This survey provided information on the sources, spatial distribution, and potential migration characteristics of PFASs in a typical agricultural area of North China.

KEYWORDS

perfluoroalkyl and polyfluoroalkyl substances, water source, groundwater, agricultural activity, health risk assessment

Introduction

Per- and polyfluoroalkyl substances (PFASs) have occurred ubiquitously in the environment, causing global concerns due to their long-distance migration, bioaccumulation, and severe toxicity (Cao et al., 2019; Chen et al., 2022). Serious organic pollution in the water body leads to a decrease in the availability of usable fresh water. Additionally, they have some proprietary properties such as low surface energy and high surface-active effect as uniquely hydrophobic and lipophobic characteristics (Tang et al., 2022). However, limited information is available on PFAS contaminations in the sources of groundwater and surface water affected by agricultural activities. The Chinese government issued the *Regulations on Groundwater Management (Order No. 748 of the State Council of the people's Republic of China)* at the end of 2021 to further strengthen the monitoring and protection of groundwater, especially in agriculture and rural areas. Besides, the limit values for PFOS and PFOA in drinking water are 40 and 80 ng/L, respectively, according to the *Standards for Drinking Water Quality of China* (GB5749-2022).

PFASs have been widely applied in various fields involving people's daily consumer goods, business, and industry, such as surfactants, fire retardants, additives, lubricants, carpet cleaners, paper coatings, and cosmetics (Sims et al., 2022). PFASs have also been widely used in pesticides (herbicides, insecticides, etc.) as auxiliary agents and their packaging (Nascimento et al., 2018). As always, concerns about PFASs are increasing owing to their particular features and wide applications, as well as their global distributions and potential hazards. Therefore, PFOS, perfluorooctanoic acid (PFOA), and related compounds were listed as priority pollutants in the International Stockholm Convention (Chen et al., 2022). In the past decades, short-chain PFASs or no-fluorinated substances have been recommended by global manufacturers instead of short-chain PFASs (Sims et al., 2022; Tang et al., 2022).

A great amount of information has been available presently on the contaminations of PFASs in various environmental media such as soil (Gao et al., 2019; Sammut et al., 2019), water (Zhang et al., 2019; Wang et al., 2022), and air-dust (Liu et al., 2011; Zhang et al., 2020). PFASs have also been detected in biological tissue and blood (Valsecchi et al., 2013; Hu et al., 2023), human blood and urine (Zhang et al., 2013; Szabo et al., 2018), and remote polar regions (Pedersen et al., 2016). However, solving the problem of the exposure pathways of PFASs to the ecosystem is still the focus of all future work. Several studies indicated that drinking water sources could also be a potential exposure source (Gao et al., 2019; Barton et al., 2022). Evidently, there is a potential health risk of drinking water with PFAS contaminations for human bodies (Li et al., 2020; Lu et al., 2022). Notably, groundwater accounts for about one-third of the total water resources and twenty percent of the water supply in China. Groundwater, as one of the main global water resources, has been facing the pollution of various pollutants (i.e., PBDEs,

PAHs, nitrobenzene, and chloroethylene). Nevertheless, information on groundwater as a water source slightly contaminated by PFASs, including irrigation and drinking water sources, remains limited. A few existing reports suggested that the globally detected PFASs in groundwater were at various levels ranging from the typically measured levels of ng/L to several µg/L, dominated by perfluorinated carboxylates (PFCAs) with less than or equal to eight carbons and PFOS (Murakami et al., 2009; Bao et al., 2011; Sammut et al., 2019; Wang et al., 2022).

This study was focused on the occurrence of PFASs in groundwater sources from an important vegetable production base supply for Beijing and Tianjin, located in North China. The spatial distribution, compositional profiles, migration and source identification, and human health assessment of PFASs were conducted. This study will help develop effective strategies to monitor PFAS pollution by providing systematic data on the PFASs in this area. To accomplish the above goals, a total of 13 PFASs, including 9 PFCAs (C6–C14) and 4 PFSA (C4, C6, C8, and C10), were analyzed for groundwater samples collected from 16 private wells and one nearby surface water sample.

Materials and methods

Materials and chemicals

The standards, PFBS, perfluorohexanoic acid (PFHxA), PFHxS, perfluoroheptanoic acid (PFHpA), PFOA, perfluorononanoic acid (PFNA), perfluorodecanoic acid (PFDA), perfluoroundecanoic acid (PFUnDA), perfluorododecanoic acid (PFDoDA), perfluorotridecanoic acid (PFTrDA), and perfluorotetradecanoic acid (PFTeDA) were purchased from Sigma-Aldrich (Steinheim, Germany). PFOS was purchased from Dr. Ehrenstorfer GmbH (Germany). Perfluorodecanesulfonate (PFDS) and the internal standards of sodium perfluoro-1-[1,2,3,4-¹³C₄]octanesulfonate (¹³C₄-PFOS, MPFOS) and perfluoron-[1,2,3,4-¹³C₄]octanoic acid (¹³C₄-PFOA, MPFOA) were obtained from Wellington Laboratories (Guelph, Ontario, Canada).

Sample areas, collection, and preparation

Samples from groundwater and surface water were collected from a typical vegetable production area, an important vegetable production base supply for Beijing and Tianjin in North China in October 2021 (Figure 1). Groundwater samples from shallow aquifers were collected from 16 private wells at depths of 1.47–3.79 m (S1–S16). The groundwater from these wells is used for vegetable irrigation and drinking water for residents. Meanwhile, one surface water sample was collected from the Beijing–Hangzhou Grand Canal nearby the groundwater wells (S17). Three trip blanks filled with ultrapure water were

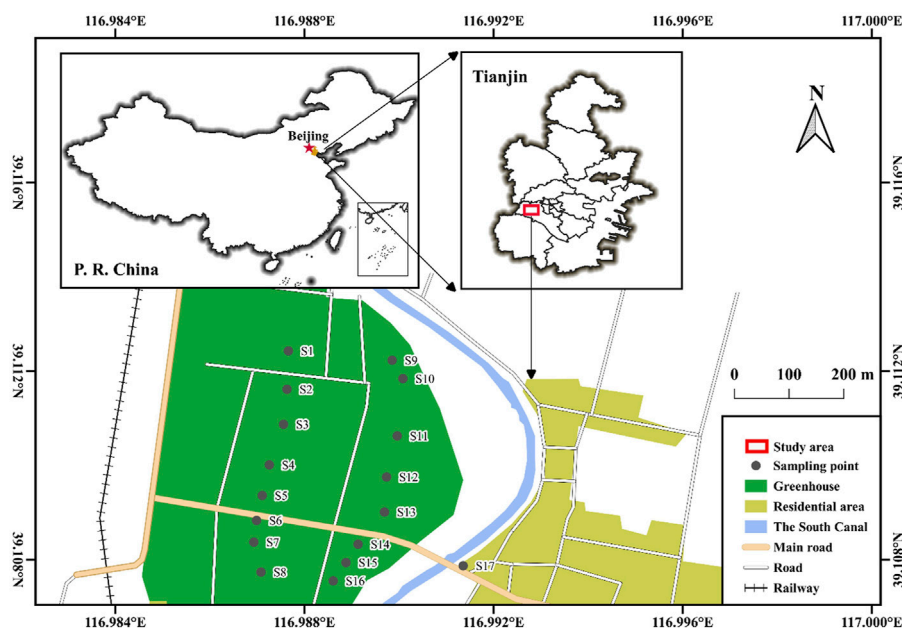


FIGURE 1

Sampling sites in the vegetable production base supply for Beijing and Tianjin, North China.

prepared. Meanwhile, six field spikes (three with target analytes of 50 ng/L, other three with target analytes of 100 ng/L) were also prepared to understand the recovery percentages of target analytes. All actual water samples were collected in duplicate. Formic acid (pH = 3–4) was added to prevent bacterial activity in water. Lastly, samples were stored at 4°C before analysis.

Sample extraction, cleanup, and instrumental analysis

The extraction, cleanup, and analysis procedures for these water samples were similar to those described previously (Wei et al., 2018). One liter of water samples was filtered through prebaked GF/F glass fiber filters (pore size: 0.7 μ m, Whatman, United States) and spiked with 2 ng of 13C4-PFOA and 13C4-PFOS as internal standards. Subsequently, the filtrates were loaded onto a single-use cartridge (Oasis® WAX), preconditioned with 4 ml of 0.1% ammonium hydroxide (in methanol), 4 ml of methanol, and 5 ml of water sequentially. Immediately, the interferences on the cartridge were washed off with 4 ml of 25 mmol/L acetate buffer solution (pH 4) and 10 ml of water. After the removal of the residual water by centrifugation for 30 min at 3,000 rpm, target analytes were eluted with 4 ml of methanol and 4 ml of 0.1% ammonium hydroxide (in methanol) successively. The flow rate was kept at 1 drop during the whole process. Then, eluate with 8 ml was concentrated to 200 μ L with a gentle stream of high-purity nitrogen before injection.

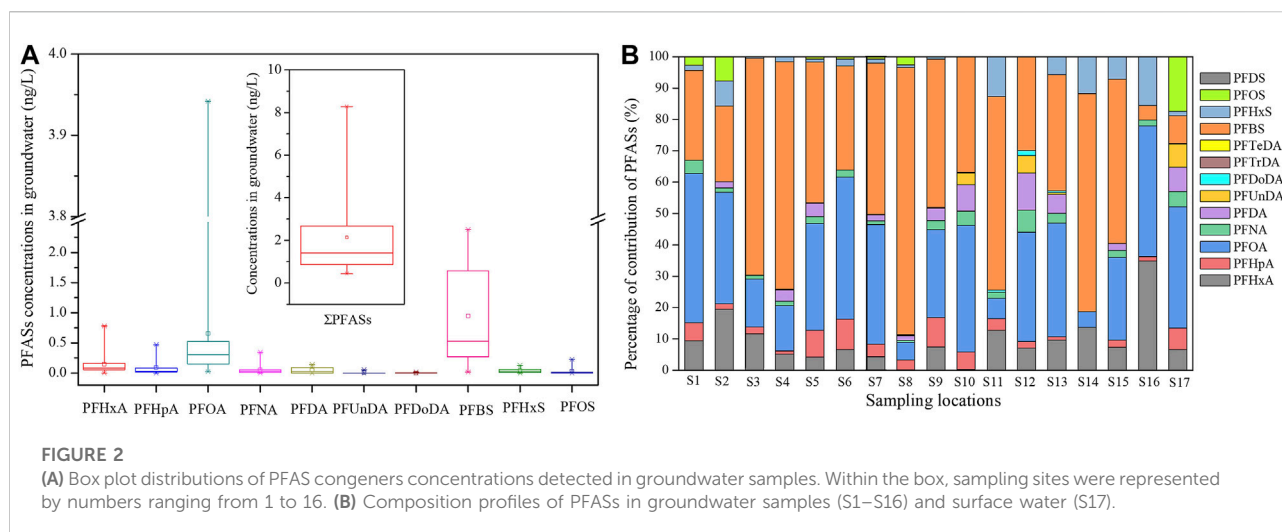
Analyses were performed for 13 PFASs using a high-performance liquid chromatography (HPLC, P680 pump, Ultimate 3000 autosampler, Dionex, Sunnyvale, CA, United States) equipped with an electrospray ionization tandem mass spectrometer (ESI/MS/MS, API 3200, Applied Biosystems/MDS SCIEX, United States) operated in negative ion and MRM mode. PFASs were separated on a 120 C18 column (5 μ m, 4.6 mm i.d. \times 150 mm length; Dionex, Sunnyvale, CA, United States) with an aliquot of 10 μ L injection. A 10 min dualistic gradient of 0.1% ammonium hydroxide (in methanol) (A) and 50 mM NH₄OAc (B) delivered at a flow rate of 1 ml/min was started with 28% B, ramped to 5% B in 4 min, held for 3 min, and then increased to 28% B gradually until the 10th min.

Quality assurance, quality control, and statistical analysis

Quantification was performed using the internal standard method. The instrumental limits of detection (LODs) varied from 0.015 to 0.047 ng/ml for each kind of PFASs at a signal-to-noise ratio (S/N) of 3 or better than 3. No detectable concentrations of PFASs were detected in trip blanks, field blanks, procedural, as well as in solvent blank in this study. Recoveries of field spikes and spiked blanks ranged from 90.2% to 107.4%, with relative standard deviations (RSD) lower than 3.8%. Average matrix spike recoveries ($n = 6$) of PFAAs in samples ranged from 80.6% to 114.7%. RSD for each kind of PFAAs were all below 10%.

TABLE 1 PFAS concentrations from worldwide in groundwater.

Location	Concentration range (mean value), ng/L										References
	PFOA	PFNA	PFBA	PFOS	PFHxS	PFBS	PFUnDA	PFDS	PFDA	PFHpA	
Tianjin, China	0.023–3.94 (0.654)	nd–0.345 (0.053)		nd–0.229 (0.026)	nd–0.129 (0.044)	0.016–2.383 (0.944)	nd–0.057 (0.008)	<LOQ	nd–0.141 (0.05)	nd–0.473 (0.094)	This study
Tianjin of China	nd–5.113	nd–0.204	0.24–5.98	nd–0.502	nd–0.23	0.08–1.21		-	-	nd–1.12	Cao et al. (2019)
Hubei, China	0.73–87.7 (8.04)	<0.03–1.08 (0.15)	22.8–8,764 (1704)	<0.04–776 (35.3)	0.4–340 (33.5)	2.98–2,744 (261)			<0.04–0.19 (0.02)	<0.04–214 (18.8)	Gao et al. (2019)
Qingdao, China	<LOQ–3.32	<LOQ–3.32	0.2–5.26	<LOQ–4.84	<LOQ–0.48	<LOQ–4.44	-	-	-	0.11–0.33	Lu et al. (2022)
Shenzhen, China (Wet)	nd–48.3 (20)	nd–10.7 (3.1)	1.2–22.6 (6.6)	0.11–47.8 (20.3)	nd–10.8 (2.2)	nd–73.5(28.3)	-	-	nd–12.6 (3.1)	nd–48.7(14.4)	Li et al. (2020)
Shenzhen, China (Dry)	nd–176.9 (31.7)	nd–4.2 (1)	nd–30.0 (11.6)	nd–49.5 (22.2)	nd–1.9 (0.58)	nd–279.3 (52.5)	-	-	nd–1.5 (0.28)	nd–31.6 (15.7)	
Suqian, China	<0.2–8.7	<0.2–8.5	<0.1–3.24	<0.53–11.6	<0.2–1.31	<0.2–23.9	<0.3–3.28		<0.5	<0.1–3.64	Wei et al. (2018)
Nanjing, China	1.275–32	0.67–16.15	1.065–8.55	0.492–24.7	<0.2–4.01	4.615–143	<0.3–3.605		<0.5	<0.1–30.8	
Xuzhou, China	<0.2–5.65	0.303–24.9	<0.1–7.85	0.299–3.8	<0.2–1.18	<0.2–29.85	<0.3		<0.5	<0.1–3.835	
North China Plain	0.03–3,540.88 (177.34)	0.01–2.85 (0.65)	<LOQ–4.77 (0.93)	<LOQ–9.31 (2.33)	<LOQ–1.09 (0.27)	<LOQ–31.98 (5.68)		<LOQ–0.76(0.04)	<LOQ–1.87 (0.23)	<LOQ–29.6 (2.59)	Li et al. (2022)
Melbourne, Australia	<0.09–6.9 (2.2)	<0.05–1.7 (<0.4)	<0.1–13 (6.1)	<0.03–34 (11)	<0.03–18 (5.9)	<0.09–9.1 (4.4)	-	<0.02–0.23 (<0.4)	<0.03–2.1 (0.31)	<0.03–5.3 (0.8)	Szabo et al. (2018)
Malta	<LOQ–8.03	nd–0.9		<LOQ–2.63	<LOQ–6.05				nd–0	nd–1.36	Sammur et al. (2019)
Greece	<0.6–0.8	<0.6	-	<0.6	<0.6	<0.6	<0.6	-	<0.6	<0.6	Zafeiraki et al. (2015)
Netherlands	<0.6–1.6	<0.6	-	<0.6–5		<0.6–0.9	<0.6	-	<0.6	<0.6	



Statistical analysis was conducted using the SPSS 18.0 (SPSS International, Chicago, United States) and OriginPro 8.0 (OriginLab, Los Angeles, United States) software. Concentrations below LOD were assigned as zero during the calculations. The possible correlations among PFASs in water samples were examined by the Spearman rank correlation analysis (2-tailed). PFASs are considered significantly different if $p < 0.05$.

Other analyses

A TOC analyzer (MultiN/C2100, Germany) was used to determine DOC after filtrating through glass fiber filters with $0.7\ \mu\text{m}$ (Whatman, United States). TN was measured by the alkali digestion method with potassium persulfate by a UV spectrophotometer.

Results and discussion

Levels and congener profiles

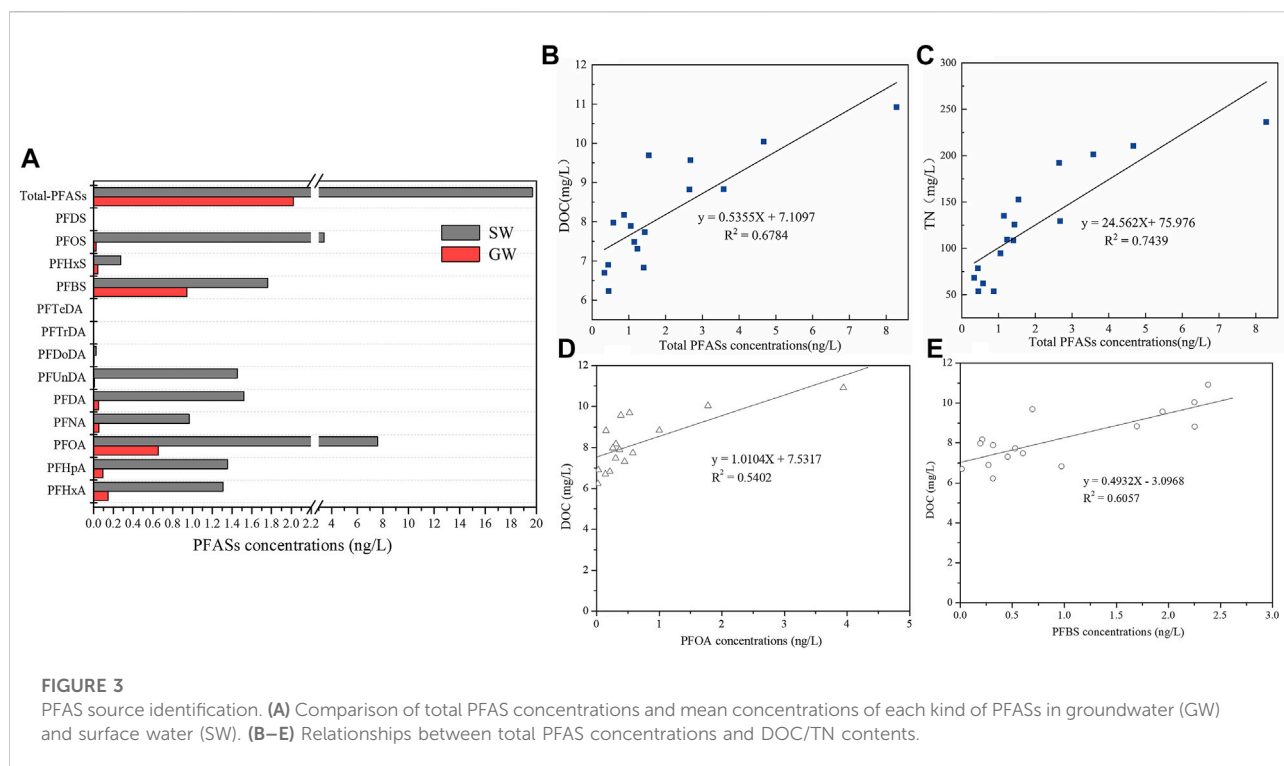
Levels and congener profiles of PFASs in the groundwater were summarized in Figure 1. It was found that $\Sigma_{13}\text{PFASs}$ in groundwater ranged from 0.321 to 8.285 ng/L (mean 2.022 ng/L). Table 1 shows that the PFAS levels in this studied area of Tianjin were close to the levels of the Yuqiao Reservoir in Tianjin found by Cao et al. (2019). However, the found levels were relatively lower than most of those in groundwater samples collected from other areas, such as Hubei, China (2.04 $\mu\text{g/L}$, nearby a PFSA manufacturing facility) (Gao et al., 2019), Shenzhen, China (dry) (135.48 ng/L) (Li et al., 2020), Melbourne, Australia (74 ng/L) (Szabo et al., 2018), Fuxin, China (485.21 ng/L) (Bao et al., 2011), and Tokyo (51.649 ng/L) (Murakami et al., 2009). This could be explained that there were neither specific point pollution sources

nor heavy industrial or commercial activities observed nearby the groundwater sampling sites. This suggested that the application of pesticides might not be a major pollution source for PFASs or a few PFAS residuals in the environment were brought back by soil, degraded by organisms in the soil, or transported elsewhere by atmosphere deposition. However, future research should be conducted on soil from the upper part, characteristics of water and soil, and other coexisting matters therein to get a comprehensive understanding of the distribution and transformation characteristics of PFASs.

Ten congeners of PFASs were traced in all groundwater samples (Figure 2B), with a detection frequency of 76.9%. Meanwhile, concentrations of congener PFCAs were also detected at a comparable frequency in this study. These chemicals were dominated by PFBS and PFOA, accounting for 46% and 33%, with concentrations of 0–2.382 (mean 1.099) and 0.025–3.942 (mean 0.806) ng/L, respectively. In detail, PFBS concentrations were significantly two magnitudes higher than PFHxS and PFOS. Interestingly, a similar phenomenon was also found in groundwater collected from Fuxi, China (Bao et al., 2011). Log K_{oc} and K_d values of PFASs were significantly correlated with the length of the carbon chain. Therefore, higher short-chain PFASs were detected in the aqueous phase compared to long chains (Chen et al., 2022). With the replacement of long-chain perfluorocarbons, the short carbon chain of PFBS is becoming the main type in environmental media.

PFAS migration and source identification

Figure 2 shows that mean concentrations of PFASs in groundwater decreased with the increase in carbon chain length, consistent with the conclusion that short-chain congeners were easier to reside in groundwater (Boiteux et al., 2012). Additionally, high water–soil ratios verified the relatively



high possibility of transfer from soil to groundwater (Lindstrom et al., 2011). Similarly, our observation was also embodied indirectly by the limited removal of short-chain PFCAs by soils (Washington et al., 2010; Bao et al., 2011). It has also been noted that short-chain PFASs with a carboxylate head group presented a decreased sorption trend (Higgins and Luthy, 2006; Chen et al., 2022). Furthermore, it was also correlated with the solubility of PFASs, which increased with the decrease in carbon chain length, suggesting that the migration ability of short-chain PFASs as the superincumbent movement of the water body would be enhanced. Moreover, the point of precursor degradation also gave a reasonable explanation for the lack of detection of long-chain PFTrDA and PFTeDA in the present study.

Figure 3A shows that one corresponding surface water sample was collected from the Beijing–Hangzhou Grand Canal. It was no surprise that PFOA and PFOS in surface water were typical PFASs, up to 7.585 and 3.421 ng/L, respectively. Differently, concentrations of Σ PFASs in surface water samples were about 8.5 times higher than those in groundwater. Additionally, concentrations of every kind of PFASs detected in surface water were higher than those in the groundwater. PFAS contaminations in surface water might be influenced by industrial activities nearby.

Correlations among various PFAS congeners and total PFAS contents between groundwater and surface water were assessed, as shown in Supplementary Table S1 and Supplementary Figure S1. At different levels, the PFAS compounds exhibited significant

correlations. In particular, there were strong correlations between PFHpA and PFOA, PFHpA and PFNA, PFHpA and PFBS, PFOA and PFNA, as well as PFDA and PFUnDA with correlation coefficients of 0.831, 0.828, 0.792, 0.917, and 0.806, respectively ($p < 0.01$). PFAS contents between groundwater and surface water showed correlation coefficients of 0.814 ($p < 0.05$). Statistically significant positive correlations suggested that these chemicals might be originated from the same or similar pollution sources.

Generally, environmental sources of PFASs are difficult to identify as PFASs used in a wide variety of fields are distributed throughout the globe and undergo complicated transformation pathways (Prevedouros et al., 2006; Chen et al., 2022). In particular, in the case that we do not know the specific activity locally, it will be hard to address source identification, except that the pollution sources are definite. Given this situation that no point pollution sources existed near the sampling sites in the present study, the highest PFBS concentrations detected may be attributed to the widespread daily usage of PFASs and then percolated through the soil after the degradation of other PFASs, such as PFHxS and PFOS (Lindstrom et al., 2011; Feng et al., 2015).

To further trace the possible pollution sources, a correlation analysis was conducted between concentrations of Σ_{13} PFASs and PFOA/PFBS and DOC/TN (Figures B–E). Positive correlations were observed between Σ_{13} PFASs/PFOA/PFBS and DOC/TN contents, conforming well to a linear equation with $R^2 = 0.5402$ – 0.6784 (DOC) and $R^2 = 0.7439$ (TN), respectively, by regression analysis. These results indicated that the distribution

and levels of PFASs in water body might be related to dissolved organic carbon, nutrients, and inorganic salts, which came from the exudation of agricultural fertilizer contaminated by PFASs (Sinclair et al., 2006; Qi et al., 2016) and domestic sewage influenced by PFAS-containing products (Xie et al., 2013). The performance was affected by dissolved organic matter in groundwater (Li et al., 2022). Besides, it might be affected by human activities such as organic fertilizer, plastic film, household garbage, pesticides, and pesticides, which were used in this vegetable production base. However, the recognized interaction mechanism between organic matter/nitrogen and PFAS in water remains to be further studied.

Health risk assessment

The *Standards for Drinking Water Quality of China* (GB5749-2022) established for PFASs are limited to PFOS and PFOA, with 40 and 80 ng/L, respectively. Obviously, the concentration of PFASs was lower than the national standard in the studied groundwater and surface water. Notably, researchers had brought up a new approach by providing the provisional health-related indication values (HRIVs) to assess the health risks of lifelong exposure to short-chain PFASs in drinking water, based on the estimated half-lives for the elimination of PFASs from the human bodies (Bao et al., 2011). Accordingly, HRIVs of the short-chain PFASs detected in the present study were separately set as follows: PFBS 2.96, PFHxA 1.03, PFHpA 0.28, and PFHxS 0.31 µg/L. However, the general precautionary value (PV_g) for all PFASs in drinking water was set to 0.1 µg/L in the long term (Wilhelm et al., 2010). The total PFAS concentrations, the total PFOA and PFOS concentrations, and each congener of PFAS concentration were all far lower than the lowest health-based guidance values reported accordingly, indicating that exposure to PFASs causes insignificantly immediate harm to residents in this area of North China.

Conclusion

This study showed that the short carbon chain of PFBS was the main type of PFASs. The mean concentrations of PFASs in the groundwater decreased with the increase in the carbon chain length. There was an insignificant potential risk of PFAS exposure in the studied groundwater source for vegetable planting and resident drinking. However, the detection of the dominant PFASs at relatively higher levels should be especially focused on to prevent the local residents from health hazards due to their longtime exposure to PFASs in drinking water. Further work should be done to study the PFAS contaminations in groundwater on a large scale in China. Meanwhile, related surface water and soil should be considered to obtain a comprehensive understanding of PFAS levels, characteristics, and sources. Therefore, it is meaningful to connect the occurrence and

distribution of PFASs with the site characterization parameters such as organic carbon, nutrients, inorganic constituents, and the coexisting organic contaminants.

Data availability statement

The raw data supporting the conclusions of this article will be made available by the authors without undue reservation.

Author contributions

XW: data curation, investigation, writing—original draft; HZ: investigation and data curation; XH: investigation; ZY: project administration; JL: investigation and writing—original draft; HZ: data curation; DY: investigation and writing—original draft; TL: investigation; BL and WZ: project administration and resources.

Funding

This study was supported by the State Key Laboratory for Free Exploration Project (2014-GOT-019-N-26).

Conflict of interest

TL was employed by CRRC Environmental Science and Technology Co, Ltd.

The remaining authors declare that the research was conducted in the absence of any commercial or financial relationships that could be construed as a potential conflict of interest.

Publisher's note

All claims expressed in this article are solely those of the authors and do not necessarily represent those of their affiliated organizations or those of the publisher, the editors, and the reviewers. Any product that may be evaluated in this article, or claim that may be made by its manufacturer, is not guaranteed or endorsed by the publisher.

Supplementary material

The Supplementary Material for this article can be found online at: <https://www.frontiersin.org/articles/10.3389/fenvs.2022.1071134/full#supplementary-material>

References

- Bao, J., Liu, W., Liu, L., Jin, Y., Dai, J., Ran, X., et al. (2011). Perfluorinated compounds in the environment and the blood of residents living near fluorochemical plants in Fuxin, China. *Environ. Sci. Technol.* 45, 8075–8080. doi:10.1021/es102610x
- Barton, K.-E., Zell-Baran, L.-M., DeWitt, J.-C., Brindley, S., McDonough, C.-A., Higgins, C.-P., et al. (2022). Cross-sectional associations between serum PFASs and inflammatory biomarkers in a population exposed to AFFF-contaminated drinking water. *Int. J. Hyg. Environ. Health* 240, 113905. doi:10.1016/j.ijheh.2021.113905
- Boiteux, V., Dauchy, X., Rosin, C., and Munoz, J.-F. (2012). National screening study on 10 perfluorinated compounds in raw and treated tap water in France. *Arch. Environ. Contam. Toxicol.* 63, 1–12. doi:10.1007/s00244-012-9754-7
- Cao, X., Wang, C., Lu, Y., Zhang, M., Khan, K., Song, S., et al. (2019). Occurrence, sources and health risk of polyfluoroalkyl substances (PFASs) in soil, water and sediment from a drinking water source area. *Ecotoxicol. Environ. Saf.* 174, 208–217. doi:10.1016/j.ecoenv.2019.02.058
- Chen, Y., Wei, L.-J., Luo, W., Jiang, N., Shi, Y.-L., Zhao, P., et al. (2022). Occurrence, spatial distribution, and sources of PFASs in the water and sediment from lakes in the Tibetan Plateau. *J. Hazard. Mat.* 13, 130170. doi:10.1016/j.jhazmat.2022.130170
- Feng, X., Matt, F.-S., Thomas, R.-H., and John, S.-G. (2015). Perfluorooctane sulfonate (PFOS) and perfluorooctanoate (PFOA) in soils and groundwater of a U.S. metropolitan area: Migration and implications for human exposure. *Water Res.* 72, 64–74. doi:10.1016/j.watres.2014.09.052
- Gao, Y., Liang, Y., Gao, K., Wang, Y., Wang, C., Fu, J., et al. (2019). Levels, spatial distribution and isomer profiles of perfluoroalkyl acids in soil, groundwater and tap water around a manufactory in China. *Chemosphere* 227, 305–314. doi:10.1016/j.chemosphere.2019.04.027
- Higgins, C.-P., and Luthy, R.-G. (2006). Sorption of perfluorinated surfactants on sediments. *Environ. Sci. Technol.* 40, 7251–7256. doi:10.1021/es061000n
- Hu, W., Zhang, M.-Y., Liu, L.-Y., Zhang, Z.-F., and Guo, Y. (2023). Perfluoroalkyl and polyfluoroalkyl substances (PFASs) crossing the blood-cerebrospinal fluid barrier: Their occurrence in human cerebrospinal fluid. *J. Hazard. Mat.* 442, 130003. doi:10.1016/j.jhazmat.2022.130003
- Li, B.-B., Hu, L.-X., Yang, Y.-Y., Wang, T.-T., Liu, C., and Ying, G.-G. (2020). Contamination profiles and health risks of PFASs in groundwater of the Maozhou River basin. *Environ. Pollut.* 260, 113996. doi:10.1016/j.envpol.2020.113996
- Li, J., Peng, G., Xu, X., Liang, E., Sun, W., Chen, Q., et al. (2022). Per- and polyfluoroalkyl substances (PFASs) in groundwater from a contaminated site in the North China Plain: Occurrence, source apportionment, and health risk assessment. *Chemosphere* 302, 134873. doi:10.1016/j.chemosphere.2022.134873
- Lindstrom, A.-B., Strynar, M.-J., Delinsky, A.-D., Nakayama, S.-F., McMillan, L., Libelo, E.-L., et al. (2011). Application of WWTP biosolids and resulting perfluorinated compound contamination of surface and well water in Decatur, Alabama, USA. *Environ. Sci. Technol.* 45, 8015–8021. doi:10.1021/es1039425
- Liu, W., Chen, S., Harada, K.-H., and Koizumi, A. (2011). Analysis of perfluoroalkyl carboxylates in vacuum cleaner dust samples in Japan. *Chemosphere* 85, 1734–1741. doi:10.1016/j.chemosphere.2011.09.024
- Lu, G., Shao, P., Zheng, Y., Yang, Y., and Gai, N. (2022). Perfluoroalkyl substances (PFASs) in rivers and drinking waters from qingdao, China. *Int. J. Environ. Res. Public Health* 19, 5722. doi:10.3390/ijerph19095722
- Murakami, M., Kuroda, K., Sato, N., Fukushi, T., Takizawa, S., and Takada, H. (2009). Groundwater pollution by perfluorinated surfactants in Tokyo. *Environ. Sci. Technol.* 43, 3480–3486. doi:10.1021/es803556w
- Nascimento, R.-A., Nunoo, D.-B.-O., Bizkarguenaga, E., Schultes, L., Zabaleta, I., Benskin, J.-P., et al. (2018). Sulfuramid use in Brazilian agriculture: A source of per- and polyfluoroalkyl substances (PFASs) to the environment. *Environ. Pollut.* 242, 1436–1443. doi:10.1016/j.envpol.2018.07.122
- Pedersen, K.-E., Letcher, R.-J., Sonne, C., Dietz, R., and Styrisshave, B. (2016). Per- and polyfluoroalkyl substances (PFASs) – new endocrine disruptors in polar bears (*Ursus maritimus*)? *Environ. Int.* 96, 180–189. doi:10.1016/j.envint.2016.07.015
- Prevedouros, K., Cousins, I.-T., Buck, R.-C., and Korzeniowski, S.-H. (2006). Sources, fate and transport of perfluorocarboxylates. *Environ. Sci. Technol.* 40, 32–44. doi:10.1021/es0512475
- Qi, Y.-J., Huo, S.-L., Hu, S.-B., Xi, B.-D., Su, J., and Tang, Z.-W. (2016). Identification, characterization, and human health risk assessment of perfluorinated compounds in groundwater from a suburb of Tianjin, China. *Environ. Earth Sci.* 75, 432. doi:10.1007/s12665-016-5415-x
- Sammur, G., Sinagra, E., Sapiiano, M., Helmus, R., and de Voogt, P. (2019). Perfluoroalkyl substances in the Maltese environment – (II) sediments, soils and groundwater. *Sci. Total Environ.* 682, 180–189. doi:10.1016/j.scitotenv.2019.04.403
- Sims, J.-L., Stroski, K.-M., Kim, S., Killeen, G., Ehalt, R., Simcik, M.-F., et al. (2022). Global occurrence and probabilistic environmental health hazard assessment of per- and polyfluoroalkyl substances (PFASs) in groundwater and surface waters. *Sci. Total Environ.* 816, 151535. doi:10.1016/j.scitotenv.2021.151535
- Sinclair, E., Mayack, D.-T., Roblee, K., Yamashita, N., and Kannan, K. (2006). Occurrence of perfluoroalkyl surfactants in water, fish, and birds from New York State. *Arch. Environ. Contam. Toxicol.* 50, 398–410. doi:10.1007/s00244-005-1188-z
- Szabo, D., Coggan, T.-L., Robson, T.-C., Currell, M., and Clarke, B.-O. (2018). Investigating recycled water use as a diffuse source of per- and polyfluoroalkyl substances (PFASs) to groundwater in Melbourne, Australia. *Sci. Total Environ.* 644, 1409–1417. doi:10.1016/j.scitotenv.2018.07.048
- Tang, Z., Song, X., Xu, M., Yao, J., Ali, M., Wang, Q., et al. (2022). Effects of co-occurrence of PFASs and chlorinated aliphatic hydrocarbons on microbial communities in groundwater: A field study. *J. Hazard. Mat.* 435, 128969. doi:10.1016/j.jhazmat.2022.128969
- Valsecchi, S., Rusconi, M., and Polesello, S. (2013). Determination of perfluorinated compounds in aquatic organisms: A review. *Anal. Bioanal. Chem.* 405, 143–157. doi:10.1007/s00216-012-6492-7
- Wang, Q., Song, X., Wei, C., Ding, D., Tang, Z., Tu, X., et al. (2022). Distribution, source identification and health risk assessment of PFASs in groundwater from Jiangxi Province, China. *Chemosphere* 291, 132946. doi:10.1016/j.chemosphere.2021.132946
- Washington, J.-W., Yoo, H., Ellington, J.-J., Jenkins, T.-M., and Libelo, E.-L. (2010). Concentrations, distribution, and persistence of perfluoroalkylates in sludge-applied soils near Decatur, Alabama, USA. *Environ. Sci. Technol.* 44, 8390–8396. doi:10.1021/es1003846
- Wei, C., Wang, Q., Song, X., Chen, X., Fan, R., Ding, D., et al. (2018). Distribution, source identification and health risk assessment of PFASs and two PFOS alternatives in groundwater from non-industrial areas. *Ecotoxicol. Environ. Saf.* 152, 141–150. doi:10.1016/j.ecoenv.2018.01.039
- Wilhelm, M., Bergmann, S., and Dieter, H.-H. (2010). Occurrence of perfluorinated compounds (PFCs) in drinking water of North Rhine-Westphalia, Germany and new approach to assess drinking water contamination by shorter-chained C4-C7 PFCs. *Int. J. Hyg. Environ. Health* 213, 224–232. doi:10.1016/j.ijheh.2010.05.004
- Xie, S., Lu, Y., Wang, T., Liu, S., Jones, K., and Sweetman, A. (2013). Estimation of PFOS emission from domestic sources in the eastern coastal region of China. *Environ. Int.* 59, 336–343. doi:10.1016/j.envint.2013.06.015
- Zafeiraki, E., Costopoulou, D., Vassiliadou, I., Leondiadis, L., Dassenakis, E., Traag, W., et al. (2015). Determination of perfluoroalkylated substances (PFASs) in drinking water from The Netherlands and Greece. *Food Addit. Contam. Part A Chem. Anal. Control Expo. Risk Assess.* 32, 2048–2057. doi:10.1080/19440049.2015.1086823
- Zhang, B., He, Y., Huang, Y., Hong, D., Yao, Y., Wang, L., et al. (2020). Novel and legacy poly- and perfluoroalkyl substances (PFASs) in indoor dust from urban, industrial, and e-waste dismantling areas: The emergence of PFAS alternatives in China. *Environ. Pollut.* 263, 114461. doi:10.1016/j.envpol.2020.114461
- Zhang, D.-Q., Zhang, W.-L., and Liang, Y.-N. (2019). Adsorption of perfluoroalkyl and polyfluoroalkyl substances (PFASs) from aqueous solution – a review. *Sci. Total Environ.* 694, 133606. doi:10.1016/j.scitotenv.2019.133606
- Zhang, Y., Beesoon, S., Zhu, L., and Martin, J.-W. (2013). Biomonitoring of perfluoroalkyl acids in human urine and estimates of biological half-life. *Environ. Sci. Technol.* 47, 10619–10627. doi:10.1021/es401905e

Frontiers in Environmental Science

Explores the anthropogenic impact on our natural world

An innovative journal that advances knowledge of the natural world and its intersections with human society. It supports the formulation of policies that lead to a more inhabitable and sustainable world.

Discover the latest Research Topics

[See more →](#)

Frontiers

Avenue du Tribunal-Fédéral 34
1005 Lausanne, Switzerland
frontiersin.org

Contact us

+41 (0)21 510 17 00
frontiersin.org/about/contact

